Combined Electron Imaging and Diffraction Methods for Understanding Disordered Rocksalt Cathodes



Emma Hedley

St Catherine's College

University of Oxford

A Thesis submitted for the degree of

Doctor of Philosophy

2023

Declaration

I hereby declare that this thesis has not been submitted to any other institution for examination purposes and was solely undertaken during my DPhil studies at the University of Oxford. I also declare that, with the exception of the part detailed below, all of the work presented in this thesis is my own and where other sources have been consulted, they have been appropriately cited.

Investigations presented in Chapters 7, 8 and 9 into the disordered rocksalt cathodes were carried out in collaboration with members of the Peter Bruce group at the University of Oxford. Materials Synthesis and electrochemical testing of the materials investigated in this chapter were carried out by Liquan Pi. The research presented in Chapter 6 was carried out in collaboration with industrial sponsors PNDetector. Specifically, the original conceptualisation and implementation of the neural network structure was carried out by Bjorn Eckert. The role of the author in this chapter was to provide insights on how this neural network training and optimisation could be tailored to be more effective for typical 4D-STEM data sets. Employees of PNDetector also assisted with enabling the extraction of the hit-list-based data from the detector software.

Acknowledgements

First and foremost, endless thanks are extended to my supervisors, Professor Peter Nellist, Professor Peter Bruce and Dr Heike Solatu, without the support of whom this research would not have been possible. Thanks are given to those who provided constructive discussion on aspects of the materials under investigation, including Liquan Pi, Dr Mikkel Juelsholt, Dr Nikolaj Roth, Dr Gregory Rees and Dr Weixin Song. Current and previous members of the PDN research group are thanked for passing on their knowledge and expertise in electron microscopy, especially to Dr Colom O'leary for his initial help when I first joined the group and Dr Alex Sheader, Dr Weixin Song, Dr Ali Mostead and for their constructive advice at various stages of the work. Thanks are given to the support scientists and technical staff in the DCCEM and ePSIC for the training and practical assistance in setting up experiments and developing my skills in electron microscopy. Thanks are extended to all of the employees at PNDetector who made me feel so welcome during my time in Munich and taught me so much about the technology behind the direct electron detectors, which have revolutionised 4D-STEM. In particular, thank you to Dr Björn Eckert for teaching me how the POE-NN works and for helpful discussions on my work to adapt to the neural network. A special thanks is also afforded to my family, friends and partner Harry, who have believed in me at every stage and provided unconditional support along the way.

Abstract

The development of lithium-ion batteries is pivotal in the wide range of technologies reacquired to make more efficient use of clean energy sources, notably the transition to the wide-scale use of electric vehicles. In recent years, research into layered cathode material has pivoted to more disordered systems, which do not require the incorporation of cobalt in the composition and aim to minimise structural changes through entropy-stabilised disorder. Disordered rocksalt (DRS) cathodes have emerged as promising candidates in the field. The nature of short range order (SRO) has been identified as a determining factor in the lithium migration properties, yet very few in-depth studies exist in the literature. This thesis uses a range of electron microscopy techniques to study structural aspects of DRS cathodes, including SRO. Prior to the structural investigation of these materials a digression is taken into optimising the workflow for 4-dimensional scanning transmission electron microscopy (4D-STEM) data, specifically, in the case of low-dose imaging of beam-sensitive materials, including potential cathode candidates.

The aforementioned digression into optimising the handling of 4D-STEM data involves an in-depth investigating the feasibility of ptychographyic reconstructions from event-based binary data. The investigation finds the method effectively reduces the data storage and processing memory requirements. An adaptation of a neural network for identifying the entry point of electrons is tested simultaneously. It is proposed that by changing the training dataset, the POE-NN method is highly adaptable to a range of experimental conditions.

The remainder of this thesis demonstrates using electron microscopy to investigate the nature of the SRO in DRS cathodes and explores its dependence on the transition metal combination. It is demonstrated that the SRO can be explained by cluster model-based correlations of 3-dimensional polyhedral. Annular dark field (ADF) imaging is used to visualise the SRO in real space and, therefore, understand the correlation length and distribution of clusters. Following this, an examination of the DRS phase of $LiMnO_2$ (LMO) is carried out, using ADF imaging to visualise the SRO for the first time. An investigation using 4D-STEM, which evidences the formation of a spinel phase upon cycling, is presented. Finally, the application of ptychography for elucidating structural aspects of DRS cathodes is established by showing that the tetrahedral sites are unoccupied in regions of the SRO and providing insights into the nature of the termination surface.

Contents

Declaration ii

Acknowledgement iii

Abstract iv

List of Figures x

List of Tables xxiii

List of Acronyms xxiv

1 Introduction 1

1.1 Background . . . 1
1.2 Motivation . . . 3
1.3 Overview of Thesis Structure . . . 3

2 Literature Review - Disordered Rocksalt Cathodes and Short Range Order 5

2.1 Introduction . . . 5
2.2 Disordered Rocksalts Short Range Order . . . 6
2.2.1 Diffuse Scattering in diffraction patterns . . . 10
2.2.2 Cluster Model for SRO . . . 11
2.3 Lithium Migration in Disordered Rocksalts . . . 14
2.4 Structural Changes on Cycling . . . 15
2.4.1 Spinel Phase . . . 15
2.4.2 Short Range Order . . . 16
2.5 O-redox in disordered rocksalts . . . 16
2.5.1 Fluorination of the anion lattice . . . 17
2.6 Summary . . . 18

3 Literature Review - Scanning Transmission Electron Microscopy and its Application to Beam Sensitive Samples 20

3.1 Advances in Scanning Transmission Electron Microscopy . . . 20
3.1.1 Annular Dark Field Imaging . . . 22

3.1.2 Developments in Electron Detectors . . . 22
3.1.3 Readout Modes of Direct Electron Detectors . . . 24
3.2 4D-STEM Techniques . . . 25
3.2.1 Ptychography Development . . . 25
3.2.2 Scanning Nano-Diffraction Techniques . . . 28
3.3 Beam Sensitive Samples . . . 29
3.3.1 Using STEM for Structural Characterisation in Battery Materials . . . 32
3.4 Summary . . . 33

4 Theory of Electron Imaging **34**
4.1 Introduction . . . 34
4.1.1 Resolution . . . 34
4.1.2 Aberrations . . . 35
4.1.3 Sample Interactions . . . 35
4.1.4 Diffraction . . . 37
4.2 Conventional-TEM . . . 40
4.2.1 STEM/CTEM Reciprocity . . . 42
4.3 Scanning Transmission Electron Microscopy . . . 43
4.3.1 Annular Bright Field . . . 43
4.3.2 Annular Dark Field . . . 44
4.3.3 Coherent STEM Imaging . . . 45
4.4 4D-STEM methods . . . 47
4.4.1 Virtual Imaging . . . 49
4.4.2 Ptychography . . . 49
4.4.3 Single Side Band . . . 52
4.4.4 Wigner Distribution Deconvolution Method . . . 52
4.4.5 Post-acquisition Aberration Correction . . . 53
4.4.6 Nanobeam Electron Diffraction . . . 55
4.5 Summary . . . 56

5 Instrumentation and Methodology **57**
5.1 Instrumentation . . . 57
5.1.1 JEOL JEM-ARM200CF . . . 57
5.1.2 JEOL JEM-3000F . . . 57
5.1.3 JEOL JEM-ARM300CF . . . 58
5.1.4 Direct Electron Detectors . . . 58
5.2 Sample Preparation and Handling . . . 61
5.3 Data Acquisition in the STEM . . . 62
5.3.1 Aberration Corrected STEM . . . 62

5.3.2 Multi-frame Data Acquisition . . . 63
5.3.3 Ptychography Data Acquisition . . . 64
5.3.4 Nanobeam Electron Diffraction . . . 64
5.4 Data Procedures . . . 65
5.4.1 Ptychography Reconstructions . . . 65
5.4.2 Nanobeam Electron Diffraction Pre-processing . . . 66
5.5 Summary . . . 69

6 Optimising Ptychographic Reconstructions in the Case of Sparse Binary Data 70
6.1 Introduction . . . 70
6.2 Fourier Transform Optimisation . . . 71
6.2.1 Discrete Fourier Transform . . . 72
6.2.2 Fast Fourier transform . . . 72
6.2.3 Simplification from binary data . . . 73
6.3 Results . . . 74
6.3.1 Discrete Fourier Transform for Ptychography Reconstruction . . . 74
6.3.2 Complexity of the Binary Fourier Transform . . . 75
6.3.3 Error Propagation . . . 76
6.4 Event Streaming . . . 77
6.4.1 HDF5 event output . . . 78
6.5 Electron Entry Point Analysis . . . 78
6.5.1 Intensity Threshold . . . 80
6.5.2 Alternative Point of Entry Determination Methods . . . 82
6.6 Basics of Neural Networks . . . 83
6.6.1 Convolutional Neural Network . . . 83
6.6.2 Training Method for Supervised Neural Network . . . 84
6.7 Point of Entry Neural Network . . . 85
6.7.1 Point of Entry Neural Network Test on Experimental STEM Data 86
6.8 Optimising the Point of Entry Neural Network . . . 88
6.8.1 Certainty Threshold Matching . . . 88
6.8.2 Training data set . . . 89
6.8.3 Optimising loss Function . . . 94
6.8.4 Gain Correction . . . 97
6.9 Reconstruction Results . . . 99
6.10 Conclusions . . . 102

7 Real Space Visualisation of SRO in DRS cathodes 104
7.1 Introduction . . . 104
7.1.1 Cluster Model . . . 105

7.1.2 Linear Combinations of Clusters . . . 107
7.2 Electron Diffraction . . . 110
7.2.1 Method . . . 110
7.2.2 Results . . . 110
7.3 Annular Dark Field Imaging . . . 115
7.3.1 Imaging Method . . . 115
7.3.2 Bragg Filtering Method . . . 115
7.3.3 Results . . . 116
7.4 Real Space Interpretation . . . 119
7.4.1 Correlations in Real Space . . . 119
7.4.2 Octahedral Cluster . . . 124
7.4.3 Further Discussion LMZO . . . 129
7.5 Limitations of this Study . . . 130
7.6 Conculsions . . . 130

8 Case Study: Imaging and 4D-Diffraction Investigation of $LiMnO_2$ 132
8.1 Introduction . . . 132
8.2 SRO in $LiMnO_2$ . . . 133
8.2.1 Results . . . 134
8.3 Ball-Milling Rates Study . . . 136
8.3.1 Results . . . 136
8.4 Cycling Induced Changes in $LiMnO_2$ . . . 137
8.4.1 Results . . . 139
8.5 Conclusions . . . 146

9 Ptychography Application to Disordered Rocksalt Cathodes 147
9.1 Motivation . . . 147
9.2 Method . . . 148
9.3 Results and Discussion . . . 149
9.3.1 Rocksalt Structure . . . 149
9.3.2 Ptychographic Reconstruction of Surface Facet . . . 151
9.3.3 Nanovoids at surface . . . 152
9.4 Additional Investigations - Fluorinated Disordered Rocksalts . . . 154
9.4.1 Motivation . . . 154
9.4.2 Study of $Li_{1.2}Mn_{0.7}Ti_{0.1}O_{1.9}F_{0.1}$ . . . 155
9.5 Conclusion . . . 157

10 Conclusions and Future Directions 159
10.1 Influence of transition Metal composition on SRO . . . 159
10.2 Investigation of LMO Structure . . . 160

10.3 Development of Ptychography for low-dose applications 160
10.4 Applying ptychography to DRS cathodes 161

A Binary Fourier Transform Extenstion **162**
A.1 Extention of Binary Fourier Transform Sum in 2D 162

B Detector Corrections **164**
B.1 Detector Corrections 164
B.1.1 Offset/Noise Map 164

C Scattering Surface Intersections **166**
C.1 Scattering Surface Intersections 166

D Scattering Surface Linear Combinations **168**
D.1 Scattering Surface Linear Combinations 168

E Post-acquisition Aberration Correction **170**
E.1 Post-acquisition Aberration Correction 170

List of Publications **172**

Bibliography **173**

List of Figures

1.1 Schematic illustration of model Li-ion electrochemical cell. Figure reproduced from [2] with permission from RSC. 2

2.1 Schematic illustration of **a**) DRS structure, red spheres represent the oxide ion, while the proportion of green and purple represents the relative occupation of the cation sites by lithium and transition metal ions, respectively. **b**) fluorinated-DRS structure where the anion sites are partially occupied by fluorine, represented in yellow. 6

2.2 **a**) The average unit cell of $Nb_{1-x}CoSb$ where grey represents Nb, blue: Co and orange: Sb. **b**) Models consist of atoms in an ideal position in a half-Heusler structure or a relaxed geometry with vacancy occupancy given by partial shading. **c**) Octahedral arrangement surrounding the Sb ion with an arrow indicating the shifted position towards the vacancy. **d**) The relaxed structure of the half-Heusler model incorporating the shifts as given by the arrow directions. Figure reproduced with permission from [44] 8

2.3 **a**) Supercell model of $Li_{1.16}Ti_{0.37}Ni_{0.37}Nb_{0.10}O_2$ showing distorted lattice positions in 2D with inset 3D model also showing the shifted position of O with long and short Ti-O bonds indicated. **b**,**c**) Distribution of all bond lengths in grey, longer than average in orange and shorted than average in green for Ni-O bonds and Ti-O bonds, respectively. **d**,**e**) Red dots represent the vector shift of the centre of octahedral units. Reprinted with permission from [7]. Copyright 2023 American Chemical Society. 8

2.4 Examples of different types of substitutional SRO shown schematically for a two-component crystalline alloy. In the case of the disperse and micro-domain SSRO, the highlighted region shows the ordered area. In each case, the average unit cell is the same [45]. 9

2.5 Powder XRD profiles of $Li_xMn_{0.4}Nb_{0.3}O_2$ (x = 1,3, 1.1, 0.5) collected us a Cu $K\alpha$ source. Showing the characteristic rocksalt reflections and a broad peak at 20-25 degrees attributed to SRO. Reprinted from [31] with permission from Elsevier, copyright 2018. 11

2.6 **a**) SAED pattern for < 110 > $Li_{1.3}Nb_{0.3}Mn_{0.4}O_2$ Reprinted from [31]. Copyright 2018, with permission from Elsevier. **b**. Simulated and observed electron diffraction pattern of along < 100 >, of $Li_{1.2}Mn_{0.4}Ti_{0.4}O_2$ (LMTO) and $Li_{1.2}Mn_{0.4}Zr_{0.4}O_2$ (LMZO) [38]. **c,d** Electron diffraction patterns of pristine and cycled LMTO respectively. Reproduced from [54] with permission from John Wiley and Sons. 12

2.7 Polyhedra based on lattice sites of an FCC lattice and their respective geometric loci in reciprocal space for **a**) octahedral, **b**) cubic, **c**) 5-point planar, **d**) tetrahedral, **e**) square pyramidal and **f**) irregular tetrahedron clusters. The equations below each figure are algebraic representations of the geometric loci in reciprocal space. Figure reproduced and adapted from [56] with permission from IUCr. 13

2.8 **a**) Schematic illustration of the hopping mechanism of Li in DRS materials, following the dashed line, between two octahedral positions (denoted O) through the tetrahedral interstitial (denoted t). **b-d**) The so-called 0-TM, 1-TM and 2-TM sites, respectively. Oxide ions are illustrated as red circles, lithium ions as grey circles and transition metals as turquoise circles. Reprinted from [9], with permission from AAAS. 14

3.1 Schematic illustration of the structure of a **a**) scintillator-based detector and **b**) a direct electron detector (DED). 23

3.2 **a**) Schematic illustration of detector geometries for ptychography and simultaneous ADF. **b**) ADF image of $Li_{1.2}Mn_{0.6}Ni_{0.2}O_2$ showing contrast from the transition metal in the layered structure. **c**) Phase image reconstructed by SSB ptychography with enhanced light element contrast. Figure adapted with permission from [18]. 27

3.3 **a**) High-resolution ADF image showing the phase change from layered to rocksalt with a transition region. **b**) ADF image of an NMC layered cathode. **c-e**) NBED patterns from regions 1 - 3, respectively. Reproduced from [155] with permission from RSC. 29

3.4 Illustration of the similarity of electron beam damage and cycling in $Li_{1.2}Ni_{0.2}Mn_{0.6}O_2$. **a**) HAADF image before beam damage or cycling effects on the surface. **b**) surface reconstruction layer (SRL) due to cycling effects in the region above the dashed line. **c**) SRL after electron beam irradiation above the dashed line. Reprinted with permission from [170]. Copyright 2015 American Chemical Society. 31

4.1 **a**) Schematic ray diagram illustrating the effect of spherical aberration. **b**) Schematic ray diagram illustrating the effect of chromatic aberration. . . . 36

4.2 Geometrical illustration of the incident wavevector $\mathbf{K}_0$,and the diffracted wavevector $\mathbf{K_D}$, the vector **K** is the difference vector. 38
4.3 Schematic illustration of the Ewald sphere intersecting reciprocal lattice points. 39
4.4 Schematic ray diagram of the optical configurations of **a**) Bright-field imaging in CTEM and **b**) Diffraction mode in the CTEM. Figure adapted with permission from [195] 40
4.5 Schematic ray diagram of the SAED. The selected area aperture is inserted in the image plane, which is conjugate with the sample plane. The virtual aperture is shown as lying above the sample but actually lies in the sample plane. Dashed lines show the paths of electrons outside of the selected area aperture and do not contribute to the diffraction pattern. Figure adapted from Williams and Carter [87]. 41
4.6 Illustrative examples of SAED patterns from different kinds of samples. **a**) SAED pattern of a single crystal with superlattice spots. **b**) SAED of the sample with many small grains contributing to the diffraction produces ring features. **c**) SAED of a predominantly glass-ceramic material with an amorphous structure leading to diffuse rings of intensity; some spots can be observed originating from regions of the sample that have a crystalline structure remaining. TEM images of each sample are inset in the respective figures. 42
4.7 Schematic illustration demonstrating the reciprocal nature of the optical setup of **a**) CTEM and **b**) STEM imaging modes. 43
4.8 Schematic illustration of the detector geometries in STEM, the BF detector collects the central region of the bright field disk, the ABF detector collects the signal from the outer annulus of the bright field disk. The HAADF detector collects signals scattered to angles greater than the bright field disk. 44
4.9 Schematic Illustration of STEM showing the ABF and ADF detector geometries with typical collection angles drawn relative to the scanning transmission electron microscope (STEM) probe semi-convergence angle α. All angles are defined as semi-angles w.r.t. to the optical axis, where $\alpha_{inner} < \alpha$ and $\alpha > \beta_1 > \beta_2$. 46
4.10 Schematic of increasing convergence angle where ($\alpha_i < \alpha_j < \alpha_k$) of the focused electron probe, the first set of diffracted beams are given as $\pm g$ **a**) probe semi-angle α_i **b**) probe semi-angle α_j **c**) probe semi-angle α_k. The position of the BF detector is also shown in **c**. 47
4.11 Schematic illustration of 4D-STEM data acquisition for a focused electron beam, scanning at 9 points in the sample plane and recording 9 CBED patterns in the diffraction plane. 48

4.12 Schematic illustration of $G(\mathbf{K_f}, \mathbf{Q_p})$ showing the overlap between the direct and scattered beams at the respective spatial frequencies $+\mathbf{Q_p}$ and $-\mathbf{Q_p}$. **a**) In the case where $\alpha < \mathbf{Q_p}$, the direct and scattered beams overlap to form double overlap regions. **b**) In the case where $\alpha > \mathbf{Q_p}$, a triple overlap region forms, which contains no phase information due to destructive interference. 50
4.13 **a**) Power spectrum of $G(\mathbf{K_f}, \mathbf{Q_p})$ plotted with respect to $\mathbf{K_f}$, for a particular spatial frequency $\mathbf{Q_p}$. **b**) The modulus in arbitrary units. **c**) The phase in radians, plotted for $Q = 10.31\,mrad$ at the point [89,112] identified by the '+' on the power spectrum. 51
4.14 Graphicsal representations of **a**) the calculated aperture phase surfaec and **b**) probe function. 55

5.1 Image of the JEOL JEM-ARM200CF (S)TEM instrument used for many of the experiments in this thesis. *Image used courtesy of JEOL (UK) Ltd.*. 58
5.2 Image of the JEOL JEM-3000F electron microscope in the DCCEM, University of Oxford. 59
5.3 **a**) Cross-section illustration of the pnCCD (S)TEM camera head. **b**) Image of the pnCCD mounted on the retractable camera housing without the shielding covers. **c**) Schematic of the pnCCD imaging chip with the imaging area and direction of shifting to the readout areas shown. **d**) Image of this setup mounted on a ceramic mount. Figures adapted from [124] with permission IOP Publishing. 61
5.4 **a**) Schematic illustration of the raster scan direction. Horizontal arrows show the fast scan direction, and the fly-back direction is shown by the diagonal arrows. **b**) The raster scan with scan rotation of $90\,^\circ$ anticlockwise applied. 63
5.5 Outline of the work-flow for processing SSB or WDD ptychography reconstructions. 67
5.6 Outline of the calibrations for NBED data, process based on calculating calibrations from gold cross grating data and applying these to the experimental datasets. 68

6.1 Schematic outline of the workflows for **a**) full frame intensity 4D-STEM data and **b**) for binary data consisting of electron coordinates. 71
6.2 Plot of the time taken to perform FT on an array varying the number of hit pixels containing a value of 1. Data points in red represent the MATLAB `fft2` function, and data points in blue represent a FT using the binary sum method. 75

6.3 Sparse, binary image with random pixels assigned a value of 1, shown in yellow. All other pixels have a value of zero. 76
6.4 Differences between binary FT and MATLAB FFT algorithm. **a**) Plotting the real part of the difference array. **b**) Plotting the imaginary part of the difference array. 77
6.5 Typical intensity-based full frame CBED pattern acquired using the pnCCD. 78
6.6 Excerpt of the hdf5 readout file from a 4D-STEM dataset, referred to as a hitlist. Each event recorded on the detector is assigned an "event_id". The "frame_id" denotes the probe position, where the first frame corresponds to the probe coordinate $(0, 0)$. The id_x and id_y terms give the detector plane coordinates of the electron hits, and "Energy" is an arbitrarily scaled value relating to the intensity of the signal. 79
6.7 Examples of full-frame CBED pattern from the pnCCD for **a**) $200\,\mathrm{kV}$ electrons and **b**) $80\,\mathrm{kV}$ electrons. **c**) and **d**) are expanded views of the selected indicated in the full frame images by red and yellow squares. These demonstrate the energy deposition for $200\,\mathrm{kV}$ and $80\,\mathrm{kV}$ electrons respectively across multiple pixels. 80
6.8 (**a-f**) The intensity CBED pattern in 6.5 with a series of threshold values of 1, 2, 10, 20, 50, and 10, respectively. Pixels with values greater than the threshold are set to 1 and displayed as yellow; those below the threshold are set to 0 and displayed as blue. 81
6.9 ABF (**top row**), ADF (**second row**), phase images(**third row**), selected area regions of interest (ROIs) from the phase images (**bottom row**). These are generated using intensity CBED patterns (**first column**) and binary CBED patterns with thresholds of 5, 500 and 1000, as indicated above the respective columns. Pink boxes in the phase images indicated the ROIs below, all images with the exception of the ROIs are 256×256 pixels. . . 82
6.10 Schematic outline of the POE-NN training and prediction workflow developed in [223]. Simulated electron tracks (ground truth data) are split into training and validation data. The training data is used to train the POE-NN. The final weights are saved when one of the stopping conditions has been reached. Experimental data can then be passed to the POE-NN, and a prediction is made for each pixel of the likelihood of it being an electron point of entry. Pixels with a probability greater than some threshold are then counted as hits. 86
6.11 **a,d**) A sparse array of random hot pixels. **b,e**) Simulated electron tracks in the detector for 200 and 300 kV, respectively. **c,f**) Probability array for each pixel containing an electron hit. 87

6.12 An example validation dataset with a series of threshold values applied to the probability matrix. **a-d**) 30-90%, yellow pixels represent probabilities greater than the threshold value, and purple pixels have values lower than the threshold. **e**) Shows the ground truth hit positions given in yellow. . . 88
6.13 Initial neural network prediction of 200 kV electrons **a**) Single CBED pattern **b**) Initial neural network probability matrix. **c-e**) the probability matrix with threshold values of 30%, 50% and 70% applied respectively . . 89
6.14 Initial neural network prediction of 80 kV electrons **a**) Single CBED pattern **b**) Initial neural network probability matrix. **c-e**) the probability matrix with threshold values of 30%, 50% and 70% applied respectively . . 90
6.15 Example of training data for neural network **a**) shape map generated to define bright and dark regions. **b**) a hit map where electron hits with the detector are **c**) Monte Carlo simulation generated of electron interactions with the detector. 90
6.16 **a**) Shape map assigned by the random polygon function, yellow represents the shape assigned as high count regions. **b**) Electron hits random assigned (based on the probability in different regions) represented by yellow pixels.**c**) Simulated energy deposition in the pixels using the Monte Carlo method. **d**) The probability assigned by the neural network that each pixel represents an electron point of entry. 91
6.17 Threshold probabilities of **a**) 30%, **b**) 50% **c**) 60% **d**) 70% and **e**) 80% applied to the prediction by the neural network. **f**) The ground truth for the validation data. In all cases, yellow pixels represent electron hits. . . . 92
6.18 Threshold probabilities of **a**) 60%, **b**) 62% **c**) 64% **d**) 66% and **e**) 68% applied to the prediction by the neural network. **f**) The ground truth for the validation data. In all cases, yellow pixels represent electron hits. . . . 93
6.19 **a**) Shape map defining high and low-count regions. **b**) Shape map predicted by the neural network. 95
6.20 An example of a POE-NN model that leads to an over-prediction of the high-count region and under-prediction of the low-count region. **a**) Ground truth hits with high and low-count regions. **b**) Simulated detector interactions with the **c**) Neural network output as probability matrix. **d**) A threshold of 50% is applied to the probability matrix. **e**) A table of the relative weight of the TNR, TPR and Δ term in the high and low-loss regions defined in the loss function. 96

6.21 An example of a POE-NN model that leads to an under-prediction of the high-count region and over-prediction of the low-count region. **a**) Ground truth hits with high and low-count regions. **b**) Simulated detector interactions with the **c**) Neural network output as probability matrix. **d**) A threshold of 50% is applied to the probability matrix. **e**) A table of the relative weight of the TNR, TPR and Δ term in the high and low-loss regions defined in the loss function. 96
6.22 **a**) Individual intensity frame. **b**) The sum of all intensity frames for 4D-STEM dataset. **c**) Individual binary frame POE-NN. **d**) The sum of all POE-NN predicted frames. 98
6.23 Comparison of single detector frames **a**) Intensity raw detector readout **b**) prediction >50%) of the initial POE-NN designed by Eckert and **c**) the prediction (>50%) probability of the POE-NN adapted by training with high and low-count regions and the adapted loss function. 99
6.24 Example of the POE-NN prediction for a single detector frame for $200\,\mathrm{kV}$ electrons. **a**) Shows the probability for each pixel containing an electron POE. **b-d**) Show the determined entry points (yellow) for thresholds of 30, 50, and 70% applied to the probability. 100
6.25 Comparison of imaging results for intensity CBED patterns of **a**) ADF image and **b**) SSB phase reconstruction with **c**) ADF image and **d**) SSB phase reconstruction, the latter two based on the binary data predicted by the POE-NN. 101

7.1 Bar chart displaying the amount accessible lithium which can be extracted (blue) and then re-inserted (purple) for each composition. Cycling was carried out between 2 and $4.8\,\mathrm{V}$ at $20\,\mathrm{mAg^{-1}}$. *Electrochemical testing carried out by Liquan Pi* 106
7.2 Polyhedra indicated on FCC lattice for **a**) cubic **b**) tetrahedral, **c**) octahedral, **d**) irregular tetrahedron, **e** 5-point planar, and **f**) pyramidal clusters, alongside the respective 3-dimensional loci in reciprocal space. Lattice sites which form the respective polyhedra are indicated in green on the FCC lattice. Figure remade and adapted from de Ridder et al., which also gives the equations for each scattering surface [56]. 107
7.3 **a)** Green circles identify points on an FCC lattice which correspond to an octahedral cluster. **b)** Intersection of $<100>$ plane with the octahedral scattering surface. **c)** Intersection of $<110>$ plane with the octahedral scattering surface. **d)** Intersection of $<111>$ plane with the octahedral scattering surface. 108

7.4 **a-c**) Plotted scattering surface for a linear combination of the octahedral and cubic scattering surface equations in ratios of 2:1, 5:1 and 10:1, according to Equation 7.1.1. In the columns below each, the intersections of the scattering surfaces with low-order zone axes are plotted for each ratio. **d-f**) intersections with the < 100 > plane, **g-i**) intersections with the < 110 > plane and **k-m**) intersections with the < 110 > plane. 109
7.5 **a**) Representative TEM image of pristine $Li_{1.2}Mn_{0.4}Ti_{0.4}O_2$ particle. **b**) Selected region of the particle within the selected area aperture. 110
7.6 SAED patterns of < 100 > zone axis for **a**) $Li_{1.2}Mn_{0.4}Ti_{0.4}O_2$, **b**) $Li_{1.2}Mn_{0.4}Zr_{0.4}O_2$, **c**) $Li_{1.2}Mn_{0.6}Nb_{0.2}O_2$, **d**) $Li_{1.2}Mn_{0.6}Ta_{0.2}O_2$ 111
7.7 < 110 > SAED patterns for **a)** $Li_{1.2}Mn_{0.4}Ti_{0.4}O_2$, **b**)$Li_{1.2}Mn_{0.4}Zr_{0.4}O_2$, **c**) $Li_{1.2}Mn_{0.6}Nb_{0.2}O_2$, **d**) $Li_{1.2}Mn_{0.6}Ta_{0.2}O_2$ 112
7.8 **a**) 3D filled scattering surface for cubic cluster type, **b**) Intersection of cubic scattering surface with the < 100 > planes. **c**) Intersection of the cubic scattering surface with < 111 > planes. **d**) Intersection of the cubic scattering surface with the < 110 > planes. 113
7.9 Example of the Bragg filtering process. **a**) ADF image of LMNO. **b**) The FT of the image in **a**. **c**) The Bragg reflections are selected by masking the bright spots. **d**) The mask applied with no smoothing at the edge of the mask, the iFT is given in **f**. **e**) The masked FT with the smoothing applied at the edge of the mask, and the iFT is given in **g** 117
7.10 ADF images of orientated along the < 100 > direction of **a**) $Li_{1.2}Mn_{0.4}Ti_{0.4}O_2$, **c**) $Li_{1.2}Mn_{0.6}Ta_{0.2}O_2$ (SA) and **e**) $Li_{1.2}Mn_{0.4}Zr_{0.4}O_2$. **b,d,f** the iFT of the respective images after masking the Bragg peaks in the FT following the previously described procedure. Raw and Bragg-filtered FTs are inset between the images in each case. 118
7.11 ADF images of orientated along the < 110 > direction of **a**) $Li_{1.2}Mn_{0.4}Ti_{0.4}O_2$ (SA), **c**) $Li_{1.2}Mn_{0.6}Nb_{0.2}O_2$ (SA), **e**) $Li_{1.2}Mn_{0.6}Ta_{0.2}O_2$ (SA) and **g** $Li_{1.2}Mn_{0.4}Zr_{0.4}O_2$. **b,d,f,h**) The iFT of the respective mages after masking of the Bragg peaks in the FT following the procedure previously described. Raw and Bragg-filtered FTs are inset between the images in each case. 120
7.12 Schematic representation of Patterson function. **a** Inter-atomic vectors, (**u**, **v**,**w**) between atomic species. **b**) The correlation function representation of the inter-atomic vectors. 121
7.13 Correlograph from unfiltered image of $Li_{1.2}Mn_{0.6}Nb_{0.2}O_2$. **a**) Unfiltered ADF image of LMNO. **b**) Square modulus of the FT of ADF image. **c**) Correlograph, derived by taking the iFT of the square modulus. 122

7.14 **a**) Bragg filtered ADF image of LMNO. **b**) Square modulus of the FT of the Bragg filtered image. **c**) Correlograph formed by taking the iFT of the square modulus. **d**) Bragg filtered ADF image of LMNO with a dampening gradient applied at the edges. **e**) Square modulus of the FT of the dampened Bragg filtered image. **f**) Correlograph formed by taking the iFT of the square modulus of the dampened Bragg filtered image. 123

7.15 Selected regions of the Bragg filtered images with the central region of each correlograph inset in the corner of each image. In figures **a**) of LMNO and **b**) of LMTaO an example of a positive correlation vector is indicated in the correlograph by an orange vector, which is translated onto the image in selected regions to indicate these correlations on the images. A green line is used to indicate a negative correlation vector on the correlograph and this is also translated onto several regions in the image where this correlation is observed. In image **c**) of LMTO only negative correlations are observed, which are indicated in the same way but in this case for two different directional correlations using yellow and orange segments. The scale and direction of the vectors indicated in the correlograph match those indicated in the images. Schematics illustrating the unit cell in this projection are shown near the scale bar on each image; only cation positions are shown, as the ADF is primarily sensitive to heavy transition metals. 124

7.16 Selected regions of the Bragg filtered images with the central region of each correlograph inset in the corner of each image. In **a**) the image of LMTO, a single negative correlation vector is indicated in the correlograph by an orange line and translated onto regions of the image where this correlation can be observed. In each of figures **b**) LMNO and **c**) LMZO example of a single positive correlation vector is indicated in the same way. Schematics close to the scale bar illustrate a single unit-cell dimension on each image. 125

7.17 Schematic illustration of two octahedra geometries based around a single anion **a**) fac - geometry **b**) mer- geometry. 126

7.18 **a**) Schematic showing the fac octahedral geometry with the < 110 > plane of an fcc lattice indicated and **b**) the corresponding ADF intensity in the < 110 > projection. **c**) Schematic showing the mer octahedral geometry with the < 110 > plane of an fcc lattice indicated and **d**) the corresponding ADF intensity in the < 110 > projection. In the ADF projection schematics, anions are shown as unfilled circles with dashed outlines. The projection of columns with only lithium are shown as dark circles, the projection of transition metal columns is shown as light grey filled circles and mixed columns are shown as representative split circles. 127

7.19 Schematic illustration of lithium metal oxide structure based on a rocksalt type lattice. Anions have been removed for clarity but occupy all octahedral sites between cations. **a**) layered structure **b**) spinel-like structure **c**) has a typical $\gamma-LiFeO_2$ structure. The connection between a single octahedral unit is highlighted in bold in each case. 128

8.1 Schematics of a series of lithium manganese oxide crystal structures namely: **a**) spinel $LiMn_2O_4$, **b**) Li_2MnO_3, **c**) $o-LiMnO_2$, **d**) $m-LiMnO_2$, **e**) $Li_{2/3}[Li_{1/3}Mn_{5/6}]O_2$, **f**) $Li_p[Li_{1/4}Mn_{4}/_{4}]O_2$ and **g**) $t-LiMnO_2$. Lithium atoms are depicted by yellow spheres, manganese by purple spheres, and oxygen by grey spheres. Figure reproduced with permission from RSC [257] 133

8.2 **a**-**b**) ADF images of $LiMnO_2$ showing mixed particle size and morphology. **c**) ADF image of small crystallite within a particle of $LiMnO_2$ which shows atomic columns tilted close to zone axis. 134

8.3 **a**) ADF image of crystalline domain in $LiMnO_2$ particle tilted along the < 110 > orientation and **b**) the corresponding FFT showing Bragg peak and structured diffuse scattering. **c**) ADF of crystalline domain in $LiMnO_2$ particle tilted along the < 100 > orientation and **d**) the corresponding FFT showing Bragg peak and structured diffuse scattering. Diffuse scattering from SRO is indicated in **b** and **d** by red dashed lines. 135

8.4 ADF images of LMO in **a**) < 100 > orientation and **b**) an extract of the respective Bragg Filtered image. **c**) < 110 > orientation ADF image and **d**) the Bragg-filtered image. 136

8.5 **a**) 1st cycle charging curve, voltage vs capacity. **b**) Plot of voltage and calculated ratio of lithium extraction on the first cycle charge and discharge. In both plots ball-milling rates of $500\,\mathrm{rpm}$ - yellow, $650\,\mathrm{rpm}$ - blue and $900\,\mathrm{rpm}$ - orange are shown. *L*iquan Pi collected Electrochemical data displayed. 137

8.6 ADF images of ball-milled $LiMnO_2$. **a** and **b**) were acquired from a sample ball-milled at $900\,\mathrm{rpm}$. **c** and **d**) were acquired from a sample ball-milled at $500\,\mathrm{rpm}$. 138
8.7 HRTEM images of pristine, 1-cycle and 8-cycle $LiMnO_2$. **a**) HRTEM image of pristine $LiMnO_2$ **b**) HRTEM image of discharged $LiMnO_2$ after 1-cycle. **c**) HRTEM image of discharged $LiMnO_2$ after 8-cycles. The Fourier transform of each of the images is given below in **d-f**, respectively. Rocksalt spacings corresponding to the $<111>$ (orange), $<200>$ (pink) and $<220>$ (blue) are annotates in **d**. The Red dashed line indicates the interplanar spacing of graphitic carbon. 140
8.8 **a**) Diffraction pattern from a single probe position acquired in NBED mode. **b**) Virtual-ADF image of the sample, with a red pixel indicating the location of a single diffraction pattern. **c**) The sum of diffraction patterns from all pixels indicated in the green box **d**. Virtual- ADF detector is also shown by a transparent annulus. 141
8.9 Integrated radial profile of summed diffraction patterns from **a**) pristine, **b**) 1 cycle and **c**) 8 cycle datasets. Lines indicate spacing corresponding to spinel $<111>$ peak - green, graphite - yellow, DRS $<111>$ - grey, DRS $<200>$ - red, DRS $<220>$ - blue. 143
8.10 Radial profiles for pristine (**top-row**), 1-cycle, (**top-row**) and 8-cycle,(**top-row**) indicating regions A, B, C, and D integrated for virtual-ADF images. The virtual ADF images are shown for the respective regions in adjacent columns to the radial profiles; the real space scale bars are $40\,\mathrm{nm}$ for the pristine dataset and $80\,\mathrm{nm}$. for both the 1-cycle and 8-cycle datasets. The colour scales are self-consistent between the datasets; for each dataset the colour bar is given at the end of each row. 144

9.1 Example masks for the formation of virtual images using pixelated detector: **a**) Average CBED across all probe positions, the dashed red line defines the outside of the bright field disk. **b**) The masked region outside the bright field disk, which is used to generate simultaneous ADF image **c**) The masked annulus region within the bright field disk is used to generate ABF images. 148

9.2 Images of $Li_{1.2}Mn_{0.4}Ti_{0.4}O_2$ reconstructed from a single 4D-STEM dataset: **a**) Virtual ADF image. **b**) Virtual ABF image **c**) Aberration-corrected SSB phase reconstruction **d**) Aberration corrected WDD phase reconstruction. **e**) Power spectrum $\sum \mid G(\mathbf{K_f}, \mathbf{Q_p}) \mid^2$, plotted as a function of spatial frequency $\mathbf{Q_p}$. Both **a** and **c** have a rocksalt structure in the $<110>$ projection overlayed with cations indicated by cyan circles and anions by red circles. 150
9.3 Schematics of representative spinel structures of various cathode materials. **a**) Mn_2O_3, manganese - pink and oxygen - red. **b**) Low temperature (LT) $LiCoO_2$, lithium - cyan, cobalt - dark blue, and oxygen - red. **c**) $LiMn_2O_4$, lithium - cyan, manganese- pink and oxygen -red. All structures are shown in both the $<100>$ and $<110>$ projections. 151
9.4 Selected region of edge facet from Figure 9.2: **a**) Integrated virtual ADF image **b**) Phase image reconstructed by SSB. In both images a rocksalt structure overlayed with cations displayed in cyan and anions displayed in red. 152
9.5 Images of defect region, highlighted in red box: **a**) virtual ABF image **b**) virtual ADF images and **c**) SSB phase image. 153
9.6 Images of nanovoid region: **a**) virtual ABF image **b**) virtual ADF images and **c**) SSB phase image. 154
9.7 Demonstration of beam damage and imaging challenges associated with fluorinated DRS: **a**) ADF image of LMTOF acquired at 200 kV at room temperature **b**) ADF image of LMTOF acquired at 300 kV at room temperature **c**) ADF image of LMTOF acquired at 300 kV using cyro-holder and **d**) ronchigram image of LMTOF after several hours of imaging shows ice build-up on the sample. 156
9.8 Demonstration of cryogenic imaging conditions for LMTOF: **a**) ADF image of LMTOF acquired at 300 kV using cyro-holder **b**) FFT of image **a**, with subtle feature from SRO indicated by arrow. 157

B.1 Example detector corrections for both **a**) Offset and **b**) noise, based on dark frames from the pnCCD. 165
B.2 Gain map acquired by homogeneous illumination of the pnCCD with 200 kV electrons. 165

C.1 Plotted intersections of the octahedral, cube and tetrahedral scattering surfaces, with the $<100>$, $<110>$ and $<111>$ reciprocal lattice planes. . . . 167
C.2 Plotted intersections of the irregular tetrahedron, pyramidal and 5-point planar scattering surfaces, with the $<100>$, $<110>$ and $<111>$ reciprocal lattice planes. 167

D.1 **a-c**) Plotted Scattering surface for a linear combination of the octahedral and tetrahedral scattering surface equation in ratios of 2:1, 1:1 and 1:2, respectively, according to Equation D.1.1. In the columns below each, the intersections of the scattering surfaces with the < 100 > plane (**d-f**), the < 110 > plane (**g-i**) and the < 110 > plane (**k-m**). 169

E.1 Calculated aperture phase surface and probe function for data in Figure 9.2 used to apply post-acquisition aberration correction to images. 171

E.2 **a**) Modulus of SSB reconstruction. **b**) Phase reconstruction without post-acquisition aberration correction i.e uncorrected phase. **c**) Aberration corrected SSB phase reconstruction. **d**) Modulus of the WDD phase reconstruction. **e**) Aberration corrected WDD phase reconsrcutions 171

List of Tables

4.1 Table of aberration coefficients up to the third order. Aberration coefficients are denoted using Krivanek notation, where the term n denotes the order and k denotes the degree of azimuthal symmetry. Adapted from [91, 149]. 54

4.2 Calculated aberration coefficients for example, experimental dataset. . . . 55

5.1 Table of the modes and corresponding readout rates for JEOL 4DCanvas. Data from the pnCCD user manual [214]. 60

6.1 Complexity of the DFT and FFT algorithms based on the dimensions of the array M and N. The complexity in two dimensions is given both in the case where the array is non-square ($M \neq N$) and where the array is square ($M = N$). 73

6.2 Table of experimental acquisition parameters for the CBED patterns shown in Figure 6.5. 77

6.3 Table summarising category of pixels when comparing the predicted electron hits to the ground truth. 92

6.4 Table of the true negative, false negative, true positive and false positive rates as a percentage of the pixels in the high-count and low-count regions. The metrics are calculated by comparing the ground truth (validation data) and probability matrix with a 50% threshold applied. 94

7.1 Table of cations present in the composition analysed in this study; the corresponding atomic number, oxidation state in the pristine material, and ionic radii. In the case of Mn, the ls and hs refer to the ionic radii for the low-spin and high-spin electron configurations, respectively. The ionic radii are given for the corresponding oxidation state in an octahedral geometry. Data in the table information from Shannon et al. [244]. 105

List of Acronyms

4D-STEM 4-dimensional scanning transmission electron microscopy.

ABF annular bright field.

ADF annular dark field.

AI artificial intelligence.

BF bright field.

C-FEG cold field emission gun.

CBED convergent beam electron diffraction.

CCD charge couples devices.

CMOS complementary metal-oxide semiconductor.

CNN convolutional neural network.

CPU central processing unit.

cryo-EM cryogenic electron microscopy.

CTEM conventional transmission electron microscopy.

CTEM conventional transmission electron microscope.

CTF contrast transfer function.

DCCEM David Cockayne Centre for Electron Microscopy.

DED direct electron detectors.

DF dark field.

DFT discrete Fourier transform.

DMC dimethyl carbonate.

DPC differential phase contrast.

DQE detector quantum efficiency.

DRS disordered rocksalt.

ED electron diffraction.

EDS energy-dispersive X-ray spectroscopy.

EELS energy loss spectroscopy.

EFTEM energy filtered transmission electron microscopy.

ePIE extended iterative ptychographic engine.

ePSIC electron Physical Sciences Imaging Centre.

FCC face centred cubic.

FFT fast Fourier transform.

FN false negative.

FP false positive.

fps frames per second.

FT Fourier transform.

GMS® Gatan Microscopy Suite ®.

HAADF high angle annular dark field.

HPD hybrid pixel detectors.

HRTEM high resolution transmission electron microscopy.

iFT inverse Fourier transform.

LAADF low angle annular dark field.

Li-ion lithium ion.

LMNO $Li_{1.2}Mn_{0.6}Nb_{0.2}O_2$.

LMO $LiMnO_2$.

LMTaO $Li_{1.2}Mn_{0.6}Ta_{0.2}O_2$.

LMTO $Li_{1.2}Mn_{0.4}Ti_{0.4}O_2$.

LMTOF $Li_{1.2}Mn_{0.7}Ti_{0.1}O_{1.9}F_{0.1}$.

LMZO $Li_{1.2}Mn_{0.4}Zr_{0.4}O_2$.

MAADF medium angle annular dark field.

MAPS monolithic active pixel sensors.

NAS network attached storage.

NBED nanobeam electron diffraction.

NMC nickel, manganese, cobalt.

nmr nuclear magnetic resonance.

NN neural network.

O-redox oxygen redox.

OTF optical transfer function.

POE point of entry.

POE-NN point of entry neural network.

RAM random access memory.

ReLU rectified linear activation unit.

SA Smart-Align.

SAED selected area electron diffraction.

SCED scanning confocal electron diffraction.

SEM scanning electron microscopy.

SEM scanning electron microscope.

SEND scanning electron nanobeam diffraction.

SFTP secure file transport protocol.

SRL surface reconstruction layer.

SRO short range order.

SSB single side band.

STEM scanning transmission electron microscopy.

STEM scanning transmission electron microscope.

SVD single value decomposition.

TEM transmission electron microscope.

TM transition metal.

TN true negative.

TNR true negative rate.

TP true positive.

TPR true positive rate.

WDD Wigner distribution deconvolution.

WPOA weak phase object approximation.

XRD X-ray diffraction.

Chapter 1

Introduction

1.1 Background

Since their invention, lithium ion (Li-ion) batteries have crept into almost every one of the electronic devices that we rely on today. John B. Goodenough, M. Stanley Whittingham and Akira Yoshino, who were awarded the Nobel Prize for their groundbreaking work on Li-ion batteries, are quoted as having ”created a rechargeable world” [1]. There continues to be an ever-growing demand for more energy storage, whether to increase computational power in hand-held electronics or drive electric vehicles further. These aspirations require us to improve the ability of batteries to store and release energy efficiently when needed.

The working principle of the Li-ion battery is shown schematically in Figure 1.1 and is generally based on a standard electrochemical cell with anode and cathode electrodes separated by an electrolyte [2]. During the charging process, a voltage is applied to extract lithium from the cathode material; in the model in Figure 1.1, this is $LiCoO_2$. Lithium ions migrate through the electrolyte and are intercalated into the anode material, commonly graphite. This reaction is reversed in the discharge step and because the electrolyte typically has very high ionic conductivity but low electronic conductivity, charge compensation occurs via a flow of electrons around an external circuit.

Materials with a layered structure have been used for Li-ion battery cathodes since the early commercial Li-ion batteries, which contained $LiCoO_2$ [3], through to modern commercial cells, which often utilise layered nickel, manganese, cobalt (NMC) based compounds [4]. In optimising the relative ratio of nickel, manganese and cobalt in NMCs, it was found that cobalt is essential in maintaining the layered structure; however, eliminating cobalt is desirable because of the high costs associated with sourcing the material and ethical issues surrounding the mining process [5, 6]. Disordered rocksalt (DRS) cathodes demonstrate energy storage capacities in the region of $300\,\mathrm{mAhg^{-1}}$ while also solving many of the critical challenges for developing new sustainable cathode materials for Li-ion batteries [7]. Specifically, the choice of constituent transition metals can be broadened significantly from the options for the traditional layered cathodes, and importantly, the possibility to entirely remove cobalt from the composition can be realised [8]. This is of particular importance as the transition to electric vehicles requires mass scale-up of the

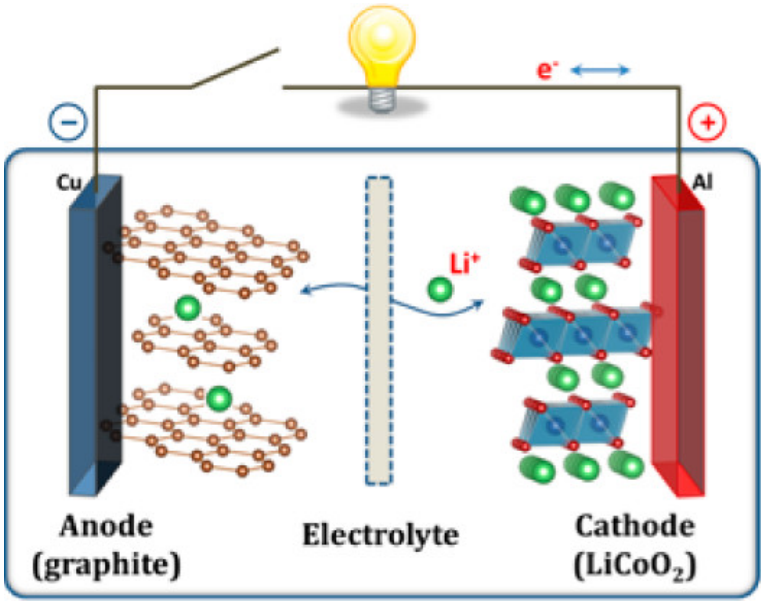


Figure 1.1: Schematic illustration of model Li-ion electrochemical cell. Figure reproduced from [2] with permission from RSC.

production of these materials, meaning scarcity and global supply chains are of critical importance [6].

To begin the push towards the practical use of DRS cathodes in Li-ion batteries, characterisation of the material's properties must be conducted, in particular, a clearer understanding of the short range order (SRO) and its link to the ability of lithium to percolate is needed [9]. SRO is understood to occur over length scales less than $1\,\mathrm{nm}$ and scanning transmission electron microscope (STEM) is the ideal tool to probe local features at such a length scale [10]. The technology in STEM has been developed to a level where atomic resolution imaging of beam-sensitive materials, such as Li-ion cathode materials, can routinely be achieved [11–14]. However, the full capabilities of STEM remain somewhat underutilised, particularly as applied to disordered materials. The disordered nature of these materials, which leads to mixed atomic columns, can make direct interpretation of images challenging; however, STEM provides an opportunity to understand the SRO at the most local scale of nearest neighbour clusters.

In relation to 4-dimensional scanning transmission electron microscopy (4D-STEM), drastic increases in the readout speeds of direct electron detectors (DED) have led to widespread application of the technique to beam sensitive materials [11]. As a result, diffraction patterns can be recorded from many more probe positions. While this has advantages, it also means that 4D-STEM experiments can produce vast quantities of data, leading to challenges in efficiently and effectively processing said data. In the case of beam-sensitive samples where dose efficiency is a primary experimental consideration, it is of particular importance that the maximum possible information from each electron-specimen interac-

tion is extracted.

1.2 Motivation

A broad range of experimental techniques is required to derive insights into the structure-property relationships of the constituent components of an electrochemical cell. A combination of X-ray diffraction (XRD), surface area analysis and magnetometry can be used to determine the material structure and morphology, which can be related to electrochemical properties, measured using techniques such as cyclic voltammetry [15, 16]. However, many of these techniques probe the average response of the material; thus, information on small features, e.g. defects, is lost. The use of electron microscopy in this thesis is motivated by a desire to understand, at the atomic scale, structural features which constitute the short range order (SRO) in disordered rocksalt (DRS) cathodes and relate these to the ability of the material to act as an effective cathode material. Several notable studies have demonstrated that STEM is an instrumental technique for providing atomic resolution imaging of cathode materials [12, 13, 17, 18]. This motivates further work to push the boundaries of the capabilities of modern direct electron detectors in their specific application to low-dose 4D-STEM experiments.

1.3 Overview of Thesis Structure

This thesis aims to draw together the latest technique advances in electron microscopy - including the development of direct electron detectors - and apply this to provide a fundamental understanding of the properties of an emerging category of cathode materials for Li-ion batteries, namely disordered rocksalts. The research work presented in the thesis is organised and structured into ten chapters. Subsequent chapters to this are each described as follows:

i) **Chapter 2** provides an overview of materials studied in this thesis and highlights the importance of characterising SRO.

ii) **Chapter 3** provides a comprehensive review of the development of electron microscopy techniques, focusing on their application to cathode materials.

iii) **Chapter 4** outlines the theoretical background of the imaging and diffraction methods utilised in the rest of the thesis.

iv) **Chapter 5** details the instrumentation and methodologies used in the following chapters.

v) **Chapter 6** presents an investigation into maximising the information available in low dose 4D-STEM datasets by identifying the electron point of entry on the detector.

vi) **Chapter 7** presents a study combining selected area electron diffraction and annular dark field imaging to give an insight into the SRO in DRS cathodes.

vii) **Chapter 8** presents a study in which 4D-STEM, scanning diffraction methods are applied to the DRS phase of $LiMnO_2$.

viii) **Chapter 9** presents initial findings of an investigation into the potential application of ptychography for understanding DRS cathodes.

ix) **Chapter 10** describes the over-arching conclusions from the studies presented and proposes future directions for further investigations.

Chapter 2

Literature Review - Disordered Rocksalt Cathodes and Short Range Order

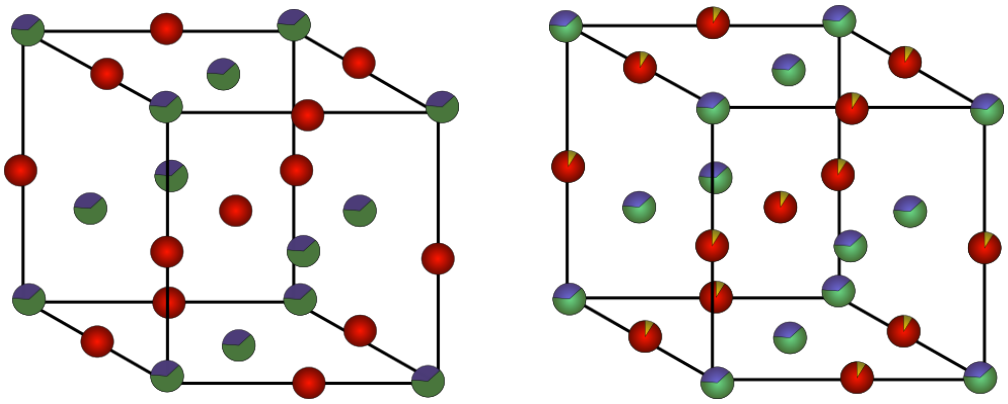
This Chapter provides the reader with an overview of the current literature on disordered rocksalt cathode materials for Li-ion batteries, focusing on the fundamental understanding of the short range order and its influence on the electrochemical performance of the cathode

2.1 Introduction

The lattice structure of disordered rocksalt (DRS) is based on two interpenetrating face centred cubic (FCC) lattices where one is occupied by anions and the other by cations. No long-range ordering exists for lithium or transition metal ions on the cation lattice sites. The anion lattice sites are predominantly occupied by oxygen, but adding fluorine can lead to disorder of the anion sub-lattice. The disordered nature is thought to improve stability by hindering structural re-arrangement during electrochemical cycling [19].

Commercial layered cathodes have distinct lithium and transition metals sites, resulting in a channel structure that allows lithium to migrate through the structure as the battery is cycled. A significant focus of the research on these materials has been focused on facilitating reversible lithium migration by maintaining the layered structure when a large proportion of the lithium has been removed [20–22]. The DRS structure was not previously considered a useful cathode material because it does not have this beneficial channel structure allowing fast rate capabilities [23]. However, further investigations revealed that cation occupations with excess lithium allow lithium to migrate through the structure via a network of percolation channels [9].

As lithium intercalates and deintercalates from the material during charging, the remaining transition metal ions change oxidation state to maintain the charge balance, most commonly utilising the $Mn^{3+} \rightarrow Mn^{4+}$ [19, 24] or $Ni^{2+} \rightarrow Ni^{4+}$ [25, 26] redox potentials. Ad-



(a) DRS structure **(b)** Fluorinated DRS structure

Figure 2.1: Schematic illustration of **a**) DRS structure, red spheres represent the oxide ion, while the proportion of green and purple represents the relative occupation of the cation sites by lithium and transition metal ions, respectively. **b**) fluorinated-DRS structure where the anion sites are partially occupied by fluorine, represented in yellow.

ditionally, the incorporation of high valence d^0 transition metals such as Ti^{4+},Zr^{4+},Nb^{5+} and Ta^{5+} allows for charge balancing of the overall formula when an excess of lithium is present. Even though d^0 transition metals can't participate in the redox behaviour, they have been shown to influence the overall electrochemical performance strongly [27]. A large variety of DRS compositions have been reported, summarised in a review by Chen et al. [28]. However, the electrochemistry of said materials is not yet optimised, with a sloping voltage profile in charge-discharge curves and gradual capacity fade commonly observed with cycling.

Electrochemical behaviour and the material's structure are inextricably linked; for example, the rate capability is determined by the ability of lithium to move through the structure [29]. Short range order (SRO) in DRS cathodes has been widely reported, but a quantitative description of the ordering is missing from the literature [26, 30–33]. The characteristics of the SRO, including length scale, homogeneity, orientation dependence, and grain boundary effects, are poorly understood. An understanding of the SRO would enable the electrochemical properties, such as rate capability and voltage hysteresis, to be linked to the preferred local arrangements of atoms, allowing rational design of high energy density DRS cathodes.

2.2 Disordered Rocksalts Short Range Order

SRO is usually defined by considering the probability of finding specific species within the first and second nearest neighbour coordination environments [34]. On this very local scale, preferential arrangements may occur more often without an identifiable regular repeating pattern on a longer length scale. Relating SRO to the properties of materials is not a

challenge unique to DRS cathodes; it affects structure-property relationships in many disordered materials such as liquid crystals [35], high entropy alloys [36], and metal-organic frameworks [37].

Using $Li_{1.2}Mn_{0.4}Ti_{0.4}O_2$ (LMTO) as an example DRS; without SRO, the occupation probability of any particular site on the FCC lattice is given only by the composition, i.e. 60% of sites are Li, 40% are transition metals (Mn and Ti). When SRO is present, the occupation of one site is no longer fully independent of its neighbours. It has been proposed by Ji et al. that interactions such as charge repulsion of high valence transition metals can lead to a statistical imbalance in the occupation of one site relative to another [38]. In the case of high valent transition metals, if one site is occupied by a transition metal (TM), then the probability that the nearest neighbour site is also occupied by TMs is less than 40%. It is then possible that such interactions can lead to energetically favourable structural motifs at a local level while the average structure remains disordered. In extreme cases, repetition of these units would form super-lattice structures [39]. Local configurations of ions may differ from the average structure and do not necessarily charge balance at the local scale. The local structure can be masked by some analytical techniques, e.g. powder-X-ray diffraction (XRD), which can only provide average structural information information [40].

Types of Short Range Order

Two common types of SRO commonly found in disordered oxides and alloys are displacive and substitutional [36, 41]. Displacive ordering involves the lengthening and contraction of bonds, which results in the displacement of atoms from their ideal lattice sites. Substitutional ordering describes ordering particular types of atoms based on the occupancy of the lattice sites.

Nan et al. attempt to categorise the SRO in $Nb_{0.8}CoSb$ as either displacive or compositional [42]. Bond lengths can vary due to the differing interaction strengths between neighbouring atoms, which can induce local positional deviations of the ions relative to the average lattice positions. The distribution of vacancies in the half-Heusler $Nb_{1-x}CoSb$ structure displays SRO, which in turn leads to a distortion in the octahedra surrounding the Sb site, as its position is shifted toward the vacancy as shown in Figure 2.2 [43, 44]. Displacive order can also be induced when the lattice site symmetry differs from the species' ideal symmetry, causing distortions in the bond angles with nearest neighbour species [41].

Displacive SRO has not been widely reported for DRS cathodes; however, at least one computational study has predicted an offset in transition metal position from the lattice site [7]. A supercell model for $Li_{1.16}Ti_{0.37}Ni_{0.37}Nb_{0.10}O_2$ generated by the reverse Monte Carlo method is shown in Figure 2.3, alongside the distribution profile of bond lengths

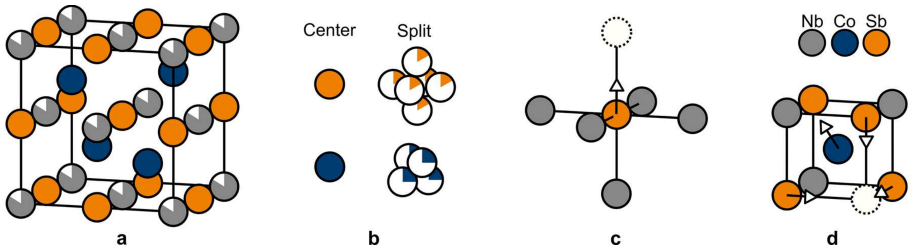


Figure 2.2: a) The average unit cell of $Nb_{1-x}CoSb$ where grey represents Nb, blue: Co and orange: Sb. **b**) Models consist of atoms in an ideal position in a half-Heusler structure or a relaxed geometry with vacancy occupancy given by partial shading. **c**) Octahedral arrangement surrounding the Sb ion with an arrow indicating the shifted position towards the vacancy. **d**) The relaxed structure of the half-Heusler model incorporating the shifts as given by the arrow directions. Figure reproduced with permission from [44]

.

and offset of the vectors for octahedral units in the supercell [7]. The authors find that considering distortions in the lattice, e.g. displacive ordering allows better agreement of predicted and experimental capacity, suggesting a more accurate interpretation of lithium percolation. The theory and application of lithium percolation are discussed further in Section 2.3.

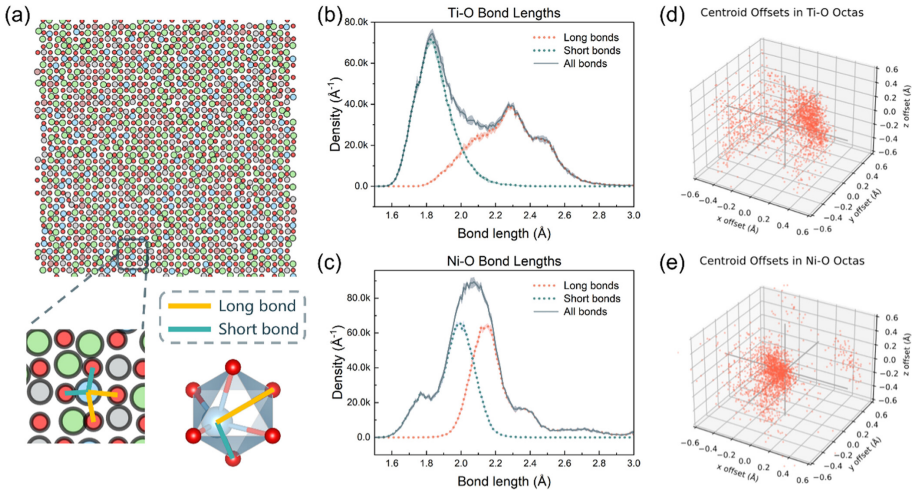


Figure 2.3: a) Supercell model of $Li_{1.16}Ti_{0.37}Ni_{0.37}Nb_{0.10}O_2$ showing distorted lattice positions in 2D with inset 3D model also showing the shifted position of O with long and short Ti-O bonds indicated. **b**,**c**) Distribution of all bond lengths in grey, longer than average in orange and shorted than average in green for Ni-O bonds and Ti-O bonds, respectively. **d**,**e**) Red dots represent the vector shift of the centre of octahedral units. Reprinted with permission from [7]. Copyright 2023 American Chemical Society.

Most studies on DRS cathodes consider substitutional ordering [31, 38]. The ordering can be either preferential configurations of the lithium relative to transition metal [38], configurations of the various transition metals relative to each other [8] or, in principle, some combination of both. Elucidating ordering preferences between transition metals relative to one another is problematic since most scattering techniques will not easily distinguish

these elements.

Substitutional SRO can be defined as statistical, disperse or micro-domain; these are shown schematically for a binary crystalline material in Figure 2.4 [45]. Statistical ordering is homogeneous throughout the sample and relates to the statistical probability of various atomic coordination arrangements. This type of SRO is typically described using Warren-Cowley parameters, which describe statistically how the composition of a particular coordination shell differs from the average stoichiometry [34]. They have since been adapted and applied to other systems, including high entropy alloys [36] and disordered rocksalts [8]. An alternative descriptor, Clapp Configurations, have also been used to describe SRO in binary alloys, based on 144 possible arrangements of nearest neighbours atoms in an FCC lattice [46]. However, extending this to DRS compounds is non-trivial as they tend to have at least three constituent elements of the cation FCC sub-lattice, leading to an enormous number of possible configurations.

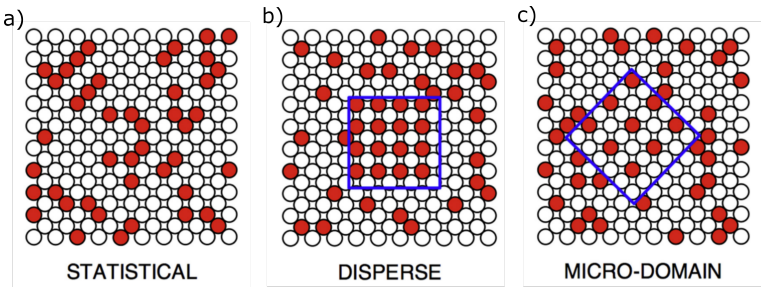


Figure 2.4: Examples of different types of substitutional SRO shown schematically for a two-component crystalline alloy. In the case of the disperse and micro-domain SSRO, the highlighted region shows the ordered area. In each case, the average unit cell is the same [45].

Micro-domain and disperse ordering are categorised by having ordered regions within an extensive disordered matrix. In the case of micro-domain, the ordered regions follow the average stoichiometry of the material. In contrast, in the disperse case, the stoichiometry of the ordered domains is different from the average composition [47]. The ordering of $Li_{1.25}Mn_{0.5}Nb_{0.25}O_2$ is found to be based on domains of γ-$LiFeO_2$ ordering which segregate onto two distinct sub-lattices, suggesting a disperse ordering type [33]. Jahn-Teller distortion of Mn-O bonds is also suggested to cause the lengthening and contraction of the axial bonds, causing a shift in the oxygen position from the octahedral site and introducing an element of displacive ordering [27, 33].

Balance of Interactions

The type of physical interactions which influence the type and nature of the SRO include magnetic effects [48], Jahn-Teller induced bond length changes [27], and a preference for local charge neutrality [33].

Experimental studies into the SRO typically keep the same redox-active transition metal and compare the effect of changing the second transition metal, commonly, Ti, Nb, Ta, and Zr [29, 38, 49]. The impact of changing the ionic radii has been compared by investigating the differences between Ti and Zr compounds. Ti and Zr ions possess the same electrostatic charge, but the ionic radii of Li is much closer to that of Zr than Ti. It is found that $Li_{1.2}Mn_{0.4}Zr_{0.4}O_2$ exhibits more extensive SRO than the titanium analogue [38].

Monte Carlo simulations have found that higher-valence transition metals tend to repel each other more; for example, Nb^{5+} and Ti^{4+} have similar ionic radii but different valence states [38]. Comparing $Li_{1.3}Mn_{0.4}Nb_{0.3}O_2$ and $Li_{1.2}Mn_{0.4}Ti_{0.4}O_2$, experimental results from electron paramagnetic resonance (EPR) and ^{7}Li NMR suggest that Mn segregates more in the Nb compound. This is in agreement with the Monte Carlo simulation, which shows the Nb compound has many more MnO_6 octahedra [29]. The paper does not clarify this reasoning and leaves scope for further study. Separate investigations into $Li_{1.3}Mn_{0.4}Nb_{0.3}O_2$ [31], and $Li_{1.3}Mn_{0.4}Ta_{0.3}O_2$ [30], both find that octahedral units of d_6^0 or Mn_5 are energetically favourable, this contradicts the idea that the high valence d^0 metals tend to repel each other. Obtaining experimental evidence distinguishing Mn from the d^0 metal is challenging in both cases.

The Role of Entropy

Increasing the number of components in a system can increase the configurational entropy; in principle, a higher entropy system will be more disordered [50]. This strategy has previously been explored for high entropy alloys [36], high entropy carbides [51] and high entropy oxides.[52]. In each case, the mixing of the transition metals is enhanced by the increased entropy of the system. Lun et al. have employed this strategy for DRS cathodes, synthesising a working DRS cathode with six transition metals and showing this principle can be expanded to up to 23 transition metals [8]. They demonstrate that increasing the number of transition metals and, therefore, increasing configurational entropy improves capacity retention at high cycling rates. In this study, the authors make a qualitative comparison of the degree of SRO by comparing the intensity of the diffuse scattering in electron diffraction patterns, which is indicative of SRO [8]. However, many subtle factors can influence the intensity of diffuse scattering, including crystal tilt and particle size, which are very difficult to control precisely.

2.2.1 Diffuse Scattering in diffraction patterns

X-ray diffraction (XRD) is the most widely used technique for the determination of crystal structure; however, powderXRD provides an average over many particles or crystallites with random orientations [40]. Typically, the broad peak at 20-25 degrees (2θ) in the XRD

data, shown in Figure 2.5, is attributed to SRO [31]. Diffraction from specific orientations can be obtained from single crystal diffraction; however, the weak interaction of X-rays with matter makes it necessary to have single crystals which are at least $100\,\mu\mathrm{m}$ in diameter [53]. It is challenging to produce DRS single crystals of sufficient size as synthesis methods lead to small particle sizes.

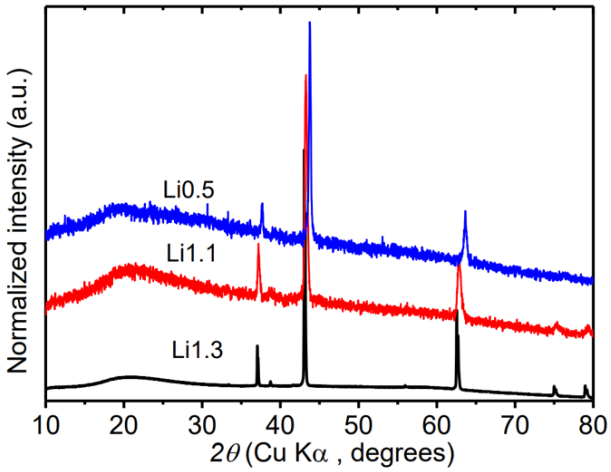


Figure 2.5: Powder XRD profiles of $Li_xMn_{0.4}Nb_{0.3}O_2$ (x = 1,3, 1.1, 0.5) collected us a Cu $K\alpha$ source. Showing the characteristic rocksalt reflections and a broad peak at 20-25 degrees attributed to SRO. Reprinted from [31] with permission from Elsevier, copyright 2018.

Selected area electron diffraction (SAED) patterns in transmission electron microscope (TEM) have been used to indicate the presence of SRO, [29, 31, 38]. Many studies highlight the presence of diffuse scattering in electron diffraction patterns as an indication of SRO; some examples of the types of diffuse scattering which has been observed are presented in Figure 2.6. The examples show that the nature of the ordering has some orientation-dependent correlations. In the $<110>$ orientations, it is common for the diffuse scattering to appear as wavy lines between the Bragg peaks, whereas in $<100>$ orientations, circles or diamond shapes appear between the bright spots.

2.2.2 Cluster Model for SRO

Structured diffuse scattering in electron diffraction patterns was observed as early as 1972 in transition metal carbides, which also have a rocksalt-type structure [55]. Many of the diffuse scattering features in these very early works resemble the diffuse scattering observed for disordered rocksalt cathodes. A cluster model for interpreting SRO was originally derived by de Ridder et al. concerning high entropy alloys to explain the ordered structures that form at the transition temperature [56]. Applying this model to DRS cathodes, we consider the SRO as being limited to the cation sublattice with the structure

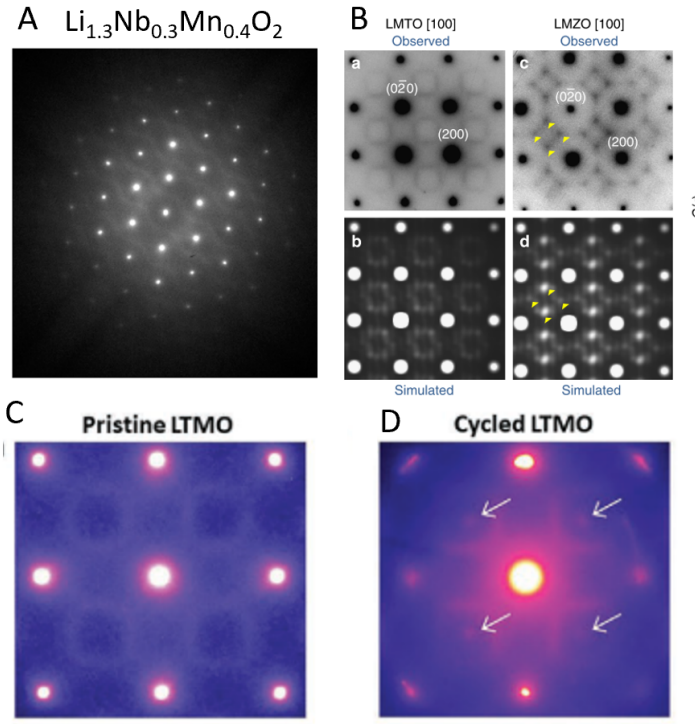


Figure 2.6: **a**) SAED pattern for $<110>$ $Li_{1.3}Nb_{0.3}Mn_{0.4}O_2$ Reprinted from [31]. Copyright 2018, with permission from Elsevier. **b**. Simulated and observed electron diffraction pattern of along $<100>$, of $Li_{1.2}Mn_{0.4}Ti_{0.4}O_2$ (LMTO) and $Li_{1.2}Mn_{0.4}Zr_{0.4}O_2$ (LMZO) [38]. **c,d** Electron diffraction patterns of pristine and cycled LMTO respectively. Reproduced from [54] with permission from John Wiley and Sons.

constrained such that all of the anions occupy a separate sublattice [52]. In one particular case, de Ridder refers to $LiFeO_2$, which, although not explicitly referred to as a DRS, has the structure of a rocksalt lattice with lithium and iron occupying the cation sites in a disordered fashion [56].

De Ridder et al. refer to the SRO in a binary alloy as correlations associated with polyhedral arrangements of atoms, formed by connecting lattice sites within an FCC lattice, examples of possible polyhedra arrangements on an FCC are shown in Figure 2.7. It is suggested that the correlations which make up the SRO exist as specific arrangments of atoms on the lattice sites which enclose the polyhedra. This fundamental work by de Ridder et al. describes the diffuse scattering, which is related to the correlations on the clusters, algebraically as three-dimensional loci in reciprocal space, the reciprocal space loci are also depicted in Figure 2.7 with the equation of each also given [56]. The intensity observed in the 2-dimensional diffraction patterns can be interpreted as slices through the 3-dimensional loci referred to as scattering surfaces. This is discussed further in Chapter 7 to interpret diffuse scattering from DRS cathodes.

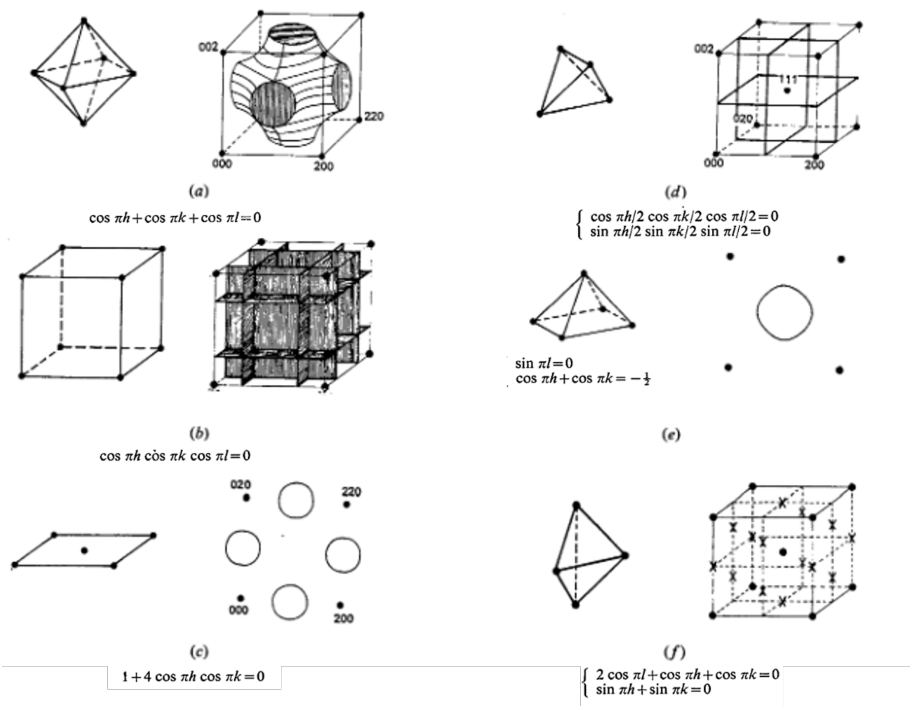


Figure 2.7: Polyhedra based on lattice sites of an FCC lattice and their respective geometric loci in reciprocal space for **a**) octahedral, **b**) cubic, **c**) 5-point planar, **d**) tetrahedral, **e**) square pyramidal and **f**) irregular tetrahedron clusters. The equations below each figure are algebraic representations of the geometric loci in reciprocal space. Figure reproduced and adapted from [56] with permission from IUCr.

The cluster model derived by de Ridder et al., only associates diffuse scattering with compositional SRO. Other studies have found that thermal vibrations and lattice relaxations, for example, due to vacancies or ionic size effects, can produce diffuse scattering [57]. It is difficult to separate the influence of these two factors, which can affect the diffuse scattering since local composition and lattice relaxation are strongly correlated [44].

As the correlations in the ordering get longer, the diffuse nature of the scattering will gradually become localised and, in the extreme case, form superlattice spots [56]. Making a direct comparison of the intensity or localisation of diffuse scattering between materials from different studies is difficult, as many factors, including the crystal thickness, have been shown to influence the SRO. Jones et al. showed that longer correlations in the ordering form when a slow cooling method is used during the synthesis of $Li_{1.25}Mn_{0.5}Nb_{0.25}O_2$ [33]. This result has also been reported for half-Heusler materials where the SRO forms in the thermally quenched sample (diffuse scattering) and a superlattice peak in the sample which was cooled slowly [44].

2.3 Lithium Migration in Disordered Rocksalts

The nature of lithium migration in DRS occurs by a different mechanism than in the traditional layered compounds, which have clear channels for lithium to hop between adjacent sites. Lee et al. have proposed a theory in which the migration process is best described by percolation [9]. They suggest that lithium migration from one octahedral site to another occurs via the tetrahedral interstitial, as shown in Figure 2.8 [9]. The atoms surrounding the tetrahedral sites determine the energy barrier to lithium moving through the tetrahedra [58]. These neighbouring sites are referred to as X-TM channels, where X refers to the number of transition metals at the vertices of the tetrahedron, as illustrated in Figure 2.8**b-d**. In this percolation model, the hopping predominately occurs via the 0-TM channels, i.e. neighbouring tetrahedra with 0-TM nearest neighbours. Some 1-TM channels may allow percolation if the interstitial site is large enough [7]. In general, it is understood that 2-TM and 3-TM channels do not allow percolation.

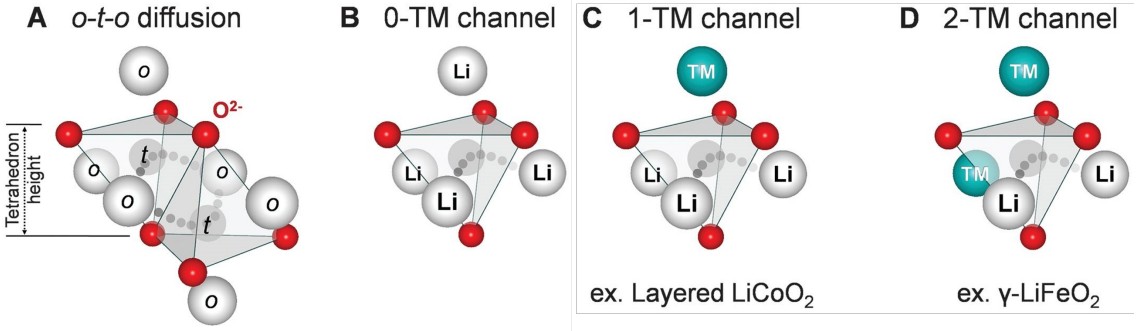


Figure 2.8: **a**) Schematic illustration of the hopping mechanism of Li in DRS materials, following the dashed line, between two octahedral positions (denoted O) through the tetrahedral interstitial (denoted t). **b-d**) The so-called 0-TM, 1-TM and 2-TM sites, respectively. Oxide ions are illustrated as red circles, lithium ions as grey circles and transition metals as turquoise circles. Reprinted from [9], with permission from AAAS.

The nature of the SRO is strongly linked to the Li percolation as the type of SRO strongly influences the nature of the percolation channels. Regular lattices with long range order are dominated by specific types of channels depending on the structure. The spinel structure can deintercalate and intercalate Li even without Li-excess [59], partly because 0-TM channels dominate the structure. If all 0-TM channels allow lithium diffusion, the spinel structure requires 0.77 Li per unit cell to have a percolation network. In contrast, the DRS with no SRO requires a slight Li excess (1.092 Li per unit cell) to achieve a lithium diffusion network [60]. The disordered nature of disordered rocksalts means that all types of channels will likely be present to a greater or lesser extent. However, it can be shown computationally that for an entirely random structure, an excess of lithium is required for electronic conductivity if only 0-TM channels allow lithium migration [60].

A material with the γ-$LiFeO_2$ structure in its stoichiometric form only has 2-TM channels

for which it can be calculated that an excess of 40% lithium would be required to be able to extract 1 Li per formula unit via 0-TM channels [60]. This helps to explain the observations by Jones et al. that the sample of $Li_{1.25}Mn_{0.5}Nb_{0.25}O_2$ with sharply defined γ-$LiFeO_2$ superstructure peaks, exhibits worse capacity retention than the more disordered sample [33]. However, it is slightly surprising that in this study, the initial capacity achieved on the first cycle for the ordered and disordered samples are very similar (over $200mAhg^{-1}$), suggesting that the SRO should have a more significant impact on the amount of lithium which can be extracted than is observed in this case.

Longer-range intercalation and deintercalation require connected percolation channels in a network-type structure. Some studies have reported that the favourable Li-F bonds influence SRO to create more connected lithium percolation channels [49]. However, calculations suggest that after partial delithiation, the remaining lithium may be left in sites with extremely high binding energies, making it impossible to extract all of the lithium [61].

2.4 Structural Changes on Cycling

2.4.1 Spinel Phase

The growth of a ”spinel-like” phase upon cycling has been reported for several manganese-based disordered rocksalts. The term ”spinel-like”, in this case, is used to describe the fact that there is partial occupancy of the tetrahedral sites by cations. Indirect evidence of the spinel phase formation on cycling has been drawn from the emergence of a characteristic plateau between 3-4 V [62, 63]. This initial evidence has since been supplemented by evidence from ^{7}Li NMR, neutron diffraction, and Raman spectroscopy, showing the formation of a ”spinel-like” phase [63]. However, the Raman evidence suggests that the stoichiometry of this phase does not match the typical spinel AB_2O_4 structure. This structural change has been argued to be beneficial in oxyfluoride-DRS with more of the specific discharge capacity being retained on extended cycling of the oxyfluoride analogues [63, 64].

In a comparison of manganese and nickel-based DRS compositions, Kwon et al. showed that the DRS to spinel transformation in the manganese compound, protects against oxygen loss and limits transition metal densification, inhibiting Li migration, when compared to the nickel compound [65]. Electron diffraction data shows that the diffuse scattering present in the pristine material remains present after 30 cycles; however, localised superlattice peaks matching the cubic spinel phase $LiMn_2O_4$ are also present [65].

2.4.2 Short Range Order

The poor Li diffusivity in DRS cathodes means that most studies reduce the particle size by ball-milling and cycle cells at elevated temperatures, to achieve reasonable electrochemical results. To avoid the many complicating factors of analysing the very small particles produced as a result of ball milling, many studies have opted to chemically delithiate [30, 31, 66]. Separate studies use a chemical delithiation method in an attempt to isolate the effect of SRO on the lithium migration in $Li_{1.3}Mn_{0.4}Nb_{0.3}O_2$ [31], and $Li_{1.3}Mn_{0.4}Ta_{0.3}O_2$ [30]. Density functional theory calculations suggest that the ordering of the two materials is similar, with clusters of d_6^0 or $Mn(d^0)_5$, having the lowest energy. Although, the structured diffuse scattering is only presented for $Li_{1.3}Mn_{0.4}Nb_{0.3}O_2$, in the case of $Li_{1.3}Mn_{0.4}Ta_{0.3}O_2$ the low angle peak in the XRD data gradually decreases in intensity as lithium is extracted. This is rationalised by calculations showing that the energy difference between supercells with cation ordering and without decreases when the fraction of Li decreases [30]. The study argues that rather than transform into a spinel structure, this material will eventually form a fully cation-disordered rocksalt.

2.5 O-redox in disordered rocksalts

It was first recognised in 1999 that oxygen was involved in the redox chemistry of $LiCoO_2$ [67]. Since then, the development of cathode materials has focused on increasing capacity by adding excess Li excess. Increasing the amount of Li in the composition decreases the ratio of the redox-active transition metal. To maintain charge balance when the additional lithium is extracted, the anions participate in charge compensation by exhibiting redox behaviour [68]. As the prevalence of Li-rich compositions has grown, understanding the anionic redox processes has also grown in importance. There has been a particular focus on establishing the mechanism of irreversible oxygen loss versus that of reversible anionic redox and, thus, being able to predict which materials are most likely to exhibit reversible anionic redox [69–71]. In the case of oxide materials, anionic redox refers to the oxidation of the O^{2-} ions and is commonly referred to as oxygen redox (O-redox).

There is a significant body of work that has already been developed to understand O-redox in layered Li-excess materials, including preventing structural re-arrangement, which induces changes in the O-redox behaviour [71–73]. This type of anionic redox behaviour was first demonstrated in a Li-rich NMC, $Li_{1.2}Ni_{0.13}Mn_{0.54}Co_{0.13}O_2$ and a mechanism suggesting oxygen loss was proposed by Luo et al. [68].

The previous discussion of lithium migration concludes that lithium excess is required to form percolation channels; most DRS compounds exhibit experimental capacities in excess of what can be accounted for by the transition metal redox [74]. It has been shown

computationally and experimentally that this excess capacity can be attributed to anionic redox [19, 74]. Some key ideas developed to understand anionic redox in layered cathodes have been considered in the context of DRS cathodes.

Density functional theory studies of Li-excess layered compounds have determined the 2p orbitals of 180-degree Li-O-Li bonds are not hybridised with metal d-orbitals; this leaves these orbital unstable, allowing oxidation of the oxygen anion [32]. In DRS cathodes, transition metal ordering influences the degree of hybridisation of these 2p orbitals and thus can influence whether the 2p orbitals can partake in O-redox processes [32]. The local SRO configurations in $Li_{1.25}Mn_{0.5}Nb_{0.25}O_2$ have been directly related to labile oxygen 2p orbitals, potentially explaining why significant anionic redox behaviour is observed in this material [33].

The existing work on oxygen loss in layered Li-excess materials suggests that transition metal migration on charging contributes to voltage hysteresis and voltage loss. House et al. demonstrated that the O-redox plateau could be reversibly cycled by control of the superstructure to minimise transition metal migration. The meta-stable nature of the O_2^- state in $Na_{0.6}[Li_{1.2}Mn_{0.8}]O_2$ presents the opportunity to study in detail the transition to an irreversible anionic redox mechanism over time [75]. ^{17}O-nmr and oxygen K-edge spectroscopy have been used to demonstrate the instability of O_2^- electron-hole state and shown that the reversible O-redox is only possible when the transition metal migration is sufficiently suppressed such that it doesn't allow the formation of voids and thus dimerisation of oxygen.

Oxygen dimerisation in the DRS Li_2MnO_2F has been linked to transition metal migration. However, in the DRS structure, oxygen dimerisation can occur without transition metal migration occurring first. The irreversible step occurs when Mn migrates into vacant O sites [76]. In both cases, for layered cathodes and disordered rocksalts, two approaches for achieving reversible anionic redox can plausibly be conceived: either to prevent transition metal migration in the charged state entirely or to find a way to allow the transition metal migration to be reversible. [32].

2.5.1 Fluorination of the anion lattice

Changes in Anionic Redox

Significant work has gone into researching structures which allow for reversible O-redox, particularly in layered materials [77]. The addition of fluorine to the anion lattice has been widely reported as a method of improving cycling stability in a variety of DRS compositions by reducing oxygen loss at the particle surface [54, 78, 79]. Fluorine reduces the anion lattice's average valence, allowing a greater capacity from the transition metal re-

dox. This has been demonstrated with $Li_{1.15}Ni_{0.45}Ti_{0.3}Mo_{0.1}O_{0.85}F_{0.15}$ displaying a greater Ni redox activity and less oxygen loss from the surface of the particles than its oxide counterpart due to irreversible anion redox [78]. Kitchaev et al. showed it is possible to minimise O-redox by combining fluorination of the anion lattice and two redox-active transition metals, namely $Mn^{2+/4+}$ and $V^{4+/5+}$ [61]. Fluorination provides an alternative route to include lower valent transition metals into d^0 based compositions [54, 79]. Lun et al. propose that this is possible due to the reduced Jahn-Teller distortion of Mn, meaning there is less overlap of the Mn e_g orbital with the O 2p states that facilitate the O-redox [79].

Influence on Short Range Order

Adding an anion with a lower valence state and higher electronegativity, namely fluorine, will result in different bonding environments in the lattice. This leads to differences in the SRO when fluorine is incorporated into the structure because the SRO is considered to be derived from the statistically preferential bonding of certain elements. Computational methods, including density functional theory and Monte Carlo simulations, predict that Li-F bonds are favoured over TM-F bonds [26, 58, 61]. Based on a model set of model compounds, the entirely random structures are unstable despite the entropy compensation because of additional TM-F bonds [58]. The nature of the SRO present in $Li_{1.166}Ni_{0.333}Ti_{0.5}O_{1.8333}F_{0.166}$ has been investigated by comparing Monte Carlo simulations and ^{19}F-nmr to demonstrate that there are fewer fluorine-rich environments than in a random structure suggesting that SRO is preferred around the fluorine sites [26]. This agrees with a preference for Li-F bonds, but the exact nature of the fluorine environments can not be quantitatively measured due to the strong interaction between Ni and F [26]. Although the magnetic susceptibility data suggests a tendency to have Ni-rich regions away from fluorine, these techniques only provide bulk average information; direct evidence requires more localised techniques.

2.6 Summary

This chapter has described the concept of SRO in the case of disordered oxides; the extensive evidence for SRO formation in disordered rocksalt cathodes has also been reviewed. It has also set this into context by considering the relative importance of the SRO in the electrochemical performance of these materials. Understanding SRO is an inherently complex task due to the vast number of configurations that can be conceived with relatively few atoms. In this thesis, scanning transmission electron microscope (STEM) is utilised to provide atomic-scale insights into the local configurations of atoms, which is the fundamental basis of the SRO.

The following chapter provides an overview of the current capabilities of STEM and, in particular, the development of the technique in its application to cathode materials.

Chapter 3

Literature Review - Scanning Transmission Electron Microscopy and its Application to Beam Sensitive Samples

This Chapter provides the reader with an overview of the developments which have allowed STEM to become an effective atomic-scale characterisation technique for beam-sensitive materials. Some challenges relating to characterising beam-sensitive materials using STEM are discussed. Studies on cathode materials that have utilised recent developments in STEM imaging methods are also outlined.

3.1 Advances in Scanning Transmission Electron Microscopy

The first electron microscope was developed by Ernst Ruska and Max Knoll in 1931; it was understood the diffraction limit proposed by Abbe was a physical limitation for optical microscopy and that the de Broglie wavelength of electrons is much smaller, enabling higher resolution. Relatively quickly, the technology was improved to allow the electron microscope to exceed the optical microscopes available at the time [80].

The versatility of the technique has meant that electron microscopy has become a fundamental characterisation technique in almost every discipline of scientific research. Scanning electron microscope (SEM) is primarily a surface-sensitive technique [81], which can provide information over a wide range of length scales on microstructure and elemental composition information [82]. An image is formed by detecting either backscattered electrons which have interacted with the sample or secondary electrons ejected from the interaction volume of the sample from the electron beam. Transmission electron microscope (TEM) uses electrons with a higher acceleration voltage and thin specimens to pass electrons through the sample, and the detector is placed after the sample. The scanning transmission electron microscope (STEM) combines the focused probe aspect of SEM and

the transmission aspect of TEM; this enables highly localised specimen information and extremely high-resolution imaging.

It took several decades from the initial electron microscope designs for the technology required to focus and scan an electron beam using magnetic lenses to be developed [83]. In 1968, Crewe et al. demonstrated the first use of the STEM, which achieved $3\,\mathrm{nm}$ resolution [84]; soon after, it was possible to image single atoms [85]. A limiting factor in the initial proposal for a STEM was the probe current available, therefore it was realised that a cold field emission gun (C-FEG) would be required to achieve enough electrons in a sufficiently small probe [86]. The brightness of the source B is given by Equation 3.1.1; where I is the total emitted current, A is the area from which electrons are emitted at the source, and Ω represents the angle of the electron spread. The C-FEG gives significantly better brightness than the thermionic emission source primarily because of the small effective source size from which electrons are emitted [87]. Field emission sources also produce more electrons with a narrower energy spread, making for a more coherent probe with improved resolution and allowing greater analytical capabilities [88, 89].

$$B = \frac{I}{A\Omega} \tag{3.1.1}$$

The resolution of the STEM would be severely hampered without the development of aberration correctors. In STEM, aberration correction allows for smaller, more intense probes with larger semi-angles. This is beneficial for spectroscopic techniques such as energy loss spectroscopy (EELS) and energy-dispersive X-ray spectroscopy (EDS), which can be limited by the signal to noise [90]. The first aberration correctors were applied to STEM in 1999, producing an electron probe less than $1\,\text{Å}$ [91], followed by a new generation able to achieve a $0.5\,\text{Å}$ probe [92]. However, the most challenging materials to study in STEM are very beam sensitive, and it has been noted that for many samples, the stability of the sample under the electron beam is a more significant limit on the resolution than the fundamental resolution capabilities of modern instruments [93].

These developments have culminated in the STEM becoming an instrument suitable for visualising a wide range of material properties. In materials science, spectroscopic methods allow composition mapping of elements, ranging from interfaces [94], to single atomic columns [95]. The crystallographic structure of materials can be directly visualised in atomic resolution images [96]. This has enabled a plethora of scientific discoveries, including visualising single atom dopants and defects in monolayers [97], and fundamental insights into structural changes in materials for Li-ion batteries [18]. In the development of nanotechnology, magnetic domains [98] and electric fields have been mapped in devices [99, 100]. Even in structural biology where high resolution transmission electron

microscopy (HRTEM) has previously dominated in electron microscopy, low-dose STEM techniques combined with cryogenic electron microscopy have emerged, allowing protein and virus structures to be visualised [101, 102].

3.1.1 Annular Dark Field Imaging

Annular dark field (ADF) imaging has become one of the most routinely utilised techniques in STEM, particularly in the area of catalysis, where heavy atoms are imaged on a support made of lighter elements [103]. The contrast in ADF imaging varies strongly with the atomic number (Z) of the species; the mechanism is described in Section 4.3.2. The attractive quality of the technique is the ability to produce quantitative results; the reader is directed toward several in-depth reviews which cover this subject in much more detail [104, 105].

A limitation of STEM is that all images of 3D atomic structures are a 2D projection in the direction of the electron beam. In cases where samples are sufficiently resilient to the electron beam, it is possible to utilise electron tomography, which involves obtaining images from different tilt angles to obtain information on the 3D structure [106]. Depending on the reconstruction algorithm, accurate tomographic reconstructions can require as many as 70 different projections [107]. This exposes the sample to a significant dose, and results in a trade-off between depth resolution demanding more projections and the damage inflicted by the electron beam [108]. This led to the development of methods to obtain information on 3D structure from a single projection ADF image [109–111].

Quantifying column intensities in ADF images is based on the theory of scattering cross sections [112, 113]. Careful measurement of the dependency of detector efficiencies is required to convert the analogue signal of the ADF detector into an absolute measurement of intensity, taking into account the variation in detector efficiency based on scattering angle [114, 115]. Measurement of the scattering cross section can be compared to simulations [116]. Alternatively, a statistical analysis of the column intensities can infer the number of atoms in atomic columns [117].

Quantitative measurements in ADF images can also include precise measurements of inter-atomic distances, the basis of atomic resolution measurements of lattice strain [118]. This has been applied in cathode materials to calibrate atomic position in phase images, allowing measurement of shifts in the oxygen sub-lattice [119].

3.1.2 Developments in Electron Detectors

Pixelated detectors were installed in electron microscopes as a direct replacement for photographic film; they provided directly accessible digital images to the microscopist for

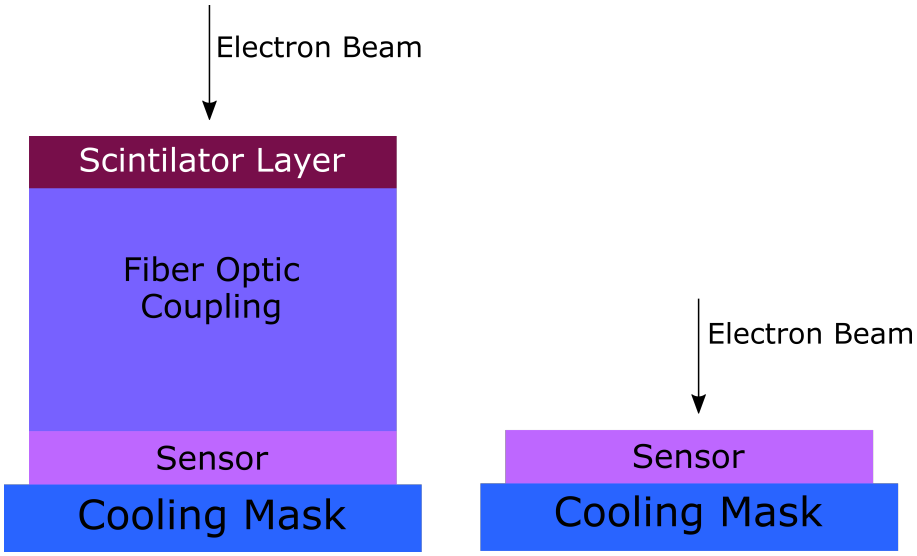


Figure 3.1: Schematic illustration of the structure of a **a**) scintillator-based detector and **b**) a direct electron detector (DED).

the first time. These detectors were primarily charge couples devices (CCD) or complementary metal-oxide semiconductor (CMOS) devices. Both detector designs comprise a scintillator, where high energy electrons generate photons; this layer sits on top of the pixel structure, coupled by either a lens system or fibre optics [120]. The main difference between the two types is how electrons readout from the pixel structure [121]. These detectors are radiation hard and have a high dynamic range, meaning their application to electron diffraction has been highly successful [122].

For several reasons, scintillator-based detectors have been severely limiting for the practical implementation of 4D-STEM experiments, where a single diffraction pattern is recorded for every pixel in a scan consisting of at least $65,536$ pixels (256×256). First, the scan rate is prohibitively slow as it is limited by the readout speed of the detector, which means the sample is exposed to a considerably higher dose during the imaging. The instrument is also susceptible to small instabilities and sample movements, leading to significant image distortions at high resolution. Sample drift contributes to this issue over the long scan duration required. Secondly, the detector quantum efficiency (DQE), which measures the proportion of electrons that hit the detector and are converted to a signal, is poor [123]. As a consequence of a poor DQE, the signal to noise is low.

Direct electron detectors (DED) do not require the scintillator layer and associated coupling mechanism; instead, the high energy electrons interact directly with the sensor, creating electron-hole pairs which are used to generate a signal [121]. Generating the signal directly has two major benefits: noise in the readout process is minimised, and the readout speed is dramatically improved. Both benefits have dramatically impacted the breadth of techniques possible in STEM and the types of samples it has been possible to study.

DEDs used in 4D-STEM applications are either hybrid pixel detectors (HPD), as in the pnCCD [124], EMPAD detector [125] and the Medipix [126] or they can be monolithic active pixel sensors (MAPS), such as the DE-64 detector [127]. MAPS are akin to traditional CMOS detectors in terms of read-out mode; a full description can be found in [128]. They have thin sensors with many pixels, up to $8,192 \times 8,192$ pixels in the case of the DE-64 detector [127]. The sensors are extremely sensitive and can detect single electrons; however, at high dose rates, they can quickly saturate [129]. Hybrid pixel detectors (HPD) contain integrated photodiodes within each pixel, which are then bump-bonded to the readout chip; a full description is available in [130]. HPD generally contain much thicker and fewer pixels than the MAPS; they have the advantage that they are radiation-hard and provide a very good dynamic range [129]. Both types of detectors offer readout speeds compatible with 4D-STEM experiments.

3.1.3 Readout Modes of Direct Electron Detectors

The primary readout modes for most DED are either an integrating or counting mode. The integrating mode used by detectors, such as the pnCCD, integrates accumulated charge on the backside of the detector. Specifically in the pnCCD, the charge is quickly transferred to the frame store section of the detector where it is readout as an analogue signal [124]. Detectors such as the MerlinEM operate in a counting mode where each electron interaction is readout as a single event [131].

Bit-depth corresponds to the range of numerical values pixels can be assigned in a digital readout; a bit depth of n corresponds to pixel values ranging from $0 \Rightarrow 2^n - 1$. Counting detectors such as the Merlin3 allow the bit depth to be sacrificed to optimise readout speed [132]; for example, imaging with a bit-depth of 24 corresponds readout speed of 600 frames per second (fps) but can be increased to $12,000$ fps for a bit-depth of 1 [133]. For detectors with an integrating readout mode, the pixel values recorded measure the electron energy deposited in each pixel rather than the number of electrons counted. As such, for pnCCD, there is no speed improvement for lowering the bit depth and allowing a high dynamic range to be achieved [1]. Instead, the pnCCD allows the user to sacrifice the number of pixels recorded by either binning or windowing to improve the acquisition rate. A full frame of 256×256 pixels can be acquired with a readout rate of 2000 fps; by binning in one direction, by a factor of four, this improves to $7,500$ fps [124].

The latest DED to be developed for 4D-STEM, such as the TimePix, are event-driven detectors [134]. Instead of reading out a full frame of pixel values, only the coordinates and time stamps of electrons arriving at the detector are stored. Then, by synchronising

[1] Dynamic range refers to the bit depth of the intensity values of the pixelated detector; for an integrating detector, the dynamic range depends on the amount of charge which can be stored within a pixel.

the detector with the scan generator in the microscope, these electrons are assigned to a frame, and the 4D dataset is built up [135]. These detectors have essentially no limitation on how fast the STEM can run. Still, the major limitation is based on the uncertainty in the time to record an electron and, thus, the ability to distinguish that two electrons are distinct events. This means that these detectors are best suited to low-dose applications; the TimePix detector can detect up to 40 million counts per second, equivalent to a beam current of $6.4\,\mathrm{pA}$ [135].

3.2 4D-STEM Techniques

4-dimensional scanning transmission electron microscopy 4D-STEM refers to the broad spectrum of techniques that involve recording the entire diffraction plane rather than integrating a signal, such as in BF or ADF STEM. This results in a 4D dataset with two dimensions in real space - the probe position - and two dimensions in reciprocal space [136]. Many of the advances and applications of 4D-STEM in the subsequently mentioned techniques can be directly related to the improvement in resolution of the STEM itself and the evolution of detector technology. In particular, the ability to apply imaging methods to beam-sensitive samples, such as those for battery application, can be directly linked to faster detectors [18].

3.2.1 Ptychography Development

Ptychography is a method for reconstructing the phase component of the electron beam by utilising interference effects in the diffraction patterns recorded from multiple probe positions. A full explanation of the theoretical basis is given in Section 4.4.2; here, only the development and application of the technique are considered.

This principle has been applied across a range of wavelengths. Electron ptychography was originally developed to overcome issues surrounding resolution due to the poor quality of lenses in the electron microscope [137]. The theoretical basis for the technique was established in electron imaging, but the implementation was limited by the technology in electron microscopes at the time [138]. Instead, the technique was adopted by the X-ray community since the technique is not affected by the quality of the probe-forming lenses [139]. It thus can provide super-resolution imaging, beating the standard diffraction limit; the resolution has become less important with the development of aberration-corrected electron microscopes, but it remains important in the X-ray field where the quality of lenses is even more limiting [11, 140].

Initially, atomic resolution imaging using electron ptychography was limited to materials which could withstand significant doses, such as silicon [141]. It wasn't until the avail-

ability of DED and the computational power to process large datasets that the full benefits of the technique were realised. These technological advancements have enabled images with in-plane resolution limited by lattice vibrations to be achieved [142]. This experiment required extraordinary computational power to reconstruct 30 slices through the sample's thickness by considering the beam spreading to achieve a resolution of 0.2 Å[142].

Reconstruction Methods

The wave function of the electron beam comprises both magnitude and phase; all electron detectors record the modulus squared of the complex transmission function, $|M(\mathbf{K_f}, \mathbf{R_p})|^2$, meaning only the magnitude component is known - referred to as the phase problem [137]. Ptychography allows the phase shift of the electron beam to be determined by utilising the interference between more than one diffracted beam; this is similar to in-line holography, which also makes reference to this [143].

Current ptychographic reconstruction methods fall into two categories: direct methods, applied to focused probe ptychography and iterative methods, generally applied to defocused probe ptychography but applicable to both under the correct sampling conditions. The first methods to retrieve the phase by ptychography were direct methods, such as the Wigner distribution deconvolution (WDD) method first proposed in 1992 (for mathematical details, see Section 4.4.4) [144]. This was followed in 1993 by a method which assumes a weak phase object approximation (WPOA) to simplify the Fourier overlap function, $G(\mathbf{K_f}, \mathbf{Q_p})$ - further details of the WPOA and details of the Fourier overlap function are discussed in Sections 4.1.3 and 4.4.2, respectively [138]. The 4D dataset is then Fourier transformed with respect to probe position [138], a full mathematical description is again given later in Section 4.4.2. This method was then further adapted by Pennycook et al. into the single side band (SSB) method, described in Section 4.4.3 [145].

The first iterative reconstruction method was demonstrated in 2004; these methods are generally applied to defocused probe ptychography because significant overlap in the probe positions is required [146]. For some highly beam-sensitive samples, especially biological specimens, spreading the incident energy in the electron probe over a larger area is useful by defocusing the probe [101]. Defocused probe ptychography has also produced high-quality reconstructions under very low dose conditions [147, 148]. However, the disadvantage of defocusing the probe is that this makes it incompatible with simultaneous imaging with ADF, which is highlighted later as a key advantage of ptychography [149]. One of the most widely used iterative algorithms, extended iterative ptychographic engine (ePIE), can simultaneously solve for the probe and sample function, allowing post-acquisition aberration correction [150].

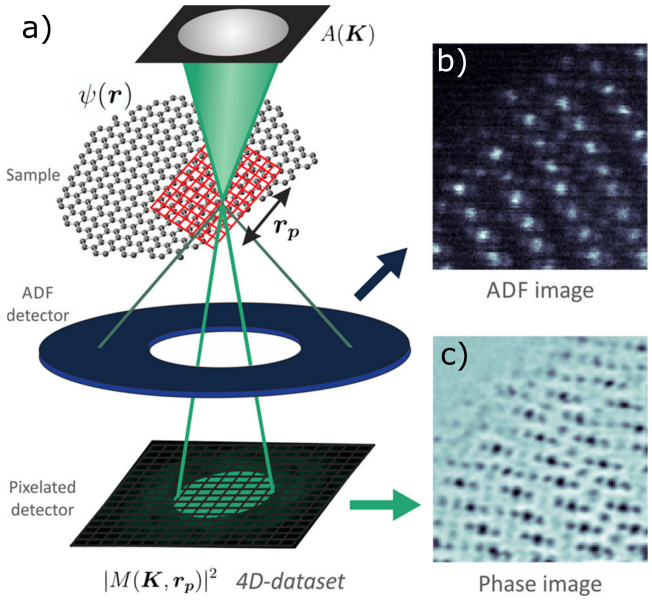


Figure 3.2: **a**) Schematic illustration of detector geometries for ptychography and simultaneous ADF. **b**) ADF image of $Li_{1.2}Mn_{0.6}Ni_{0.2}O_2$ showing contrast from the transition metal in the layered structure. **c**) Phase image reconstructed by SSB ptychography with enhanced light element contrast. Figure adapted with permission from [18].

Applications of Ptychography

The low dose capabilities of the techniques are compared by simulating the contrast obtained from a weak phase object under a dose of $100\,\mathrm{C\,cm^{-2}}$ and $10\,\mathrm{C\,cm^{-2}}$. This demonstrated that although differential phase contrast (DPC) and low angle-ADF (LAADF) show some contrast under $100\,\mathrm{C\,cm^{-2}}$, a single carbon atom can only be resolved by reconstructing the phase with an applied dose of $10\,\mathrm{C\,cm^{-2}}$. Thus demonstrating that ptychography is the more effective technique for low-dose imaging of weak-phase objects.

Providing appropriate synchronisation of the detector and scan system is achieved, focused probe ptychography and ADF images can be formed in a single scan, increasing the information which can be extracted for a given dose and allowing a more comprehensive analysis. Given the detector geometry shown in Figure 3.2, an annular detector can acquire the dark field signal at the same time, as the convergent beam electron diffraction (CBED) pattern is recorded on the pixelated detector. Some other phase imaging techniques, such as holography, are incompatible with incoherent imaging because they require a phase plate or residual aberrations to form the image contrast. Simultaneously acquiring Z contrast images greatly enhances the interpretability of the images. This has been demonstrated by combining ptychography with ADF images to locate atoms inside carbon nanotubes [149]. The method has also been applied to cathode materials to study the role of phase changes during the cycling process, as shown in Figure 3.2-**b**-**c** [18].

There is significant redundancy in ptychographic datasets that can be used to provide in-

formation about aberrations in the electron probe post-acquisition. Phase in the overlap regions can be described as a linear sum of lens aberrations, which can be solved by using the matrix inversion single value decomposition method [151]. The process was first possible using iterative methods to reconstruct the phase with a highly defocused probe [150]. Yang et al. later applied aberration correction to the Wigner distribution deconvolution (WDD) method, allowing them to image carbon nanotubes [149]. This process improves the ability to capture data from extremely beam-sensitive samples as the microscopist can quickly acquire an image close to focus and correct any residual aberrations post-acquisition, reducing the time illuminating the sample and reducing radiation damage to the sample [149].

The same report by Yang et al. also takes the previously redundant information in the ptychographic data to reconstruct carbon nanotubes at different heights by changing the defocus value [149]. In the more recent study, using multi-slice ptychography, a depth resolution of ≈3.9 nm was demonstrated to identify interstitial dopant atoms in $PrScO_3$ [142]. This method requires only a single 4D-dataset, reducing the dose the sample is exposed to in comparison to other optical sectioning methods, which require multiple passes of the beam [152].

3.2.2 Scanning Nano-Diffraction Techniques

Ptychography relies on the overlap between the central and diffracted disk, which requires a highly converged probe; reducing the convergence angle leads to more localised diffraction spots, similar to those in TEM diffraction conditions, where parallel illumination is used. In nanobeam electron diffraction (NBED), a close-to-parallel scanning probe is rastered across the sample to obtain a stacked dataset of diffraction patterns for every probe position [153]. This technique is sometimes referred to as scanning electron nanobeam diffraction (SEND) in the literature [154]. NBED combines the spatial resolution afforded by a focused probe - which can be as small as $1\,\mathrm{nm}$ - with the type of crystallographic information in parallel beam diffraction patterns such as crystal orientation and lattice parameters.

The structural change from layered ($R\bar{3}m$) to rocksalt structure ($Fm\bar{3}m$) has been documented by NBED, as shown in Figure 3.3 [155]. The crystallographic information in the detector plane can be visualised in real space by mapping the orientation or crystallographic phase to colour images [156, 157]. The software has been developed which allows diffraction patterns to be categorised according to the domain crystallinity automatically over the thousands of diffraction patterns obtained in a 4D-STEM dataset [154, 158].

As well as spatial information and visualisation of domain mapping, quantitative informa-

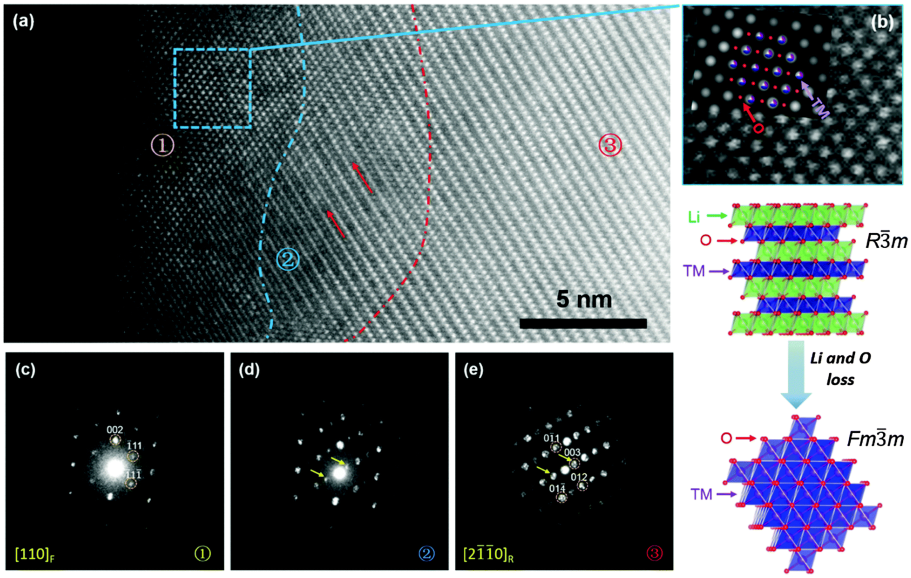


Figure 3.3: **a**) High-resolution ADF image showing the phase change from layered to rocksalt with a transition region. **b**) ADF image of an NMC layered cathode. **c-e**) NBED patterns from regions 1 - 3, respectively. Reproduced from [155] with permission from RSC.

tion on the size distribution and ordering parameter can be determined [159]. The field of view of NBED is determined only by the number of probe positions and step size between probe positions; this allows the crystallographic structure to be mapped over a much larger area than atomic resolution imaging [153]. For example, strain analysis can be carried out over much larger areas using NBED than using methods based on atomic resolution images [153, 160]. Subtle differences in the electron diffraction patterns can also be studied and used to analyse other material properties, such as polarity in ferroelectric materials [161, 162].

Recently, a new method of performing scanning electron diffraction, using a confocal set-up in the STEM, has been reported [163]. This is an adaptation of previously reported confocal geometries in the STEM [164]. The scanning confocal electron diffraction (SCED) method has been shown to provide improved angular resolution and better dose efficiency in comparison to NBED [163]. The development of fast electron detectors also plays a critical role in applying scanning diffraction techniques to beam-sensitive materials, as the detector speed is usually the limiting factor to the scan speed.

3.3 Beam Sensitive Samples

While electron microscopy is a useful tool to study battery materials, it should also be considered that by the nature of these materials, they are subject to interactions with the electron beam, which can damage the materials [165]. STEM focuses this beam to a

very small point, thus focusing the energy delivered to a highly localised area. Typical cathode materials present a challenge for imaging as they combine heavy transition metals with light elements such as oxygen and lithium, which are susceptible to different damage mechanisms [166].

There are different mechanisms by which the electron beam can cause damage; the most prevalent mechanisms are radiolysis, knock-on, and ionisation. Depending on the specimen interactions, different sample types are often more susceptible to one type of damage mechanism over another. If one type of damage mechanism is prevalent, the acceleration voltage can be adjusted to minimise the primary damage mechanism [167]. Knock-on damage occurs through elastic collisions of the incident beam with the atoms in the sample and is more significant for higher beam energies. On the other hand, radiolysis damage is decreased for higher beam energies. Radiolysis occurs due to inelastic scattering of the beam in the sample and is a consequence of electronic excitations, which result in bonds breaking and atoms being displaced [168].

There is no consensus in the literature on the mechanism of electron beam damage in cathode materials. It has been shown that lowering the acceleration voltage from $200\,\mathrm{kV}$ to $80\,\mathrm{kV}$ significantly reduced the beam damage which occurred in some layered cathode materials [169]. Meanwhile, many of the high-resolution studies on cathode materials have been carried out with acceleration voltages in the region of $200 - 300\,\mathrm{kV}$ with impressive results [12, 14, 18, 148].

The argument for lowering the acceleration voltage is based on the main damage mechanism being knock-on. This is supported by a report from Shim et al. that structural re-arrangement was observed in $LiNiO_2$ at $200\,\mathrm{kV}$ but not at $80\,\mathrm{kV}$ [169]. Comparatively, in the same study, it is reported that $LiCoO_2$ does not undergo cation rearrangement for the equivalent dose at either 80 or $200\,\mathrm{kV}$. In the same report, a study using EELS showed that it was also possible to induce an oxygen loss in $LiNiO_2$, as is often seen in the charging and discharging cycle of these materials [169]. A study by Lin et al. presents a complex damage mechanism where the electron beam reduces the transition metal. At the same time, the lighter elements, such as lithium, are susceptible to knock-on damage [165].

It is not disputed that beam damage can change the crystallographic phase of materials or cause the crystalline nature to be lost entirely [170, 171]. Materials in the charged state are more susceptible to damage from the electron beam since removing lithium from the structure leaves it in an unstable state [18, 165]. A study showed that upon illumination with an electron beam, the layered cathode structure transforms first to a spinel phase, and upon further exposure to the beam, a rock salt phase evolves [165]. As is highlighted in Figure 3.4, several studies have urged caution to the fact that these changes are identical

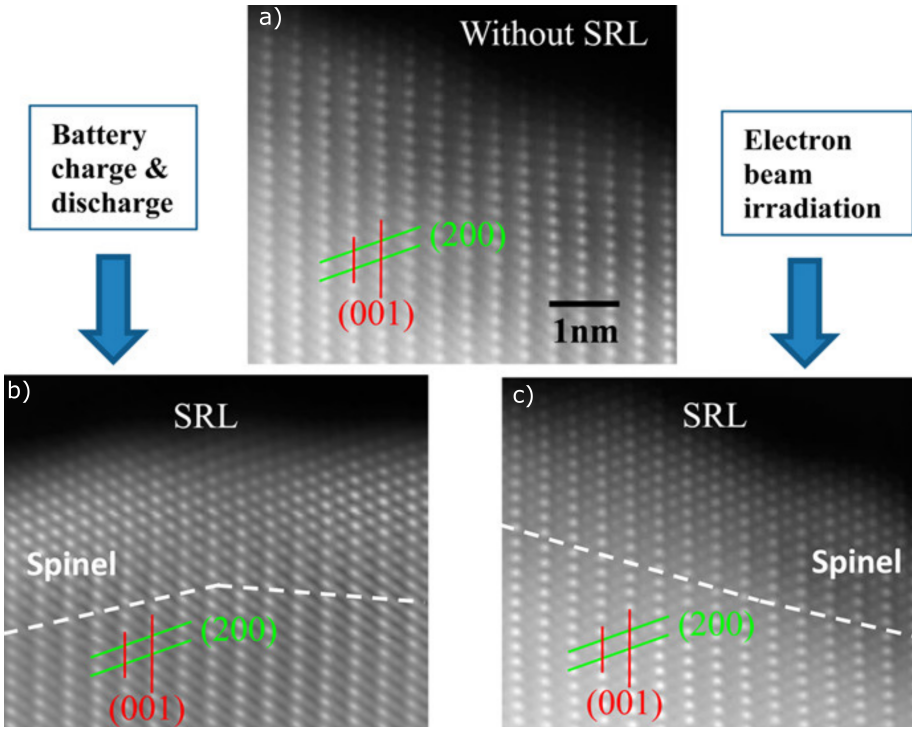


Figure 3.4: Illustration of the similarity of electron beam damage and cycling in $Li_{1.2}Ni_{0.2}Mn_{0.6}O_2$. **a**) HAADF image before beam damage or cycling effects on the surface. **b**) surface reconstruction layer (SRL) due to cycling effects in the region above the dashed line. **c**) SRL after electron beam irradiation above the dashed line. Reprinted with permission from [170]. Copyright 2015 American Chemical Society.

to those which occur during the charging and discharging cycling of these materials; this complicates the analysis of images we may wish to use to study changes in the structure during cycling [13, 17, 170, 172]. Similar studies of electron beam damage mimicking irradiation effects in nuclear materials have also been reported [173]. To the author's knowledge, no studies have been conducted specifically analysing the mechanism of beam damage in DRS materials. However, studies of other Mn-based oxides have shown that the spinel to rocksalt transformation observed in DRS can be observed reversibly under electron beam irradiation [174].

With the opportunities to solve many material science problems in beam-sensitive materials, many other strategies have been developed that aim to mitigate the effects of beam damage in STEM. Multi-frame imaging involves reducing the dwell time per pixel and acquiring multiple passes over the same area to improve the signal-to-noise. Reducing beam damage and removing scanning artefacts contribute to achieving higher precision in multi-frame images for a particular dose limit [175]. It has been shown that dividing a set dose over multiple frames can reduce the damage incurred [176]. Additionally, the microscopist can view a series of images with an accumulated dose; scans after damage has occurred can then be discarded. Scan patterns which do not follow the typical raster

scan patterns are helpful in minimising damage; in particular, acquiring an array of probe positions but in random order has been shown to reduce damage [177]. This is hypothesised to be because the interaction volume of the probe in adjacent positions tends to overlap; by using a random scan, the energy deposited by the probe in a region has time to dissipate before the area is scanned again.

Other experimental methods to reduce the beam damage include cooling the sample, for example, using liquid nitrogen in a process known as cryogenic electron microscopy (cryo-EM). This has become commonplace for biological materials [178], but has also been shown to be effective for battery materials [179]. Cryo-EM has been demonstrated to be compatible with other low-dose techniques, including ptychography [101].

3.3.1 Using STEM for Structural Characterisation in Battery Materials

Unlike many other techniques used to characterise battery materials, the local nature of STEM can provide insight into the structural changes at a very local level. In some instances, the local nature of the STEM probe has been argued to be a downside of the technique because the field of view is relatively limited and collecting data over many areas can be time-consuming and expensive. New computational methods to automate data acquisition have improved this and have been applied in some fields, but the most sophisticated experiments still require significant user input. This is likely to become increasingly important in the field of energy materials as disordered systems grow in importance. Several results using STEM to characterise SRO in DRS cathodes are highlighted in Section 2.2.1, particularly electron diffraction. Dedicated studies taking full advantage of the breadth of characterisation techniques available in STEM have not been published.

A lack of understanding of the underlying science behind the degradation mechanisms has held back the optimisation of new cathodes. In particular, the role of anion redox in Li-rich cathodes has been widely identified as a question of major scientific importance [69, 70, 77]. Aided by the development of imaging techniques that enable visualisation of the light elements, studies using STEM have added significant value to the current understanding of oxygen redox. Annular bright field ABF, which encompasses the outer ring of the bright field signal, is effective at imaging light elements and has been used to image various cathode materials [12, 14, 18, 180]. Although it has been used to study distortions in the oxygen sub-lattice of Li-rich transition metal oxides, it is limited by difficulties in interpreting the contrast which is formed from both coherent and incoherent scattering [12].

Spectroscopic analysis using STEM can provide information on the location of each el-

ement [165]. This information can be used to study the composition of the spinel phase that forms during cycling in Li-rich layered cathodes and has demonstrated that this phase contains a higher concentration of nickel than elsewhere in the bulk [17]. EELS can also provide valuable information on the valence state of the transition metals; for example, it has been reported that in NMC cathodes, it is predominantly nickel which undergoes oxidation to balance the charge on the removal of the lithium [155].

Although not covered in this work, STEM has been used to study other component materials implemented in Li-ion batteries. The intercalation of lithium within graphite anodes has been studied [181], and cryogenic techniques have been used to study the growth of lithium dendrites on lithium anodes [182]. In-situ techniques have also emerged, making it possible to image chemical processes while applying external stimuli, mimicking the cycling process; this has been particularly important for understanding interface effects [183, 184].

3.4 Summary

This chapter provides the reader with an overview of the developments in STEM which have enabled its suitability as a technique to characterise SRO in DRS cathodes. The capabilities of 4D-STEM techniques in materials characterisation have been outlined. A particular emphasis is placed on the importance of the development of DED and their role in allowing 4D-STEM techniques to be applied to beam-sensitive materials, such as cathodes. The damage mechanisms and methods to reduce damage in such materials have also been discussed.

The following chapter outlines the theoretical aspects of various electron imaging methods and expands on the details of particular methods used in the preparation of this thesis.

Chapter 4

Theory of Electron Imaging

This chapter provides the reader with the theoretical background of STEM and the associated imaging methods. The general principles of STEM are described, followed by an introduction to a series of imaging methods which are applied in later chapters.

4.1 Introduction

Electron microscopes use a beam of electrons to form images using similar principles to those in which optical microscopes use light. Unlike photons, electrons are charged particles and thus can be controlled using the Lorentz force, induced by a magnetic field, instead of the typical lenses applied in optical microscopes. The path of the electrons can be finely tuned by varying the current passing through the electromagnets, changing the strength of the magnetic fields. The three most common methods in electron microscopy are scanning electron microscopy (SEM), conventional transmission electron microscopy (CTEM) and scanning transmission electron microscopy (STEM). SEM is mainly concerned with surface imaging, as electrons typically don't have enough energy to pass through the sample. In CTEM, a broad parallel electron beam, equivalent to plane wave illumination, passes through the sample, and information is collected below the sample. Finally, in STEM, electrons also pass through the sample but the illumination is a finely focused probe which is rastered across the sample. In each case, information can then be extracted by detecting electrons which have interacted with the sample in different ways; more details on the electron interactions with the specimens are given in Section 4.1.3.

4.1.1 Resolution

A primary advantage of TEM in materials science is that it allows for atomic-scale resolution imaging of materials. Diffraction occurs in every optical system and limits the resolution; diffraction from circular apertures produces intensity with an Airy disc function. The diameter of the Airy disk is related to the wavelength of the light and the size of the aperture; when the Airy disks overlap, the objects are no longer considered to be resolvable by the imaging system. The resolution R is the distance between two objects where the objects can be clearly distinguished and is commonly defined by the Rayleigh Criterion, given in Equation 4.1.1 [185]. The Rayleigh Criterion depends on the wave-

length of the illumination; λ and NA, which represents the numerical aperture of the imaging system.

$$R = \frac{0.61\lambda}{NA} \tag{4.1.1}$$

The wavelength of the illumination source limits the ability to resolve features - typical atomic spacings in most crystals are in the order of $10^{-10}\,\mathrm{m}$. Visible light ($400 - 700\,\mathrm{nm}$) has a maximum resolution of around $0.2\,\mu\mathrm{m}$; as such, much smaller wavelengths are required for atomic-scale imaging. The de Broglie wavelength, λ, for relativistic electrons, with a rest mass, m_0 and charge, e is given by Equation 4.1.2. The acceleration voltage is denoted by V, and h is Planck's constant. For a typical acceleration voltage of $200\,\mathrm{kV}$, this corresponds to a wavelength of $2.51\,\mathrm{pm}$. This wavelength can theoretically achieve sub-atomic resolution imaging; however, the practical resolution limit for electron microscopes is caused by aberrations in imperfect electromagnetic lenses.

$$\lambda = \frac{h}{\sqrt{2m_0eV(1 + \frac{eV}{2m_0c^2})}} \tag{4.1.2}$$

4.1.2 Aberrations

It is impossible to build electromagnetic lenses which are completely aberration-free [186, 187]. Aberrations in the electron microscope include coma, astigmatism, spherical aberration and chromatic aberration; the latter two are the primary limiting factors to the spatial resolution in the electron microscope [91]. Spherical aberrations arise because the magnetic field focuses electrons travelling further from the optical axis more strongly. Chromatic aberrations result from electrons of different energies being focused on a different point. Each is illustrated schematically in Figure 4.1. Chromatic aberrations can be improved by using an electron beam with a narrower energy range; this can be achieved by reducing the energy spread of the electron source or adding a monochromator [188]. A series of quadrupole-octupole lenses can be used to correct spherical aberrations in the electron microscope column [189]. The impact of the development of spherical aberration correctors on the resolution of the STEM has been discussed in Section 3.1.

4.1.3 Sample Interactions

The combined effects of the information transfer of the imaging system and the interaction of the electrons with the specimen generate the contrast in the electron microscope. Electrons are charged particles that interact strongly with matter; to allow electrons to

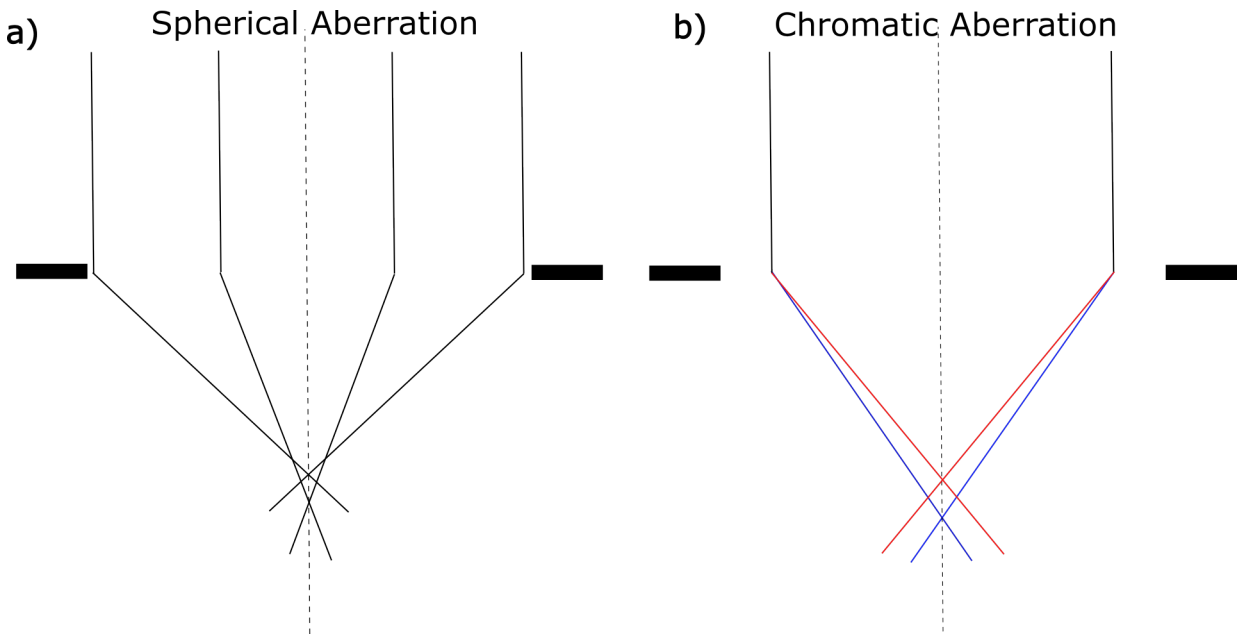


Figure 4.1: **a**) Schematic ray diagram illustrating the effect of spherical aberration. **b**) Schematic ray diagram illustrating the effect of chromatic aberration.

pass through, samples must be sufficiently thin. Interactions between the electrons and the specimen can either be elastic, not involving the transfer of energy or inelastic, involving the transfer of energy. This description of electron interactions with the specimen treats electrons as particles. However, electrons behave as quantum particles and simultaneously exhibit properties of particles with mass and waves with amplitude and phase. This was also eluded to in the description of the de Broilge wavelength in Equation 4.1.2.

The scattering of the electrons by a crystal can be treated as an example of solving for the wavefunction of an electron scattered by an atomic potential $V(\mathbf{r})$ which is dominated by the electrostatic coulomb potential of the nuclei. The electron wavefunction $\psi(\mathbf{r})$ is a solution to the in the time-independent Schrödinger equation, which can be written in the form of in Equation 4.1.3 for an electron accelerated by an electrostatic potential E, within the coulomb potential of a crystal [87, 190]. In this notation absorptive effects are neglected and since the electron charge is negative and the specimen potential is dominated by the Coulomb potential of the nuclei, by convention the potential energy associated with the interaction between the electron and sample is taken to be positive [191]. Equation 4.1.3 is given for an incident electron with relativistic mass m, and charge e, which refers to $\mid e \mid$ in the Equation 4.1.3.

$$\nabla^2\psi(\mathbf{r}) + \frac{8\pi^2 me}{h^2}[E + V(\mathbf{r})]\psi(\mathbf{r}) = 0 \tag{4.1.3}$$

For thin samples, most of the scattering is elastic in nature, which mostly maintains the

coherent relationship of the incident and scattered electrons. As the scattering angle increases, the coherent nature of the electron beam is lost; this is referred to as incoherent imaging and is the case in HAADF imaging discussed later in Section 4.3.2. Weakly scattering specimens, to a good approximation, only change the phase of the exit electron wavefunction ψ_{exit} which is given by Equation 4.1.4. The specimen potential is given by $V(\mathbf{r})$, and σ is known as the interaction constant related to the phase and specimen potential. This can be written as a power series expansion, with the first three terms given in Equation 4.1.4.

$$\psi_{exit} = e^{i\sigma V(\mathbf{r})} \approx 1 + i\sigma V(\mathbf{r}) - \frac{\sigma V(\mathbf{r})^2}{2} \tag{4.1.4}$$

In such cases that the phase is only changed by a small amount, the weak phase object approximation (WPOA) can be applied. This simplifies Equation 4.1.4 to $\psi_{exit} = 1 + i\sigma V(\mathbf{r})$, by only considering the first two terms of the expansion. Electron detectors can only record the amplitude component of the electron wavefunction, and information about the phase is lost. This is known as the phase problem, and Section 4.4.2 describes ptychography - one method of phase imaging developed to solve the phase problem.

4.1.4 Diffraction

A crystal can act as a grating to an electron wave; interference of the diffracted waves in the back focal plane produces a diffraction pattern that contains crystallographic information. This kinematic approach to electron diffraction assumes that each electron only undergoes a single scattering event. In thicker samples with multiple scattering, a dynamical approach to electron scattering is needed and may be described by a Bloch wave approach [191]. This is not discussed in detail here, but other publications have described this in-depth [191, 192].

In cases where the scattering by the potential in the sample is weak, i.e. the sample is sufficiently thin, the first-order Born approximation can be applied. As the electron is only scattered once in the sample, a kinematical approach is valid, leading to the approximate form of the scattering amplitude can be written as Equation 4.1.5 [191].

$$f(\mathbf{K}) = \frac{-2\pi}{k} \int V(\mathbf{r}) e^{-2\pi i \mathbf{K}\cdot\mathbf{r}} d\mathbf{r} \tag{4.1.5}$$

Equation 4.1.5 describes the scattering amplitude as a Fourier transform of the crystal potential, demonstrating kinematic electron diffraction to be mathematically equivalent to the optical description of Fraunhofer diffraction [193]. The scaling factor depends on the

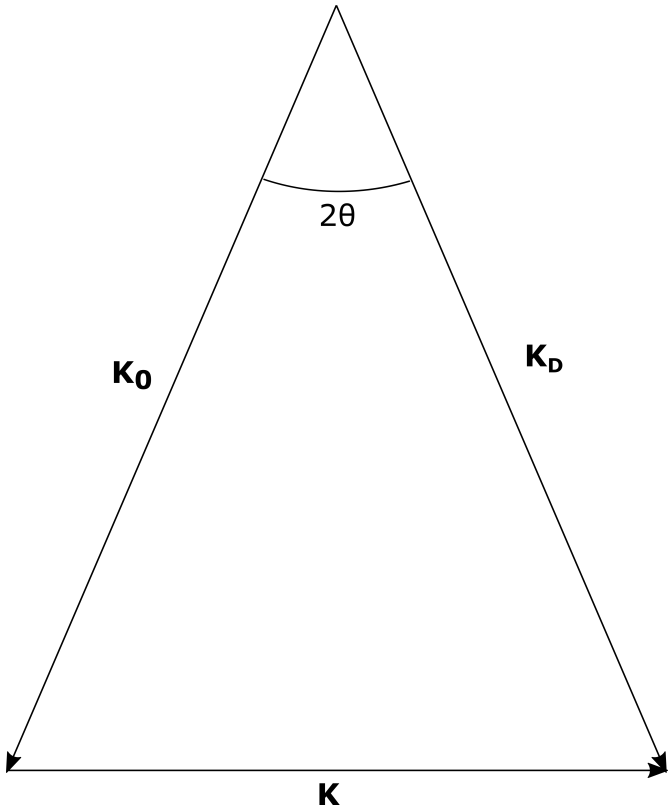


Figure 4.2: Geometrical illustration of the incident wavevector $\mathbf{K}_0$,and the diffracted wavevector $\mathbf{K_D}$, the vector **K** is the difference vector.

magnitude of the incident wavevector, known as the wavenumber, k.

The scattering vector **K** is the difference between the incident and diffracted wave vectors, $\mathbf{K} = \mathbf{k_D} - \mathbf{k_0}$. This is illustrated geometrically in Figure 4.2, where the angle, θ is defined as $sin^{-1}(\mathbf{K}/2\mathbf{K_0})$. Given that the wavenumber k can be written $1/\lambda$, the difference in the paths of the wavefronts can be written as Equation 4.1.6. The Bragg angles, when the path difference is equal to $n\lambda$, give the conditions for which interference between the incident and scattered waves is constructive.

$$|\mathbf{K}| = k = \frac{2sin\theta}{\lambda} \tag{4.1.6}$$

The reciprocal lattice represents planes in the crystal structure as points in reciprocal space. The reciprocal lattice vector **g**, in Figure 4.3 is normal to the lattice planes in real space and has a magnitude defined as $|g_{hkl}| = \frac{1}{d_{hkl}}$. Given that the wavenumber is defined as $K = \frac{1}{\lambda}$, the interplanar spacing of the lattice planes can be written in terms of the wavelength and scattering angle, known as Braggs law, Equation 4.1.7.

$$d_{hkl} = \frac{\lambda}{2sin\theta} \tag{4.1.7}$$

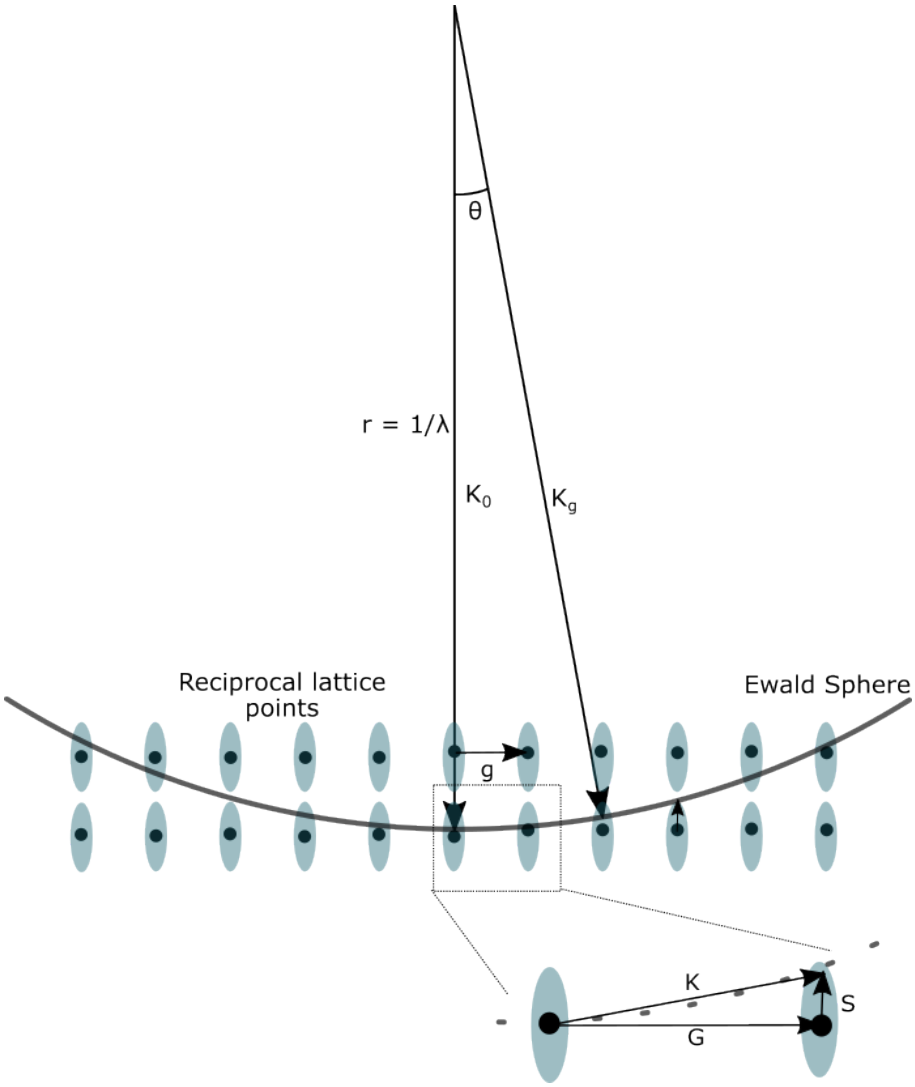


Figure 4.3: Schematic illustration of the Ewald sphere intersecting reciprocal lattice points.

The Ewald sphere is a geometrical construction which intersects reciprocal lattice points, which satisfy the Bragg condition [194]. The radius of the Ewald sphere is inversely proportional to the wavelength; the short wavelength of electrons results in a very large Ewald Sphere. Reciprocal lattice points have dimensions inverse to the crystallographic planes. Samples prepared for electron diffraction (ED) should be thin in the direction of travel of the electron beam, resulting in reciprocal lattice points being elongated in this direction, as shown in light blue in Figure 4.3. The elongation of the reciprocal lattice points, referred to as relrods for specimens of finite thickness, is inversely proportional to the specimen thickness. This means that for thinner specimens, the Ewald sphere interacts with more relrods and the vector $\mathbf{S}$, where $\mathbf{K} = \mathbf{S} - \mathbf{G}$ is introduced to denote the deviation from the reciprocal lattice point as illustrated in Figure 4.3.

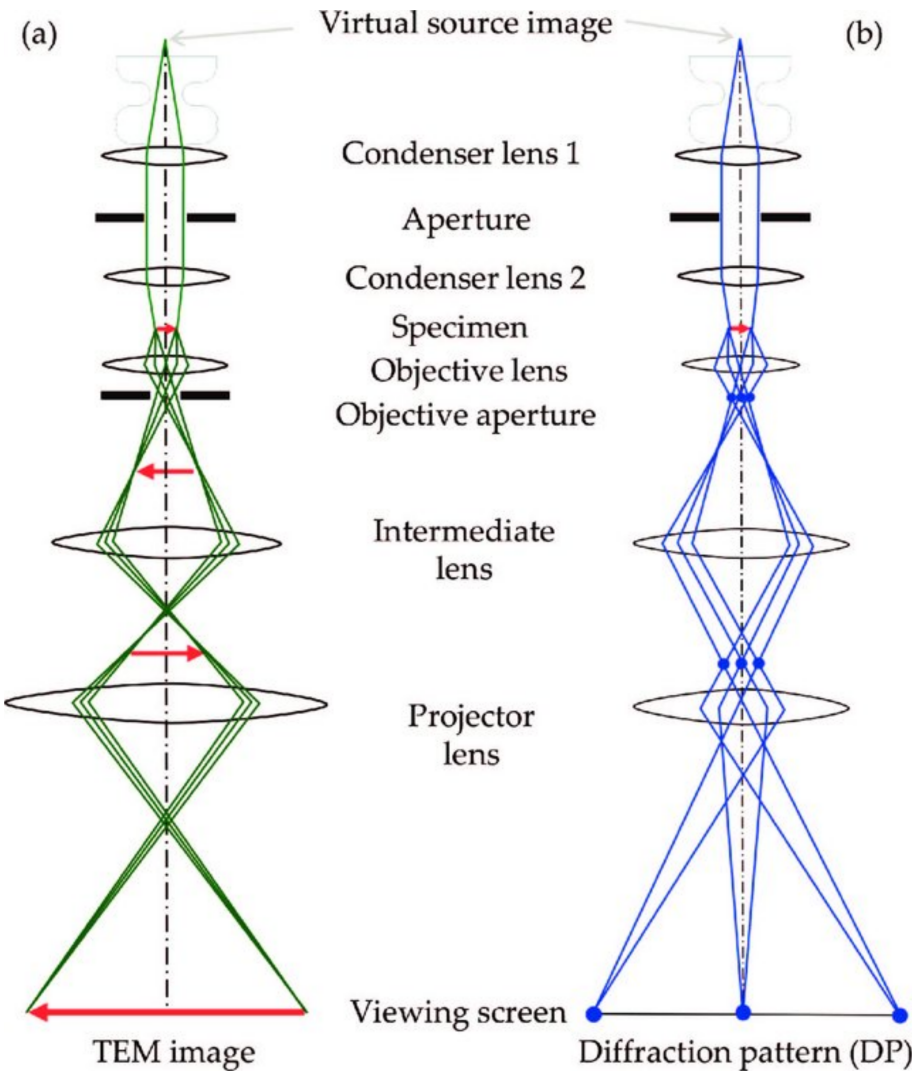


Figure 4.4: Schematic ray diagram of the optical configurations of **a**) Bright-field imaging in CTEM and **b**) Diffraction mode in the CTEM. Figure adapted with permission from [195]

4.2 Conventional-TEM

Illumination of the sample in the CTEM is by a columnated electron beam, which can be modelled as a plane wave illumination. Two common modes, imaging mode and diffraction mode, are shown schematically in Figure 4.4. The condenser lens system controls the electron beam illumination of the sample, changing the field of view of the illumination and the brightness. A diffraction pattern of the object is formed at the back focal plane of the objective lens. Switching between the modes is controlled by changing the intermediate lens configuration such that either a bright field image is formed or a diffraction pattern is formed on the detector or viewing screen.

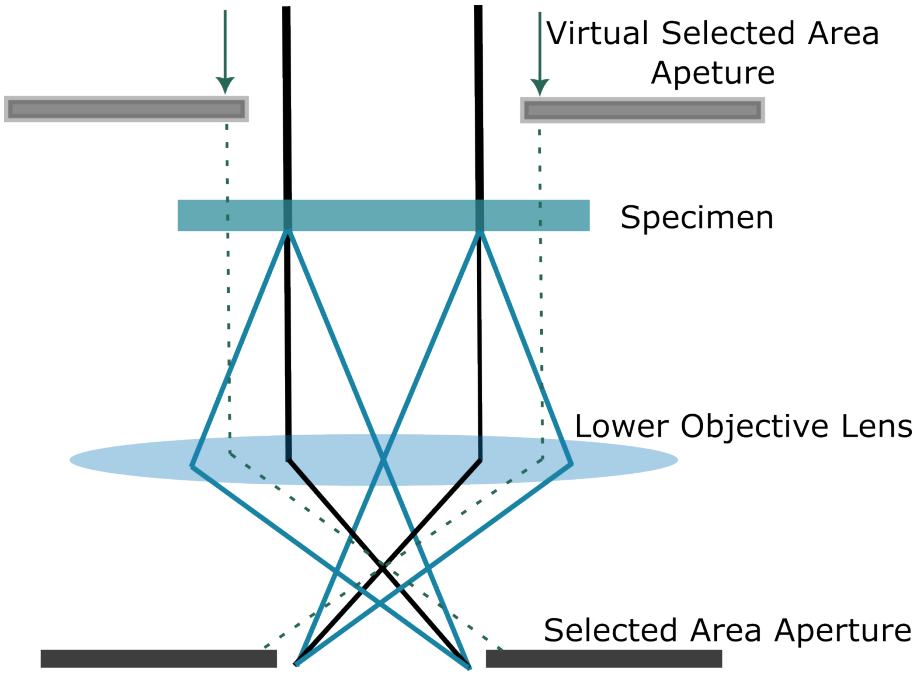


Figure 4.5: Schematic ray diagram of the SAED. The selected area aperture is inserted in the image plane, which is conjugate with the sample plane. The virtual aperture is shown as lying above the sample but actually lies in the sample plane. Dashed lines show the paths of electrons outside of the selected area aperture and do not contribute to the diffraction pattern. Figure adapted from Williams and Carter [87].

Selected Area Electron Diffraction

SAED is used to form diffraction patterns from regions of a sample on the detector. SAED can be used to produce sharp electron diffraction patterns, which can be used to identify crystallographic phases. It is especially useful when it is impossible to grow single crystals large enough for single-crystal X-ray diffraction.

The electron beam in CTEM is a broad parallel beam illuminating a large region of the sample. A selected area aperture is used to obtain diffraction from a limited area of the sample. The selected area aperture is placed in the image plane of the objective lens, as shown in Figure 4.5. The aperture appears in the sample plane as a virtual aperture, which is demagnified by the objective lens. It blocks diffracted beams from regions outside of the virtual aperture.

SAED patterns from single crystals, which are oriented with a zone axis aligned with the direction of the electron beam, show sharp, bright peaks corresponding to reciprocal lattice points, Figure 4.6.**a**. In materials with several contributing crystal orientations, known as grains, the diffraction spots can appear spread out, Figure 4.6.**b**. In cases where many grains contribute to the electron scattering, the spots are smeared to become ring features.

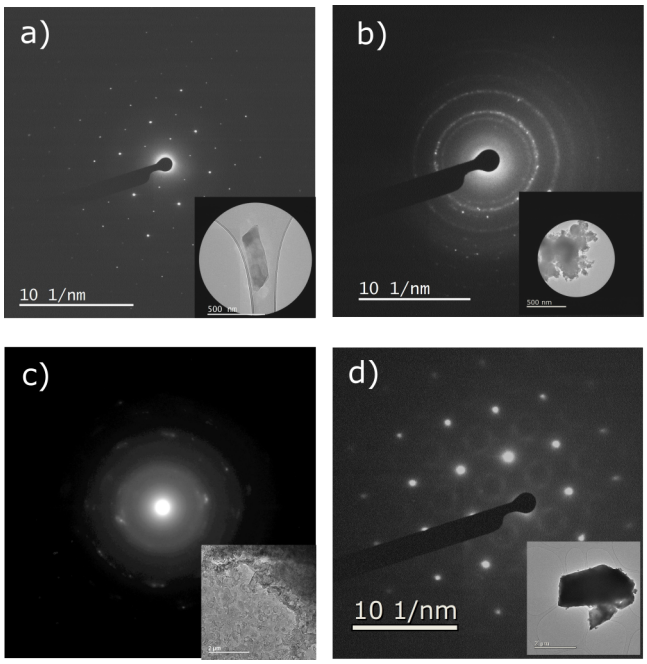


Figure 4.6: Illustrative examples of SAED patterns from different kinds of samples. **a**) SAED pattern of a single crystal with superlattice spots. **b**) SAED of the sample with many small grains contributing to the diffraction produces ring features. **c**) SAED of a predominantly glass-ceramic material with an amorphous structure leading to diffuse rings of intensity; some spots can be observed originating from regions of the sample that have a crystalline structure remaining. TEM images of each sample are inset in the respective figures.

Superlattice spots are extra peaks originating from periodicities in the crystal on a length scale longer than the associated unit cell, for example, due to superstructure ordering. Diffuse scattering is often used to describe the scattering observed from amorphous materials, with a gradual radial decay in intensity from the central spot, Figure 4.6.**c**. However, when the diffuse scattering has a structured nature, for example, Figure 4.6.**d**, this is commonly attributed to the presence of short-range order.

4.2.1 STEM/CTEM Reciprocity

The imaging concepts in CTEM and STEM are based on the same principles, applied in reciprocal ways [196, 197]. The diagram in Figure 4.7 shows that by inverting the optical arrangement of the STEM, the position of the point source in STEM becomes a point in the detector plane of the CTEM arrangement. This is also applied to the electron source in the far field in CTEM, which is reciprocally equivalent to the bright field detector in STEM. Thus, the finite size of the source in STEM can be considered equivalent to the finite size of detector pixels in CTEM. The diagram can also be viewed as a time reversal of the direction of travel of the electron beam. The principle of reciprocity was detailed and rigorously proven using the Bloch wave theorem in 2003 [198]. The results from the

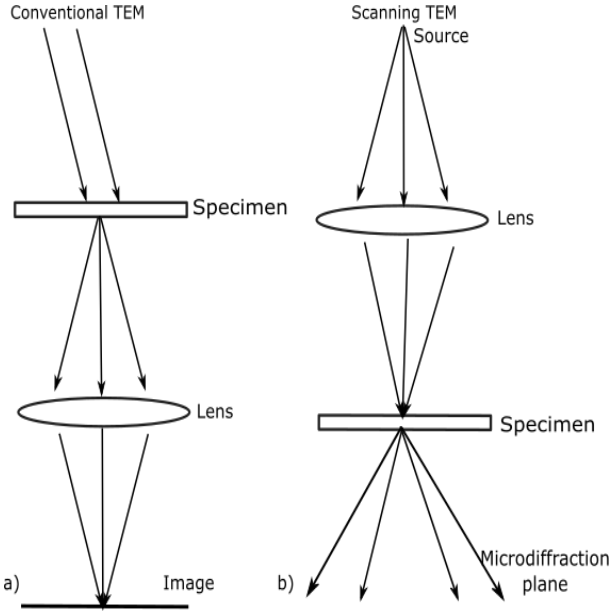


Figure 4.7: Schematic illustration demonstrating the reciprocal nature of the optical setup of **a**) CTEM and **b**) STEM imaging modes.

principle of reciprocity mean that the origins of aberrations and resolution in CTEM and STEM are the same.

4.3 Scanning Transmission Electron Microscopy

STEM images are formed by rastering a focused probe across the sample [199]. The image contrast is determined by the signal collected by the detector in the detector plane. Examples of various detector geometries are shown in Figure 4.8. Atomic resolution imaging is feasible, as long the focused probe is sufficiently small and the sample is sufficiently thin. The addition of aberration correctors further improved resolution by enabling smaller probes with a larger convergence angle [92, 200]. As the probe passes over atomic columns, the signal in the bright field (BF) and annular bright field (ABF) decreases, so the columns appear dark. In contrast, as the probe scans across atomic columns, the scattering to the dark field (DF) region increases, meaning atomic columns appear bright in dark field images. A key strength of the STEM configuration is the local nature of the interaction with the sample, which allows the possibility for spatially resolved spectroscopic techniques such as EELS [201] and spatially resolved diffraction techniques such as nanobeam electron diffraction [202].

4.3.1 Annular Bright Field

Annular bright field (ABF) imaging integrates the signal from an annular ring within the bright field disk but excludes the central region; this geometry is outlined in Figure 4.9.

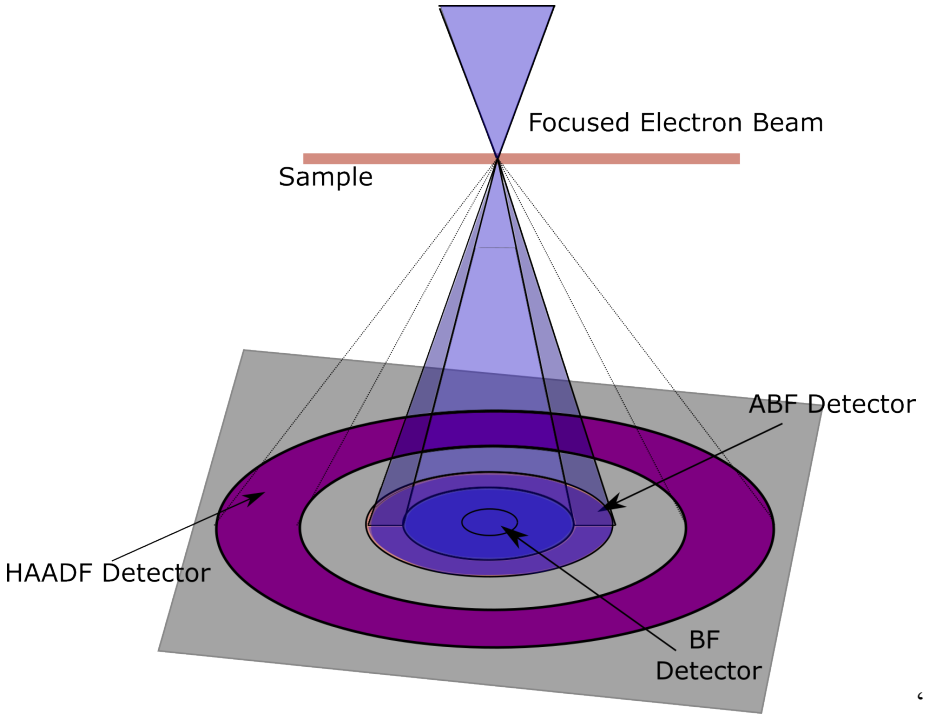


Figure 4.8: Schematic illustration of the detector geometries in STEM, the BF detector collects the central region of the bright field disk, the ABF detector collects the signal from the outer annulus of the bright field disk. The HAADF detector collects signals scattered to angles greater than the bright field disk.

Typically, the outer collection angle α_2 is less than or equal to the probe semi-angle α [203]. As the probe scans across atomic columns, some electrons are scattered to the dark field region of the detector plane. Additionally, channelling effects draw some electrons closer to the atomic column centre, giving the overall reduced intensity in the ABF detector as the probe scans over atomic columns [204]. ABF imaging has been shown to be particularly useful for simultaneous imaging of heavy and light elements [12, 203]. However, the ABF imaging mechanism is particularly sensitive to small degrees of sample mistilt or changes in thickness [203, 205].

4.3.2 Annular Dark Field

The signal in annular dark field (ADF) images is collected by an annular disc detector outside the bright field disk, as shown in Figure 4.9; the inner and outer angles labelled β_1 and β_2 can be tuned by a combination of the probe convergence angle and post-specimen lenses [85]. As the focused electron probe in the STEM scans across atomic columns, strong scattering from the nucleus scatters electrons to high angles, increasing the signal in the DF regions of the detector plane, thus giving rise to bright atomic columns in this imaging mode. The term annular dark field (ADF) imaging is sometimes used interchangeably with HAADF imaging, however in practice, ADF imaging can be defined as either, low angle - ADF, (LAADF), medium angle-ADF (MAADF) or high angle-ADF

(HAADF) imaging depending on the collection angle of the annular detector. Electron scattering at high angles, where the collection angle is much greater than the probe semi-angle, α (in general, $\beta_1 > 3\alpha\,\mathrm{mrad}$), is predominantly by thermal diffuse scattering and phonon scattering. At lower scattering angles, such as those included in LAADF imaging, Bragg scattering is non-negligible; however, these images are still often regarded as incoherent because annular detector geometry integrates the signal over $\mathbf{K_f}$, which further removes any coherence [206]. The loss of coherence means that the phase relationship of the incident beam and scattered electrons is not maintained.

HAADF imaging has grown in popularity for atomic resolution imaging for several reasons. HAADF images are easier to interpret than coherent imaging techniques, such as high resolution transmission electron microscopy (HRTEM). ADF images are easier to interpret than HRTEM because the optical transfer function (OTF), which is equivalent to contrast transfer function (CTF) of HRTEM, follows a straightforward decay, rather than the oscillations of the HRTEM CTF, which leads to contrast reversals [207]. In HAADF images, the intensity of columns can be directly related to the chemical species since the strength of the scattering depends on atomic number (Z) and sample thickness. In the case of a uniform thickness, the atomic column intensity follows a Z^n power-law. The value of n is related to the detector geometry and the contribution from inelastic scattering but generally, around 1.7 [208]. In addition, the development of aberration-corrected STEM probes (discussed in Section 3.1) allows higher resolution, whereas ideal coherent imaging in HRTEM imaging requires the presence of aberrations to generate contrast in the images.

4.3.3 Coherent STEM Imaging

For a focused STEM probe, the probe function $P(\mathbf{R})$, is defined as a Fourier transform of the aperture function $A(\mathbf{K})$ as defined in Equation 4.3.1. The probe-forming aperture defines the convergence angle of the probe. A larger convergence angle gives a larger range of incident wavevectors, translating at the detector plane to a larger angular range of the scattering vectors. This is illustrated in Figure 4.10, showing that increasing the convergence angle of the probe leads to the diffraction spots which would be observed in a SAED pattern spreading out to become disks [209].

$$P(\mathbf{R}) = \int A(\mathbf{K}) exp(i2\pi\mathbf{K}\cdot\mathbf{R}) d\mathbf{K} \tag{4.3.1}$$

Bright-field STEM uses a small detector close to the optical axis to integrate the coherent electron signal. Considering the principle of reciprocity (section 4.2.1), BF-STEM is equivalent to CTEM and likewise is a phase imaging technique, meaning that the CTF has

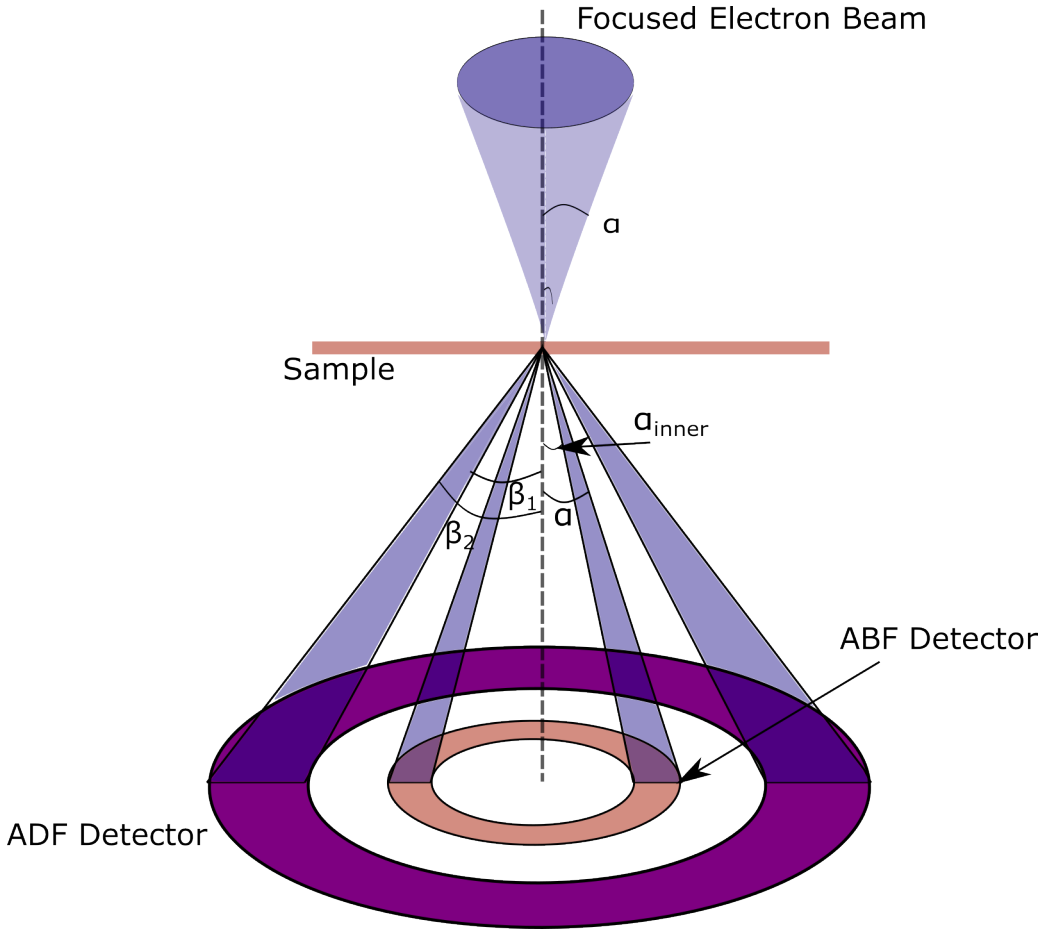


Figure 4.9: Schematic Illustration of STEM showing the ABF and ADF detector geometries with typical collection angles drawn relative to the scanning transmission electron microscope (STEM) probe semi-convergence angle α. All angles are defined as semi-angles w.r.t. to the optical axis, where $\alpha_{inner} < \alpha$ and $\alpha > \beta_1 > \beta_2$.

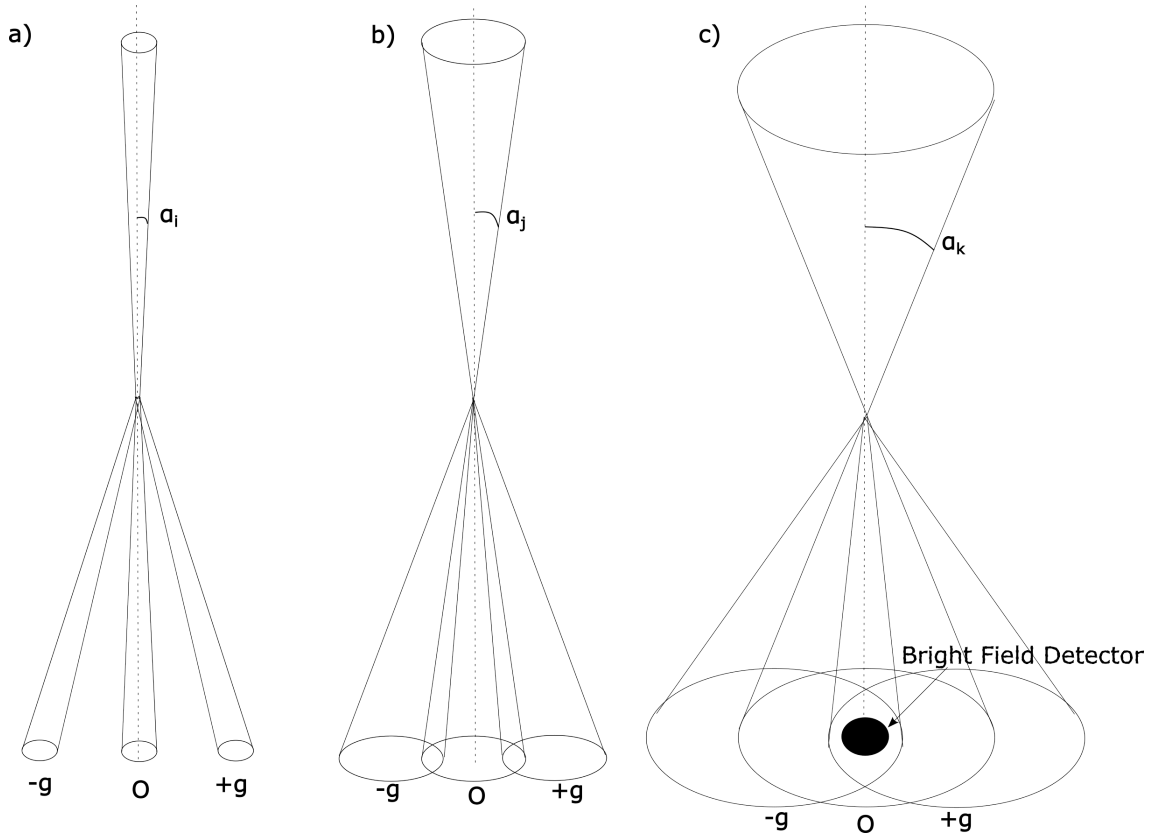


Figure 4.10: Schematic of increasing convergence angle where ($\alpha_i < \alpha_j < \alpha_k$) of the focused electron probe, the first set of diffracted beams are given as $\pm g$ **a**) probe semi-angle α_i **b**) probe semi-angle α_j **c**) probe semi-angle α_k. The position of the BF detector is also shown in **c**.

a similar oscillatory nature [198, 210]. The contrast in BF-STEM imaging relies on interference effects between the direct beam and the first set of diffracted beams [210]. This interference can only be observed by an axial bright field detector when the magnitude of g is less than the radius of the bright field disk, as illustrated in Figure 4.10.**c**.

4.4 4D-STEM methods

Similar to the STEM methods described above, 4D-STEM is based on the configuration of a probe scanned across the sample. The major difference is that a pixelated detector records spatially resolved information in the diffraction plane rather than integrating the signal in a particular region. The four dimensions refer to the two dimensions of the probe scan ($\mathbf{R_x}, \mathbf{R_y}$) and the two dimensions in reciprocal space ($\mathbf{K_x}, \mathbf{K_y}$). This geometry is illustrated in Figure 4.11 for a focused electron probe scanning a sample with a 3×3 scan in the sample plane. A CBED pattern of 256×256 pixels is recorded for each probe position. As was previously illustrated in Figure 4.10, the nature of the diffraction information recorded on the detector is controlled by changing the probe convergence angle.

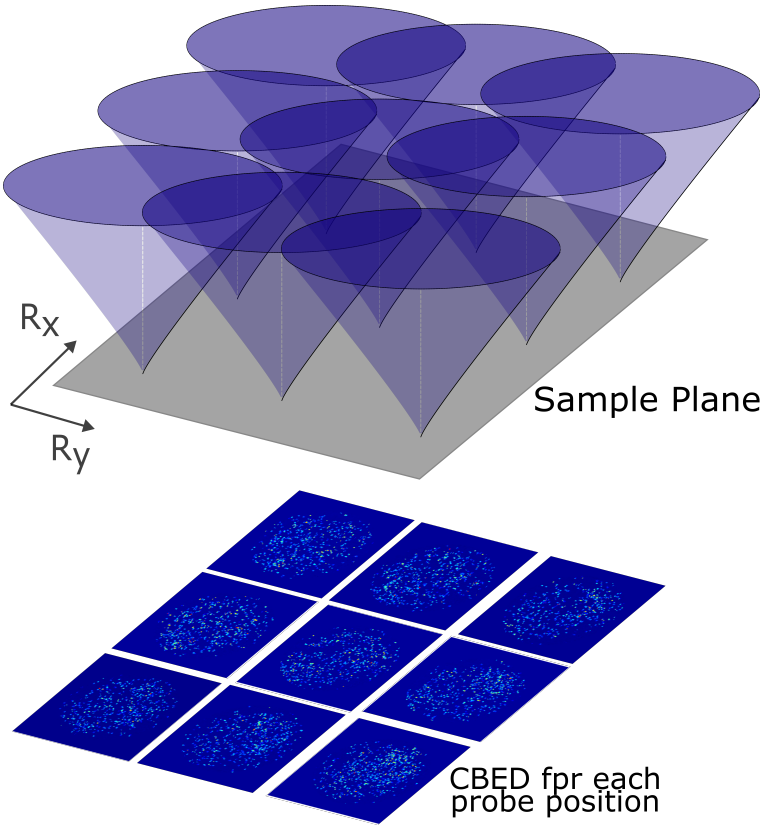


Figure 4.11: Schematic illustration of 4D-STEM data acquisition for a focused electron beam, scanning at 9 points in the sample plane and recording 9 CBED patterns in the diffraction plane.

4.4.1 Virtual Imaging

Integrating the signal in regions of a pixelated detector to form conventional STEM images is called virtual imaging. Using a 4D-STEM set-up can provide a highly flexible method to tune the detector geometry [211]. Although the acquisition may be slower, in some cases the ability to record an entire 4D dataset during the experiment and integrate the signal in some regions of the detector post-acquisition may be beneficial.

4.4.2 Ptychography

The 4D-STEM dataset, denoted by $M(\mathbf{R_p}, \mathbf{K_f})$, is recorded by a pixelated detector as the square modulus $|M(\mathbf{K_f}, \mathbf{R_p})|^2$, i.e. only the intensity information is recorded. Ptychography is a method by which, the phase information that is lost by recording $|M(\mathbf{K_f}, \mathbf{R_p})|^2$ can be retrieved. The physical origin of the technique relies on interference between diffracted beams to reconstruct the relative phase and, therefore, build an image where the contrast can be directly related to the projected potential of the specimen. A unique solution to the exit wavefunction can be inferred by the fact that in STEM, the shifting of the probe in real space corresponds to a phase ramp in reciprocal space [137].

In this thesis, only focused probe ptychography is considered. This is performed using a highly focused electron probe, and thus, the information recorded at each probe position is a CBED pattern, illustrated in Figure 4.11. As is also briefly mentioned in Section 4.4.2, defocused probe ptychography is also possible. However, using a focused probe means obtaining ADF images simultaneously is possible. This is particularly useful for obtaining incoherent scattering from the heavy transition metals present in battery materials, generating a more complete picture of the structure. The development and application of the technique were covered in Section 3.2.1; this section will outline the theoretical background.

The wavefunction exiting the specimen, $\psi(\mathbf{R}, \mathbf{R_p})$ can be described as a product of the probe function and the complex transmission function. The propagation from the specimen plane to the detector is represented mathematically as a Fourier transform in real space of $\psi(\mathbf{R}, \mathbf{R_p})$ Equation 4.4.1. This function, $M(\mathbf{K_f}, \mathbf{R_p})$, denotes the complex amplitude of the wavefunction.

$$M(\mathbf{K_f}, \mathbf{R_p}) = \mathcal{F}[P(\mathbf{R} - \mathbf{R_p}) \cdot \psi(\mathbf{R})] \tag{4.4.1}$$

The data recorded by the detector $|M(\mathbf{K_f}, \mathbf{R_p})|^2$ can be written, as in Equation 4.4.2, as a convolution of the probe function and $\Psi(\mathbf{K_f})$, which for a phase object is the Fourier transform of the specimen projected potential.

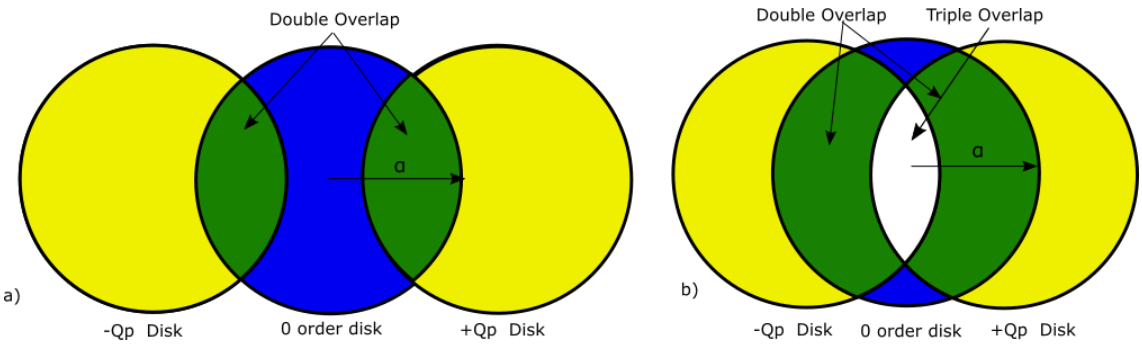


Figure 4.12: Schematic illustration of $G(\mathbf{K_f}, \mathbf{Q_p})$ showing the overlap between the direct and scattered beams at the respective spatial frequencies $+\mathbf{Q_p}$ and $-\mathbf{Q_p}$. **a**) In the case where $\alpha < \mathbf{Q_p}$, the direct and scattered beams overlap to form double overlap regions. **b**) In the case where $\alpha > \mathbf{Q_p}$, a triple overlap region forms, which contains no phase information due to destructive interference.

$$|M(\mathbf{K_f}, \mathbf{R_p})|^2 = \mid A(\mathbf{K_f}) exp(i2\pi \mathbf{K_f} \cdot \mathbf{R_p}) \circledast \Psi(\mathbf{K_f}) \mid^2 \tag{4.4.2}$$

Performing a Fourier transform on Equation 4.4.2 with respect to the probe position $\mathbf{R_p}$, as in Equation 4.4.3, gives the function $G(\mathbf{K_f}, \mathbf{R_p})$. The result, given in Equation 4.4.4, is known as the Fourier overlap function and is a convolution of the aperture function for a particular scattering vector ($\mathbf{K_f}$) and complex transmission function for the same $\mathbf{K_f}$, each multiplied respectively by the aperture function and complex transmission function, separated by $\mathbf{Q_p}$ [138].

$$G(\mathbf{K_f}, \mathbf{Q_p}) = \int \mid M(\mathbf{K_f}, \mathbf{R_p}) \mid^2 exp(2\pi i \mathbf{R_p} \cdot \mathbf{Q_p}) d\mathbf{R_p} \tag{4.4.3}$$

$$= A(\mathbf{K_f}) A^*(\mathbf{K_f} + \mathbf{Q_p}) \circledast_{\mathbf{K_f}} \Psi(\mathbf{K_f}) \Psi^*(\mathbf{K_f} - \mathbf{Q_p}) \tag{4.4.4}$$

$G(\mathbf{K_f}, \mathbf{Q_p})$ is also a 4-dimensional dataset but is a complex function, in which information on both the magnitude and phase is encoded, thus solving the phase problem. Retrieving the Fourier overlap function is a common step in both single side band (SSB) and Wigner distribution deconvolution (WDD) reconstruction methods.

The sum of $|G(\mathbf{K_f}, \mathbf{Q_p})|^2$ across all $\mathbf{K_f}$ values can be plotted with respect to $\mathbf{Q_p}$, this is referred to as the power spectrum. The interference between the direct and diffracted beams can be visualised by selecting spatial frequencies with high signal-to-noise, as in Figure 4.13.

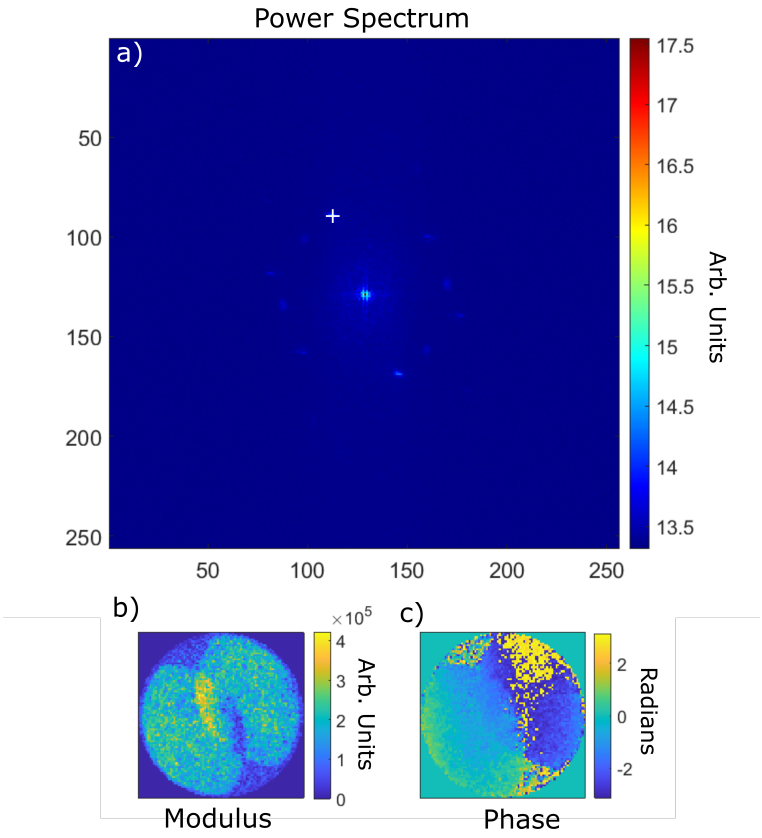


Figure 4.13: a) Power spectrum of $G(\mathbf{K_f}, \mathbf{Q_p})$ plotted with respect to $\mathbf{K_f}$, for a particular spatial frequency $\mathbf{Q_p}$. **b**) The modulus in arbitrary units. **c**) The phase in radians, plotted for $Q = 10.31\, mrad$ at the point [89,112] identified by the '+' on the power spectrum.

4.4.3 Single Side Band

In the SSB method, the WPOA, defined previously as $\psi_{exit} = 1 + i\sigma V(r)$, is applied to simplify Equation 4.4.4. This gives Equation 4.4.5; a simplified expression for $G(\mathbf{K_f}, \mathbf{Q_p})$, which has three components, where the first is related to the unscattered component of the beam. The second and third terms are the complex conjugates of each other, referring to the overlap regions between the direct beam and the scattered beams at the spatial frequencies $+\mathbf{Q_p}$ and $-\mathbf{Q_p}$ respectively. This is demonstrated for an experimental dataset in Figure 4.12 in the cases where either the spatial frequency $\mathbf{Q_p}$ is less or greater than the probe convergence semi-angle α.

$$\begin{aligned} G(\mathbf{K}, \mathbf{Q_p}) =\mid A(\mathbf{K}) \mid^2 \delta(\mathbf{Q_p}) + A(\mathbf{K_f})A^*(\mathbf{K_f} + \mathbf{Q_p})\Psi_s^*(-\mathbf{Q_p}) \\ +A^*(\mathbf{K_f})A(\mathbf{K_f} - \mathbf{Q_p})\Psi_s(\mathbf{Q_p}) \end{aligned} \tag{4.4.5}$$

To retrieve the phase component of $M(\mathbf{K_f}, \mathbf{R_p})$, the intensity within one of the double overlap regions $+\mathbf{Q_p}$ or $-\mathbf{Q_p}$ is summed for all $\mathbf{Q_p}$, to form the Fourier transmission function. Then, by performing an inverse Fourier transform with respect to $\mathbf{Q_p}$, the real space transmission function with respect to probe position, $\psi(\mathbf{R_p})$, can be extracted. The complex component can then be plotted for each probe position to form the phase image.

In the weak phase approximation, the modulus of both double overlap regions is identical, and the phase is π radians out of phase. Therefore, the reconstructed image quality should be unaffected by the choice of double overlap region. The difference in the phase will lead to a contrast reversal in the phase reconstruction images.

4.4.4 Wigner Distribution Deconvolution Method

The WDD method follows the same derivation of the function $G(\mathbf{K_f}, \mathbf{Q_p})$, what is subsequently done with this function differs. The WDD method does not rely on the WPOA approximation. Instead, in the WDD method, the first step is to perform an inverse Fourier transform with respect to $\mathbf{K_f}$ to obtain a function with variable $\mathbf{Q_p}$ and the inverse variable $\mathbf{K_f}$. Further details can be found in the work by Rodenburg and Bates [144], but to summarise the result, $H(\mathbf{r}, \mathbf{Q_p})$ can be expressed (as in Equation 4.4.6) as the product of the Wigner distribution function of the imaging system, $\xi_P(\mathbf{r}, -\mathbf{Q_p})$ and the Wigner distribution function of the specimen $\xi_\psi(\mathbf{r}, \mathbf{Q_p})$.

$$H(\mathbf{r}, \mathbf{Q_p}) = \xi_P(\mathbf{r}, -\mathbf{Q_p}) \cdot \xi_\psi(\mathbf{r}, \mathbf{Q_p}) \tag{4.4.6}$$

The deconvolution of these functions can conveniently be carried out by a Wiener deconvolution method to obtain the specimen transmission function. This is defined in Equation 4.4.7, where the addition of ϵ, typically a small constant term, avoids non-physical results due to divisions by zero [144].

$$\xi_{\psi}(\mathbf{r}, \mathbf{Q_p}) = \frac{\xi_P(\mathbf{r}, \mathbf{Q_p}) \cdot H(\mathbf{r}, \mathbf{Q_p})}{\mid \xi_P(\mathbf{r}, -\mathbf{Q_p}) \mid^2 + \epsilon} \tag{4.4.7}$$

The deconvolved function $\xi_{\psi}(\mathbf{r}, \mathbf{Q_p})$ is then Fourier transformed with respect to the probe position $\mathbf{r}$ and can be written as Equation 4.4.8 [144]. By taking the direct beam as having a particular phase, all other phases can be calculated relative to this. An inverse Fourier transform of the assigned phases gives the transmission function in terms of $\mathbf{R_p}$, i.e. $\psi(\mathbf{R_p})$, the desired function.

$$G(\mathbf{K_f}, \mathbf{Q_p}) = \Psi(\mathbf{K_f})\Psi(\mathbf{K_f} - \mathbf{Q_p}) \tag{4.4.8}$$

4.4.5 Post-acquisition Aberration Correction

As discussed within the literature overview, in Section 3.2.1, a particular advantage of ptychography is enabling the correction of aberrations post-acquisition. This is particularly favourable for imaging of beam-sensitive materials since the data can be acquired faster, with less exposure to the beam. The following discussion demonstrates that it is possible to write the aberrations as a set of linear equations, which can be solved using the redundant information within datasets acquired for ptychography reconstructions. The redundancy in the 4D-STEM dataset, which allows the aberration coefficients in the set of linear equations to be solved, refers to the fact that the number of values of (K_u, K_v, Q_u, Q_v) is much larger than the number of coefficients.

Taking the terms corresponding to only one of the double overlap regions ($-\mathbf{Q_p}$) in Equation 4.4.5 an expression for the phase in the double overlap region $\angle G(\mathbf{K_f}, \mathbf{Q_p})$, can be obtained and is given by Equation 4.4.9 [149].

$$\angle G_{-\mathbf{Q_p}}(\mathbf{K_f}, \mathbf{Q_p}) = \chi(\mathbf{K_f}) - \chi(\mathbf{K_f} + \mathbf{Q_p}) - \angle \psi'(-\mathbf{Q_p}) \tag{4.4.9}$$

The term $\chi(\mathbf{K_f})$ corresponds to a set of linear equations containing the aberration coefficients of interest; these are given for aberrations up to the third order in Table 4.1. The final term $\angle \psi'(-\mathbf{Q_p})$ refers to the scattered components of the Fourier expression. The overall aberration function, χ, is given by the sum of each scattering vector function in terms

Aberration	Coefficient $C_{n,k}$	Scattering vector functions $\alpha_p(u,v)$
Defocus	C_1	$\frac{1}{2}(u^2+v^2)$
Two-fold astigmatism	C_{12a}	$\frac{1}{2}(u^2-v^2)$
Two-fold astigmatism	C_{12a}	uv
Three-fold astigmatism	C_{23a}	$\frac{1}{3}u(u^2-3v^2)$
Three-fold astigmatism	C_{23b}	$\frac{1}{3}v(3u^2-v^2)$
Axial coma	C_{21a}	$\frac{1}{3}u(u^2+v^2)$
Axial coma	C_{21a}	$\frac{1}{3}v(u^2+v^2)$
Spherical aberration	C_3	$\frac{1}{4}(u^2+v^2)^2$
Four-fold astigmatism	C_{34a}	$\frac{1}{4}(u^4-6u^2v^2+v^2)$
Four-fold astigmatism	C_{34b}	u^3v-uv^3
Star aberration	C_{23a}	$\frac{1}{4}(u^4+v^4)$
Star aberration	C_{23b}	$\frac{1}{2}uv(u^2+v^2)$

Table 4.1: Table of aberration coefficients up to the third order. Aberration coefficients are denoted using Krivanek notation, where the term n denotes the order and k denotes the degree of azimuthal symmetry. Adapted from [91, 149].

of (u,v) multiplied by the respective coefficient, as given in Equation 4.4.10 [212]. The set of linear equations combines the coefficients of interest, with the respective scattering vectors in Cartesian coordinates in terms of u and v, defined in Table 4.1. An equivalent equation for the $+\mathbf{Q_p}$ overlap region can be written, giving the same overall result.

$$\chi(u,v) = \sum_{p=1}^{p} c_{n,k}\alpha_p(u,v) \tag{4.4.10}$$

A matrix representation of this is given in Equation 4.4.11, where $\mathbf{b}$ contains the phase values of $G_{-\mathbf{Q_p}}(\mathbf{K_f})$, and the observations of $A(-\mathbf{Q_p},\mathbf{K_f})$, and χ contains the aberration coefficients [149]. As there are many more observed values of $A(-\mathbf{Q_p},\mathbf{K_f})$, than coefficients of the linear equation, a matrix inversion method, such as single value decomposition (SVD), can then be used to solve for the aberration values. For a full mathematical description of SVD, the reader is referred to other sources [151].

$$\mathbf{b} = A(-\mathbf{Q_p},\mathbf{K_f})\cdot\chi \tag{4.4.11}$$

Due to the issues caused by phase wrapping, $\mathbf{b}$ is calculated iteratively from the highest to lowest order aberrations. The equation can theoretically be calculated for any value of $\mathbf{Q_p}$, but is usually selected by choosing those $\mathbf{Q_p}$ values with the largest modulus in the double overlap regions. This is equivalent to choosing strong $\mathbf{Q_p}$ values from the power spectrum, as discussed in Section 4.4.2.

Aberration	Value
C_1	-2.901 nm
C_{12a}	1.831 nm
C_{12b}	-1.377 nm
C_{23a}	11.753 nm
C_{23b}	18.934 nm
C_{21a}	13.018 nm
C_{21b}	82.050 nm
C_3	1.777 μm
C_{34a}	0.300 μm
C_{34b}	-0.070 μm
C_{32a}	-7.894 μm
C_{32b}	10.609 μm

Table 4.2: Calculated aberration coefficients for example, experimental dataset.

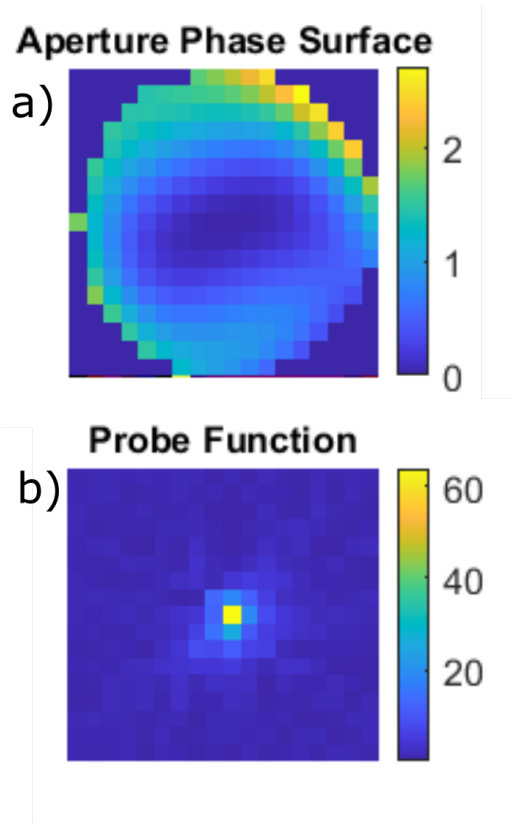


Figure 4.14: Graphicsal representations of **a**) the calculated aperture phase surfaec and **b**) probe function.

Once the aberration values have been determined, the calculated values are input into the reconstruction process. In the SSB reconstruction, an aperture function accounting for the phase distortions from the calculated aberrations is used. In the WDD method, aberrations can be used to calculate a modified probe function. Examples of calculated aperture and probe functions are shown in Figure 4.14, alongside a typical set of calculated aberration coefficients (Table 4.2).

4.4.6 Nanobeam Electron Diffraction

In nanobeam electron diffraction (NBED), the convergence angle of the scanning probe is reduced while, as far as possible, maintaining a small spatial extent of the probe. As in other 4D-STEM methods, the probe is scanned across the sample and a diffraction pattern is recorded for each probe position. Providing that the probe is sufficiently parallel, diffraction spots are produced, very similar to those in SAED. However, instead of illuminating a large area and using an aperture to select rays from a region of the sample, only a small region of the sample, (corresponding to the interaction volume of the probe) contributes to each diffraction pattern recorded. Therefore, NBED can combine the spatial resolution of the STEM probe with the angular resolution on the detector plane of CTEM

diffraction methods.

4.5 Summary

This chapter has described the theoretical background underpinning transmission electron microscopy and the imaging and diffraction techniques used in the preparation of this thesis. This includes methods in CTEM such as SAED, STEM - ABF and ADF imaging - in addition to the 4D-STEM methods used. The mathematical principles of the ptychography reconstruction process are also outlined.

The following chapter provides the reader with the details of the instrumentation and methodology used in the experiments utilised in the preparation of this thesis.

Chapter 5

Instrumentation and Methodology

This Chapter describes the instrumentation, sample preparation methods and data processing procedures used in this thesis.

5.1 Instrumentation

5.1.1 JEOL JEM-ARM200CF

The JEOL JEM-ARM200CF is shown in Figure 5.1 is located in the David Cockayne Centre for Electron Microscopy (DCCEM), University of Oxford. The instrument is fitted with a cold field emission gun (C-FEG) and can be operated at an operating voltage of either $200\,\mathrm{kV}$ or $80\,\mathrm{kV}$. The instrument is fitted with a CEOS aberration correction system for the STEM probe, providing atomic resolution imaging. For analytical and spectroscopic analysis, the microscope is fitted with $100\,\mathrm{mm}^2$ Centurion EDS detector and Gatan GIF Quantum 965 ER, which can perform dual EELS and is capable of being operated in energy filtered transmission electron microscopy (EFTEM) mode.

The instrument has an upper and a lower ADF detector, allowing flexibility in the choice of inner and outer collection angles. The HAADF images in Chapter 7 were acquired using the upper (ADF-1) detector. Experiments in Chapter 6 make use of the 4D-STEM imaging capability of the instrument. For this application, the instrument is fitted with a DED, specifically the JEOL 4D Canvas. The technology for the detector is based on the pnCCD and further details of this are given in Section 5.1.4 [124].

5.1.2 JEOL JEM-3000F

The JEOL JEM-3000F, shown in Figure 5.2, is located in the DCCEM facility, University of Oxford. The instrument is operated at $200\,\mathrm{kV}$ and does not have aberration correction capability, but the field emission source provides a high-brightness electron source. The instrument can be operated in CTEM or STEM mode. The instrument was primarily used in this thesis to obtain SAED data in Chapter 7, and various initial sample screenings. The instrument is fitted with a 4K Gatan Ultrascan camera, used to record SAED patterns.



Figure 5.1: Image of the JEOL JEM-ARM200CF (S)TEM instrument used for many of the experiments in this thesis. *Image used courtesy of JEOL (UK) Ltd.*.

5.1.3 JEOL JEM-ARM300CF

The JEOL JEM-ARM300CF at electron Physical Sciences Imaging Centre (ePSIC), located at Diamond Light Source, was primarily used to perform scanning electron diffraction experiments detailed in Chapter 8 and also investigate the fluorinated-DRS with higher acceleration voltage, as described in Chapter 9. This instrument is a cold-field emission (S)TEM with double spherical aberration correction and can be operated between 30 and 300 kV. The instrument is fitted with a MerlinEM 4D-STEM detector. A Gatan OneView camera was used for locating an appropriate region of the sample and correcting aberrations since the microscope is operated remotely from an adjacent room to minimise vibrations. The instrument can also be used for analytical work using the Oxford Instruments XMAX 100 EDX detector.

5.1.4 Direct Electron Detectors

DED, such as the pnCCD, fulfil the two principle requirements for 4D-STEM experiments; they are radiation-hard and have very fast frame readout speeds. The development of DEDs, an overview of their application to 4D-STEM experiments, and a summary of the available readout modes have been outlined in Section 3.1.2.



Figure 5.2: Image of the JEOL JEM-3000F electron microscope in the DCCEM, University of Oxford.

Binning	Pixels	Standard Readout (fps)	Fast Readout (fps)
Full-frame	264x264	1,150	2,000
2-fold binning	128x264	2,000	4,000
4-fold binning	66x264	4,000	7,513
2-fold Windowing	264x128	2,000	4,000

Table 5.1: Table of the modes and corresponding readout rates for JEOL 4DCanvas. Data from the pnCCD user manual [214].

JEOL 4DCanvas

The JEOL 4DCanvas is a 4D-STEM detector system mounted within the JEOL JEM-ARM200CF microscope described in Section 5.1.1. The system has a pnCCD direct electron detector specifically designed for (S)TEM applications, located within a retractable camera housing, shown in Figure 5.3. This provides the microscope with 4D-STEM capability and can also be used for low-dose TEM imaging. The pnCCD is a monolithic integrating design that inherently has radiation hardness and allows a very thin entrance window, maximising sensitivity to low energy electrons [124]. In terms of radiation hardness, minimal damage has been observed to the pnCCD for $300\,\mathrm{kV}$ electrons with doses up to 10^{15} electrons per cm^2 [213]. The dynamic range of the pnCCD, operating at $1000\,\mathrm{fps}$, is equal to the charge of $13,800$, electrons with an energy of $80\,\mathrm{keV}$, per pixel, which can be summed. Electrons deposit their energy over several pixels; there is significant discussion of this in Chapter 6 [124].

The pnCCD sits perpendicular to the electron beam inside the housing, which consists of a cooling system. Thermoelectric coolers reduce the temperature of the CCD to $-20\,°\mathrm{C}$. The cooling mask also protects other areas of the camera to prevent them from being exposed to the electron beam. The imaging area is $12.7 \times 12.7\,\mathrm{mm}^2$, consisting of 264×264 pixels which each have dimensions $48 \times 48\,\mu\mathrm{m}^2$. The camera is capable of a full-frame read-out speed of 2000 frames per second (fps), and with binning, readout speeds up to $7,500$ fps are possible. A full table of read-out speeds for possible binning and windowing conditions is given in Table 5.1. In binning modes, the full sensor area is used, but the data is binned in the readout step, whereas in the windowing mode, the physical area of the detector which is readout is reduced.

The pixel structure of the pnCCD is on the opposite side of the detector to where the electrons enter the CCD. A voltage is applied to propagate the charge through the column structure to the pixel structure on the backside of the detector. Shift voltages then transfer the charges in a single direction to one of two frame readout areas on either side of the exposed area; the readout process can then take place from this region while another frame is recorded. The shifting process is extremely fast; however, the possibility of out-of-time

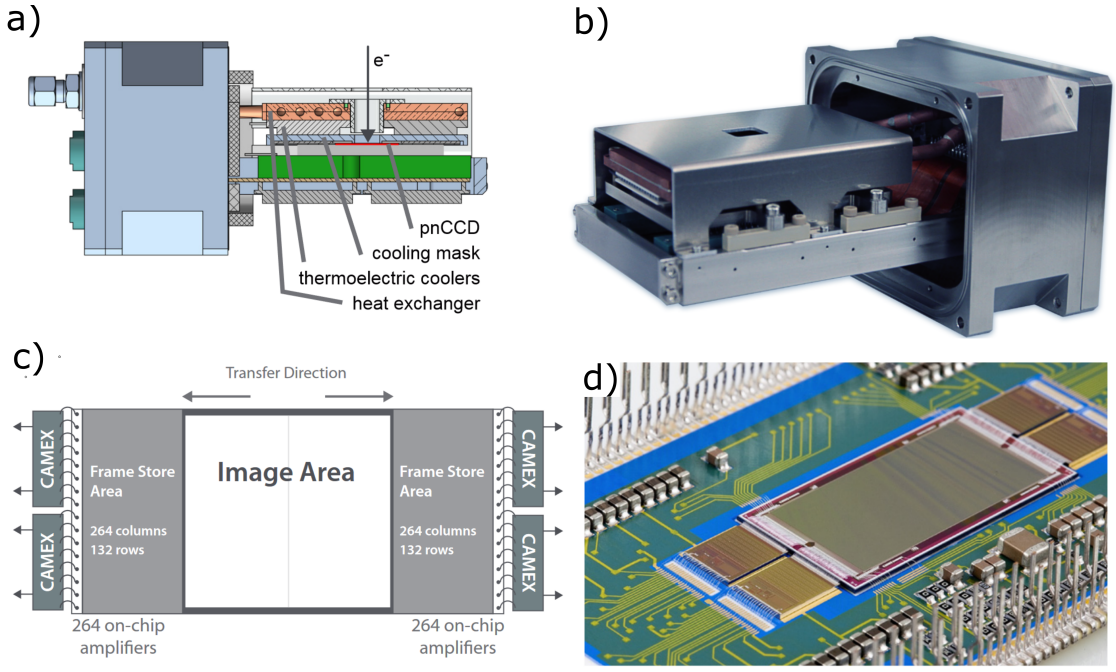


Figure 5.3: **a**) Cross-section illustration of the pnCCD (S)TEM camera head. **b**) Image of the pnCCD mounted on the retractable camera housing without the shielding covers. **c**) Schematic of the pnCCD imaging chip with the imaging area and direction of shifting to the readout areas shown. **d**) Image of this setup mounted on a ceramic mount. Figures adapted from [124] with permission IOP Publishing.

events can not be disregarded completely [1]. A schematic illustration in Figure 5.3.**c** shows the readout area and shifting direction with the device set-up imaged in 5.3.**d**.

MerlinEM

The Merlin EM detector is based on the Medipix3 chip and is a hybrid pixel detector. The detector has 256×256 pixels, but on the JEOL JEM-ARM300CF, four chips are combined in a quadrant array. The number of pixels readout is fixed; however, the readout speed is based on the bit-depth (range of values assigned to a pixel) of the pixels readout. The maximum bit-depth of the Merlin-EM is 24-bit, offering a readout speed of 600 fps, which can be increased to a maximum of $12,500$ fps by reducing the bit depth to 1-bit.

5.2 Sample Preparation and Handling

Samples were synthesised by members of the Bruce group at the University of Oxford. In particular, Liquan Pi synthesised most of the DRS compositions studied.

Cathode materials are known to be sensitive to oxygen and moisture; evidence has shown

[1] Out-of-time events are electron landing events which happen between frames and are not recorded by the detector.

that to react with water to form surface layers and the oxidation state of transition metals can be affected by reactions with O_2 [215]. For this reason, after synthesis, samples were stored in an argon atmosphere with consistently less than $0.1\,\mathrm{ppm}$ of oxygen and H_2O.

Prior to imaging, the cathode powder was suspended in the solvent dimethyl carbonate [DMC], and sonicated for 10 minutes to improve the dispersion of the cathode powder in the suspension. A pipette was then used to drop cast 1-2 drops of the suspension onto a support grid. Copper grids with a holey or lacey carbon mesh were used to support the sample. DMC is a volatile solvent, so it can be easily evaporated by placing the grid into the glovebox anti-chamber under vacuum. The grid was placed into a vial, and the lid was placed on top without tightening to allow the solvent to evaporate but prevent the grid from being pulled into the vacuum pump. Due to some residual contamination being found on some samples during high-resolution imaging, these samples were baked under vacuum in a custom-built vacuum heating chamber or using the vacuum heating function of a Fishone 1020 Plasma cleaner. The samples were exposed to air during the transfer in and out of the vacuum oven, but the heating process was not applied until high vacuum conditions had been achieved.

The prepared TEM grids were transported to the microscope inside a sealed vial, which was then placed inside a centrifuge tube and further sealed by parafilm® to prevent the leakage of argon. Pristine samples can be exposed briefly to the atmosphere as they are transferred into the microscope; this time was typically less than two minutes. This is not the case for charged samples, which have to be transferred to the microscope using a vacuum transfer holder.

5.3 Data Acquisition in the STEM

5.3.1 Aberration Corrected STEM

In addition to the manual alignment of the low-order aberrations, namely, defocus coma and astigmatism, both the JEOL JEM-ARM200F and the JEOL JEM-ARM300CF are fitted with aberration correction systems able to correct aberration up to the third order. In the case of the JEOL JEM-ARM200F, the CEOS software acquires images of the probe at various tilt ranges in order to calculate the aberration coefficients. The residual aberrations can then be corrected iteratively using hexapole lenses until all aberration coefficients are fitted and satisfactorily corrected [216]. The JEOL JEM-ARM300CF is fitted with a double aberration correction system, which uses the JEOL COSMOS software to obtain over-focused and under-focused ronchigram images from an amorphous region, usually an area of the lacey carbon grid. Automated fitting and correction of the aberrations is then performed by the JEOL COSMOS software using pre-defined routines [217].

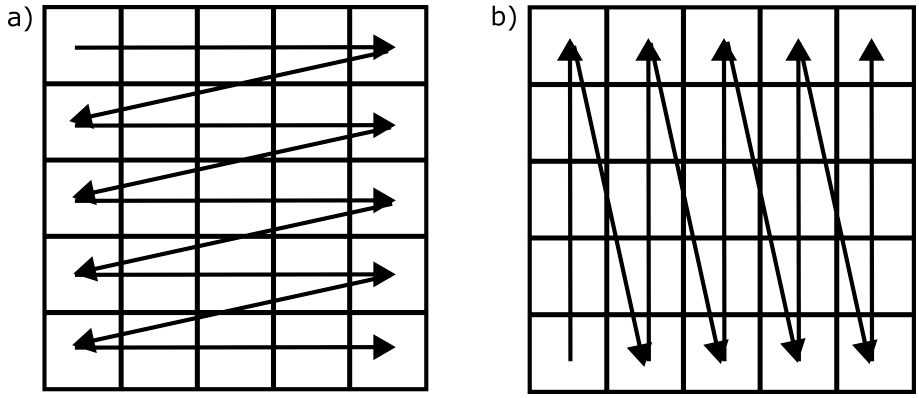


Figure 5.4: a) Schematic illustration of the raster scan direction. Horizontal arrows show the fast scan direction, and the fly-back direction is shown by the diagonal arrows. **b**) The raster scan with scan rotation of 90 ° anticlockwise applied.

5.3.2 Multi-frame Data Acquisition

High-resolution HAADF images in this thesis were acquired using multi-frame acquisition techniques. High-resolution STEM images are extremely sensitive to external effects, which can result in distortion of the images; these can include sample movement during the scanning time, often appearing as a smearing in a particular direction. The scan system itself has a fast scan direction and a slow scan direction, which can lead to imperfections in the scan array, causing scan distortions. Multi-frame imaging involves scanning the STEM probe several times over the same region, typically rotating the scan direction 90 ° for each frame, such as in Figure 5.4. The SmartAlign plug-in for Digital Micrograph was used to set the parameters for the data acquisition and reconstruction [218].

The set of images, referred to as a frame stack, can then be aligned using either rigid registration or non-rigid registration methods; aligning these images can compensate for both sample drift and scan distortions. The primary method for aligning the frame stack in the preparation of this thesis was non-rigid registration. The reader is referred to other works, particularly by Jones et al., for details of non-rigid registration [218] and Zitova et al. for rigid registration methods [219].

Acquiring multi-frame image stacks offers additional benefits, particularly when imaging beam-sensitive materials. First, when viewed in a series, images can show the effects of the cumulative electron dose after each scan. This means that when initial signs of damage are observed in a particular frame, subsequent frames can be removed before the registration of the images. Faster scan rates with multiple passes have been demonstrated to reduce the damage incurred for the same electron dose; furthermore, a higher signal-to-noise in the images can be achieved for the same dose [176, 218].

5.3.3 Ptychography Data Acquisition

All of the ptychography experiments described in this thesis were carried out using the JEOL ARM200F at the University of Oxford and data was acquired on the pnCCD.

In the first instance, standard alignment procedures were followed, including the correction of high-order aberration as described in Section 5.3.1. Selection of an appropriate particle and tilting to the desired zone-axis was carried out using the shadow image in ronchigram mode. Then, the final adjustment of defocus and astigmatism was carried out on the ADF image viewed live in the Digital Micrograph software. In order to minimise the effect of any damage that occurred while focusing, the sample was moved slightly prior to the acquisition of the ptychography datasets.

The scan parameters for the acquisition of the ptychography datasets are set in JEOL TEM Center software. The combination of the magnification and the number of pixels in the scan, which ultimately define the step size, are both set in the JEOL TEM Center Software. To achieve optimal sampling, the step size $\Delta\mathbf{R_p}$, must fall within the Nyquist limit of the imaging system [220]. The imaging system is limited in the spatial frequencies that can be represented by the convergence angle α and the wavelength λ, as $\lambda/2\alpha$. For optimal sampling, the step size should be matched to twice the resolution of the imaging system where the sampling limit in reciprocal space is defined as $|\mathbf{K}| < 1/2\Delta\mathbf{R_P}$, giving the result that the optimal step size is $\lambda/4\alpha$ [192]. It is important to consider, especially for beam-sensitive materials, that oversampling will cause an increase in dose with no corresponding increase in resolution beyond the Nyquist limit of the imaging system.

The nominal camera length value, also set in JEOL TEM Centre software, defines the reciprocal space sampling, i.e. the milliradians per pixel at the detector plane. Yang et al. have shown that for detectors with large pixel arrays, such as the pnCCD, which has 256×256 pixels, increasing the reciprocal space sampling does not significantly impact the final result [221]. Nonetheless, a sensible value should be chosen such that the entire bright field disk is within the detector, and choosing a smaller value may be helpful in reducing the memory occupied by the data after the bright field disk is masked, as described later in the description of the data processing methods, Section 5.4.1.

5.3.4 Nanobeam Electron Diffraction

The NBED experiments carried out in the preparation of this work were carried out using the JEOL JEM-ARM300CF at ePSIC with the assistance of the staff scientists, in particular Mohsen Dahnie.

The main step in setting up the microscope to perform NBED is the alignment of a small

probe with a low convergence angle. The method of doing this depends on the exact configuration of condenser lenses within a particular microscope, which can have significant variation depending on the manufacturer and specific specifications of the instrument. The JEOL JEM-ARM300CF, used in this particular instance, consists of a triple condenser lens system. In this instance, the convergence angle is reduced by de-exciting the CL-2 lens, and the small spatial extent of the probe is maintained by increasing the excitation of the CL-3 lens [222].

In practical terms, as such experiments are routinely carried out on this instrument, predetermined alignment files are saved in the JEOL TEM Center software and can be loaded by the user. The probe aberration correction system is typically turned off for NBED experiments using the JEOL JEM-ARM300CF instrument; this leaves only the standard correction of coma and astigmatism to be carried out by the user. Finally, the smallest available aperture, $10\,\mu\mathrm{m}$ can then be inserted to achieve a convergence angle of approximately $1\,\mathrm{mrad}$.

5.4 Data Procedures

5.4.1 Ptychography Reconstructions

All ptychographic reconstruction processes described in this thesis were based on data obtained from the pnCCD mounted on the JEOL JEM-ARM200CF. The raw data readout from the pnCCD is in .frms6 format. All ptychographic datasets were transferred via secure file transport protocol (SFTP) from the detector PC to a network attached storage (NAS) server in .frms6 format, with the exception of datasets used for the event-steaming work, which were converted to .hdf5 format before being transferred. Again, with the exception of the work described in Chapter 6 on the event-based datasets, ptychographic reconstructions were carried out using pre-existing scripts in MATLAB [2].

Following the conversion of the data to .mat files, the data is arranged into a structured array containing metadata as variables as well as the 4-dimensional array containing the diffraction patterns. Experimental parameters such as wavelength and step size are loaded into the structured array; based on these, real and reciprocal space mesh arrays are defined. Specific masks can be applied to the diffraction patterns to produce virtual images, including ADF, ABF and BF images, as described in Section 4.4.1. The data used in the ptychographic reconstruction process is also masked since most of the useful information for the reconstruction is contained within the bright field disk, and it can be helpful to reduce the size of the data by removing the DF region [221].

[2] These scripts were developed within in the STEM group at the University of Oxford and are openly available at: https://gitlab.com/ptychoSTEM/ptychoSTEM

The next step involves performing a Fourier transform of the 4D array with respect to the probe position to calculate the variable, $G(\mathbf{K_f}, \mathbf{Q_p})$, as described in Section 4.4.2. This can then be plotted as the power spectrum of $G(\mathbf{K_f}, \mathbf{Q_p})$, referring to the sum of $|G(\mathbf{K_f}, \mathbf{Q_p})|^2$, across all $\mathbf{K_f}$, also described in section 4.4.2. From the power spectrum, spatial frequencies which correspond to high signal to noise in the double overlap regions can be identified. Examining the overlap regions for the strong spatial frequencies, the fit of the experimental parameters can be checked, especially the rotation angle, which is an empirical factor that has to be fitted for a particular experimental setup. This is particularly important for the SSB method, such that the mask applied to obtain the double overlap region is aligned with the correct region. In the final step prior to the phase reconstruction, the method of applying residual aberration correction depends on the chosen method of phase reconstruction. Details of the processes of calculating the aberration coefficients and applying the aberration correction in the case of each reconstruction technique have been outlined in Section 4.4.5. The final step is to perform the chosen phase reconstruction method; the mathematical processes of each are outlined in Sections 4.4.3 and 4.4.4 for SSB and WDD methods respectively. An overview of the process described above is summarised in Figure 5.5.

5.4.2 Nanobeam Electron Diffraction Pre-processing

Pre-processing of nanobeam electron diffraction (NBED) data was carried out using Juypter Notebooks based on an adaptation of sample code provided by Mohsen Dahnie.

Prior to any analysis, several calibration steps must be carried out on NBED datasets. During the experiment, datasets are acquired for a gold cross-grating at a series of magnifications and camera lengths in order to calculate the calibration values, which are then applied to the experimental datasets. An outline of this process is detailed in Figure 5.6. The most important steps are calibration of real and reciprocal space, centring the diffraction patterns and correction of elliptical distortions.

Calibrations

A gold diffraction grating was imaged during each session at a series of magnifications as a well-known calibration standard. These were used to plot a series of points of magnification and real space pixel size, resulting in a linear from which the appropriate value can be set for any magnification. The sum of the diffraction plane for all pixels in real space was used to calculate the reciprocal space pixel size based on the ring diameter and the known lattice spacing of gold.

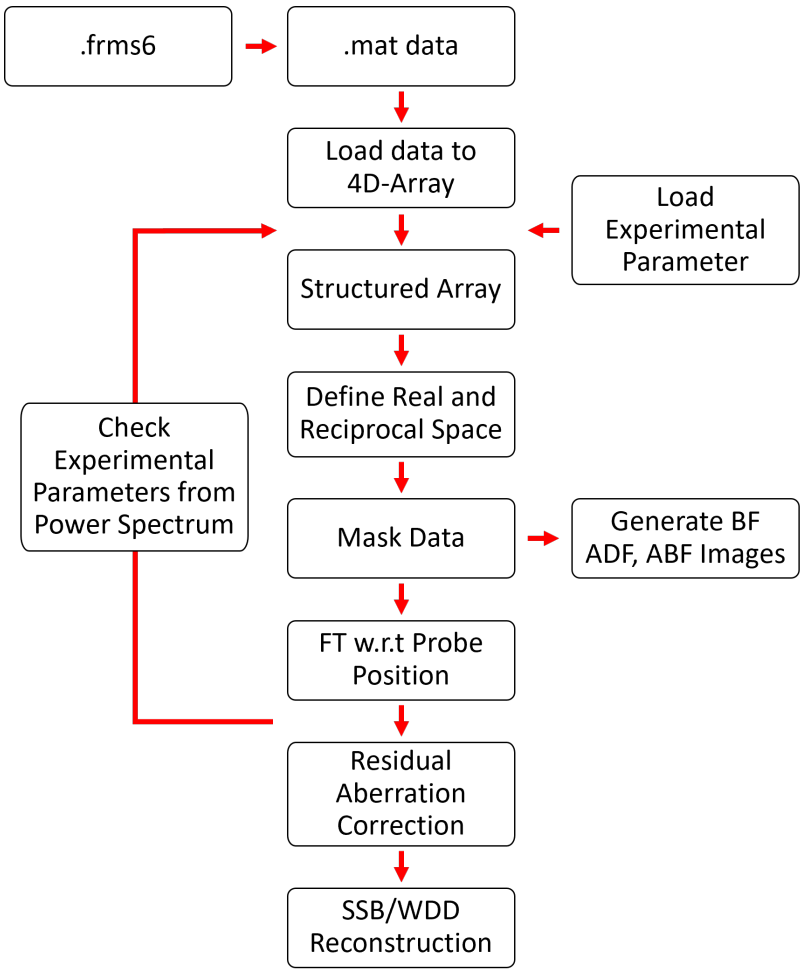


Figure 5.5: Outline of the work-flow for processing SSB or WDD ptychography reconstructions.

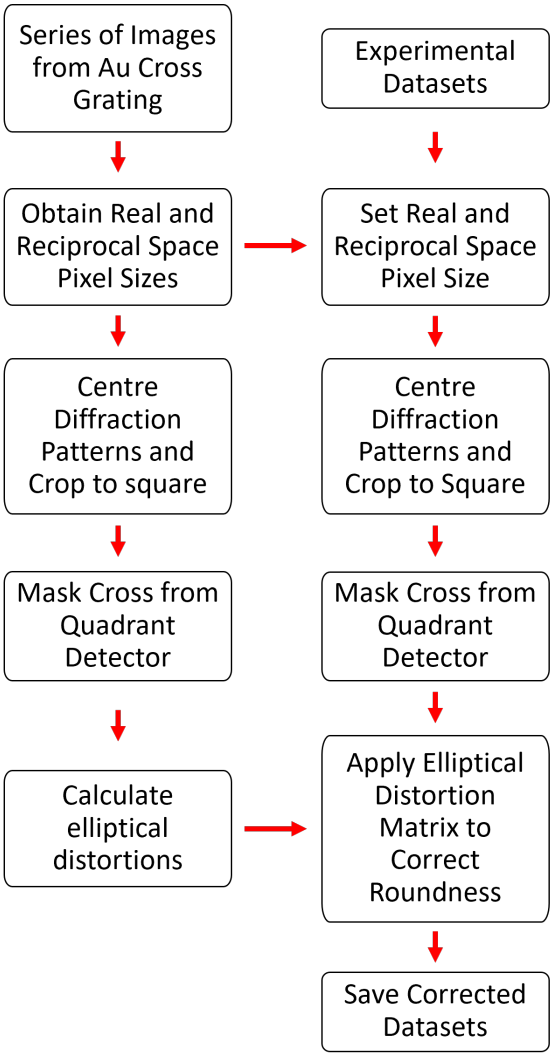


Figure 5.6: Outline of the calibrations for NBED data, process based on calculating calibrations from gold cross grating data and applying these to the experimental datasets.

Centring Diffraction Patterns

The centre pixel of the diffraction patterns is calculated by finding the maximum value of the sum diffraction patterns. All of the diffraction patterns are then cropped to be square with the direct beam at the centre.

Correcting Elliptical Distortions

Due to distortion in the projector lens system, the diffraction pattern in the detector plane may not be perfectly round. This can be interpreted as slightly different reciprocal space pixel values in the x and y directions. This distortion can be corrected by calculating the elliptical distortion for the sum of the gold diffraction patterns and applying an affine transformation to correct this in the experimental datasets.

5.5 Summary

This chapter has provided the reader with an overview of the instrumentation and methodologies used in the preparation of this thesis with regards to both the experimental procedures and analytical methods used.

The following chapter introduces the concept of optimising the the analysis of 4D-STEM data using event-based binary data. The specific challenges of converting frame based dataset to event based datasets is addressed for the specific use case of ptychography reconstructions.

Chapter 6

Optimising Ptychographic Reconstructions in the Case of Sparse Binary Data

This chapter outlines methods explored to optimise the handling of large 4D-STEM datasets with particular consideration for the case of sparse low-dose data as is typically acquired for beam-sensitive material such as Li-ion battery materials. The event streaming method in the camera software was supported by PNDetector and the original implementation of the point of entry neural network was developed by Björn Eckert [223]. The author's role in this work was the development of a binary Fourier transform method for event streamed data, optimising the neural network for STEM data sets and developing the new network training data specific to CBED patterns typical of ptychography experiments.

6.1 Introduction

This work aims to speed up the ptychographic reconstruction of phase images with the potential to enable real-time reconstructions. This will allow the microscopist to work more efficiently by performing the reconstruction during the experiment. Currently, the microscopist can view simultaneous ADF images live during imaging. However, this only allows visualisation of the heavy elements in the structure and lighter elements, if present, only become visible in the post-processing. There are two reasons why it is now feasible to consider real-time ptychographic reconstruction, the first being that the computational power available in computers has increased drastically in recent years [224]. In conjunction, the increased speeds of the detectors enable short dwell times, allowing in low dose 4D-datasets to be acquired [101].

The data acquired in these fast, low-dose scans is often a scattering of single electron interaction events recorded by the pixelated detector [225]. Previous work has demonstrated the robustness of ptychography to lowering the bit depth of a counting detector as low as one and reconstructing the phase [225]. This study considers data which is both sparse and binary; from this, two opportunities to streamline the reconstruction can be envisaged.

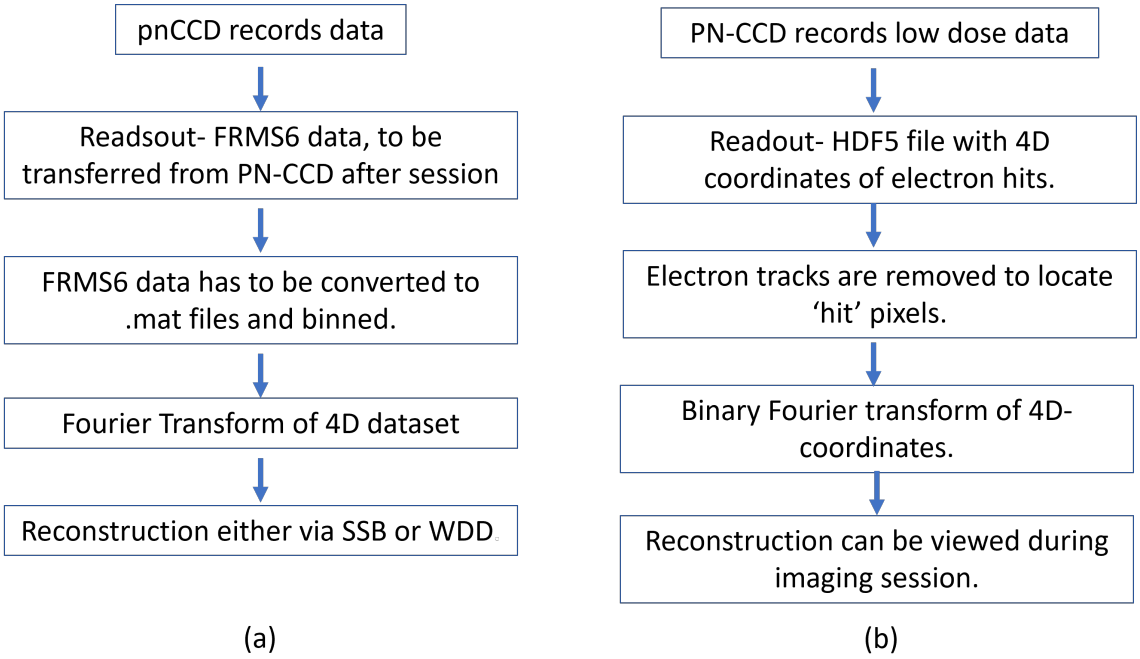


Figure 6.1: Schematic outline of the workflows for **a**) full frame intensity 4D-STEM data and **b**) for binary data consisting of electron coordinates.

First, by considering how such a dataset is stored and then, during the reconstruction process, by simplifying the Fourier transform (FT) step to a series of exponential components based on the electron coordinates on the DED.

The workflow schematics in Figure 6.1.**a** shows the commonly used workflow for full frame readouts of intensity scaled CBED patterns and the proposed workflow for a readout mode of binary coordinates. Implementing the binary FT is codependent on a detector readout based on electron coordinates, referred to as an event streaming mode, which is discussed in Section 6.4. Later sections explore a NN approach as an alternative to a simple intensity threshold for generating an event-based dataset from the pnCCD, which records accumulated charge as an intensity signal.

6.2 Fourier Transform Optimisation

Fourier transforms are inherently slow computationally, and over the years, many algorithms have been devised to speed up the FT. Recalling the first step in the ptychography reconstruction analysis described in Section 4.4.2, a FT of Equation 6.2.1, [1], is performed with respect to the probe position to give the Fourier overlap function, given in Equation 6.2.2. This FT is the slowest step in direct reconstruction methods and is a common step in both the SSB and WDD methods, which have been outlined in Section 4.4.2. The speed of ptychographic reconstructions is limited by this FT step; the remaining steps depend

[1] The square modulus of the 4D-dataset, as originally defined in Equation 4.4.2

on the chosen reconstruction method and do not impact as severely on the reconstruction time.

$$\mid M(\mathbf{K_f}, \mathbf{R_p}) \mid^2 = \mid [A(\mathbf{K_f}) exp(2\pi i \mathbf{K_f} \cdot \mathbf{R_p})] \circledast \Psi(\mathbf{K_f}) \mid^2 \tag{6.2.1}$$

$$G(\mathbf{K_f}, \mathbf{Q_p}) = \int \mid M(\mathbf{K_f}, \mathbf{R_p}) \mid^2 exp(2\pi i \mathbf{R_p} \cdot \mathbf{Q_p}).d\mathbf{R_p} \tag{6.2.2}$$

6.2.1 Discrete Fourier Transform

The discrete Fourier transform (DFT) is a special case of the general FT, where a discrete number of steps are sampled. This is generally the case for experimental data and is always the case for an image formed from an array of $m \times n$ pixels. A two-dimensional DFT, such as that of an image, is written as Equation 6.2.3, where M and N are the numbers of discretely sampled points in the m and m directions, respectively. A two-dimensional DFT can be calculated as two one-dimensional transforms in series, as written in Equation 6.2.4, calculated first in the m dimension and then n or vice versa.

$$F[k,l] = \frac{1}{MN} \sum_{m=0}^{M-1} \sum_{n=0}^{N-1} f[m,n] e^{-j2\pi(\frac{k}{M}m + \frac{l}{N}n)} \tag{6.2.3}$$

$$F[k,l] = \frac{1}{M} \sum_{m=0}^{M-1} f[m,n] e^{-2\pi j \frac{km}{M}} \frac{1}{N} \sum_{n=0}^{N-1} f[m,n] e^{-2\pi j \frac{ln}{N}} \tag{6.2.4}$$

6.2.2 Fast Fourier transform

The fast Fourier transform (FFT) is an efficient algorithm deriving from the DFT, for Fourier transforming discretely sampled data. The one-dimensional DFT, can be written as Equation 6.2.5, where k and x are defined below.

$$F(n\Delta k) = F_n = \sum_j f(j\Delta x) exp[2\pi i (n\Delta k)(j\Delta x)] \tag{6.2.5}$$

$$k = n\Delta k; \Delta k = 1/a; n = 0, 1, 2, ...(N-1)$$
$$x = j\Delta x; \Delta x = a/N; j = 0, 1, 2, ...(N-1)$$

Using the simplification that $f_j = f(j\Delta x)$ one dimensional DFT given in Equation 6.2.5 can be simplified to:

	DFT	FFT
1D	N^2	$Nlog(N)$
2D (M)	$N^2 \times M^2$	$MN(log(M) + log(N))$
2D ($M = N$)	N^4	$2N^2log(N)$

Table 6.1: Complexity of the DFT and FFT algorithms based on the dimensions of the array M and N. The complexity in two dimensions is given both in the case where the array is non-square ($M \neq N$) and where the array is square ($M = N$).

$$F_n = \sum_j f_j exp[2\pi i(nj/N)] \tag{6.2.6}$$

Rewriting equation 6.2.6 as $F[n] = \sum_j f_j W_N^{nj}$, it becomes clear the same value is calculated repeatedly, such as each time the integer product of $n \cdot j$ repeats for different values of n and j, respectively. Removing this repeat calculation significantly reduces the computational effort to perform the transform, particularly for large N. The complexities of the DFT and FFT algorithms for both a one and two-dimensional FT are compared in Table 6.1.

6.2.3 Simplification from binary data

If we consider a binary signal, i.e. consisting of 1's and 0's such as $x(n) = [1, 0, 1, 0]$, it does not take much effort to compute the DFT using Equation 6.2.7 for the one-dimensional FT.

$$X[K] = \sum_{k=0}^{N-1} x(n) e^{-ikn\frac{2\pi}{N}} \tag{6.2.7}$$

We can express this as a sum of exponential components, which are only non-zero for the cases where $x(n)$ is non-zero, and where the terms are non-zero, then the value of $x(n)$ is always 1, Equation 6.2.8. This is written in Equation 6.2.9 for the example signal $X(n) = [1, 0, 1, 0]$, in this case, the exponential components for terms where $n = 0, 2$ are the only non-zero terms, giving the simplified expression, Equation 6.2.10.

$$X[K] = \begin{cases} \sum_{k=0}^{N-1} e^{-ikn\frac{2\pi}{N}}, & x(n) = 1 \\ 0, & x(n) = 0. \end{cases} \tag{6.2.8}$$

$$X[K] = e^{-i\frac{2\pi}{4}k\cdot 0} + e^{-i\frac{2\pi}{4}k\cdot 2} \tag{6.2.9}$$

$$X[K] = 1 + e^{-ik\pi} \tag{6.2.10}$$

The computational complexity is reduced because we can ignore the multiplication step between $x(n)$ and the exponential term in Equation 6.2.7. Instead, the corresponding exponential term is included in the sum for each indexed position where the signal is one. The number of terms in the sum is determined by the number of non-zero terms in $x(n)$; hence, this method is most effective for sparse data.

The expression in Equation 6.2.10 is then evaluated for $K = 0, 1, 2, 3$ to get the discrete FT $X[K] = [2, 0, 2, 0]$. A similar example for a 2D array is given in Appendix A.

6.3 Results

6.3.1 Discrete Fourier Transform for Ptychography Reconstruction

The initial FT step in the ptychographic reconstruction is defined previously in Equation 6.2.2; since the data, recorded by a pixelated detector is discrete and regularly sampled, this can be written as a DFT, as in Equation 6.3.2.

$$G(\mathbf{K_f}, \mathbf{Q_p}) = \sum_{R_x=1}^{M} \sum_{R_y=1}^{N} \mid M(\mathbf{K_f}, \mathbf{R_p}) \mid^2 exp(2\pi i \mathbf{R_p} \cdot \mathbf{Q_p}) \tag{6.3.1}$$

Taking a list of electron events, where the events are regarded as having an intensity of 1, we can treat this as a binary signal. It then becomes possible to apply the simplification to the FT described above in Equation 6.2.7 - 6.2.10. Each interaction event can then be written as an exponential component of the summation in Equation 6.3.2, based on the coordinates of the electron landing event.

$$G(\mathbf{K_f}, \mathbf{Q_p}) = \sum_{R_x=1}^{M} \sum_{R_y=1}^{N} \exp(2\pi i \mathbf{R_p} \cdot \mathbf{K_f}) \tag{6.3.2}$$

As the dose is reduced further, the number of electrons recorded for each probe position is reduced. Thus, the benefits of recording data by electron coordinates are further improved in terms of reducing the dataset's size and the number of components in the exponential sum.

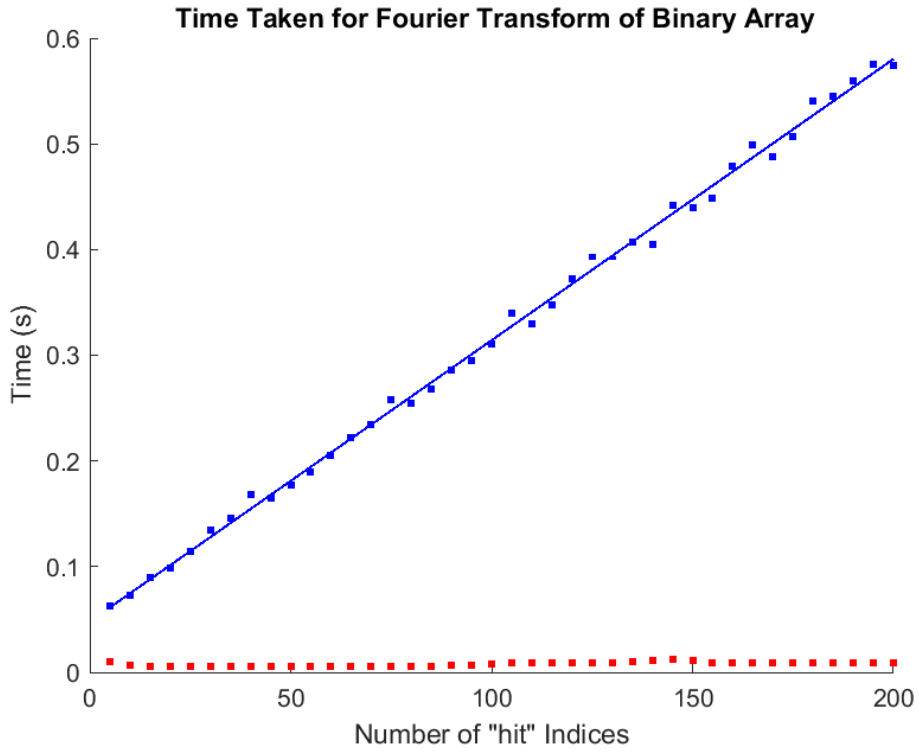


Figure 6.2: Plot of the time taken to perform FT on an array varying the number of hit pixels containing a value of 1. Data points in red represent the MATLAB `fft2` function, and data points in blue represent a FT using the binary sum method.

6.3.2 Complexity of the Binary Fourier Transform

The time taken to perform the standard DFT and FFT algorithms scale with the complexity, as defined in Table 6.1, multiplied by some constant value k, depending on the computational power. Both algorithms scale depending on the dimensions of the array (M and N); on the other hand, a FT performed by a binary sum scales in complexity linearly with the length of the sum, defined by the number of "events," i.e. instances of the value 1 in the array. To demonstrate this, a MATLAB script was generated to perform both the standard FFT algorithm and the binary FT on a 2D array (dimensions 256×256) with between 5 and 200 hit pixels represented by a value of 1, such as that shown in Figure 6.3. The resulting plot in Figure 6.2 shows the linearity of the time scaling for the binary FT and the independence of the FFT algorithm on the number of indexed events.

It is observed that the FFT algorithm is extremely highly optimised to the point where the binary summation process is always slower, regardless of the number of elements in the summation. Based on the highly optimised nature of the FFT algorithm, it is likely that it is not the FFT step in itself which is limiting the speed but instead some complex issue around the transfer of data between the hard disk, RAM and CPU. This problem requires investigation into the specific data-handling routines implemented by MATLAB code and is not within the scope of this study. In reality, the FT in Equation 6.3.2 corresponds to a

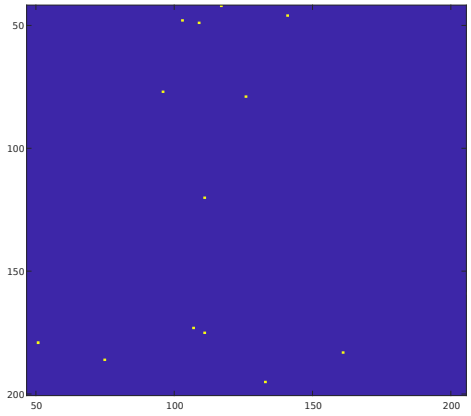


Figure 6.3: Sparse, binary image with random pixels assigned a value of 1, shown in yellow. All other pixels have a value of zero.

two-dimensional FT, which in the MATLAB code is performed iteratively over a double loop with dimensions M by N, for this a large amount of random access memory (RAM) is required. Nevertheless, the work thus far is not rendered fruitless by this result, as the binary summation method remains useful for carrying out a FT based directly on event streamed data, which for sparse data offers substantial benefits in terms of the volume of data which has to be stored. A further advantage of the binary FT, which has not yet been tested due to the memory limitations of the detector computer, is that the summation process can be carried out as data is being acquired using this method.

6.3.3 Error Propagation

Small numerical differences were observed in the array elements for the binary sum method and the in-built `fft2` Matlab function. To assess the size of this error, the FT of a random binary array with dimensions 256×256, where three elements with value one are indexed, was calculated ten times. The in-built `fft2` function and the sum of exponential component methods were used to calculate the FT on each iteration. The difference between the resulting arrays was calculated by element-wise subtraction of the matrices. The mean value of the difference array was calculated for each iteration before being averaged over all iterations. The mean value of the error was $(43.07 - 3.0926i) \times 10^{-17}$, while the magnitude of the maximum difference value was 2.0223×10^{-12}. Figure 6.4, shows the resulting difference array plotted as an image.

Small numerical errors have been observed between other types of FT algorithms, and the accuracy of the FFT can vary between different central processing unit (CPU) architectures [226]. This comes from the difference in how the numbers are rounded as typical 64-bit CPU's can handle double precision calculations with a precision of 15 to 17 decimal places

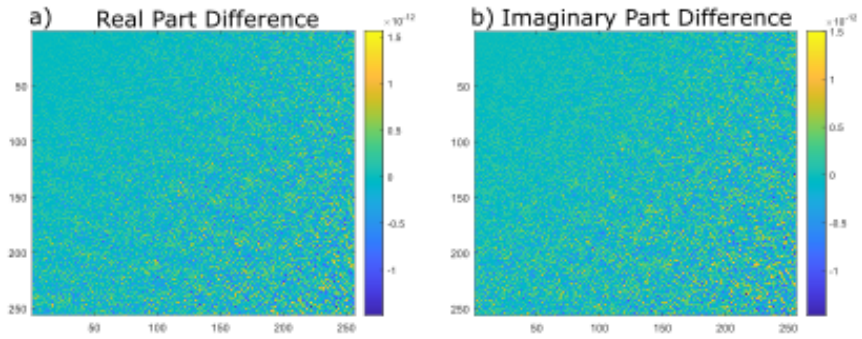


Figure 6.4: Differences between binary FT and MATLAB FFT algorithm. **a**) Plotting the real part of the difference array. **b**) Plotting the imaginary part of the difference array.

Beam Energy (kV)	Detector Setting	Emission Current (μA)	Camera Length (nominal value)
200	full frame	1	20

Table 6.2: Table of experimental acquisition parameters for the CBED patterns shown in Figure 6.5.

[227]. However, it is notable and not fully understood why there is a periodic element to the difference arrays' real and imaginary parts in Figure 6.4. These effects are most likely due to the order in which the calculations are handled by the CPU. The impact on any reconstructed images would be immeasurable; hence, further investigations are outside the scope of this study.

6.4 Event Streaming

The pnCCD is a charge-integrating detector, readout modes for DED are discussed in Section 3.1.3, meaning that the standard output of the detector is an intensity-based frame image as shown in Figure 6.5. It is impossible to perform the binary FT method on this type of data, and it is not an efficient way to store data when we have sparse data, as most of the pixels record a value of 0. Due to the integrating nature of the pnCCD, it is impossible to lower the dynamic range to increase the frame rate or to read electron hits as time-stamped hits directly from the detector, as is the case in other detector modes. However, it is possible to perform post-acquisition conversion of the data to an event streaming mode, equivalent to operating in a 1-bit mode, i.e., the intensity is either 1 or 0, and an electron is either recorded or not. Event streaming involves setting a threshold where an electron interaction with a pixel is considered significant and then reading out from the CCD only the locations of the pixels which have recorded an electron interaction event [135]. The following sections of this chapter describe some possible ways of determining the ideal threshold for an electron interaction to be considered as an event and the challenges of each.

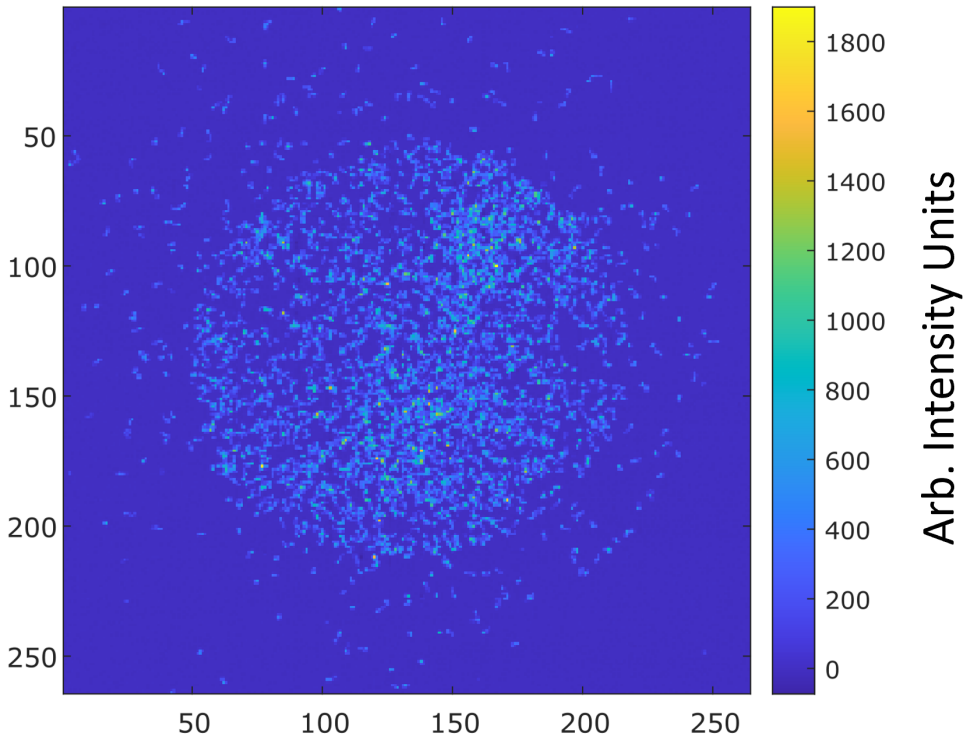


Figure 6.5: Typical intensity-based full frame CBED pattern acquired using the pnCCD.

6.4.1 HDF5 event output

As a preliminary test of an event-based analysis mode for the pnCCD, a script installed by PNDetector allows the frame data to be converted to hdf5 format with the events listed. The output lists all electron interactions recorded as a primary interaction with a default value of 5 times the standard deviation from the dark reference. An excerpt of a sample file is given in Figure 6.6; the frame id refers to the CBED pattern produced at each probe position. The columns id_x and id_y refer to the pixel's x and y coordinates where an electron is recorded. For a typical 4-D dataset with 256×256 pixels and a detector plane of 256×256 pixels, the file size can be compressed by at least a factor of 8 for doses such as those used in acquiring the experimental datasets in this work. Even lower doses would lead to more substantial reductions. More hits will be counted for a lower threshold, so more data is stored. The file size can be reduced further by either increasing the threshold or reducing the number of counts of the detector by lowering the beam current.

6.5 Electron Entry Point Analysis

When electrons interact with a direct electron detector, it is expected that the energy deposition is spread over several pixels. This can be seen in the excerpt of the file in Figure

```
\list of keys: ['hitlist', 'meta_data', 'noise_map', 'offset_map']
Read hitlist
                    event_id  frame_id  id_x  id_y  energy
0       1413732204554745942         0     0    63      10
1       1413732204554745942         0     0    64     338
2       1413732204554745942         0     0    65     492
3       1413732204554745942         0     0    66     291
4        521621399895797933         0     0    74     619
...                      ...       ...   ...   ...     ...
714460   720713172712266403     55679    65   188      10
714461   720713172712266403     55679    65   189       6
714462   720713172712266403     55679    65   190       6
714463  1405260330623778167     55679    65   209       9
714464  1405260330623778167     55679    65   210      58

[573961886 rows x 5 columns]
```

Figure 6.6: Excerpt of the hdf5 readout file from a 4D-STEM dataset, referred to as a hitlist. Each event recorded on the detector is assigned an "event_id". The "frame_id" denotes the probe position, where the first frame corresponds to the probe coordinate $(0, 0)$. The id_x and id_y terms give the detector plane coordinates of the electron hits, and "Energy" is an arbitrarily scaled value relating to the intensity of the signal.

6.6 as electron events with very close detector plane coordinates, and it is shown for a full detector frame in Figure 6.7. Spreading the energy deposited in the detector over multiple pixels is mathematically equivalent to a blurring filter on the image. The amount of energy deposited in each pixel across the track by a particular electron is not maximum in the first pixel, meaning that selecting the highest intensity pixels within a frame does not necessarily represent the electron hit locations.

This phenomenon can be understood from a modified version of the Bethe-Bloch formula (Equation 6.5.1), which empirically describes the interactions of electrons in a material [228]. This equation consists of a series of physical constants: $\beta = v/c$, where v is the velocity and c the speed of light, z is the charge number and e the electron charge, N_A is Avagadros constant, ϵ_0 is the vacuum permittivity and m_e the rest mass of an electron. In addition to the material properties, which are: ρ the density of the material, Z the atomic number and the atomic number A. I is the mean excitation energy, which for silicon is $174\,\mathrm{eV}$ [229], E_k is the average kinetic energy of the electrons and k is the modification term added to correct the formula for lower energy electrons; for silicon, an appropriate value is found to be 0.882 [228]. Examining this formula shows that the interaction cross-section for silicon is higher for low-energy electrons, meaning that higher-energy electrons create longer tracks.

$$-\frac{dE}{dx} = \frac{z^2 e^4}{4\pi\epsilon_0^2 m_e c^2} \frac{N_A \rho Z}{A} \beta^{-2} ln(1.166 \frac{E_k + kI}{I}) \tag{6.5.1}$$

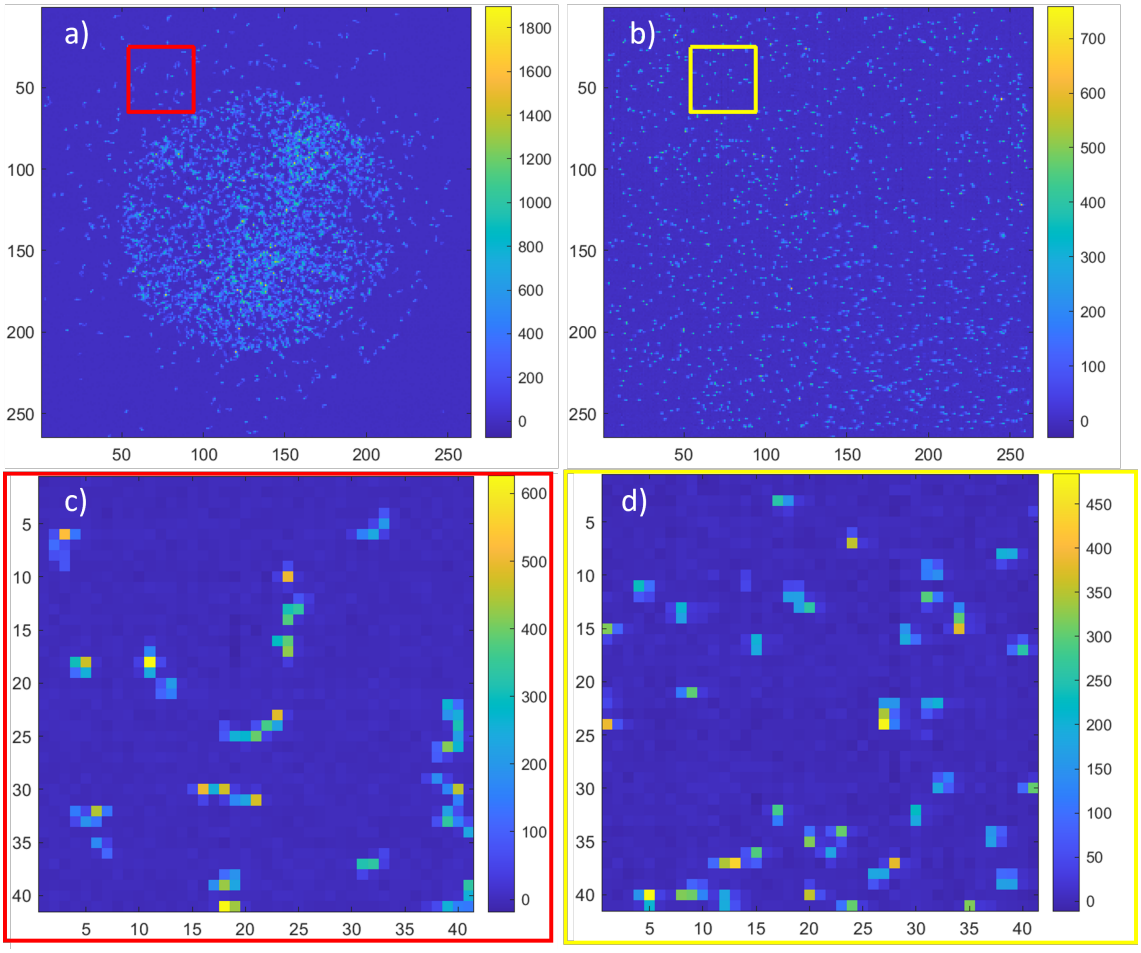


Figure 6.7: Examples of full-frame CBED pattern from the pnCCD for **a**) 200 kV electrons and **b**) 80 kV electrons. **c**) and **d**) are expanded views of the selected indicated in the full frame images by red and yellow squares. These demonstrate the energy deposition for 200 kV and 80 kV electrons respectively across multiple pixels.

6.5.1 Intensity Threshold

The simplest method of defining electron hits within intensity-based images is setting a threshold on the intensity value of a pixel considered an electron hit. All pixels with a value greater than the threshold are recorded as a one and those below the threshold are set to zero. Figure 6.8 demonstrates applying different intensity value thresholds to the intensity-based CBED shown previously in Figure 6.5. Increasing the threshold for the pixel intensity decreases the number of pixels considered to be an electron hit. Based on visual analysis, a threshold between 20 and 100 appears to be a reasonable value; however, there is no way to directly measure whether this is an appropriate threshold as the number of actual electron hits in any given frame is unknown.

To evaluate the effect of changing the threshold, the same dataset was reconstructed with varying intensity thresholds applied to all CBED patterns. Figure 6.9 compares ADF, ABF and phase images from SSB reconstructions from intensity CBED patterns and binary

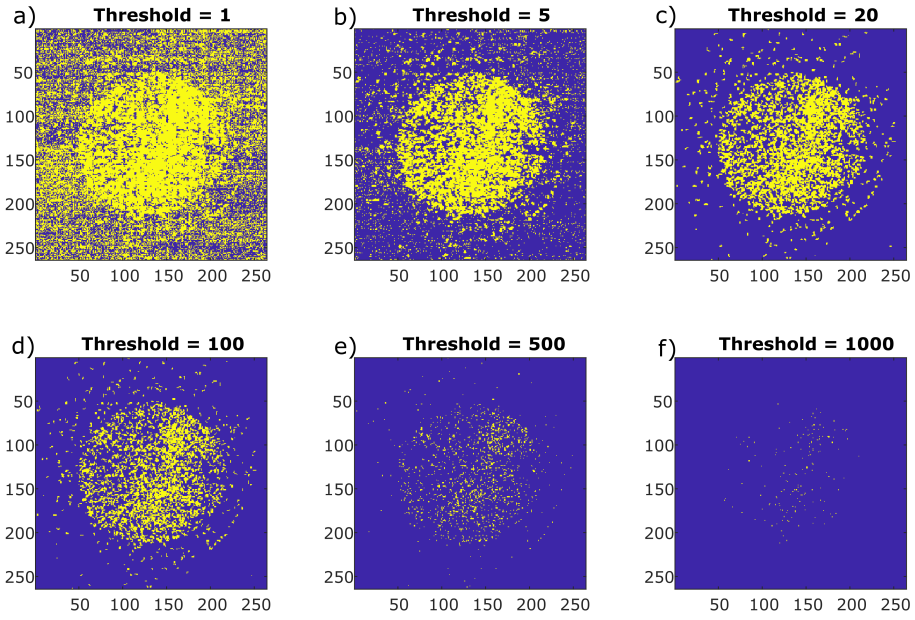


Figure 6.8: (**a-f**) The intensity CBED pattern in 6.5 with a series of threshold values of 1, 2, 10, 20, 50, and 10, respectively. Pixels with values greater than the threshold are set to 1 and displayed as yellow; those below the threshold are set to 0 and displayed as blue.

CBED patterns with intensity thresholds of 5, 500 and 1000 applied. The image quality for the ABF and ADF images in Figure 6.9 do not appear to be significantly impacted by changing the intensity signal to a binary frame or by changing the threshold used to convert between the intensity signal to a binary signal. However, the reconstruction of the phase image is affected by the change from the intensity image to a binary signal. Yet, considering the single frames for a threshold value of 1000 in Figure 6.5 have significantly fewer events recorded than that with a threshold of 5, it is still possible to resolve atoms in the reconstruction with a threshold of 1000. There is a slight decrease in the signal-to-noise around the edge of the nanoparticle in Figure 6.9 visible in the expanded regions of interest in the phase images.

Optimising this threshold value is essential in maintaining the reconstruction quality when converting to a binary signal; however, determining this cut-off is problematic. Several points to consider are the following: electrons do not necessarily deposit all of their energy in a single pixel (highlighted in the inset regions of Figure 6.7); the amount of energy the electron deposits in each pixel is stochastic and multiple electrons may land very close to each other or even on the same pixel. Although fast and straightforward, defining a single intensity value as the cut-off is not physically meaningful. The result from the Bethe-Bloch formula is that the interaction cross-section for silicon is higher for low-energy electrons, which means that more energy will be deposited near the end of the electron track after some energy has been lost in the material. The maximum signal position is the simplest

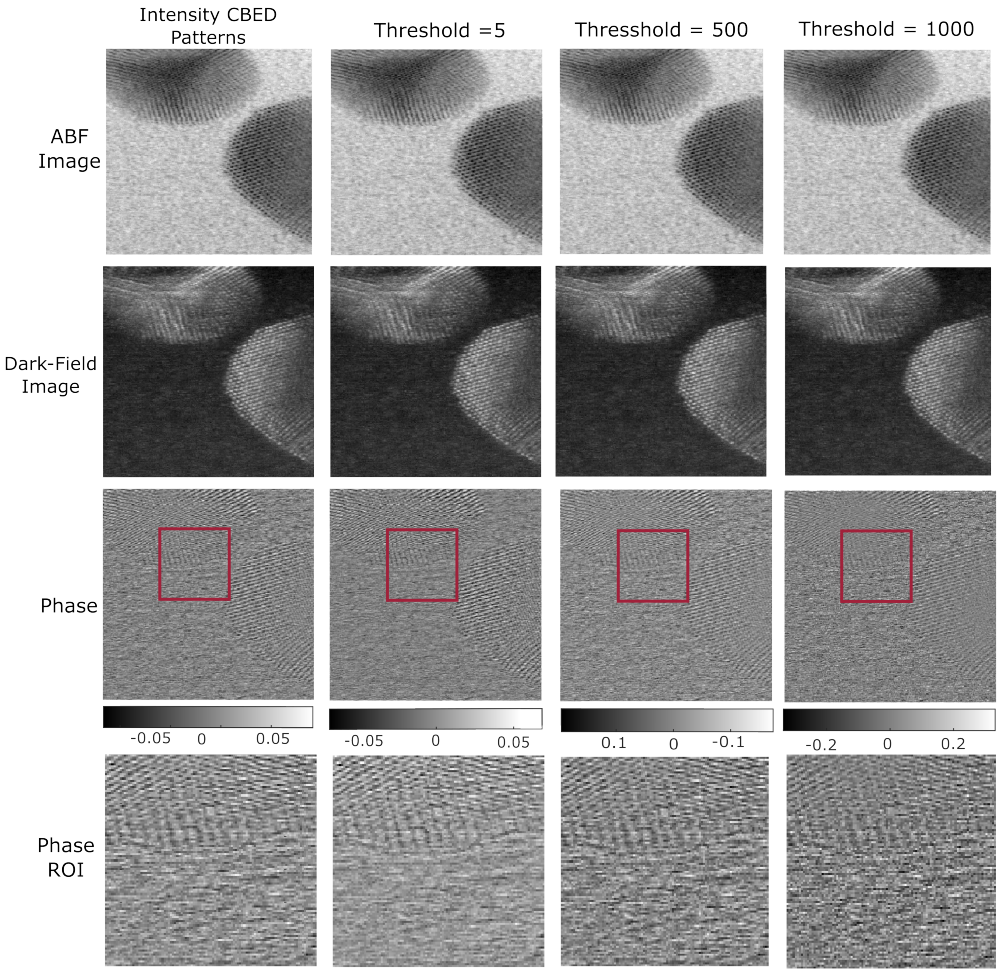


Figure 6.9: ABF (**top row**), ADF (**second row**), phase images(**third row**), selected area regions of interest (ROIs) from the phase images (**bottom row**). These are generated using intensity CBED patterns (**first column**) and binary CBED patterns with thresholds of 5, 500 and 1000, as indicated above the respective columns. Pink boxes in the phase images indicated the ROIs below, all images with the exception of the ROIs are 256×256 pixels.

method and requires the least computation; however, it does not perform well for higher energy particles, which produce track-like features [230].

6.5.2 Alternative Point of Entry Determination Methods

An alternative method of determining the point of entry (POE) for high-energy electrons is known as the furthest away method. The furthest away method involves taking the POE as the pixel furthest from the maxima but still regarded as within the electron track. Determining the pixels within the electron track still involves setting a threshold and is restricted to distinct electron tracks without overlap. In contrast, lower energy electrons interact more like photons, where energy spreads out from a point, and here, the centre of gravity method can be applied reliably [124, 231]. However, these methods have a fundamental underlying flaw in that they can only be used when individual electron tracks

are separate from each other. While this is often the case in the dark field region, it can be seen in Figure 6.5 that even for relatively modest electron doses, the bright field disk has many overlapping electron tracks.

Eckert et al. have proposed a neural network (NN) method to assign the electron hits; it has been suggested that this may allow greater precision when assigning the electron POE and offers greater flexibility as it can adapt to the specific conditions of each dataset [232]. The following section introduces the point of entry neural network (POE-NN) structure designed by Eckert et al. as a more physically meaningful approach to determining the electron POE. It also outlines the tests and adaptations to the POE-NN specific to STEM datasets carried out by the author.

6.6 Basics of Neural Networks

A neural network (NN) is one method of achieving what is commonly referred to as machine learning, meaning a computer system with the ability to make decisions and solve problems based on experience. A NN attempts to mimic the ability of biological neural networks to process information using interconnected connected neurons; it consists of an input layer, one or more hidden layers of interconnected parts called neurons and an output layer [233]. Neural networks lie within the wider field of artificial intelligence (AI), which aims to develop computer systems and algorithms that mimic human learning mechanisms. For example, the AI system AlphaZero taught itself the rules of chess and, in just a few hours, was able to beat a world champion player [234].

6.6.1 Convolutional Neural Network

A convolutional neural network (CNN) is any neural network which applies at least one convolution step [235]. It is most appropriately applied to regularly sampled data and is therefore widely applied to image analysis and pattern recognition [236]. CNNs consist of several layers: convolution layer, activation layer [2], pooling layer, and fully connected layer. The convolution layer takes the image as an input array and convolves the array with a smaller array known as a kernel; this process assigns a bias or importance to certain features within the image [237]. During the training process, the kernel is optimised to perform a specific task [237]. The activation function can be thought of as the process that takes place inside the neuron to produce an output, which is passed onto the next layer/neuron. Mathematically, this requires a function that takes the weighted inputs from the previous layer and has one output [233]. The activation function is predetermined, and there are several commonly used functions; descriptions of these can be found in other

[2] A common activation function is the rectified linear activation unit (ReLU); hence this layer is sometimes referred to as the ReLU layer

sources [238]. The pooling layer reduces the complexity of the data and speeds up the process by combining outputs from several neurons. The methods chosen for pooling can be optimised for a specific task; common methods are maximum or average pooling, which takes either the maximum or average value from a predefined region, respectively [233]. In many CNNs, a fully connected layer takes the output from the final hidden layer and converts it back to a physically meaningful output. However, in the POE-NN described here, a fully connected layer would limit the NN to a specific frame size, reducing its generality.

6.6.2 Training Method for Supervised Neural Network

Machine learning methods can be either supervised or unsupervised. Supervised machine learning methods involve building the NN weights from training data for which the true ground state is well known. In the case of a NN for sorting images, a set of labelled images is first used to train the NN before a set of unknown data can be sorted [239]. The process of training the initialisation parameters, which minimises the errors of the neural network, is an iterative process.

The training data is split into two categories: training and validation. The initial weights are defined randomly, and for each particular set of weights, the network's output is compared to the ground truth data using a function known as the loss function. The training must be carried out across a sufficiently large set of training data to minimise the loss function across all of the validation data [240, 241]. One of the simplest loss functions is the mean square error, defined by Equation 6.6.1, y_i is the i$^{\text{th}}$ measurement, and $\hat{y}_i$ is the corresponding predicted measurement, giving the difference as the error, the number of measurements is n. This is defined in terms of the ground truth $y_{gt(i)}$, and predicted output $y_{predict(i)}$, in Equation 6.6.2.

$$MSE = \frac{1}{n}\sum_{i=1}^{N}(y_i - \hat{y}_i)^2 \tag{6.6.1}$$

$$Loss = \frac{1}{n}\sum_{i=0}^{n-1}(y_{gt(i)} - y_{predict(i)})^2 \tag{6.6.2}$$

The loss is back propagated to each neuron based on its initial weight, and then the weights and biases are updated in such a way as to minimise the contribution to the loss function [236]. This is repeated until all training data has been passed through the network, known as a single epoch.

The validation data is then passed through the network, and the network output for the

validation data is compared to the ground truth. It is important that the validation data has not been used in the training process as this comprises the result of the validation data and the generality of the network [242, 243]. The entire training and validation process is repeated either until a sufficiently low loss has been achieved or a predefined number or epochs is reached, whichever comes first.

6.7 Point of Entry Neural Network

The development of a machine learning approach to the point of entry determination method using a convolution neural network has been the work of the thesis of Björn Eckert. The following section of this thesis details work carried out by the author to test the application of the neural network on experimental STEM datasets and tailor the approach specifically to the fast and accurate analysis of STEM datasets.

Supervised machine learning approaches require labelled data for which the ground truth is known; however, it is impossible in typical STEM experiments for the true point of entry to be known for each electron. Instead, a set of training data must be generated by simulation methods able to predict the electron interactions within the detector material [232].

Figure 6.10 shows the workflow developed by Eckert for the point of entry neural network (POE-NN). First, training data is generated by simulating electron tracks using a Monte Carlo-based approach. Most of this data is used in the training of the network, but some data is held back for the validation step. Once either a certain number of epochs has been run, or the network is sufficiently accurate for a series of consecutive epochs, the training is complete and the weights and biases are saved. Experimental data is then analysed by the POE-NN for which the true POE is unknown. The result of the POE-NN is a probability matrix where each pixel is assigned a probability that an electron hit occurred. A binary dataset is then generated based on applying a threshold probability. For a successful NN, a reasonable result for a probability threshold greater than 50% would be expected [232].

Figure 6.11 applies this work-flow designed by Eckert to a single frame of randomly dispersed hit pixels, first simulating the electron tracks and then applying the POE-NN to calculate the probability that each pixel contains a point of entry. Example frames of the initialisation of hits, simulation of electron energy deposition, and probability matrix are given $200\,\mathrm{kV}$ electrons and $300\,\mathrm{kV}$ electrons.

Figure 6.12 shows the effect of varying the threshold for the probability matrix, which is output from the POE-NN. Choosing a threshold that is too low leads to large clusters of hits and offers no advantage in reducing the number of electron hits. As the data is

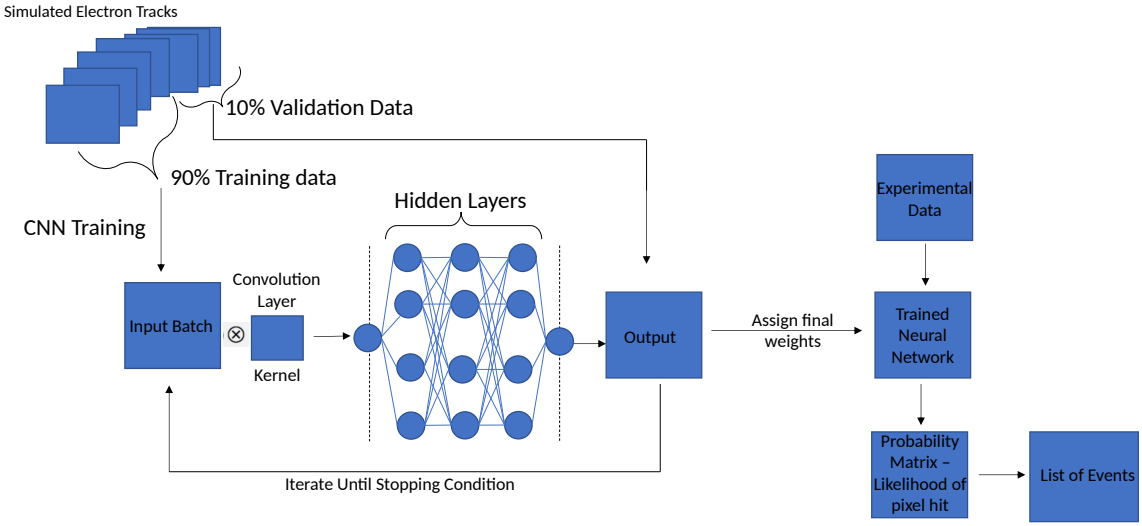


Figure 6.10: Schematic outline of the POE-NN training and prediction workflow developed in [223]. Simulated electron tracks (ground truth data) are split into training and validation data. The training data is used to train the POE-NN. The final weights are saved when one of the stopping conditions has been reached. Experimental data can then be passed to the POE-NN, and a prediction is made for each pixel of the likelihood of it being an electron point of entry. Pixels with a probability greater than some threshold are then counted as hits.

now binary, the effect of clusters of hit pixels will have a stronger blurring effect on the resolution than in the case of an intensity image. Setting the threshold too high means that there are electrons that have interacted with the sample and are not utilised in the reconstruction process. This is especially a problem for beam-sensitive samples where maximising the dose efficiency is an important consideration.

6.7.1 Point of Entry Neural Network Test on Experimental STEM Data

The POE-NN model Eckert developed was sub-optimal when applied to experimental CBED patterns. Figures 6.13 and 6.14 show the probability for each pixel being an electron point of entry predicted by the initial neural network for $200\,\mathrm{kV}$ and $80\,\mathrm{kV}$ datasets with the same beam current and camera lengths. Examining the probability matrix in each case by varying the threshold for a pixel to be considered an electron hit, we find that the POE-NN produces significantly more certainty when finding the POE in the dark field region. It is particularly obvious for the $80\,\mathrm{kV}$ dataset that the predicted bright field disk has disproportionately low probabilities. This, in fact, leads to fewer hits in the bright field region than in the dark field region, which is clearly a non-physical result. Overall, the effect of applying the threshold is that either the threshold has to be set higher, which means too many hits in the dark field region are counted, or with a lower threshold, the population of hits in the bright field and dark field region are inverted.

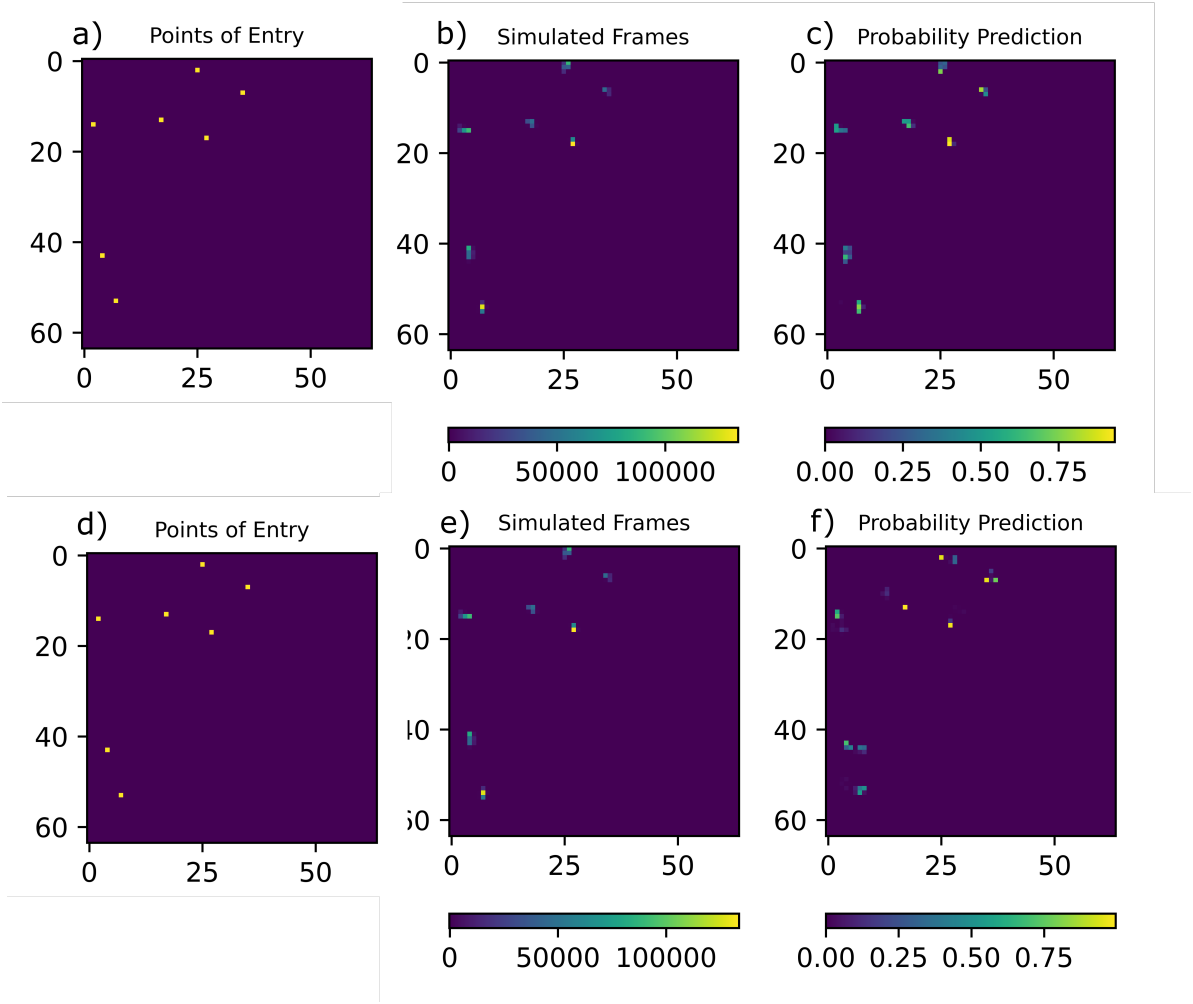


Figure 6.11: **a,d**) A sparse array of random hot pixels. **b,e**) Simulated electron tracks in the detector for 200 and 300 kV, respectively. **c,f**) Probability array for each pixel containing an electron hit.

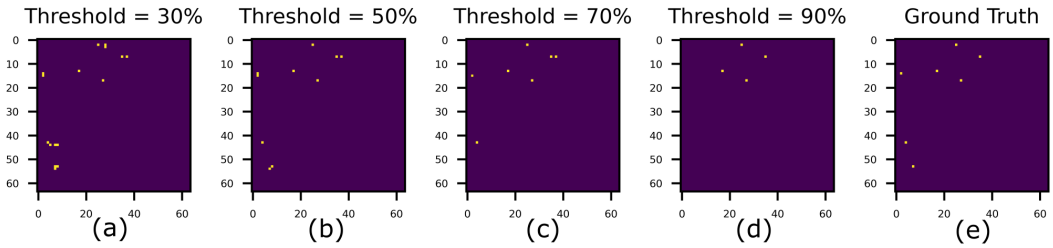


Figure 6.12: An example validation dataset with a series of threshold values applied to the probability matrix. **a-d**) 30-90%, yellow pixels represent probabilities greater than the threshold value, and purple pixels have values lower than the threshold. **e**) Shows the ground truth hit positions given in yellow.

In both Figure, 6.13 and 6.14, it is also observed that the binary images show pronounced vertical features where several pixels close to each other in one column are all counted as hits. Examples of such regions are highlighted in respective figures by white boxes. Given the sparsity of the data, this is a statistically unlikely result. Investigations have shown that this results from poor gain correction of the raw data, which is discussed further in the results of the adapted POE-NN in Section 6.8.4.

6.8 Optimising the Point of Entry Neural Network

The basis of the POE-NN tested in the previous section was designed with the aim of finding individual points of entry for single electrons very accurately, using training data based on homogenous illumination [223]. The specific requirements of a POE-NN with the application to 4D-STEM are quite different to this. Since ptychography can be accurately performed on a detector with significant binning or larger pixel size, it is reasonable to suggest that a minor deviation in the estimated POE is less important than the loss of dose efficiency caused by missing hits altogether. In this case, the primary aim is to reduce the number of electron hits recorded to speed up the reconstruction process while maintaining the reconstruction quality.

6.8.1 Certainty Threshold Matching

Although the location of electron hits on the detector can't be known exactly, a prediction can be made by assuming that all electrons which are emitted at the source should be detected. An estimate of the number of electrons expected to be detected in the time it takes for a single frame to be recorded based on the beam current. However, due to the quantum nature of the electron, there will be a degree of uncertainty in the time of arrival of the electrons, meaning this will always be an estimate. It also affords no information

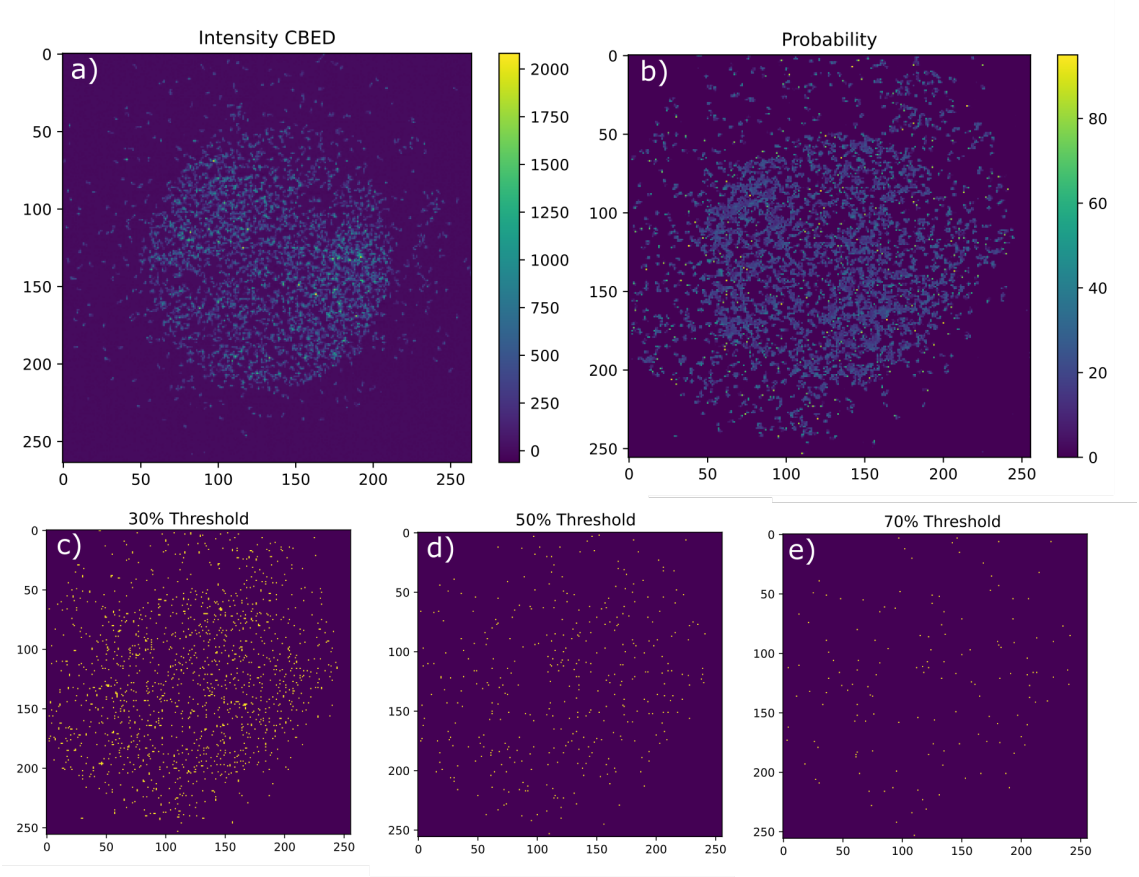


Figure 6.13: Initial neural network prediction of 200 kV electrons **a**) Single CBED pattern **b**) Initial neural network probability matrix. **c-e**) the probability matrix with threshold values of 30%, 50% and 70% applied respectively

on the spatial distribution of the electrons of the detector.

6.8.2 Training data set

One potential way to improve the neural network's outcome for STEM data is to make the training data more closely resemble the experimental data. The work by Eckert et al. places a sparse random set of electron hits on the detector. In the typical CBED patterns used in ptychographic reconstructions, such as the frame shown in Figure 6.5, where there is a central bright field disk area and a surrounding dark field region with significantly fewer hits.

A new training data set was generated with sparse regions and areas with overlapping electron tracks within the same detector frame, referred to subsequently as low and high-count regions. Bright and dark regions were defined using an array of random polygons to maintain a general and random nature to the dataset and not to give an implicit bias to the network. Up to 4 random shapes that were allowed to overlap were generated on each detector frame. This array then defines two regions with differing electron hit probabilities

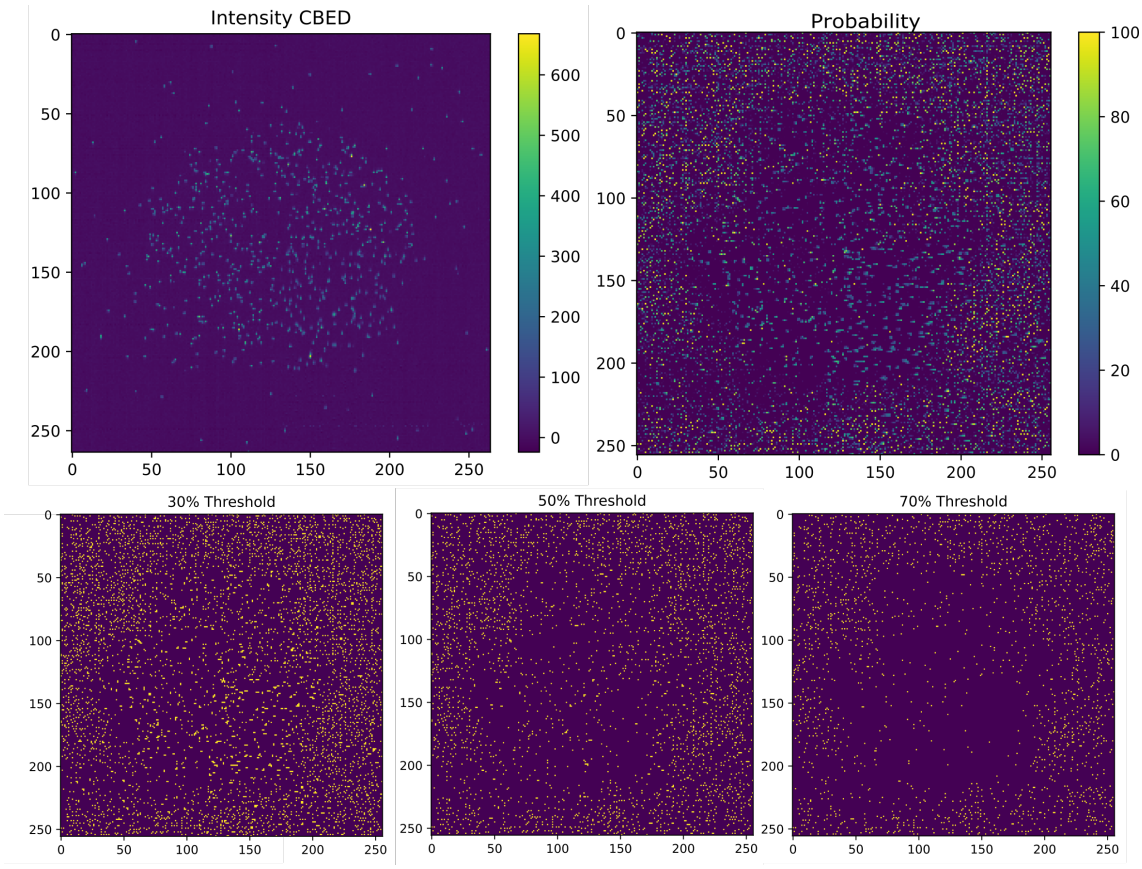


Figure 6.14: Initial neural network prediction of 80 kV electrons **a**) Single CBED pattern **b**) Initial neural network probability matrix. **c-e**) the probability matrix with threshold values of 30%, 50% and 70% applied respectively

within which the hits are randomly assigned. These true electron hits are converted to tracks in the same way as before to the energies deposited in each pixel. An example frame generated as part of the new training data is shown in Figure 6.15. A total of 10,000 frames were generated using this function, each with 64×64 pixels; 90% of the data was used for training and the remaining 10% for validation.

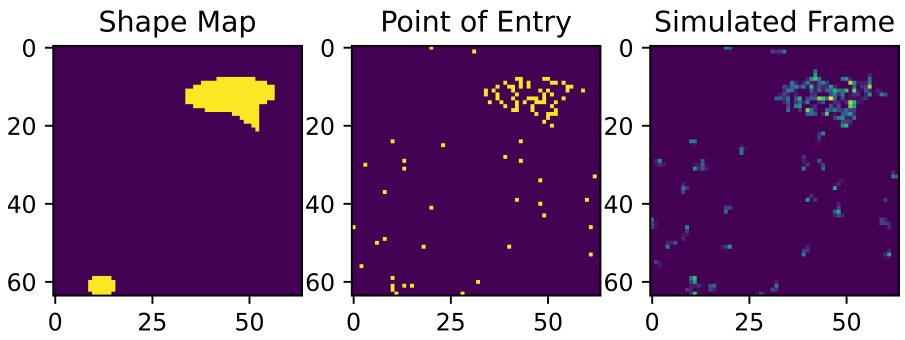


Figure 6.15: Example of training data for neural network **a**) shape map generated to define bright and dark regions. **b**) a hit map where electron hits with the detector are **c**) Monte Carlo simulation generated of electron interactions with the detector.

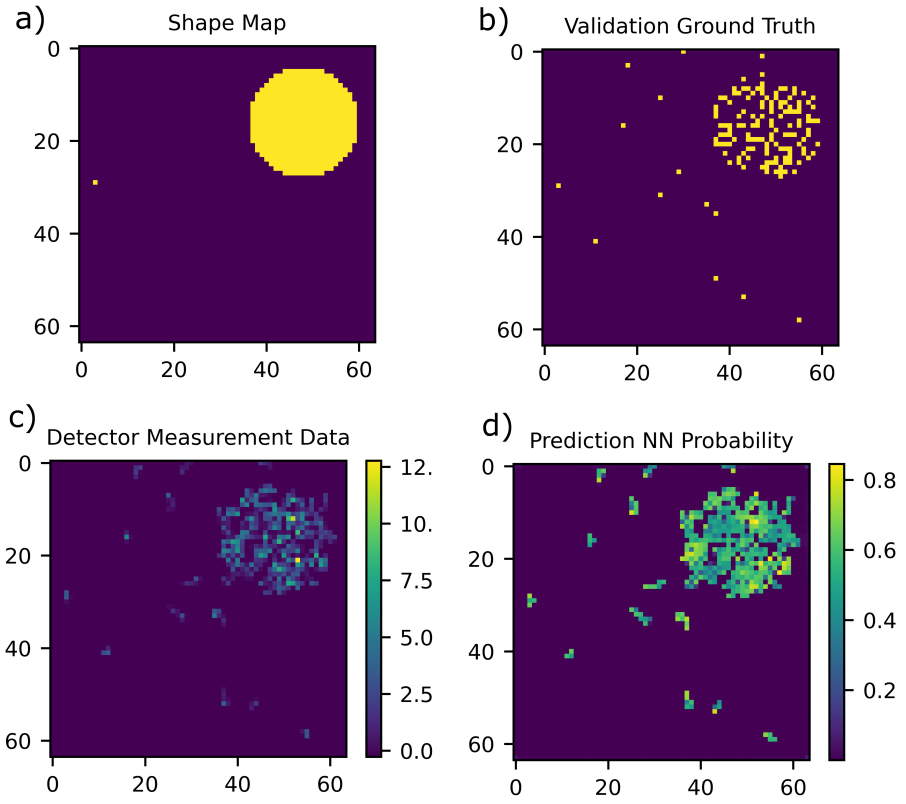


Figure 6.16: **a**) Shape map assigned by the random polygon function, yellow represents the shape assigned as high count regions. **b**) Electron hits random assigned (based on the probability in different regions) represented by yellow pixels.**c**) Simulated energy deposition in the pixels using the Monte Carlo method. **d**) The probability assigned by the neural network that each pixel represents an electron point of entry.

Frames from the validation batch are used to test the accuracy of the POE-NN in predicting the true POE; an example is shown for one validation datasets in Figure 6.16. The probability of each pixel containing a point of entry as predicted by the POE-NN and then a threshold is applied to this probability array to determine which pixel should represent a point of entry, resulting in a binary dataset.

Figure 6.17 shows the effect of varying the threshold for an electron hit on the probability array shown in Figure 6.16.**d**. For threshold values of 50% and below, the number of hits is overestimated in both the high and low-count regions. Increasing the probability to 60% leads to many hits from the high-count region being excluded while the individual hits in the low-count regions are still counted over multiple pixels. It is also observed that a sudden decrease in the number of predicted hits drops across all frames between 60 and 70 %. The threshold predictions for this range are plotted separately in Figure 6.18. It is observed that for this particular frame, the POE-NN makes the most reasonable prediction of the points of entry in the low-count regions at around 64%; however, at this threshold, many hits in the high-count region are already lost. This type of visual analysis is helpful,

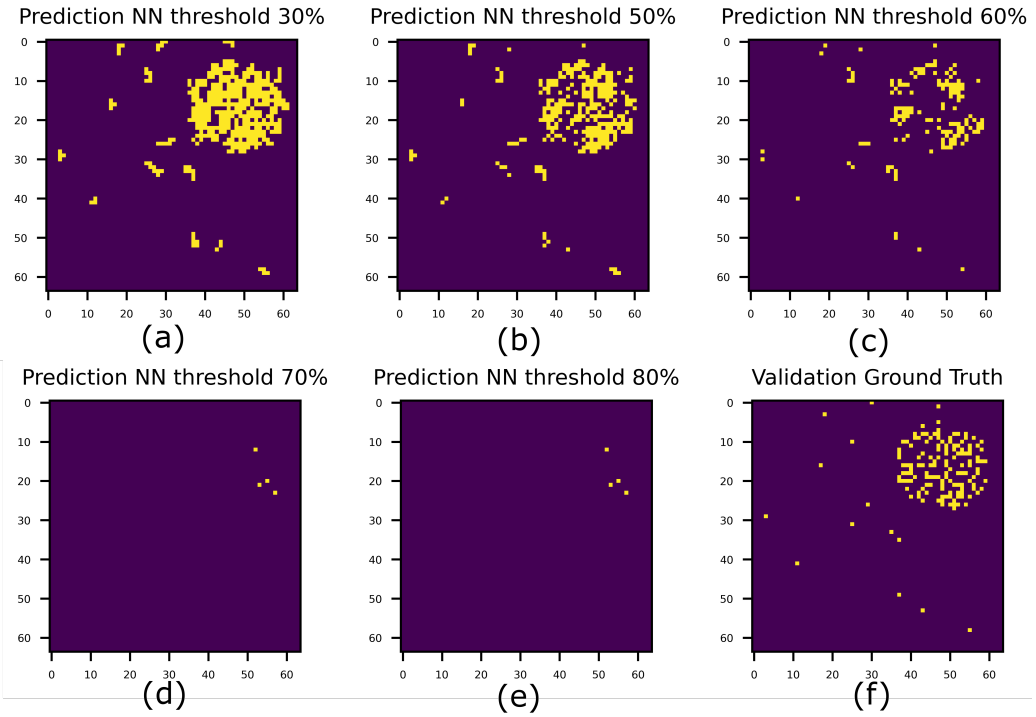


Figure 6.17: Threshold probabilities of **a**) 30%, **b**) 50% **c**) 60% **d**) 70% and **e**) 80% applied to the prediction by the neural network. **f**) The ground truth for the validation data. In all cases, yellow pixels represent electron hits.

		Ground Truth Actual PoE	Not a PoE
Prediction	PoE	True Positive	False Positive
	No PoE	False Negative	True Negative

Table 6.3: Table summarising category of pixels when comparing the predicted electron hits to the ground truth.

but an analysis of many frames is required to estimate the accuracy of the POE-NN.

The prediction can be analysed by comparing a statistical analysis of all of the frames separated into two distinct regions. Using the validation data to do this is essential because we know the ground truth and the location of the high and low-count regions. True positive (TP) pixels are those pixels which are points of entry in the ground truth and correctly counted in the prediction. False positive (FP) pixels are those pixels predicted to be a hit in the prediction but do not actually contain a point of entry in the ground truth. true negative (TN) are pixels which do not contain a point of entry in the ground truth and are not considered a point of entry in the prediction, false negative (FN) are pixels which contain a point of entry in the ground truth but are not predicted to have a point of entry. These are summarised in table 6.3.

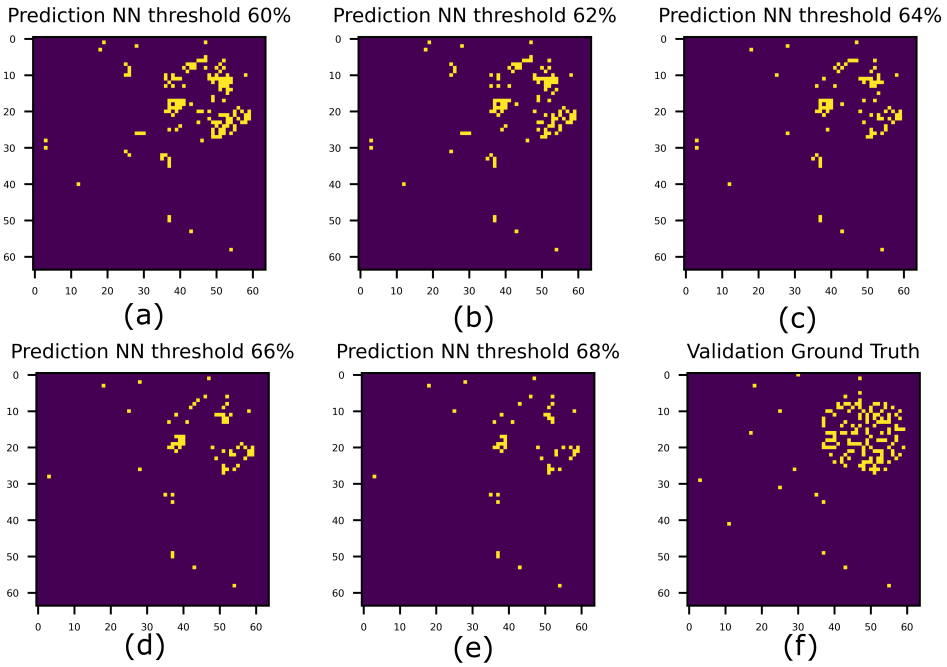


Figure 6.18: Threshold probabilities of **a**) 60%, **b**) 62% **c**) 64% **d**) 66% and **e**) 68% applied to the prediction by the neural network. **f**) The ground truth for the validation data. In all cases, yellow pixels represent electron hits.

$$\%accuracyTP = \frac{\sum(TP \odot PP)}{\sum TP} \times 100 \tag{6.8.1}$$

$$\%accuracyTN = \frac{\sum(TN \odot PN)}{\sum TN} \times 100 \tag{6.8.2}$$

$$\%accuracyFP = \frac{\sum(FP \odot PP)}{\sum FP} \times 100 \tag{6.8.3}$$

$$\%accuracyFN = \frac{\sum(FN \odot PN)}{\sum FN} \times 100 \tag{6.8.4}$$

Each region has a different number of pixels and it is therefore more accurate to compare them as percentages, as in Equations 6.8.1 - 6.8.4. These values can also be calculated separately for the high-count and low-count regions, such as the low-TP and high-TP accuracy. Table 6.4 shows all of the accuracy measurements for the full set of validation data tested by this NN. In the low-count region, where the electron hits are sparse, the accuracy is higher than in the high-count regions. In the high count region, the number of TP counts is higher than that of TN, meaning that the number of hits is overestimated.

	TN (%)	FN (%)	TP (%)	FP (%)
Low Region	98.2	1.8	81.8	18.2
High Region	54.4	45.6	81.8	18.2

Table 6.4: Table of the true negative, false negative, true positive and false positive rates as a percentage of the pixels in the high-count and low-count regions. The metrics are calculated by comparing the ground truth (validation data) and probability matrix with a 50% threshold applied.

6.8.3 Optimising loss Function

The loss function compares the neural network's prediction with the ground truth during the optimisation of the weight by categorising the pixels in the same way as TP, FN, etc. The same loss function is applied across the entire frame in the initial implementation of the high and low-count regions. However, by creating these two distinct regions, we are driving the POE-NN to make an over-prediction of electron hits in the dark field region and an under-prediction in the bright field region in order to minimise the overall loss function. This is caused by the overlapping electron tracks in the bright field region, leading to a lower certainty in the NN. Therefore, the loss function was changed to optimise the two regions differently.

The loss function 6.8.5 is calculated based on the true positive rate (TPR) and true negative rate (TNR), which are derived from the number of true positives and true negatives, respectively. The $\Delta(g, \bar{g}, p)$ term accounts for the ratio between the predicted number of points of entry and the actual number of points of entry. Weighting factors a, b and c, scale the relative importance of these terms in the overall loss function. This results in a different loss function minima, so the optimised initial weights are different.

$$\mathcal{L}(g, p) = a \cdot TPR(g, p) + b \cdot TNR(\bar{g}, \bar{p}) + c \cdot \Delta(g, \bar{g}, p) \tag{6.8.5}$$

The loss function was altered to have different weights applied to the TPR and TNR in the separate regions; for example, the loss function for the low-count region is given by Equation 6.8.6. The loss function for the high-count region is defined equivalently by the high-TPR and high-TNR in Equation 6.8.7. These two equations are then combined as a linear sum to form an overall loss function as in Equation 6.8.8, with scaling factors to define the relative importance of each region in the total loss function.

$$\mathcal{L}_{low}(g, p) = a \cdot TPR_{low}(g, p) + b \cdot TNR_{low}(\bar{g}, \bar{p}) + c \cdot \Delta_{low}(g, \bar{g}, p) \tag{6.8.6}$$

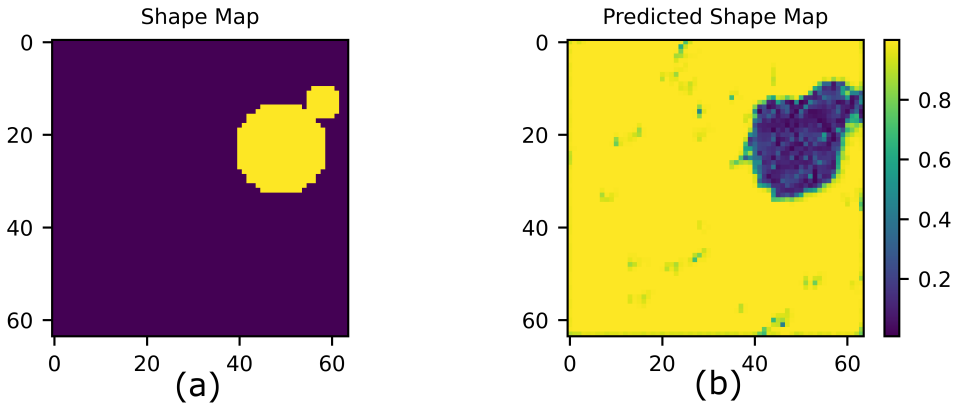


Figure 6.19: a) Shape map defining high and low-count regions. **b**) Shape map predicted by the neural network.

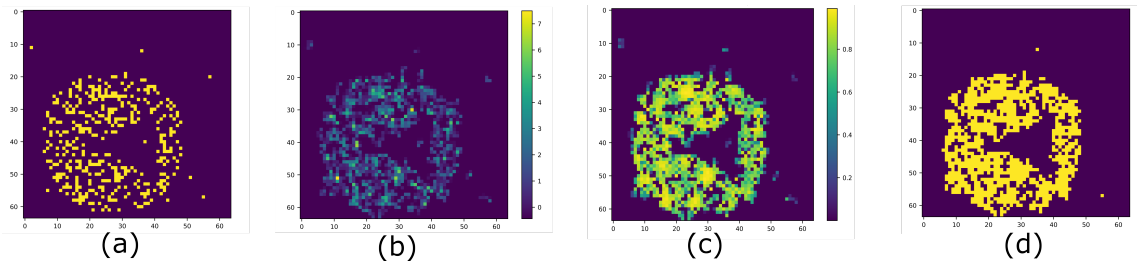
$$\mathcal{L}_{high}(g,p) = d \cdot TPR_{high}(g,p) + e \cdot TNR_{high}(\bar{g},\bar{p}) + f \cdot \Delta_{high}(g,\bar{g},p) \tag{6.8.7}$$

$$\mathcal{L}_{overall}(g,p) = x \cdot \mathcal{L}_{low}(g,p) + y \cdot \mathcal{L}_{high}(g,p) \tag{6.8.8}$$

In order to apply the correct loss function in the appropriate regions without exposing the POE-NN to the ground truth of the predefined shape regions, during the training process, a step was added to produce a predicted shape map from the neural network. The shape map defines the regions where the high and low loss functions are applied; Figure 6.19 shows an example of a predicted shape map. The accuracy measurements of the validation data are calculated based on the ground truth shape maps, as this data is only used for testing and does not influence the training step of the network.

The neural network algorithm has less certainty in the bright-field region because of overlapping electron tracks. The loss function should penalise the two regions differently to compensate for this. In the low-count region, the sparsity of the hits makes finding the true positives more important than the true negatives. In the high-count region, finding the true negatives is crucial to avoid predicting too many hit pixels. The effect of changing the relative weights of the TNR and TPR is demonstrated by two examples. Figure 6.20 and 6.21 where the relative ratios of the TPR and TNR are inverted, and the effect of over-predicting and under-predicting in the relative regions are illustrated.

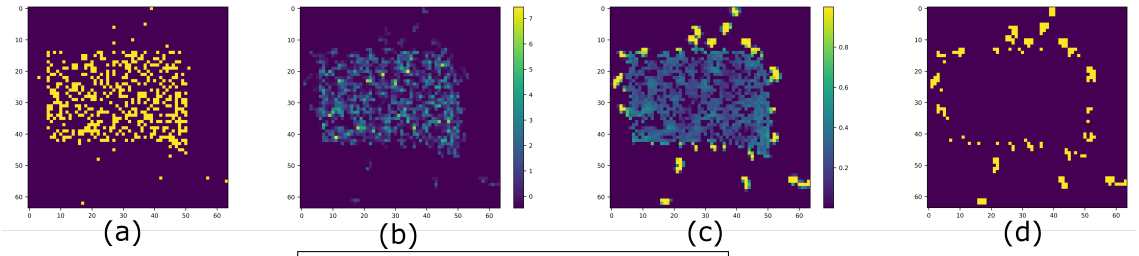
When the TNR in the low count region has greater weight than the TPR, then many counts are missed, Figure 6.20 shows that the hits in the how region are over-predicted if the



	TNR	TPR	Δ
Low Loss	100	1	100
High Loss	1	100	100

(e)

Figure 6.20: An example of a POE-NN model that leads to an over-prediction of the high-count region and under-prediction of the low-count region. **a**) Ground truth hits with high and low-count regions. **b**) Simulated detector interactions with the **c**) Neural network output as probability matrix. **d**) A threshold of 50% is applied to the probability matrix. **e**) A table of the relative weight of the TNR, TPR and Δ term in the high and low-loss regions defined in the loss function.



	TNR	TPR	Δ
Low Loss	1	100	100
High Loss	100	1	100

(e)

Figure 6.21: An example of a POE-NN model that leads to an under-prediction of the high-count region and over-prediction of the low-count region. **a**) Ground truth hits with high and low-count regions. **b**) Simulated detector interactions with the **c**) Neural network output as probability matrix. **d**) A threshold of 50% is applied to the probability matrix. **e**) A table of the relative weight of the TNR, TPR and Δ term in the high and low-loss regions defined in the loss function.

weight of the TPR is much higher 6.21. In the high count regions, a similar effect is observed when the TPR is greater, too many pixels are assigned a high probability of being a hit 6.20. If the TNR is assigned a much higher weight, then the probability of the pixels in the high count region is too low, and most hits are missed 6.21.

The examples above apply the same weight to the low-loss function as the high-loss function. Since ptychographic reconstruction relies on the bright field region under consideration, it is more important to assign the bright field region accurately. Since the loss function is a hyperparameter of the model, the individual weights of the $\mathcal{L}_{low}$ and $\mathcal{L}_{high}$ terms in Equation 6.8.8 can also be optimised. Optimising the neural network becomes an iterative process of finding the best-suited ratio of weights for each term in the overall loss function.

6.8.4 Gain Correction

In section 6.7.1, it was observed for the initial implementation of the POE-NN by Eckert that vertical lines of hit pixels were observed in the predicted POE maps for individual CBED patterns, indicated in Figures 6.13 and 6.14. Summing all detector frames on the dataset shows that these are related to wider horizontal banding in the likelihood that pixels are identified as a hit. On investigation of various detector correction procedures, which are described in Appendix B, this would be found to be related to poor gain correction of the data. In typical intensity-based CBED patterns, the gain correction is small relative to the pixels' intensity; thus, gain correction is not typically carried out prior to ptychography reconstructions. In the intensity CBED pattern, effects of gain correction are only visible by summing many CBED patterns (Figure 6.22). However, the impact of the POE-NN appears to amplify the issue, resulting in the strong banding feature in the sum of many binary predicted CBED patterns (Figure 6.22.**d**).

Requiring accurate gain correction presents two issues for an event-based readout and reconstruction method. First, the primary aim of implementing an event-based process is to speed up the reconstruction and adding another step to perform a gain correction would negate at least some of this benefit. Second and more consequentially, carrying out a gain correction required acquiring homogeneous illumination of the detector and recording every pixel, which is fundamentally incompatible with an event-based method. For this reason, in the reconstructions presented in the following section, a gain correction was not performed before using the POE-NN to predict the hit pixels. In this case, these issues were not found until the training and adaptation of the loss function was complete, and adding steps to take these effects into account would require substantial redesigning of the POE-NN. Any subsequent iterations a POE-NN of this type should include steps to account for such detector corrections from its initial conceptualisation.

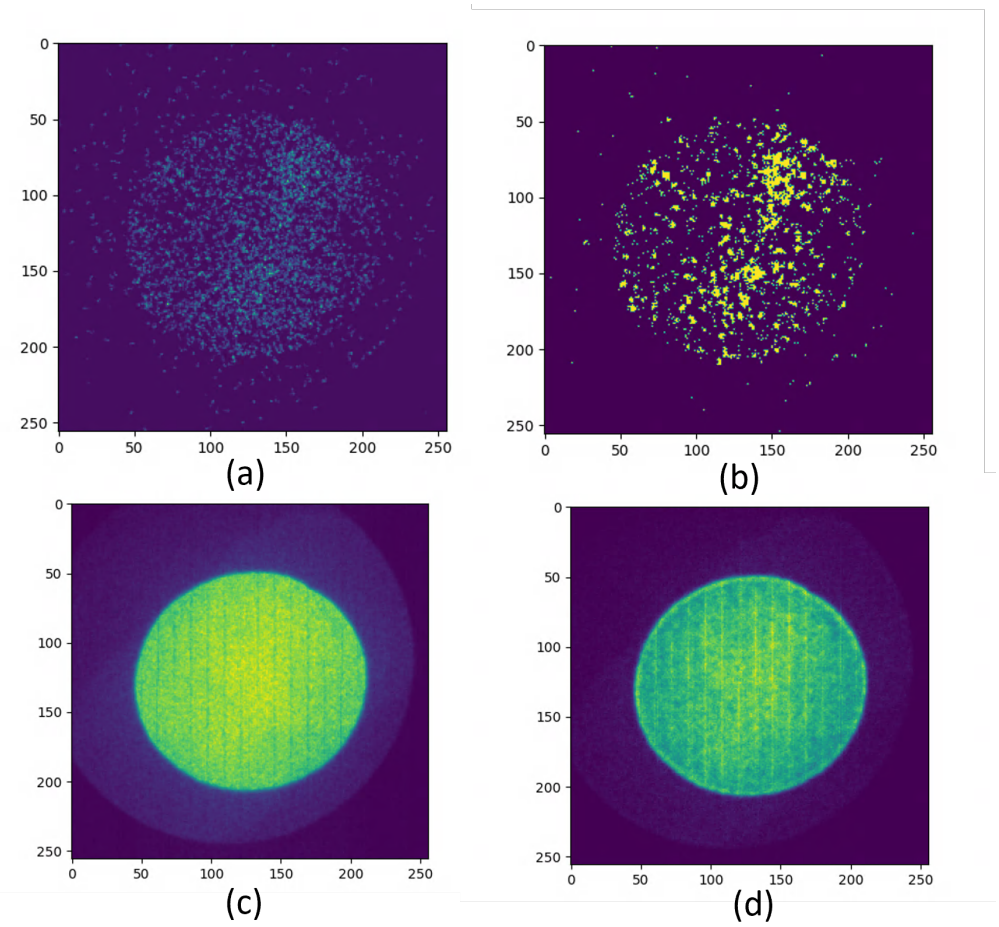


Figure 6.22: **a**) Individual intensity frame. **b**) The sum of all intensity frames for 4D-STEM dataset. **c**) Individual binary frame POE-NN. **d**) The sum of all POE-NN predicted frames.

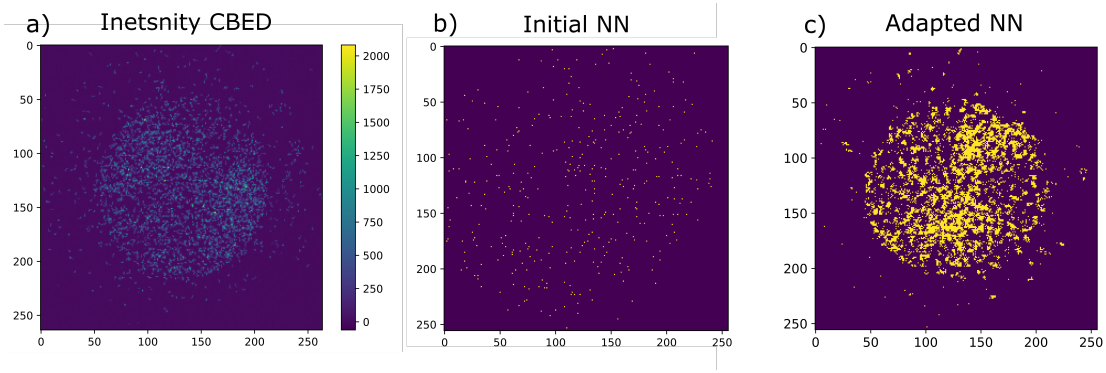


Figure 6.23: Comparison of single detector frames **a**) Intensity raw detector readout **b**) prediction >50%) of the initial POE-NN designed by Eckert and **c**) the prediction (>50%) probability of the POE-NN adapted by training with high and low-count regions and the adapted loss function.

6.9 Reconstruction Results

The POE-NN was trained using the high and low-count data, and the optimised loss function and then applied to experimental STEM CBED patterns. The impact of implementing the adaptations described above to the POE-NN is demonstrated in Figure 6.23, both threshold images are shown with a 50% threshold applied. In contrast to the initial POE-NN, a significant improvement in the resemblance of the bright field disk and surrounding dark-field regions is achieved by application of the adapted POE-NN. Figure 6.24 shows the raw prediction of the POE-NN as a probability assigned to each pixel and the impact changing the probability threshold.

Performing ptychography reconstructions with the output of the initial neural network was not possible with current processing methods because the CBED patterns lack a defined bright field disk, which is needed for the truncation of the data as described in Section 5.4.1. The reconstruction can theoretically be carried out without the truncation step, but this negates the aim to speed up the process and would not produce physical results because the intensity of the bright-field disk is where the signal for the SSB reconstruction process originates. Figure 6.25 compares ADF images and ptychographic phase reconstructions from raw intensity based CBED patterns and binary data predicted by the adapted POE-NN. In both imaging results, contrast is decreased by applying the POE-NN, particularly the high spatial frequencies. Comparing the dark-field regions of the CBED patterns, it is clear that there are fewer recognised hits in the POE-NN CBED, which can at least partially account for the lower contrast in the ADF image. The most significant effect on the phase reconstruction image is most likely to be the over-prediction of hits in the bright field disk, which is most likely to affect high spatial frequencies. The over-prediction of hits in the bright-field disk is a consequence of the loss function being adapted to accept greater uncertainty in high-count regions and is, therefore, a necessary compromise to prevent the

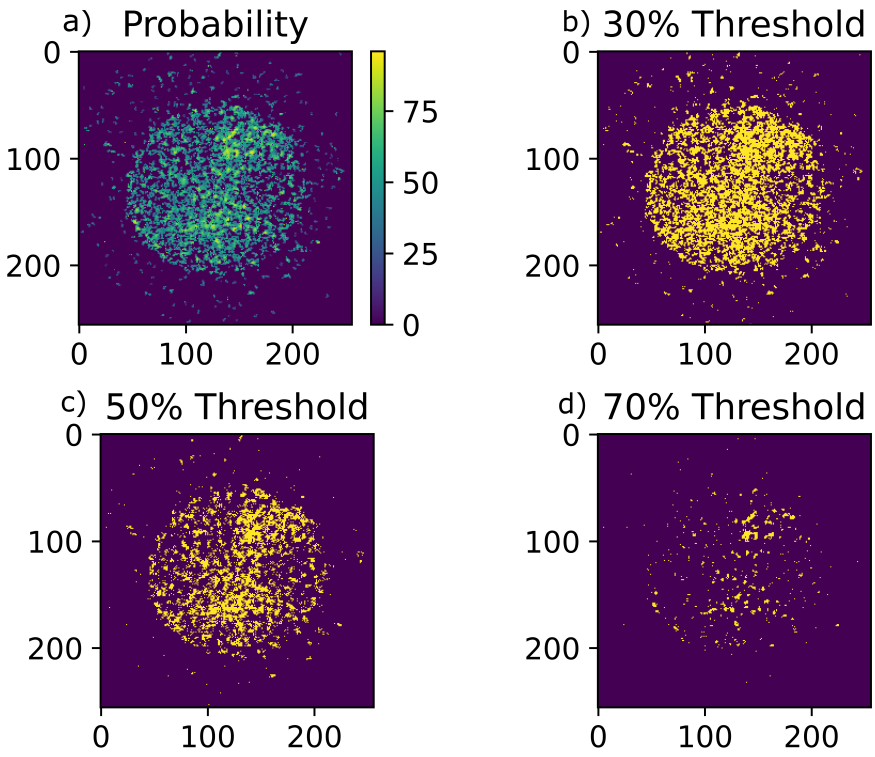


Figure 6.24: Example of the POE-NN prediction for a single detector frame for 200 kV electrons. **a**) Shows the probability for each pixel containing an electron POE. **b-d**) Show the determined entry points (yellow) for thresholds of 30, 50, and 70% applied to the probability.

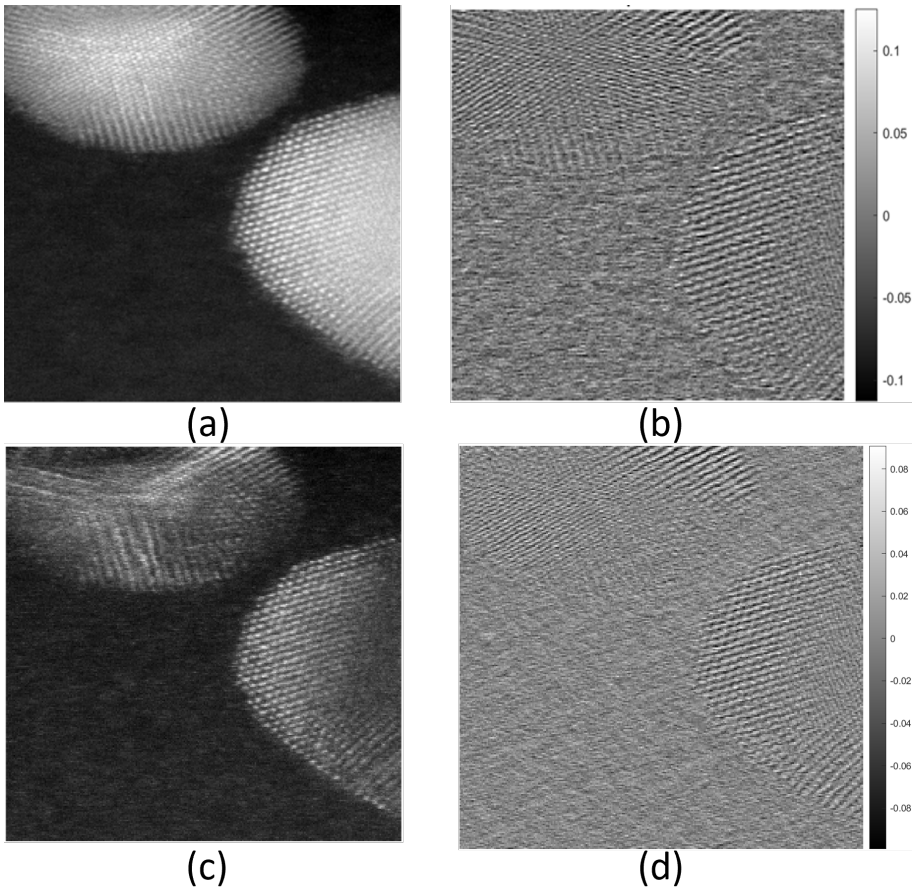


Figure 6.25: Comparison of imaging results for intensity CBED patterns of **a**) ADF image and **b**) SSB phase reconstruction with **c**) ADF image and **d**) SSB phase reconstruction, the latter two based on the binary data predicted by the POE-NN.

issue of contrast reversal observed in the initial implementation. As noted before, it is known that the POE-NN amplifies the features of the imperfect gain correction; this has not been accounted for in this procedure and may have an additional impact on the image quality. Nevertheless, it remains possible in both imaging methods to achieve atomic resolution images using the adapted POE-NN prediction. Despite the imperfections in this approach, it demonstrates an improvement on the initial implementation by Eckert for STEM applications and provides a basis for future improvements.

This study has thus far only been applied to test images of gold nanoparticles, which were acquired for the specific purpose of testing the POE-NN. Despite this, the primary application of the data handling methods discussed in this chapter concerns beam-sensitive samples, such as the DRS cathodes, which are the focus of the other studies presented in this thesis. The data obtained on these samples was obtained prior to the results on the importance of accurate gain correction and minimising the overlapping electron tracks, which can be achieved by spreading the bright field disk over a larger area.

6.10 Conclusions

The FFT algorithm used by the Matlab `fft` function has been highly optimised, and it is challenging to out-compete. Although the time improvements for the binary FT are not substantial, an additional benefit is a considerable reduction in the memory required. While it may not be possible to perform the binary FT faster than the FFT, the memory saving could be combined with the appropriate implementation of the relevant algorithms to produce on-the-fly reconstructions. This reconstruction method could operate directly from the same computer as the detector. Creating an event-based data stream from the existing detector is useful to take advantage of the data reduction for low-dose data. While the latest electron detectors allow direct read-out of event-based data, it is not feasible for many labs to use only event-based detectors, as upgrading involves substantial costs. Event-based detectors have limited applications for experiments that involve significant electron doses. This method provides the option of an event-based readout, only when it is best suited to the experimental conditions.

Although the physical interpretation of applying an intensity threshold is flawed, this work aims to increase the speed of the reconstruction process. Thus, in this case, the aim of the POE-NN should primarily be to reduce the number of hits, which will linearly decrease the time to perform a binary summation FT. Although the aim remains to produce high-quality phase images, whether the POE-NN can improve the reconstruction quality is a separate question that this work does not address. In order to take the research further and address this question, significant further optimisation of the POE-NN for overlapping tracks would be required. Alternatively, in experimental data, the number of overlapping tracks could be reduced further by lowering the electron dose or increasing the camera length to spread the bright-field disk over a larger detector area.

The reconstruction with the adapted neural network shows that despite the recognised flaws, the reconstruction quality remains high even with the adapted POE-NN. One down-side to the POE-NN is a requirement to train the network on data resembling the experimental datasets. Detector binning is commonly applied when using the pnCCD to increase data acquisition speed using the detector [124]. To apply the strategy of the POE-NN to predict the electron hits, the NN needs to be re-trained with a new set of training data with the same binning style and pixel size as the experimental data.

A discussion on the correction procedures for detector frames is given in Appendix B. Still, it has been shown in the prediction of the experimental data that an appropriate gain correction is required for the accurate prediction of the neural network. In order to accurately account for this, it would add an extra step in the reconstruction process, which partially negates the purpose of speeding up the reconstruction and requires full frame

rather than even-based data. Instead, future adaptations to the POE-NN should consider accounting for detector corrections in the training process.

The following chapter represents the first in a series of three chapters presenting studies of the SRO in DRS cathodes, using a variety of TEM and STEM methods. Specifically in the next chapter, the effect of changing the transition metal combination on the nature of the SRO is investigated.

Chapter 7

Real Space Visualisation of SRO in DRS cathodes

This chapter details electron diffraction and atomic resolution STEM imaging studies carried out on DRS cathodes. The work aims to provide insight into the nature of the SRO in these materials, which is ultimately essential to their implementation as commercial cathodes. Particular thanks are given to Liquan Pi for synthesising the samples and providing electrochemical testing results used in this investigation.

7.1 Introduction

The differences in the SRO for a series of DRS compositions have been investigated, namely, $Li_{1.2}Mn_{0.4}Ti_{0.4}O_2$ (LMTO), $Li_{1.2}Mn_{0.4}Zr_{0.4}O_2$ (LMZO), $Li_{1.2}Mn_{0.6}Nb_{0.2}O_2$ (LMNO), $Li_{1.2}Mn_{0.6}Ta_{0.2}O_2$ (LMTaO). The effect of changing the combination of transition metals is compared by maintaining the same lithium content and redox-active transition metal (Mn) while varying the second transition metal component (Ti, Nb Ta or Zr). To maintain charge neutrality in the average composition, the ratio of the metals [Mn:d^0] changes depending on the oxidation state of the d^0 metal.

Previously reported evidence for SRO, the importance of understanding its nature and factors influencing its formation are all detailed in Chapter 2. The literature review also provides evidence that the ions' ionic size and oxidation state play an important role in determining the nature of the SRO. Table 7.1 lists the atomic numbers, oxidation state, and ionic radii of the relevant cations in the compositions used in this study.

The importance of local arrangements of ions in influencing the ability of lithium to percolate in these materials is also discussed in Chapter 2. Specifically, Section 2.3 discusses the energy barrier for lithium migration through tetrahedral sites. Since the nature of the local coordination environments that make up the SRO is a statistical distribution of environments, which is difficult to explain experimentally, hence the existing studies in the literature are predominantly computational models [60].

The proposed cathode materials in this study have different theoretical capacities because

Element	Atomic Number	Oxidation State	Ionic Radii ()
Li	3	1+	0.76
Mn	25	2+	0.67(ls) 0.83(hs)
Ti	22	4+	0.605
Zr	40	4+	0.72
Nb	41	5+	0.64
Ta	73	5+	0.64

Table 7.1: Table of cations present in the composition analysed in this study; the corresponding atomic number, oxidation state in the pristine material, and ionic radii. In the case of Mn, the ls and hs refer to the ionic radii for the low-spin and high-spin electron configurations, respectively. The ionic radii are given for the corresponding oxidation state in an octahedral geometry. Data in the table information from Shannon et al. [244].

the compositions have different ratios of the redox-active transition metal (Mn) to d^0 transition metals. Hence, the capacity alone is not a good comparator of how well lithium can percolate through the material; instead, a less indirect measurement is the amount of lithium that can be extracted and re-inserted on the first cycle, normalised per formula unit. Figure 7.1 displays a bar chart of the amount of lithium per formula unit present in the composition, which can be extracted on the first cycle for each composition. LMZO, shows the least amount of accessible Li, followed by LMTO, while LMNO and LMTaO are very similar to each other and show the most amount of accessible lithium.

Highly structured diffuse scattering has been reported in various studies for the same or very similar compositions for; LMTO [38, 54], LMZO [38], LMNO [31]. In the case of LMTaO, no reported studies show structured diffuse scattering in electron diffraction. However, evidence of a broad low-angle peak, typical of SRO, has been observed in the powder-XRD [30]. This chapter presents an investigation using electron diffraction (ED) and annular dark field (ADF) imaging to interpret the correlations that constitute the SRO and investigate the coupling of correlation length of the SRO to the amount of percolating lithium.

7.1.1 Cluster Model

In this study, the cluster model first described in Section 2.2.2, in its application to describe SRO in alloys, is applied in relation to DRS's cathodes. The polyhedral arrangements of correlated lattice sited are used to explain the specific shapes in the diffuse scattering intensity, which are observed in SAED patterns and also transferred to the Fourier transform of ADF images. The diffuse intensity contours can be attributed to the 3D geometrical loci, originally defined mathematically by de Ridder et al. and reproduced in Figure 7.2 [56]. The intensity maxima in the diffuse scattering in the two-dimensional ED patterns can be interpreted as slices through the three-dimensional scattering surfaces. The slices

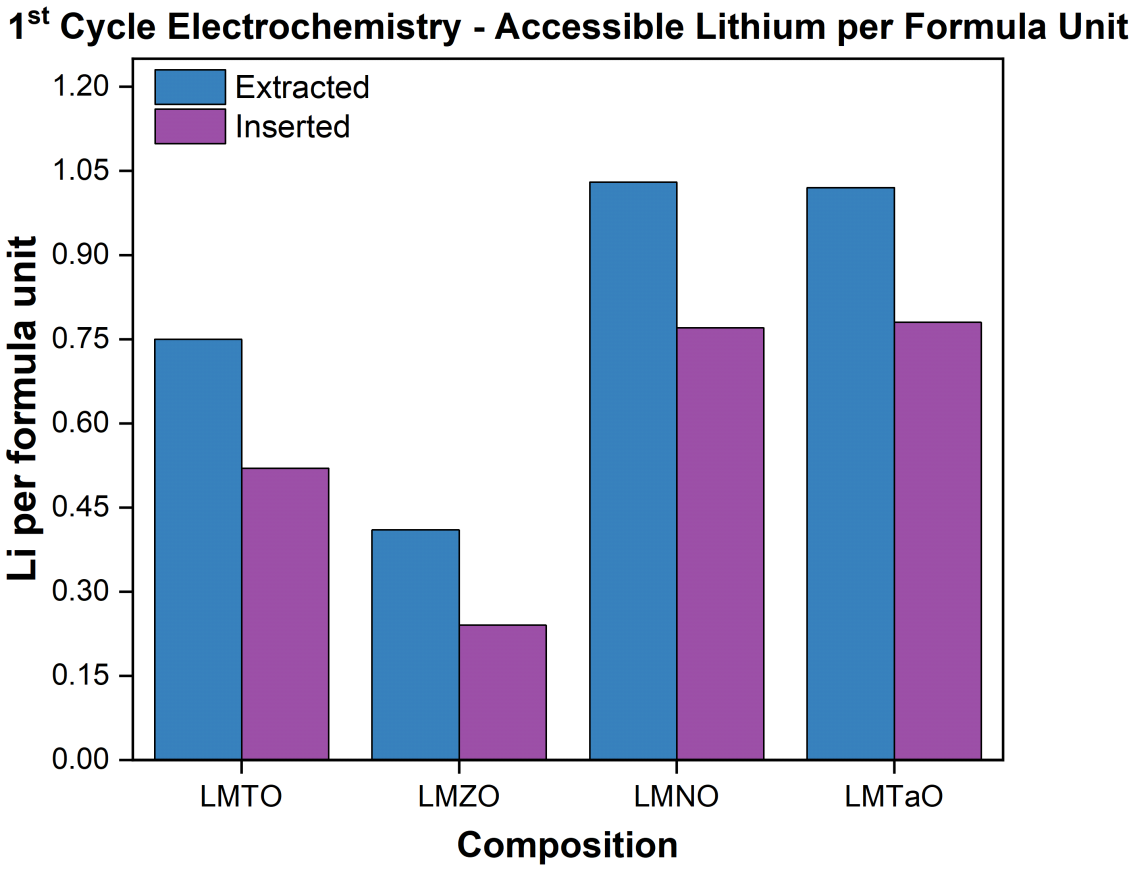


Figure 7.1: Bar chart displaying the amount accessible lithium which can be extracted (blue) and then re-inserted (purple) for each composition. Cycling was carried out between 2 and 4.8 V at $20\,\mathrm{mAg^{-1}}$. *Electrochemical testing carried out by Liquan Pi*

relate to planes in reciprocal space corresponding to the crystallographic orientation of the diffraction pattern. This is shown schematically relating to an octahedral cluster scattering surface intersecting with the <100>, <110>, and <111> planes in Figure 7.3. Other scattering surface intersections with the main low-order zones axes are given in Appendix C.

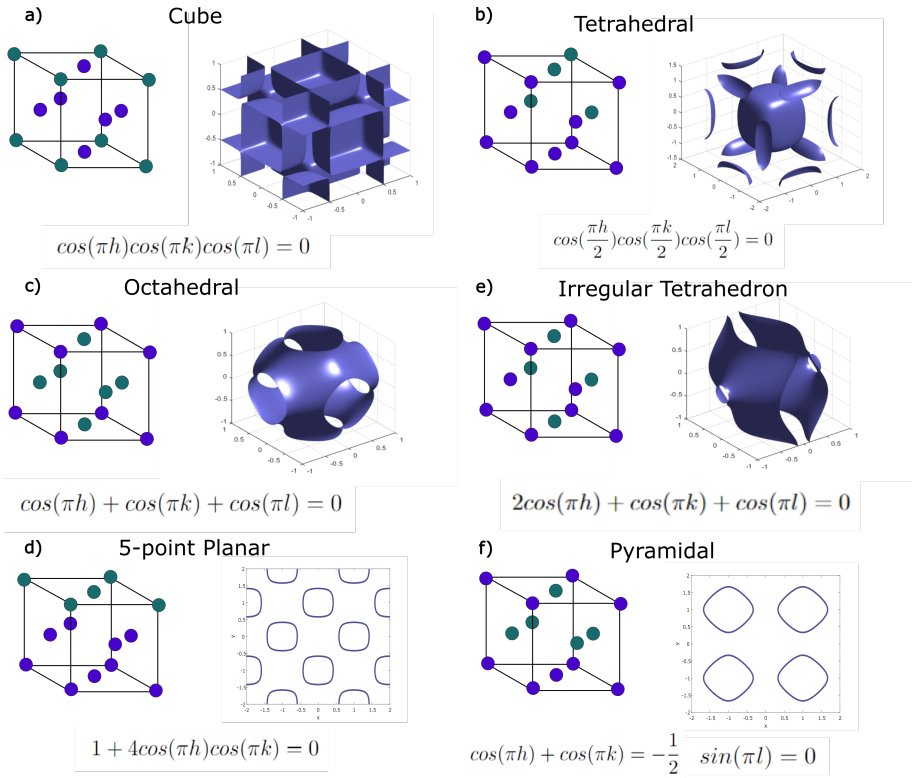


Figure 7.2: Polyhedra indicated on FCC lattice for **a**) cubic **b**) tetrahedral, **c**) octahedral, **d**) irregular tetrahedron, **e** 5-point planar, and **f**) pyramidal clusters, alongside the respective 3-dimensional loci in reciprocal space. Lattice sites which form the respective polyhedra are indicated in green on the FCC lattice. Figure remade and adapted from de Ridder et al., which also gives the equations for each scattering surface [56].

7.1.2 Linear Combinations of Clusters

It has also been proposed by de Ridder et al. that when more than one cluster type is present, then the resulting scattering surface can be described as a linear combination of the equations relating to the scattering surfaces of each applicable polyhedra [56]. For example, the scattering surface for a combination of octahedral and cubic clusters can be given by Equation 7.1.1. The geometry of the scattering surface depends on the ratio of the two equations, set by the scaling parameters *a* and *b*. The ratio of the two equations can be considered as the relative importance of the cluster types in the SRO but is not a quantitative measure of the number of each type of cluster. The scattering surfaces for a linear combination with different ratios of octahedral and cubic influence are plotted in Figure 7.4 alongside their respective intersections with the <100>, <110>, and <111>

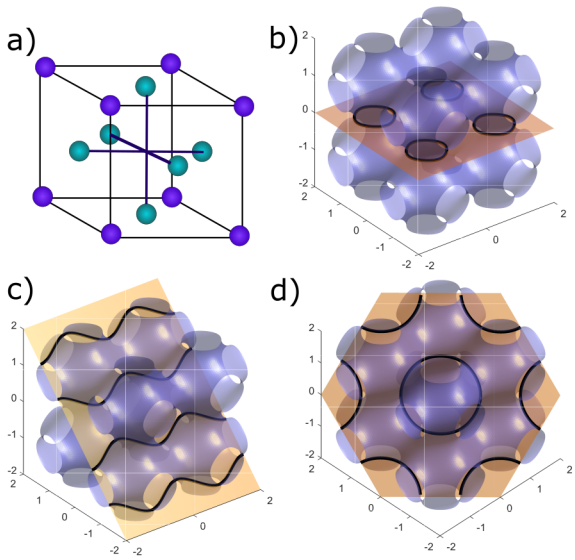


Figure 7.3: **a)** Green circles identify points on an FCC lattice which correspond to an octahedral cluster. **b)** Intersection of $<100>$ plane with the octahedral scattering surface. **c)** Intersection of $<110>$ plane with the octahedral scattering surface. **d)** Intersection of $<111>$ plane with the octahedral scattering surface.

planes. Examples of linear combinations of octahedral and tetrahedral cluster types are given in Appendix D. De Ridder et al. showed that a linear combination of the cubic and octahedral scattering surfaces can be used to describe diffuse scattering in $LiFeO_2$ which the separate cluster types can't fully describe [56].

$$a(cos(\pi h) + cos(\pi k) + cos(\pi l)) + b(cos(\pi h)cos(\pi k)cos(\pi l)) = 0 \qquad (7.1.1)$$

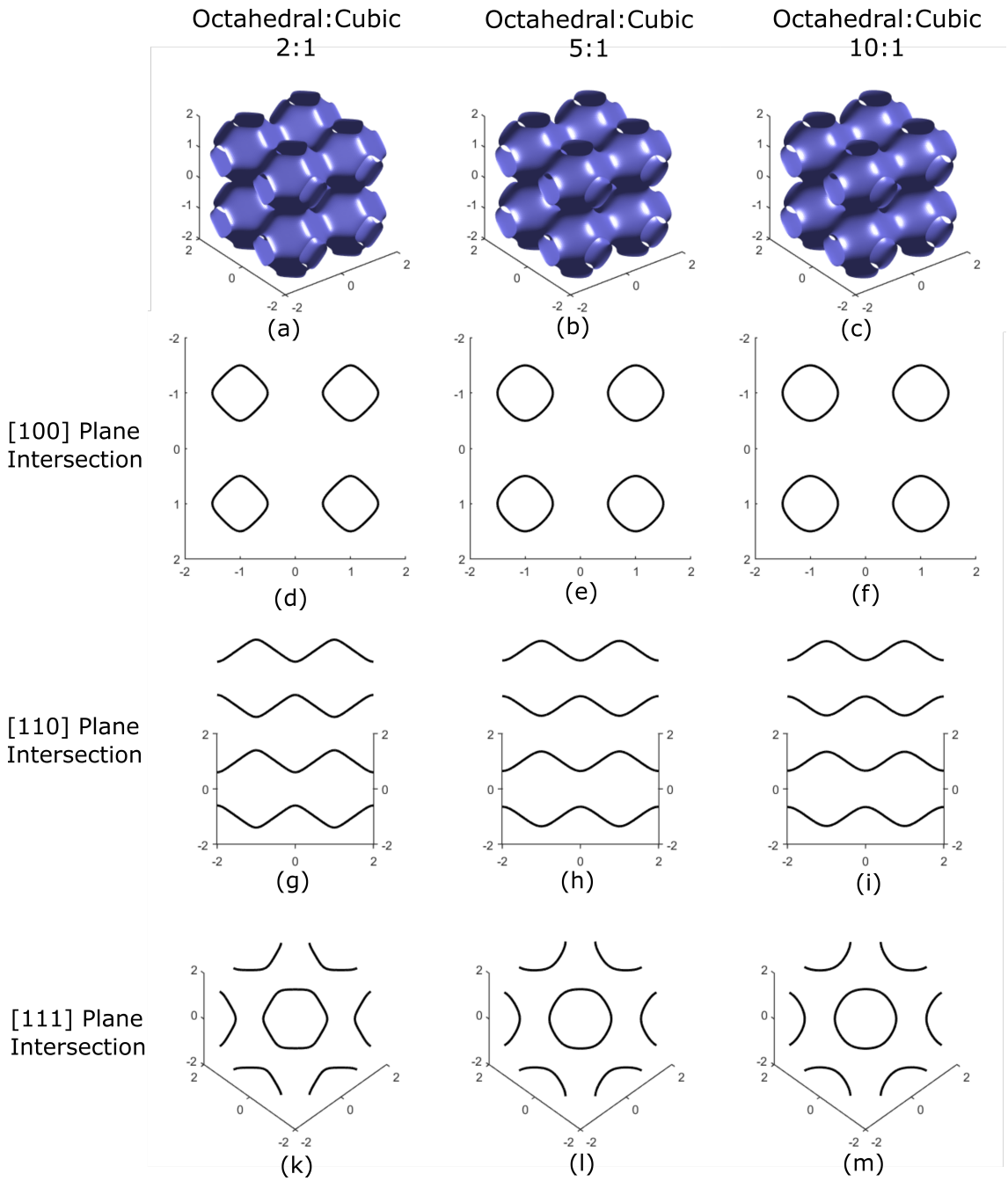


Figure 7.4: a-c) Plotted scattering surface for a linear combination of the octahedral and cubic scattering surface equations in ratios of 2:1, 5:1 and 10:1, according to Equation 7.1.1. In the columns below each, the intersections of the scattering surfaces with low-order zone axes are plotted for each ratio. **d-f**) intersections with the <100> plane, **g-i**) intersections with the <110> plane and **k-m**) intersections with the <110> plane.

7.2 Electron Diffraction

The cluster model by de Ridder discusses the intersection of the scattering surfaces with planes in reciprocal space. In order to understand the correlations based on this model, diffraction from single-zone axes is required. The samples being examined in this study are too small for single-crystal XRD, and differences in the nature of the diffuse scattering can't be observed in powder XRD [53]. The particle size of the pristine samples chosen for SAED were in the region of $500 - 1000\,\mathrm{nm}$. Electrons have significantly stronger interactions with matter; therefore, single-crystal diffraction patterns from much smaller particles can be achieved using electrons than with X-rays.

7.2.1 Method

This study uses SAED to analyse the variation in the diffuse scattering between compositions. Particles were selected for SAED based on identifying isolated particles on the lacey carbon grid of an appropriate size and having a low-order zone axis within the tilt range of the holder. A representative particle and region within the selected area aperture is given in Figure 7.5. All of the compositions in the study produced particles with a similar microstructure; all particles chosen for SAED were single-crystalline in nature and in the region of $200 - 1000\,\mathrm{nm}$ in diameter in diameter.

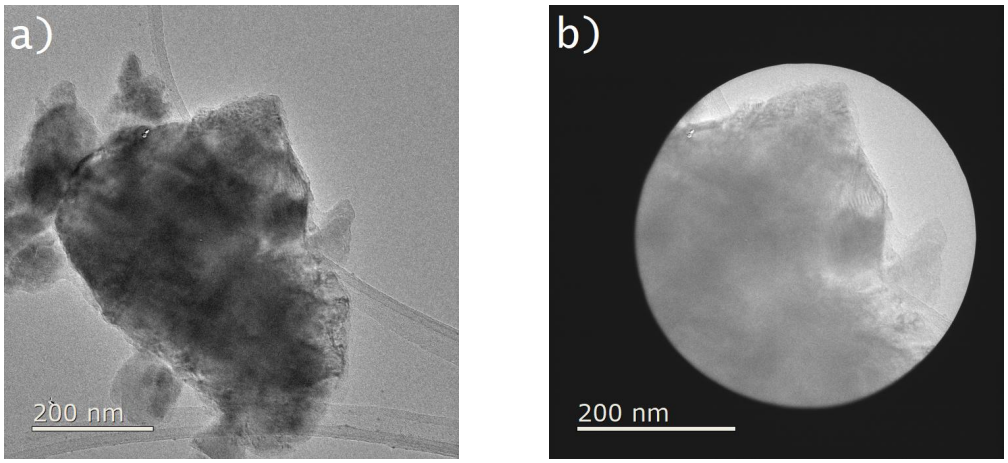


Figure 7.5: **a**) Representative TEM image of pristine $Li_{1.2}Mn_{0.4}Ti_{0.4}O_2$ particle. **b**) Selected region of the particle within the selected area aperture.

7.2.2 Results

The SAED patterns in Figure 7.6 and Figure 7.7 generally agree with those previously reported in the literature for the same or very similar compositions. Although, to the author's knowledge, for the $Li_{1.2}Mn_{0.6}Ta_{0.2}O_2$ composition, no single-crystal electron diffraction patterns have previously been reported. The $<100>$ diffraction for $Li_{1.2}Mn_{0.4}Zr_{0.4}O_2$

shows some subtle differences in the location of the intensity maxima of the diffuse scattering in comparison to the previously reported example by Ji et al. [38]. However, the aforementioned study only provides one electron diffraction pattern, so comparing other orientations is impossible.

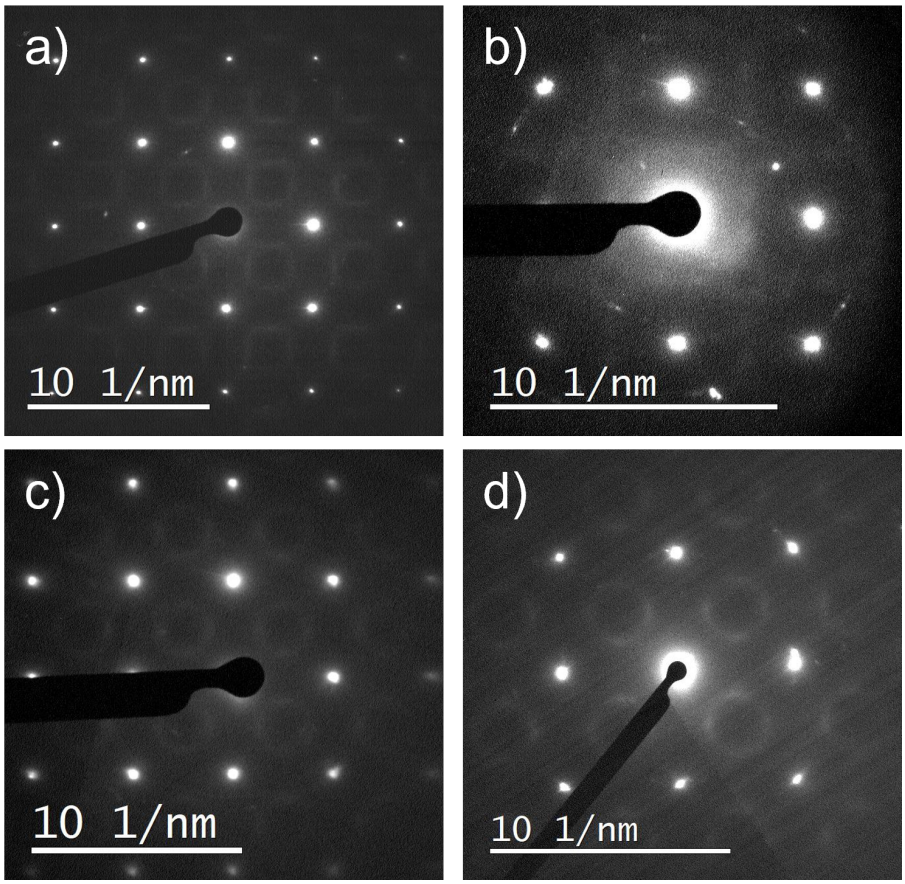


Figure 7.6: SAED patterns of <100> zone axis for **a**) $Li_{1.2}Mn_{0.4}Ti_{0.4}O_2$, **b**) $Li_{1.2}Mn_{0.4}Zr_{0.4}O_2$, **c**) $Li_{1.2}Mn_{0.6}Nb_{0.2}O_2$, **d**) $Li_{1.2}Mn_{0.6}Ta_{0.2}O_2$

The <100> diffraction patterns for the Ti, Nb and Ta samples (Figures 7.6.**a**, 7.6.**c**, 7.6.**d** respectively) initially appear to be very similar; however, on closer inspection, it can be observed that the diffuse structure in the Ti sample is more square in comparison to the more rounded shapes in the Nb and Ta samples. This can be interpreted as a contribution to the diffuse scattering from the cubic cluster, to the dominating octahedral geometry of the scattering surface. For an increased contribution from cubic clusters, it would be expected that the <110> orientation would also follow the trend in Figure 7.4, which for the <110> appears as the oscillating lines becoming more sharply defined zig-zags. However, combined with the dominating intensity of the central spot, the fact that the diffuse scattering is significantly weaker than the Bragg scattering makes it hard to distinguish subtle differences in the diffuse scattering from SAED. Since the diffuse scattering is particularly weak in the <110> SAED patterns for Nb and Ta (Figures 7.7.**c** and 7.7.**d**), it is not possible to tell whether the <110> orientation follows the trend that would be ex-

pected. However, in Figure 7.6.**d**, it is possible to distinguish that the Ta sample has more intensity variation along the lines with maxima at the turning points of the zig-zagging lines. The scattering surfaces do not explain variations in the intensity along the scattering surface intersections. Instead, these can be considered more localised diffuse intensity, corresponding to order over a greater extent in real space.

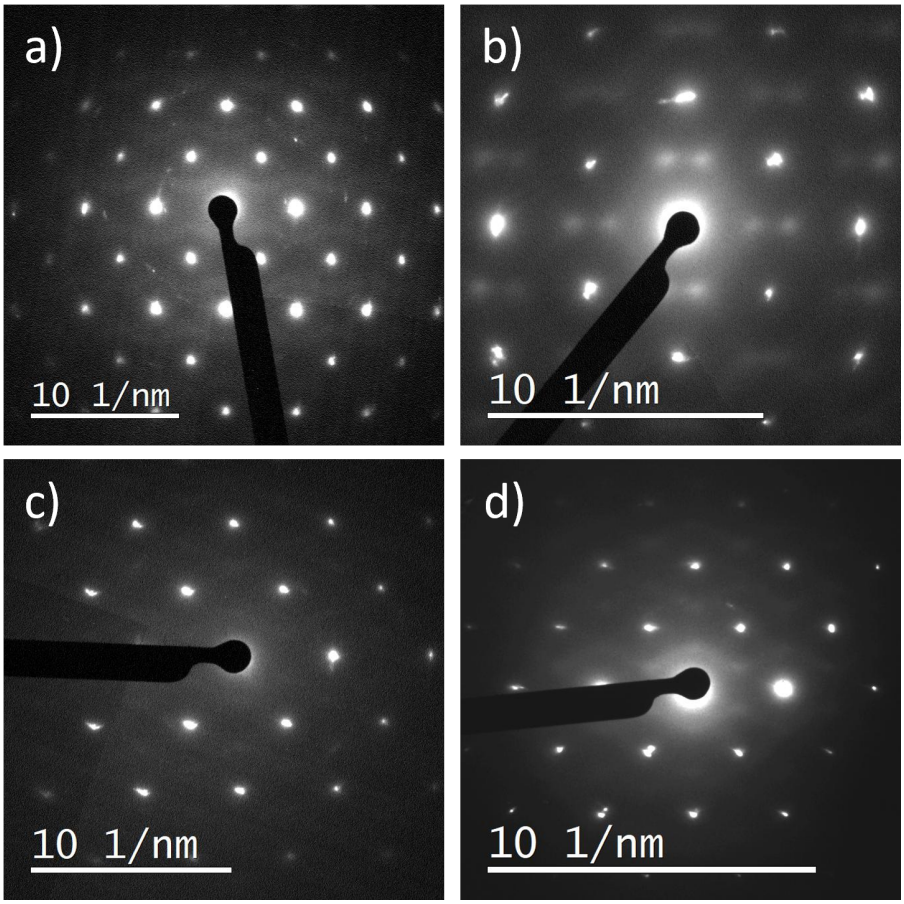


Figure 7.7: <110> SAED patterns for **a)** $Li_{1.2}Mn_{0.4}Ti_{0.4}O_2$, **b**)$Li_{1.2}Mn_{0.4}Zr_{0.4}O_2$, **c**) $Li_{1.2}Mn_{0.6}Nb_{0.2}O_2$, **d**) $Li_{1.2}Mn_{0.6}Ta_{0.2}O_2$

The intensity maxima of the diffuse scattering in the Ti, Nb and Ta all qualitatively lie along the intersection of the scattering surface for the octahedral cluster with some contribution from cubic clusters, particularly in the case of Ti. The diffuse scattering in both the <100> and <110> planes of these samples is similar, which is a strong indication that the type of SRO is similar.

In both the <100> and <110> patterns the Ti, Nb and Ta compositions (Figures 7.7.**a**, 7.7.**c**, 7.7.**d** and 7.6.**a**, 7.6.**c**, 7.6.**d**) are much more similar to each other than they are to the equivalent diffraction pattern of the Zr sample (Figure 7.7.**b** and 7.6.**b**). It is also the only sample where the diffuse scattering across both zone axes is not consistently explained by a single scattering surface equation for any of the polyhedra or a simple linear combination of polyhedra. Comparing Figures 7.6.**a** and 7.6.**b**, rather than the rounded squares, the Zr

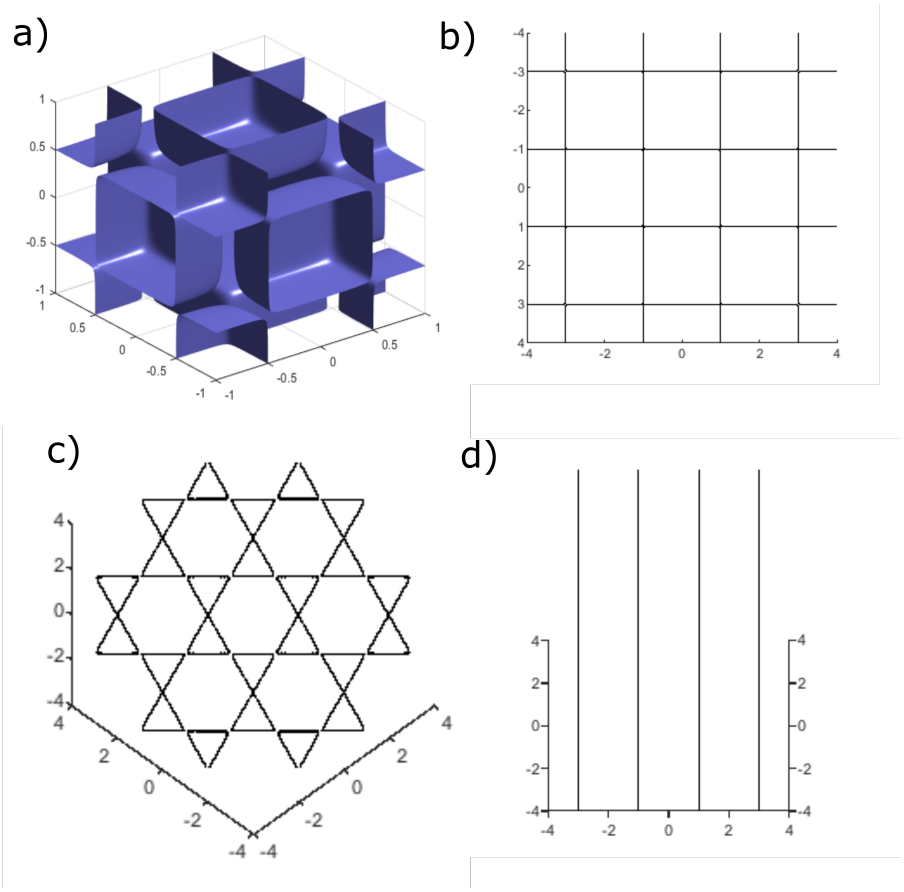


Figure 7.8: **a**) 3D filled scattering surface for cubic cluster type, **b**) Intersection of cubic scattering surface with the < 100 > planes. **c**) Intersection of the cubic scattering surface with < 111 > planes. **d**) Intersection of the cubic scattering surface with the < 110 > planes.

sample has straight lines vertically and horizontally between the Bragg peaks, there are also small square features halfway between the central peak and <220> peaks, centred on the same location as the squares in the other samples. The horizontal and vertical lines fit the expected scattering surface intersection in the <100> planes with the cubic cluster model, as shown in Figure 7.8. However, unlike for the other samples, the correlation between zone axes does not hold for the Zr sample. If the diffuse scattering could be explained simply by cubic clusters, then the <110> orientation would be expected to show stripes along a single axis. Instead, a hexagonal pattern is observed in Figure 7.7.**b**, between the Bragg peaks, with distinctive intensity maxima on the horizontal lines.

Additionally, comparing the <100> and <110> ED patterns (Figures 7.6.**b** and 7.7.**b**) for the Zr sample, it is noted that the diffuse scattering in the <110> direction is significantly more localised, producing clear spots along the lines of diffuse scattering. The SRO in this sample is distinctly different from the other samples, and the cluster model used to explain the other sample is insufficient to explain the SRO in the Zr sample. In electrochemical testing performed by Liquan Pi, this sample also shows a significantly reduced quantity of accessible lithium, providing further evidence that the SRO and electrochemistry are strongly linked.

There are some limitations to the analysis of the SRO that can be made from the SAED results. First, the diffuse scattering can't identify the types of ions on the correlated lattice sites in each sample. The secondary transition metals have different atomic numbers, which affects their scattering cross sections and, hence, could lead to subtle differences in the diffuse scattering. Second, it is also notable that electron diffraction does not provide any spatial information or indication of compositional arrangements of the clusters which form these particular correlations. This is important because the work by de Ridder et al. discussed the clusters as precursors to a long-range ordered state; this, in turn, necessitates that the clusters must have the same composition as the bulk average [56]. It is also discussed in the literature review (Section 2.2) that SRO in alloys is regularly categorised as either statistical, disperse, or microdomain. Both microdomain and disperse ordering refer to ordered regions within a disordered matrix, consistent with the de Ridder cluster model used to explain the diffuse scattering in these samples. Distinguishing between microdomain and disperse is determined by whether the ordered regions have the same composition as the average structure or a different composition. Making this distinction from SAED, is impossible since it is not possible to determine the composition of the clusters by electron diffraction.

7.3 Annular Dark Field Imaging

The SAED results show that varying the transition metal combination does influence the nature of the diffuse scattering, which in turn indicates that the type of correlations that make up the SRO are different. However, as previously explained SAED does not contain any spatial information about how these polyhedra are dispersed in the sample or the number of unit cells to which the ordering is extended. In the following section, we make use of the fact that SRO is related to arrangements of lithium and transition metals, which have a large difference in their atomic numbers, and that ADF images are particularly sensitive to atomic number contrast. This means that transition metal-rich columns appear bright and lithium-rich columns dark. This work examines the relationship between these intensity variations and SRO by the information transferred to the FT of atomic resolution ADF images.

7.3.1 Imaging Method

ADF images were acquired using the JEOL JEM-ARM200F microscope operated at $200\,\mathrm{kV}$; probe currents in the region of $57 - 95\,\mathrm{pA}$ were used. The upper ADF detector was used with a camera length of $8\,\mathrm{cm}$, resulting in a collection angle ranging from $72 - 271\,\mathrm{mrad}$, as measured for this particular instrument by Jones et al. [245]. The samples were in powder form dispersed on lacey carbon grids, prepared as previously described in Section 5.2. The images referred to in captions for Figure 7.10 and 7.11 with the abbreviation Smart-Align (SA) were acquired using multi-frame acquisition. An explanation of the acquisition method and procedure for alignment of the frames is given in Section 5.3.2.

7.3.2 Bragg Filtering Method

To more clearly visualise the contrast which arises from the SRO, filtering of the Bragg reflections in the FT of the ADF images was carried out. This process is outlined in Figure 7.9; the Bragg reflections were selected using the mask feature in GMS® 7.9.**c**. The selected regions were masked to eliminate the intensity of the Bragg peaks. This process is outlined in Figure 7.9 using either a mask with a hard cut-off (Figure 7.9.**d**) or smoothing the edge by averaging towards the centre (Figure 7.9.**e**), the results of the respective Fourier transform (FT) are given below each. Removing the contrast from the Bragg spots in the FT is equivalent to removing the spatial frequencies associated with the average lattice in real space. The intensity variations remaining in the iFT are from spatial frequencies associated with the diffuse scattering. Since the SRO lies on the lattice, the intensity variations also correspond to lattice sites but are associated with deviations from the average lattice contrast.

The effect of Bragg filtering and the possibility of artefacts should always be considered when undertaking this type of image processing. Discontinuities, in contrast, correspond to infinite spatial frequencies in reciprocal space [246]. The FT of a discontinuity results in oscillations in the Fourier series even as the number of components tends towards infinity; this is known as the Gibbs phenomenon [247]. This is typically illustrated by the example of a square wave whose Fourier representation can be described by a series of sine waves. In this example, as the number of terms in the Fourier series increases, the oscillations become smoother in the flat part of the square wave; however, the peaks around the discontinuity never disappear [247]. To minimise artefacts in the iFT, smoothing was applied to the edge of the mask to result in a more continuous background. The smoothing filter is applied as a convolution of the smoothing kernel, pre-determined by the GMS® software, across a user-defined number of pixels from the edge of the spot mask. This has the effect of producing a more continuous background which does not have harsh discontinuities. The vertical and horizontal cross present through the centre of every FT occurs due to the discrete boundary at the edge of the image [248].

7.3.3 Results

HAADF images of the <100> orientation for LMTO, LMTaO and LMZO, are shown in Figure 7.10. The bright and dark regions of the iFT of the Bragg-filtered images (right-hand column) correspond to regions where the spatial frequencies translate to the diffuse scattering observed in the FT. The contrast from the lattice is averaged to a noisy grey background. Across all images in the <100> orientation, the distribution of the bright and dark regions in the Bragg-filtered images strongly correlates to regions in the raw data, which show particularly strong intensity variation between neighbouring columns. Given the strong Z contrast nature of ADF imaging, this indicates that the intensity variation is inherently linked to the compositional arrangements of the SRO.

HAADF images of the <110> orientation for LMTO, LMNO, LMTaO, and LMZO [1], are shown in Figure 7.11. In all samples, the diffuse scattering in the FT is similar to the diffuse scattering in the SAED patterns, including the Zr sample, which is again an outlier amongst the other results. Studying the Ti, Nb and Ta samples, which all show similar diffuse scattering, an observable difference from the filtered ADF images which can't be obtained from SAED is the spatial extent of the ordered bright and dark layered features. Blue boxes highlight regions in Figure 7.11, showing that the bright and dark pairs repeat over more units from the Ti to Nb composition and further to the Ta sample. The repeating units are consistently a series of darker columns alongside brighter columns.

[1] It should be noted that the vertical banding of regions in focus and out of focus in the Zr sample is due to an instability that developed in the microscope and was unable to be resolved prior to the completion of the work.

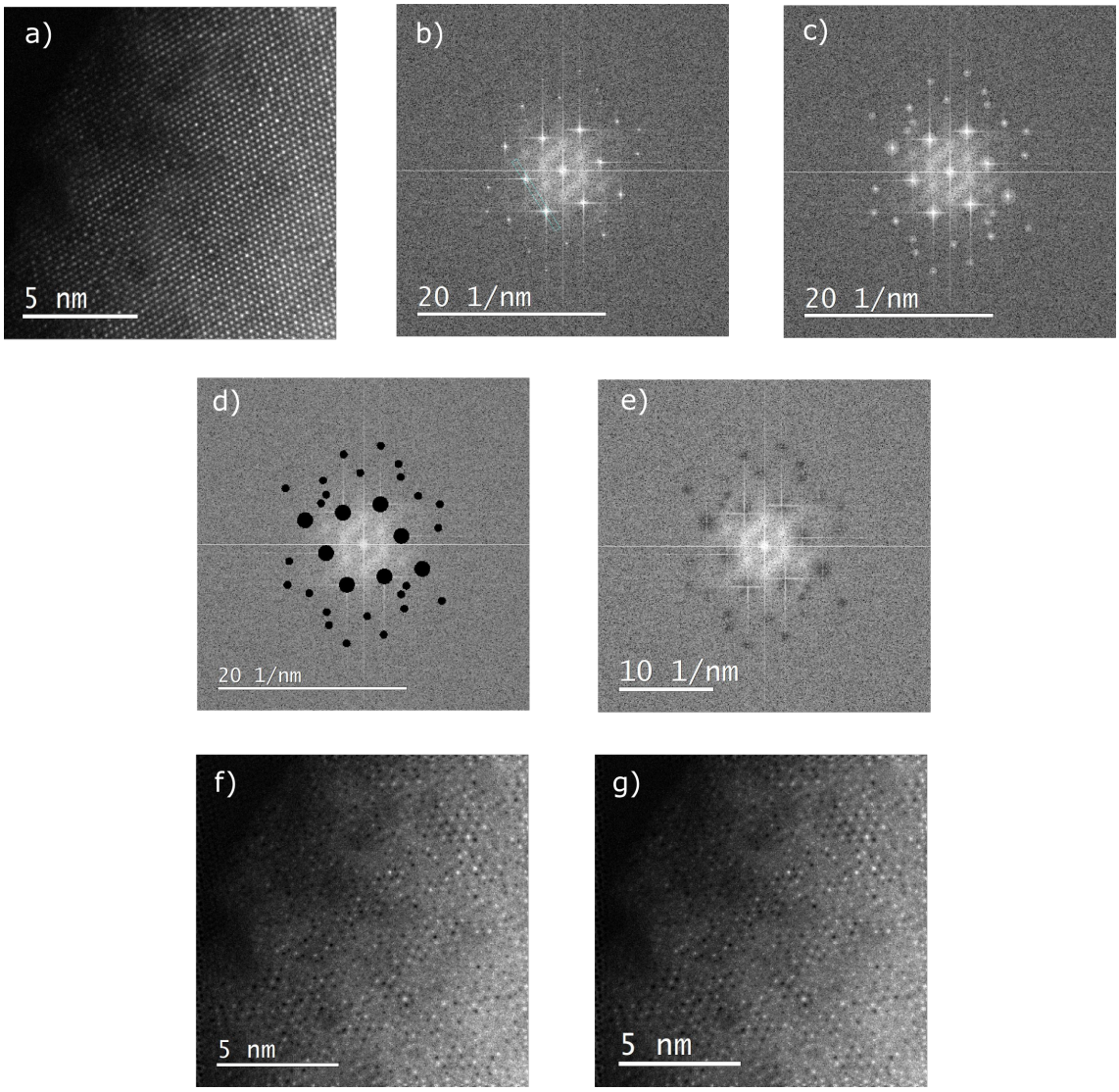


Figure 7.9: Example of the Bragg filtering process. **a**) ADF image of LMNO. **b**) The FT of the image in **a**. **c**) The Bragg reflections are selected by masking the bright spots. **d**) The mask applied with no smoothing at the edge of the mask, the iFT is given in **f**. **e**) The masked FT with the smoothing applied at the edge of the mask, and the iFT is given in **g**

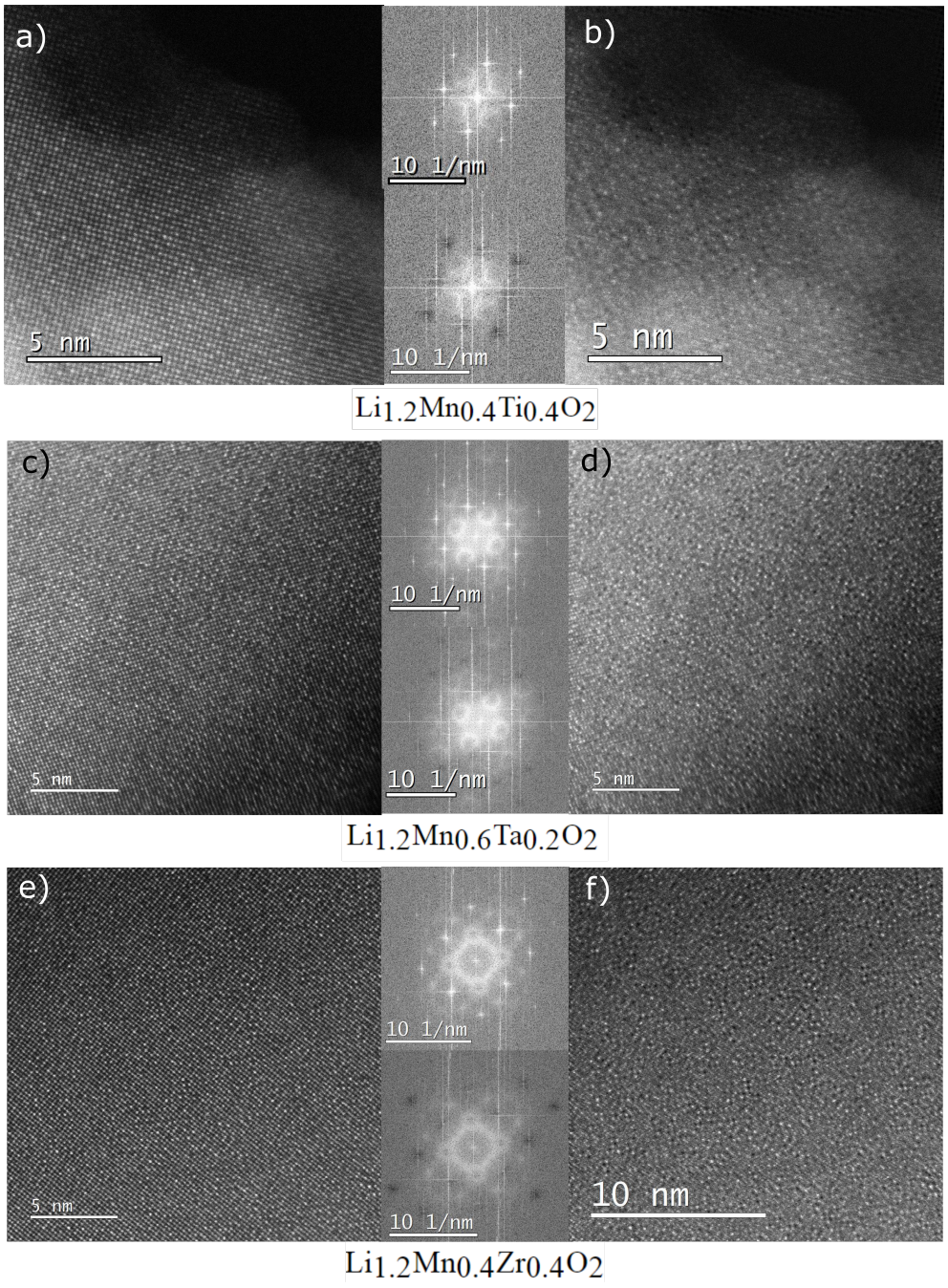


Figure 7.10: ADF images of orientated along the < 100 > direction of **a**) $Li_{1.2}Mn_{0.4}Ti_{0.4}O_2$, **c**) $Li_{1.2}Mn_{0.6}Ta_{0.2}O_2$ (SA) and **e**) $Li_{1.2}Mn_{0.4}Zr_{0.4}O_2$. **b,d,f** the iFT of the respective images after masking the Bragg peaks in the FT following the previously described procedure. Raw and Bragg-filtered FTs are inset between the images in each case.

The following section describes how a combination of the cluster model from the electron diffraction and the strong Z contrast nature of HAADF imaging can be used to assign this contrast to particular clusters within the sample.

7.4 Real Space Interpretation

.

In the following section, the interpretation of the intensity fluctuations in the Bragg-filtered images is expanded via two methods. The first method aims to derive real space information on the distribution of SRO, using a method related to the Patterson to examine the real space nature of the correlations which result in the diffuse scattering. The second is an interpretation of the bright and dark pairs in the previous section by relating the Z-contrast nature of ADF imaging and the cluster model proposed by de Ridder.

7.4.1 Correlations in Real Space

The Patterson function was developed as a workaround to the phase problem during the early development of X-ray diffraction methods to interpret the intensities recorded by diffraction methods in real space without any knowledge of the phase information [249]. The Patterson function, given in Equation 7.4.1, is defined as a Fourier summation of the diffraction intensities with all phase components set to zero. The intensity in the diffraction is represented by F_{hkl} where (h, k, l) are the reciprocal space lattice vectors, and the Patterson function is defined in terms of real space inter-atomic vectors (u, v, w) [250].

$$P(u,v,w) = \frac{1}{V} \sum_{h} \sum_{k} \sum_{l} \mid F_{hkl} \mid^2 e^{2\pi i(hu+kv+lw)} \tag{7.4.1}$$

Equation 7.4.1, can also be expressed in the form of an inverse Fourier transform (iFT), denoted by $\mathcal{F}^{-1}$, of the product of $F(hkl)$ with its complex conjugate, written as in Equation 7.4.2. Using the convolution theorem, the FT of the product of two functions can be written as the convolution of the individual FT. Hence, the definition given in Equation 7.4.3 of the Patterson function as an autocorrelation of the structure with itself becomes obvious.

$$P(u,v,w) = \frac{1}{v} \mathcal{F}^{-1}[F_{hkl} \cdot F^*_{hkl}] \tag{7.4.2}$$

$$P(u,v,w) = \frac{1}{V} [\mathcal{F}^{-1}(F_{hkl}) \circledast \mathcal{F}^{-1}(F_{hkl})] \tag{7.4.3}$$

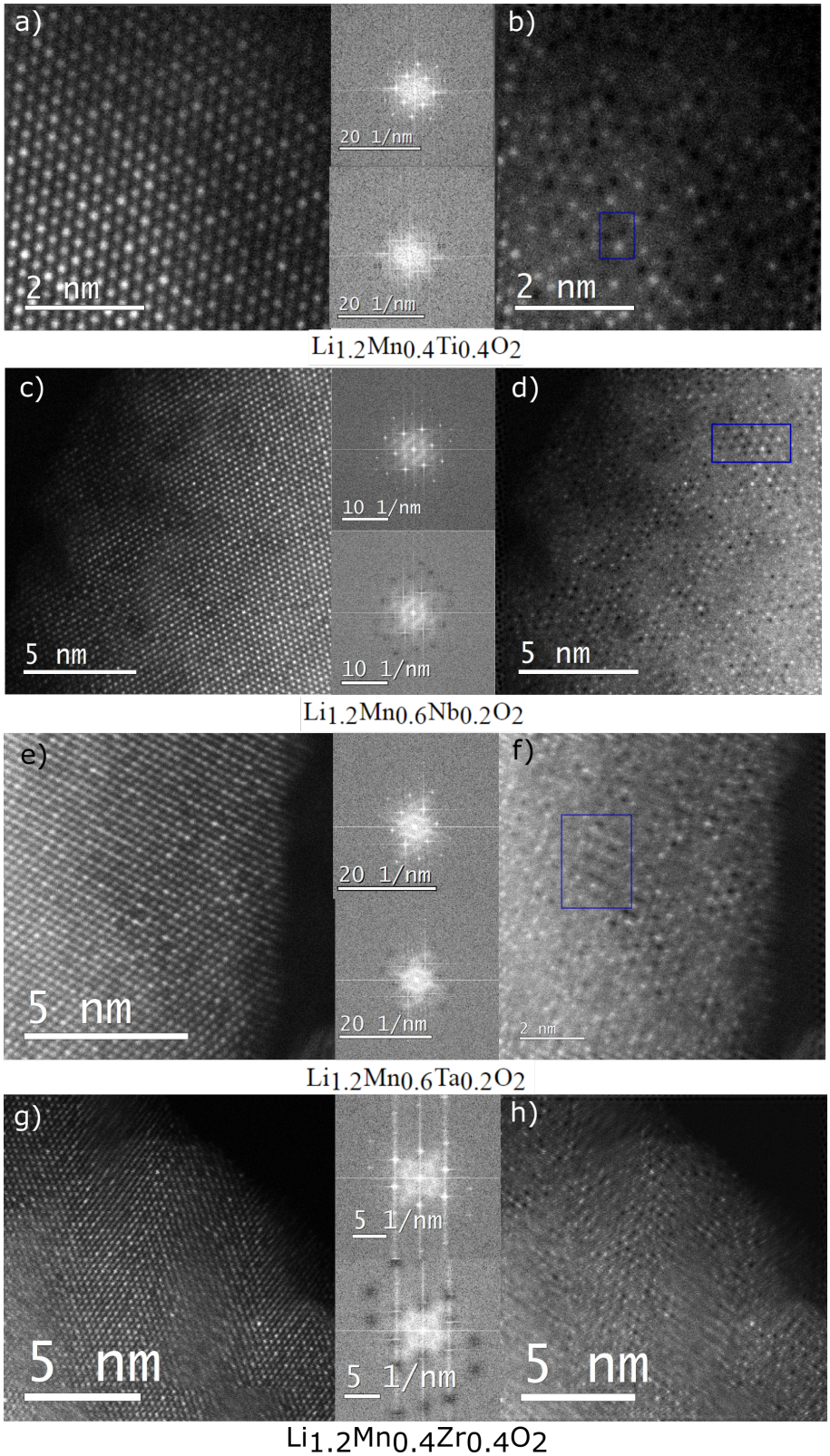


Figure 7.11: ADF images of orientated along the < 110 > direction of **a**) $Li_{1.2}Mn_{0.4}Ti_{0.4}O_2$ (SA), **c**) $Li_{1.2}Mn_{0.6}Nb_{0.2}O_2$ (SA), **e**) $Li_{1.2}Mn_{0.6}Ta_{0.2}O_2$ (SA) and **g** $Li_{1.2}Mn_{0.4}Zr_{0.4}O_2$. **b,d,f,h**) The iFT of the respective mages after masking of the Bragg peaks in the FT following the procedure previously described. Raw and Bragg-filtered FTs are inset between the images in each case.

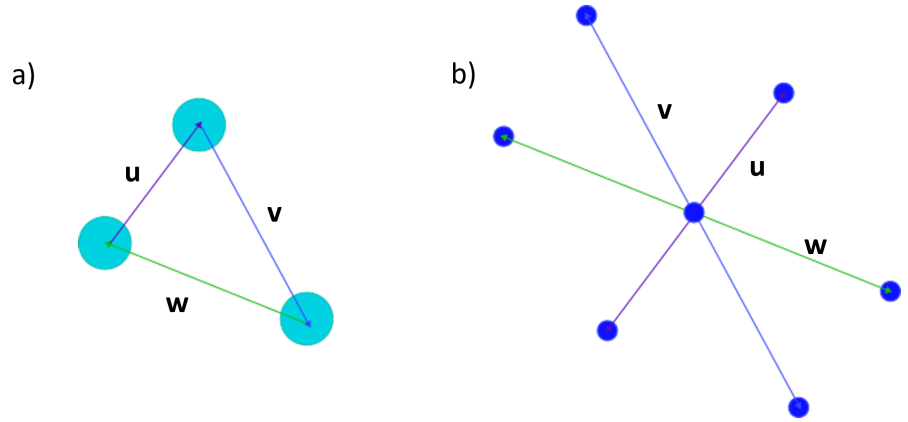


Figure 7.12: Schematic representation of Patterson function. **a** Inter-atomic vectors, (**u**, **v**,**w**) between atomic species. **b**) The correlation function representation of the inter-atomic vectors.

A physical interpretation of the Patterson function can be thought of as plotting the similarity of a function to itself, shifted by a vector. The result of the Patterson function plotted as a function of the shift vector is a set of intensity maxima at the positions where there are positive correlations in the lattice; in other words, intensity maxima connected to the origin by the inter-atomic vectors. This is shown schematically in Figure 7.12.

Unlike recording diffraction, taking the FT of an ADF image maintains the phase information; hence, the iFT relates to the image and retains the positions of the correlations. We obtain the equivalent information to a diffraction pattern in the FT by taking the square modulus, thus neglecting the phase. Following a similar idea to the Patterson function, calculating an iFT of the square modulus gives a correlation function for the image. Bright points in the correlation function with respect to the origin correspond to positive correlation vectors. In the context of an image, this means starting from a bright pixel and shifting by the relevant vector is likely to correspond to another bright pixel or, equivalently, a dark to a dark. Dark points on the correlation function correspond to negative correlation vectors, i.e. shifting by the negative correlation vector from a bright pixel likely corresponds to a dark pixel or vice versa. These will be referred to here as a correlograph - a two-dimensional plot (in real space) depicting the correlations in an image.

Correlation Function Method

Since the diffuse scattering is typically orders of magnitude weaker than the Bragg scattering, as can be observed in Figure 7.13, the lattice correlations dominate the correlograph from the unfiltered FT images. In suppressing the Bragg reflections, the edge effects, which are described in Section 7.3.2 in the context of the Bragg filtering method, become the next dominating effect of the correlograph. Figure 7.14, compares obtaining the correlograph with the edge effect present and following the method described subsequently

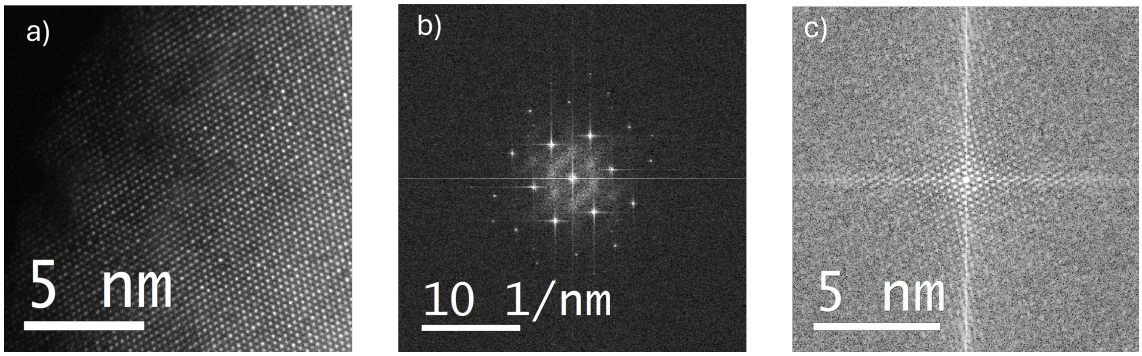


Figure 7.13: Correlograph from unfiltered image of $Li_{1.2}Mn_{0.6}Nb_{0.2}O_2$. **a**) Unfiltered ADF image of LMNO. **b**) Square modulus of the FT of ADF image. **c**) Correlograph, derived by taking the iFT of the square modulus.

to suppress the edge effects as far as possible. The edge artefacts appear as a cross of correlations centred in the middle of the correlograph, as in Figure 7.14.**c**. Applying a gradual fade to the edge (Figure 7.14.**d**) of the filtered image before obtaining the modulus squared of the FT, in Figure 7.14.**f**. This sufficiently suppresses these artefacts and leaves correlations primarily resulting from the diffuse scattering.

As the correlations in the image from the SRO occur over relatively short length scales, in most cases first and second nearest neighbours, the bright and dark intensities in the correlograph occur close to the centre of the iFT. Figures 7.15 and 7.16 are shown with cropped regions and the Bragg filtered images and correlographs, such that the inherent matching of the scale is maintained. In each case, the correlograph is annotated with lines, which can then be matched to features in the images, indicating either positive or negative correlations corresponding to the same length and direction as the correlograph annotation.

The results indicated in Figure 7.15 show that for LMTO, correlations are only indicated for the first nearest neighbours; these are negative correlations, indicated by dark spots. In contrast, both LMNO and LMTaO show both positive and negative correlations. In accordance with the results for the diffuse scattering, the correlographs are very similar, both indicating negative correlations in the next nearest neighbour coordination and positive correlations in the second nearest neighbour coordination environments.

In Figure 7.16, the correlographs from the $<100>$ projection appear more complex in the arrangement of positive and negative correlations than the $<110>$ projection. However, similarly to the $<110>$ projection, only negative correlations are found for LMTO. In the case of both LMTaO and LMZO, a complex arrangement of positive and negative correlations are present. For the LMZO, the correlations extend over a longer length scale, which is consistent with the observation in the SAED data and in the FT of the ADF image where the diffuse scattering is more localised in its nature.

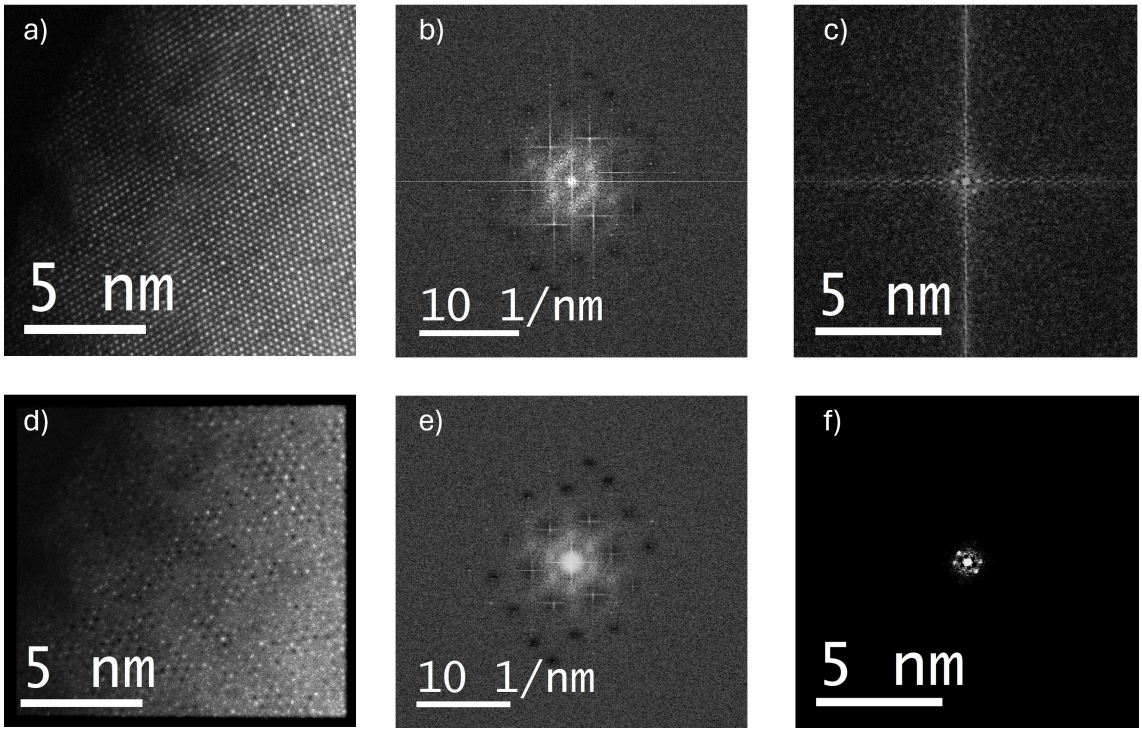


Figure 7.14: a) Bragg filtered ADF image of LMNO. **b**) Square modulus of the FT of the Bragg filtered image. **c**) Correlograph formed by taking the iFT of the square modulus. **d**) Bragg filtered ADF image of LMNO with a dampening gradient applied at the edges. **e**) Square modulus of the FT of the dampened Bragg filtered image. **f**) Correlograph formed by taking the iFT of the square modulus of the dampened Bragg filtered image.

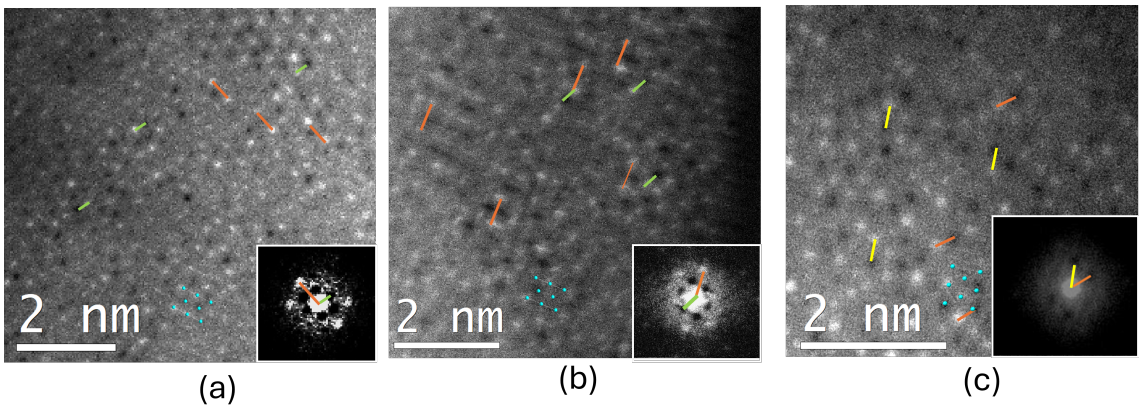


Figure 7.15: Selected regions of the Bragg filtered images with the central region of each correlograph inset in the corner of each image. In figures **a**) of LMNO and **b**) of LMTaO an example of a positive correlation vector is indicated in the correlograph by an orange vector, which is translated onto the image in selected regions to indicate these correlations on the images. A green line is used to indicate a negative correlation vector on the correlograph and this is also translated onto several regions in the image where this correlation is observed. In image **c**) of LMTO only negative correlations are observed, which are indicated in the same way but in this case for two different directional correlations using yellow and orange segments. The scale and direction of the vectors indicated in the correlograph match those indicated in the images. Schematics illustrating the unit cell in this projection are shown near the scale bar on each image; only cation positions are shown, as the ADF is primarily sensitive to heavy transition metals.

In theory, this process could be performed in an equivalent manner on electron diffraction patterns, such as those presented in Section 7.2. Since the scattering in electron diffraction is dominated by low-angle scattering, the diffuse scattering is orders of magnitude weaker than the Bragg scattering. In comparison, the annular geometry of the ADF detector largely eliminates the low-angle scattering, and instead, the image contrast is dominated by Z contrast, which is ultimately the origin of the diffuse scattering in the ADF images. Another advantage of deriving a correlograph from the ADF image is that the scale and direction of the correlation vectors exactly match the scale and direction of the features in the image that produce the correlations. These vectors can then be directly translated onto the image, identifying positive and negative correlations without the need for calibrating the scale and rotation. The correlograph correlations are most easily identified by translating the correlation vectors onto the Bragg-filtered images, but these necessarily correspond to lattice sites, which can be identified in the unfiltered raw data.

7.4.2 Octahedral Cluster

Previously, it was discussed that electron diffraction cannot distinguish the composition of the clusters, whereas the atomic number sensitivity in HAADF STEM can give an indication of the local compositional arrangements by the relative intensity of neighbouring

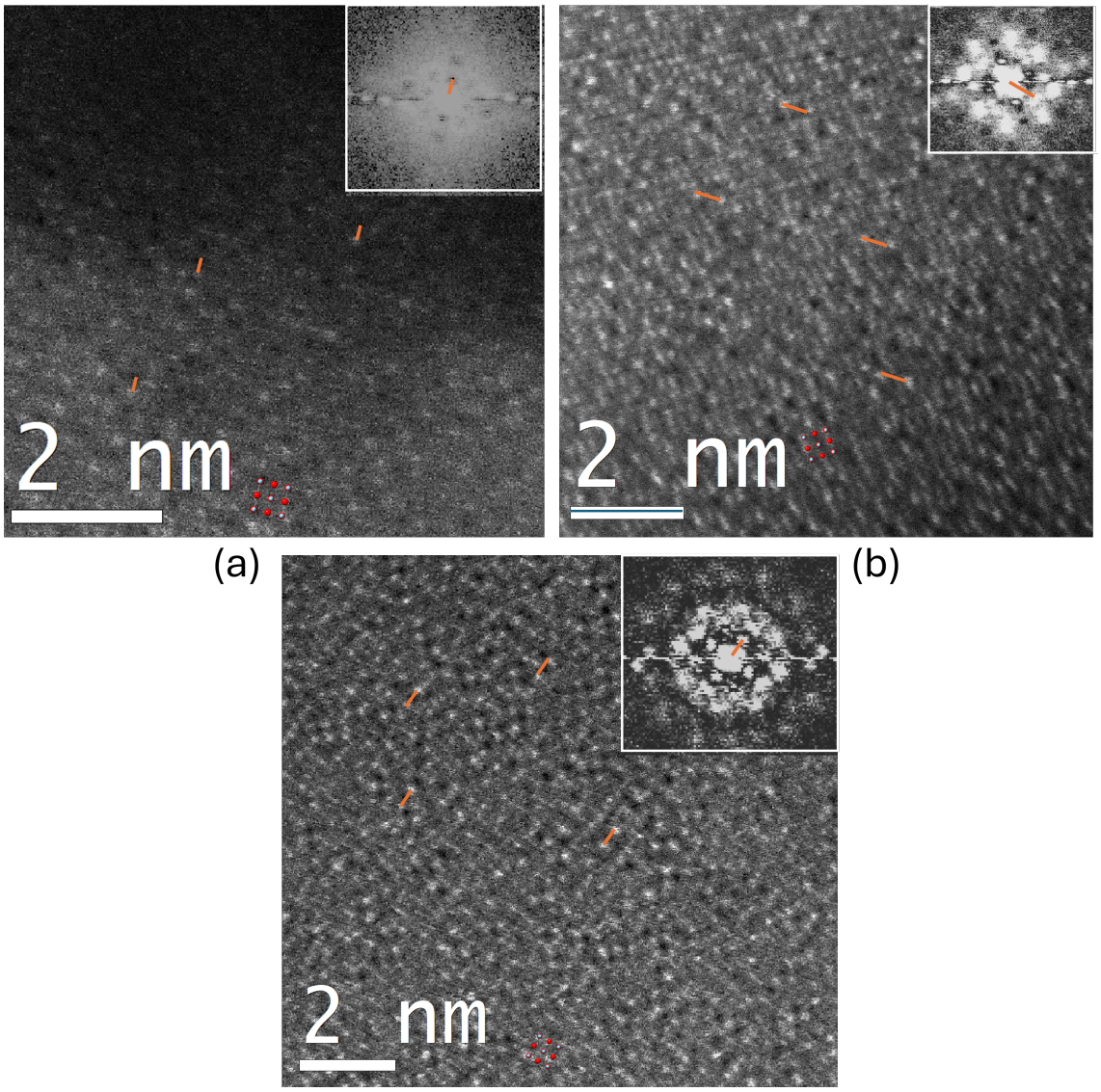


Figure 7.16: Selected regions of the Bragg filtered images with the central region of each correlograph inset in the corner of each image. In **a**) the image of LMTO, a single negative correlation vector is indicated in the correlograph by an orange line and translated onto regions of the image where this correlation can be observed. In each of figures **b**) LMNO and **c**) LMZO example of a single positive correlation vector is indicated in the same way. Schematics close to the scale bar illustrate a single unit-cell dimension on each image.

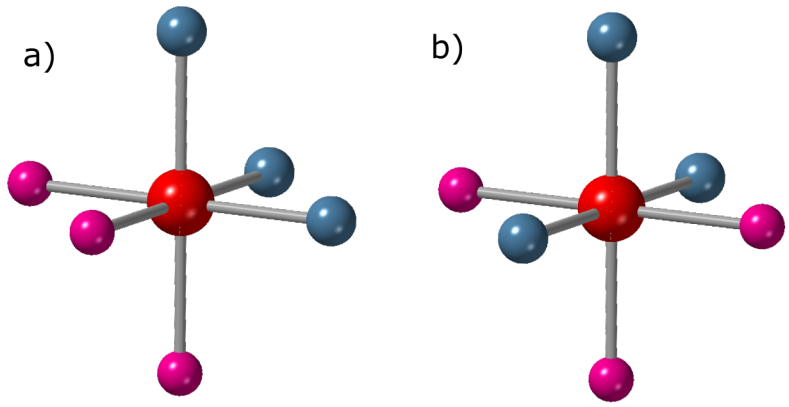


Figure 7.17: Schematic illustration of two octahedra geometries based around a single anion **a**) fac - geometry **b**) mer- geometry.

atomic columns. In the following analysis, the cation species are categorised only as transition metals or lithium, which will have a much larger Z contrast than differentiating the transition metal species. In general, the important aspect of the ordering for the lithium migration is the number of transition metals surrounding the tetrahedral interstitial; the transition metal type is not considered as influential [60].

A defining feature of the filtered <110> images is the bright and dark pairs, particularly in the case of the Ta sample where the spatial extent of the order is greatest, resulting in the ordered regions having clearly distinguishable layers of bright transition metals and dark layers with light lithium atoms. In the samples where the SAED indicates that the dominant cluster type is octahedral, i.e. Ti, Nb, and Ta samples, it is possible to link a specific octahedral arrangement with the imaging evidence for a layered-type arrangement of transition metals and lithium. Considering a single octahedral unit with three transition metals and three lithium ions, two geometries of the transition metals and lithium arrangement can be conceived. In one case, all of the transition metals are arranged on one face of the octahedron and lithium on the other; in the other case, the transition metals are arranged across the centre of the octahedra; these arrangements are demonstrated for a single octahedral unit with an anion at the centre (shown in red) in Figure 7.17. In the context of stereoisomers, these two geometries are commonly referred to as ”fac”, meaning facial, and ”mer”, meaning meridional, isomers- where ligands of the same type are located on the same face or across the meridian of the octahedra respectively.

In section 4.3.2, the Z contrast nature of ADF imaging in the context of DRSs refers to the columns containing more transition metals being brighter than those with more lithium. Figure 7.18 compares the expected intensity of both octahedral cluster arrangements as a

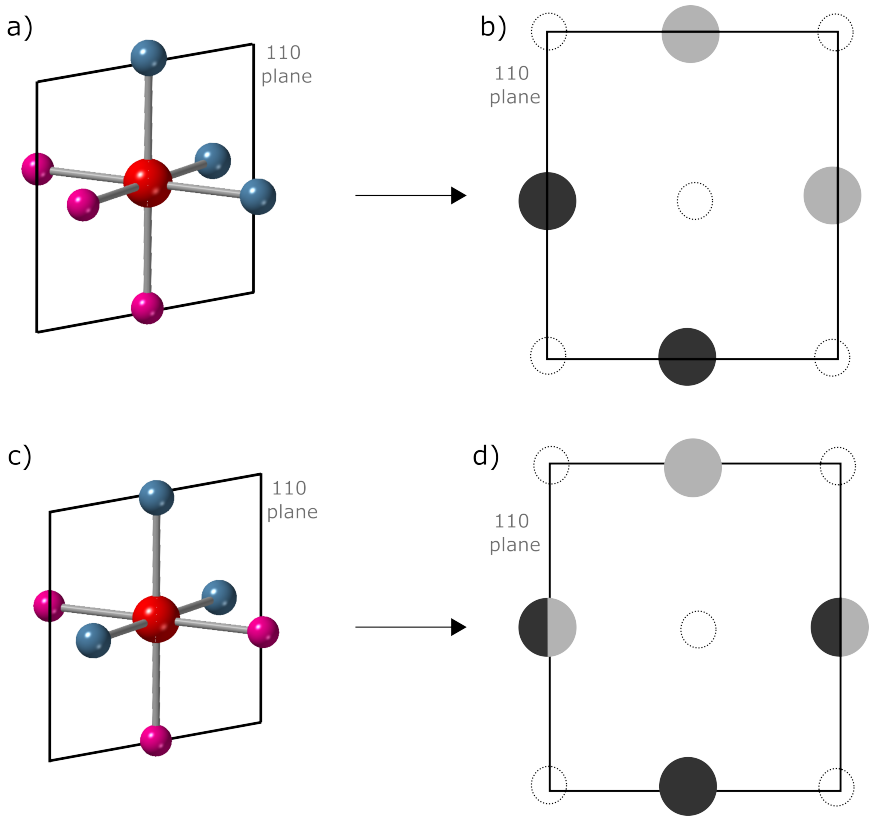


Figure 7.18: **a**) Schematic showing the fac octahedral geometry with the <110> plane of an fcc lattice indicated and **b**) the corresponding ADF intensity in the <110> projection. **c**) Schematic showing the mer octahedral geometry with the <110> plane of an fcc lattice indicated and **d**) the corresponding ADF intensity in the <110> projection. In the ADF projection schematics, anions are shown as unfilled circles with dashed outlines. The projection of columns with only lithium are shown as dark circles, the projection of transition metal columns is shown as light grey filled circles and mixed columns are shown as representative split circles.

projection of each arrangement in the <110> orientation. The fac geometry isomer results in bright and dark pairs along the $[\bar{1}10]$ reciprocal lattice vector, as shown in Figure 7.18.**a**. These bright columns correspond to the projection of two transition metal species, and the dark column to the projection of two lithium atoms. In contrast, the same projection of the mer geometry octahedral cluster gives a combination of a mixed columns along the $[\bar{1}10]$ vector, which does not give well-defined bright and dark neighbouring columns in the <110> projection.

Relationship to Long Range Order

Figure 7.19 shows a series of lithium and transition metal-based oxides based on the rock-salt lattice structure. The cation arrangements can be broken down into smaller units, similar to the clusters we refer to as SRO. Octahedral polyhedra within each structure are shown to be connected by bold lines. The octahedral cluster identified in Figure 7.19.**a**

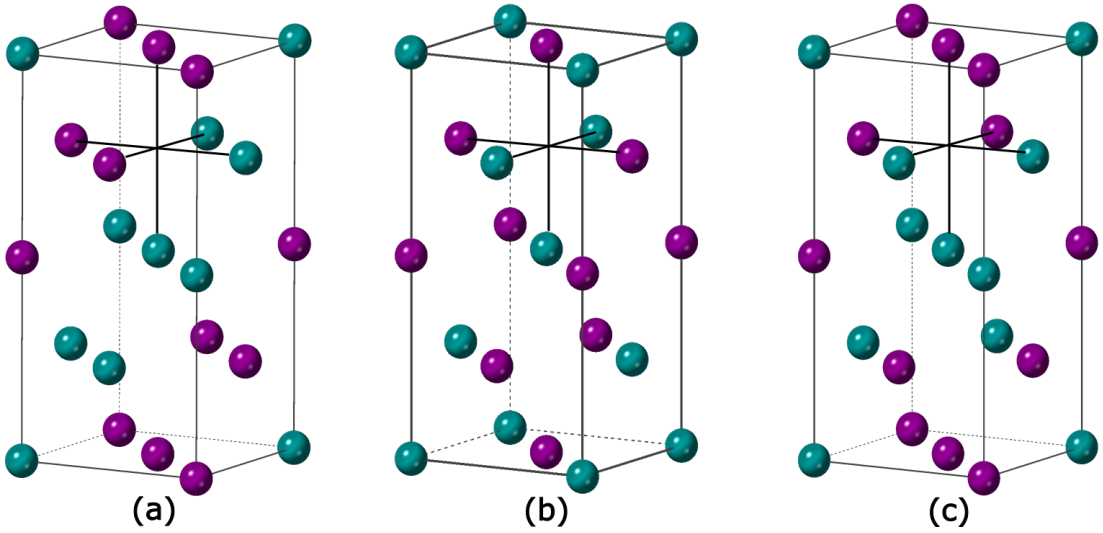


Figure 7.19: Schematic illustration of lithium metal oxide structure based on a rocksalt type lattice. Anions have been removed for clarity but occupy all octahedral sites between cations. **a**) layered structure **b**) spinel-like structure **c**) has a typical $\gamma-LiFeO_2$ structure. The connection between a single octahedral unit is highlighted in bold in each case.

has a fac - geometry and is typical of the octahedra in layered cathodes, which results in the separation of the lithium and transition metals along channels where the lithium can percolate.

The cation ordered form of $\gamma-LiFeO_2$ has a tetragonal structure with the space group $I4_1/amd$ and only contains the meridional geometry octahedral units around the oxygen anions [251]. The meridional geometry octahedral arrangement has been connected with poor electrochemical performance due to the prevalence of 2-TM channels, which do not allow lithium percolation [60]. The only previously reported study which investigates the composition arrangement for octahedral clusters is based on $Li_{1.25}Mn_{0.5}Nb_{0.25}O_2$ which is very similar to the composition of Nb sample in this study ($Li_{1.2}Mn_{0.6}Nb_{0.2}O_2$) [33]. Based on a combination of X-ray and neutron studies, Jones et al. propose that isolated octahedra within the structure have a meridional geometry. The study goes on to justify decreasing electrochemical performance with an increased correlation length of this type of order based on the increase in 2-TM channels in the more ordered sample [33]. While these results are concurrent in their own right, the evidence in the ADF images presented here suggests that the octahedra have a fac geometry.

The analysis of the octahedral clusters makes the assumption that the correlated octahedra have a 1:1 ratio of lithium to transition metals, whereas the bulk composition ratio is 3:2, which is impossible to achieve within a single octahedral unit. It is statistically likely that the ordering will tend towards bulk composition, especially as the extent of the SRO is greater. However, octahedral clusters consist of correlations only within the first and

second nearest neighbours. The correlographs of the Ti, Nb and Ta indicate that the correlations only extend over first and second nearest neighbour coordination environments. This leads to the definition of the SRO as disperse, defined as, ordered domains of a within a disordered matrix of a different composition.

7.4.3 Further Discussion LMZO

As previously noted, the Zr sample does not fit in with the above explanation of octahedral clusters. The wider literature contains one report of SAED on the exact composition used in this study, the authors, make reference to the de Ridder model to suggest that the SRO is based on tetrahedral clusters [38]. As mentioned previously, the diffuse scattering in this study has subtle differences when compared to the study by Ji et al. Nonetheless, the SAED diffuse intensity and the FT of ADF images are consistent with each other in at least two crystallographic directions. The fact that the FT of the ADF, as in the other examples, reproduces the diffuse scattering suggests that the correlations can also be related to the intensity variations, which themselves originate from specific arrangements of lithium and transition metals.

The diffuse scattering results for the Zr can't be explained by a single polyhedra cluster, nor do any linear combinations of polyhedra equations which were attempted accurately produce the diffuse scattering. The relatively simple polyhedra considered in this cluster model correspond to one first and second nearest neighbour correlations, whereas the correlographs presented in Section 7.4.1 show that the correlations in the Zr sample extend up to at least the fourth nearest neighbour. In theory, there is no limit to the size or complexity of the polyhedral units which can be derived in this way, but this would be more efficiently carried out as part of an explorative modelling study which could efficiently fit many parameters and is not within the scope of this study. In addition, the diffuse scattering in the Zr sample has significant intensity variation along the contours of the diffuse scattering, which is impossible to explain using the de Ridder model. Instead, the localisation of the intensity along these contours can be thought of as an increase in the correlation length of the SRO, which is further evidenced in the analysis of the correlations in real space. Longer range SRO in itself can be a factor in a material exhibiting poorer lithium percolation as more disordered structures have been shown to have been connectivity of lithium percolation channels [33]. This is concurrent with the electrochemistry results presented in Figure 7.1, which shows that there is less accessible lithium per formula unit in the LMZO, than the other compositions.

7.5 Limitations of this Study

A limitation of the discussion thus far which must be considered is the broad reference to the ordering being based on the arrangement of transition metals relative to lithium. The independent variable in this study is the secondary d^0 metal in the composition; the elements used are listed in Table 7.1. Several possible ordering schemes can be foreseen: Mn ordering, d^0 metal ordering, or a combination of both. In the case of Mn and Ti, these have very similar atomic numbers and are therefore indistinguishable in the ADF images. In the other cases where the d^0 metal has a significantly higher atomic number than Mn, the contrast may be expected to be stronger from these elements. However, even in the ADF images, the disordered nature of the atomic columns means that it would be impossible by standard atom counting methods to determine which atoms are in each column. Simulation matching would be impossible due to the huge number of combinations possible.

It is also relevant that studying the SRO in this way does not provide direct evidence for the reasons which influence the nature of the SRO. There are several factors which can lower the overall energy to balance the entropy increase from forming SRO, for example, if a particular cluster of ions achieves local electron-neutrality [33], or if a specific arrangement forms a precursor to a structure which has much lower structural energy [10]. The reason that the Zr sample does not follow the general trend of the other results remains unclear from this study. The d^0 transition metals in this study data in Table 7.1 similar to Ti, Zr has a 4+ valence state but has a larger ionic radius.

7.6 Conculsions

In this chapter, evidence has been presented indicating the similarities and subtle differences in the SRO of LMTO, LMTaO, and LMNO, as well as the uniqueness of the SRO in LMZO. The general shape of the structure in the diffuse scattering can be understood by considering the correlations on the geometrical units which can make up the FCC lattice form allowed scattering shapes corresponding to the intersection of the allowed scattering surfaces with the reciprocal lattice planes. Correlations relating to more than one geometric cluster can be combined to form different scattering surfaces. These can allow subtle differences in the structured diffuse scattering to be analysed.

A method is then presented to relate the intensity variations in ADF images to the diffuse scattering, allowing spatial features, such as the clustering of ordered regions in LMTaO, to be observed. Further analysis is provided in terms of the interpretation of the correlations and compositional arrangements of the clusters in real space. Overall, the character of the SRO can be characterised as disperse SRO, which, in the case of the Ti, Nb and Ta

samples, is based primarily on octahedral units of a fac geometry with correlations mainly extending to first and second nearest neighbours. A more extensive study is required to accurately analyse the nature of the SRO in LMZO. However, it can be determined from the presence of the diffuse scattering in ADF images that the SRO is related to correlations between Li and transition metal. From the correlographs, it is found that these correlations extend over longer length scales and are more complex than in the other samples.

Chapter 8

Case Study: Imaging and 4D-Diffraction Investigation of $LiMnO_2$

In this Chapter, a series of experiments combining imaging and nanobeam electron diffraction to investigate the disordered rocksalt compound $LiMnO_2$ are presented. The synthesis of $LiMnO_2$ and electrochemical cycling of the samples was carried out by Liquan Pi. Samples after cycling were obtained by ex-situ cycling and removing some cathode powder from the deconstructed cell.

8.1 Introduction

For two reasons, a cathode containing only lithium, manganese, and oxygen would be highly desirable. The first is that it contains no rare or expensive transition metal, such as cobalt. The second reason is that Mn is a relatively light transition metal, and the composition does not contain any other electrochemically inactive transition metals, which add weight with no corresponding increase in capacity, resulting in a high specific capacity per unit mass. Motivated by these reasons, a spectrum of materials with the composition Li, Mn and O have been studied throughout the development of Li-ion batteries [62, 252–257]. Some of the crystal structures of lithium manganese oxides are presented in Figure 8.1.

Of the lithium manganese oxides investigated, several, such as o−$LiMnO_2$ and $LiMn_2O_4$ have been shown to achieve high capacities as Li-ion battery cathodes. However, the layered phase tends to transform into a spinel structure after the composition is altered by delithiation [258, 259]. The Li-rich phases also exhibit large voltage hysteresis after the first cycle due to O-redox processes; this is thought to be a result of a combination of irreversible anion redox and Mn dissolution into the electrolyte [260, 261]. In general, the entropically stable DRS structure is thought to inhibit many structural changes known to occur in more ordered phases, but this remains a subject of investigation.

The structures in Figure 8.1.**c** and 8.1.**d** are thermodynamically stable orthorhombic and monoclinic layered rocksalt structures, respectively, which are based on the composition $LiMnO_2$. In these structures, the crystallographic direction of the Li and Mn layering dif-

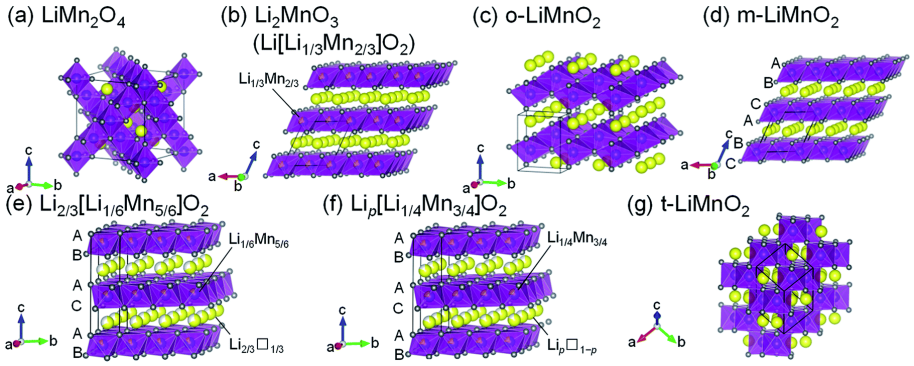


Figure 8.1: Schematics of a series of lithium manganese oxide crystal structures namely: **a**) spinel $LiMn_2O_4$, **b**) Li_2MnO_3, **c**) $o-LiMnO_2$, **d**) $m-LiMnO_2$, **e**) $Li_{2/3}[Li_{1/3}Mn_{5/6}]O_2$, **f**) $Li_p[Li_{1/4}Mn_4/_4]O_2$ and **g**) $t-LiMnO_2$. Lithium atoms are depicted by yellow spheres, manganese by purple spheres, and oxygen by grey spheres. Figure reproduced with permission from RSC [257]

fers; in the orthorhombic serrated layers of Li and Mn occur along the $<010>$ direction. In the monoclinic structure, Mn and Li layers are arranged along the $<111>$ direction, giving a channel structure perpendicular to the *c*-axis of the unit cell. The $o-LiMnO_2$ layered compound was proposed in 1995, at which time it was understood from the analysis of this structure that some intermixing of the Li and Mn cation sites [254]. It was then proposed that the phase transformation from both the $o-LiMnO_2$ and $m-LiMnO_2$ structures to a cubic spinel phase occurs via the formation of a cation disordered site and the phase transform is initiated primarily by defects at the grain boundaries [258]. The DRS phase of this composition is a kinetically metastable phase formed via ball-milling [62].

As discussed in Section 2.3, in general for DRS's, the accessibility of lithium percolation channels is primarily determined by the local ordering on the cation lattice [9]. Despite the existence of SRO being widely documented for compositions containing Mn and d^0, such as those discussed in Chapter 7, to the best of the authors' knowledge, there have been no direct studies of SRO in $LiMnO_2$. One study references the possible presence of SRO on the cation sites but does not provide any elucidating evidence [23].

8.2 SRO in $LiMnO_2$

Synthesis of the DRS phase of $LiMnO_2$ is not compatible with solid-state synthesis methods; instead, it is only accessible by ball-milling processes [23, 262]. The high energy mechanical process of ball-milling means that the crystalline domains are in the region of $5 - 15\,\mathrm{nm}$ as shown in Figure 8.2.**c**. In the samples studied in Chapter 7, the particles were tilted to a specific orientation with respect to the electron beam by centring the poles of the Kikuchi pattern on the phosphor screen. The Kikuchi patterns are not visible for such small grain sizes, making tilting particles to a specific zone axis impossible. Lower

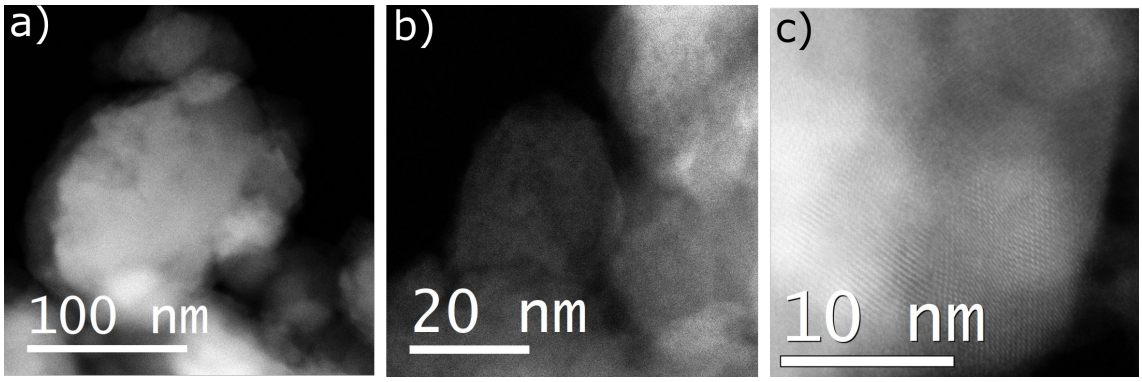


Figure 8.2: a-b) ADF images of $LiMnO_2$ showing mixed particle size and morphology. **c**) ADF image of small crystallite within a particle of $LiMnO_2$ which shows atomic columns tilted close to zone axis.

magnification images in Figure 8.2.**a** and 8.2.**b** show that the particle morphology is also affected by the synthesis with a wide range of particle sizes present and some particles having a fuzzy, textured or porous appearance.

8.2.1 Results

The small grain size makes investigating the SRO via SAED impossible. This is because the apertures available are not small enough to obtain single crystal diffraction patterns; as a result, SAED patterns are averaged over many domains and appear as ring patterns. However, it has been demonstrated in the previous chapter (Section 7.3.2) that the intensity variations in atomic columns which arise as a result of SRO are translated to the Fourier transform of ADF images. Owing to this, atomic resolution ADF images from small crystalline domains, orientated on or close to a low-order zone axis, can be used to identify SRO within $LiMnO_2$. Two such regions are shown in Figure 8.3. The Fourier transform of the image obtained of the $<110>$ projection (Figure 8.3.**b**) shows structured diffuse scattering, as lines between the Bragg peaks. This result is generally consistent with the nature of the diffuse scattering for the compositions containing Ti, Nb and Ta. It is also complemented by the result that the projection for the region in Figure 8.3.**c**, which shows the $<100>$ projection and corresponding Fourier transform shows square-like features between the Bragg peaks.

Based on the cluster model described in Section 7.1.1, the combined observation of the diffuse intensity in the $<100>$ and $<110>$ orientations in Figure 8.3 is compatible with an octahedral-based ordering scheme. None of the other diffuse scattering surfaces based on a single cluster type result in matching intensity in both zone axes. However, since the size of the crystalline regions is relatively small and differences in the column intensities are relatively weak, the intensity of the diffuse scatting translated to the Fourier transform is also weak. This makes it challenging to interpret subtle differences in the diffuse in-

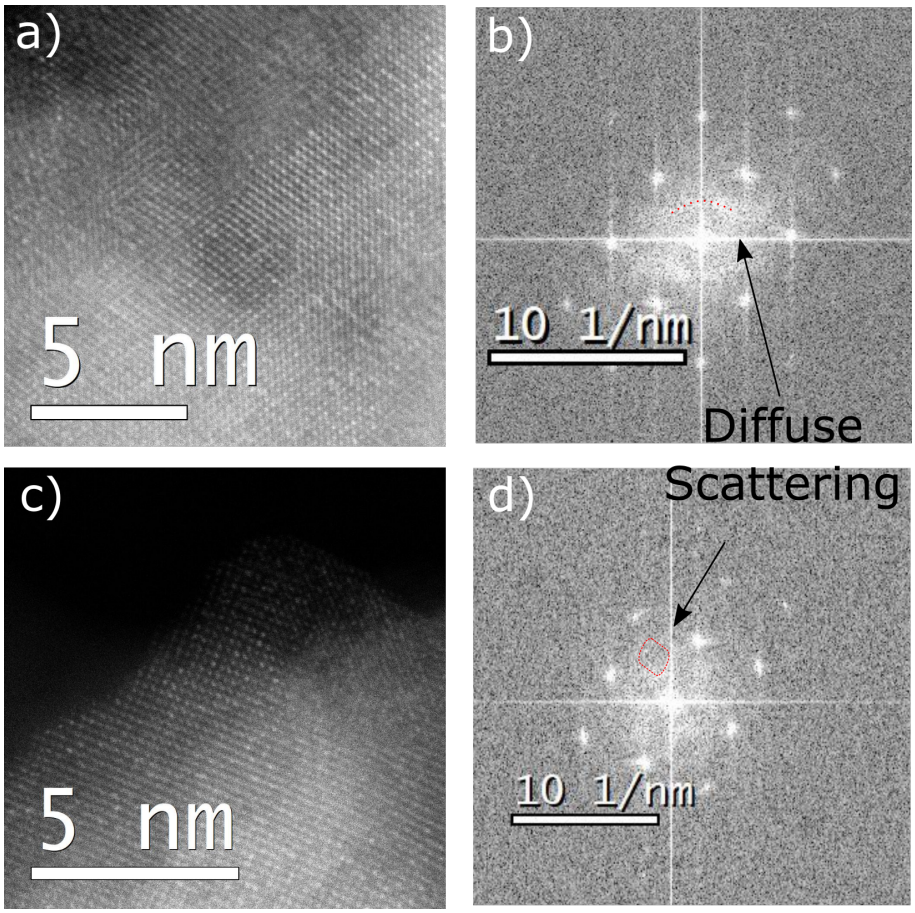


Figure 8.3: **a**) ADF image of crystalline domain in $LiMnO_2$ particle tilted along the <110> orientation and **b**) the corresponding FFT showing Bragg peak and structured diffuse scattering. **c**) ADF of crystalline domain in $LiMnO_2$ particle tilted along the <100> orientation and **d**) the corresponding FFT showing Bragg peak and structured diffuse scattering. Diffuse scattering from SRO is indicated in **b** and **d** by red dashed lines.

tensity shape, such as the more square features observed in the <100> orientation when a contribution from the cubic cluster is added, as was previously shown in Figure 7.4. It is, therefore, feasible that there is a contribution to the scattering surface from other cluster types, giving a slightly altered shape that is not easily identifiable in either Figure 8.3 or 8.4. However, the octahedral cluster type appears to be the dominant cluster type in determining the diffuse intensity. Additionally, unlike in the analysis of the compositions containing d^0 transition metals alongside Mn, the Z contrast nature of the ADF images can only be a result of ordering arrangements between Li and Mn.

The Bragg filtering procedure described in Section 7.3.2 can also be performed on these images, as demonstrated in Figure 8.4. Where the nanodomain is at the edge of the particle, such as in Figure 8.4.**b**, an expanded view of Figure 8.4.**a**, the intensity variations arising from the SRO can be observed. However, where the on-axis nanodomains are not at the edge of the particle, they tend to have other nanodomains overlapping in projection. As observed in Figures 8.4.**d** and 8.4.**e**, this makes visualising the intensity variation in the

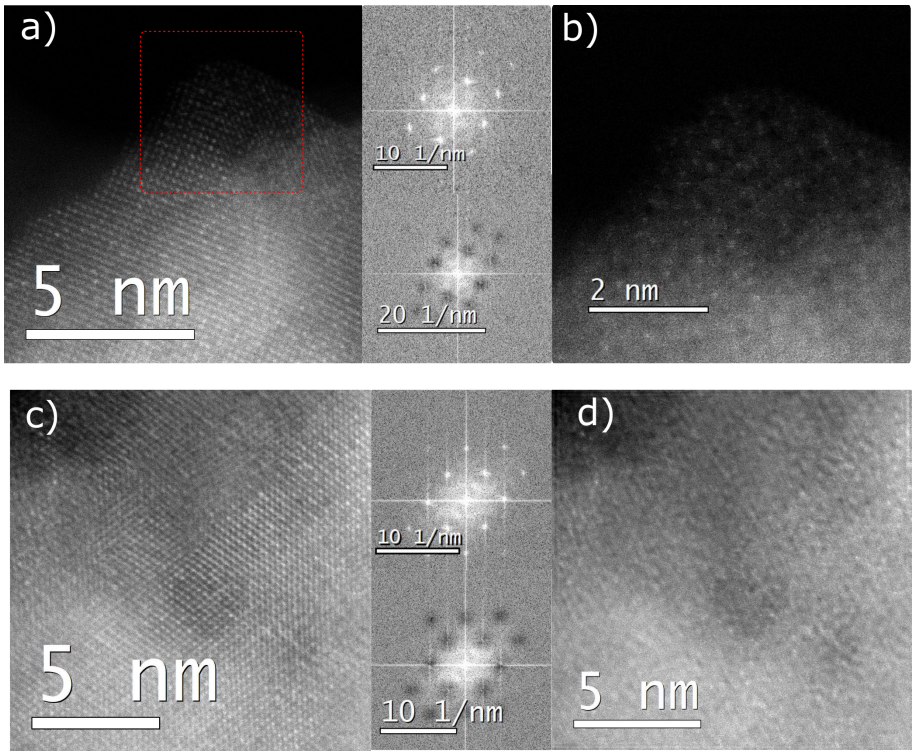


Figure 8.4: ADF images of LMO in **a**) < 100 > orientation and **b**) an extract of the respective Bragg Filtered image. **c**) < 110 > orientation ADF image and **d**) the Bragg-filtered image.

Bragg-filtered image challenging.

8.3 Ball-Milling Rates Study

In the previous chapter (Chapter 7), a link was established between the composition, its influence on the SRO and the electrochemical performance of the material. Several studies have shown both for DRSs and other materials that synthesis conditions play an important role in influencing the nature of the SRO [263]. For example, the cooling rate has been shown to influence the extent of the SRO half-heusler compounds, which impacts their properties as thermoelectric materials [44]. Having established that SRO exists on the cation lattice within the small crystalline domains, it was found that changing the ball-milling conditions impacts the electrochemical performance. Figure 8.5 shows that the lowest ball-milling rate ($500\,\mathrm{rpm}$ - yellow) gives better capacity and higher ratio of accessible lithium than the highest ball-milling rate ($900\,\mathrm{rpm}$ - orange).

8.3.1 Results

Given the previous demonstration of the SRO via ADF images, the same method was used to investigate whether differences in the SRO are induced via different ball-milling conditions and could, therefore, be linked to the differences in performance. Figure 8.6 shows

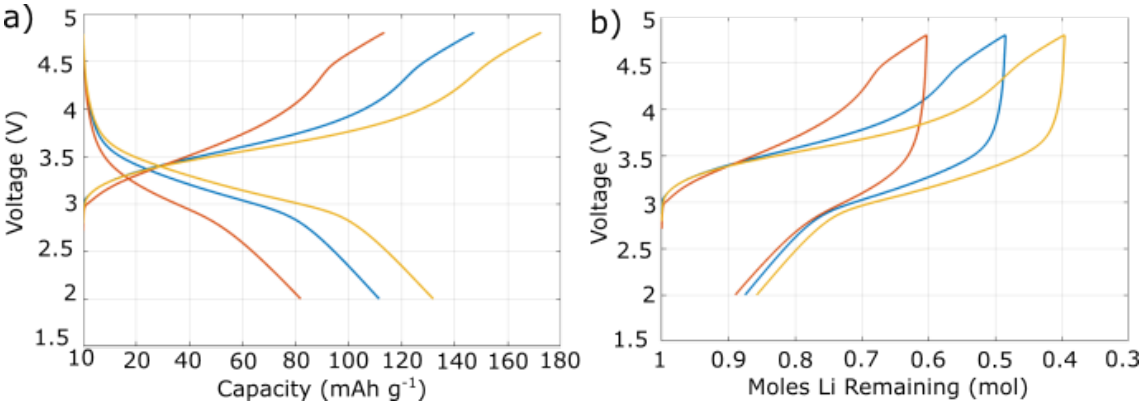


Figure 8.5: **a**) 1st cycle charging curve, voltage vs capacity. **b**) Plot of voltage and calculated ratio of lithium extraction on the first cycle charge and discharge. In both plots ball-milling rates of 500 rpm - yellow, 650 rpm - blue and 900 rpm - orange are shown. *L*iquan Pi collected Electrochemical data displayed.

ADF images from samples ball-milled at 900 rpm, the upper two images and 500 rpm, the lower two images. In both cases, there was a high degree of variability in data acquired from different particles within a given sample and even from different regions within the same particle. It was, therefore, difficult to establish whether the crystalline domains' nature was different due to different ball-milling conditions. The images in Figure 8.6 demonstrate this variability as both 8.6.**a** and 8.6.**c** acquired from samples ball-milled at 500 rpm and 900 rpm respectively show crystalline domains with very well defined edges and little amporphisation. In comparison, both 8.6.**b** and 8.6.**d**, also acquired from samples ball-milled at 500 rpm and 900 rpm respectively show regions which have a low degree of crystallinity and show a high level of amorphisation and vacancies, particularly in the surface region.

The random nature of ball-milling means that some particles within a given sample are very small, with significant surface amorphisation. At the same time, other particles that show very little change from the type of single crystal particles observed in the solid-state thermally synthesised samples could also be found. Since ball-milling is a critical step in the synthesis of $LiMnO_2$, it is possible that small amounts of precursor or impurity phases could remain and affect the subsequent electrochemical results. It is therefore only possible to conclude from the investigation that the highly localised nature of ADF imaging means that it is not the ideal technique to study materials with significant morphological variability.

8.4 Cycling Induced Changes in $LiMnO_2$

A further area of interest is the structural changes which $LiMnO_2$ undergoes upon cycling the material. The conclusion of the ball-milling study is that the information obtained

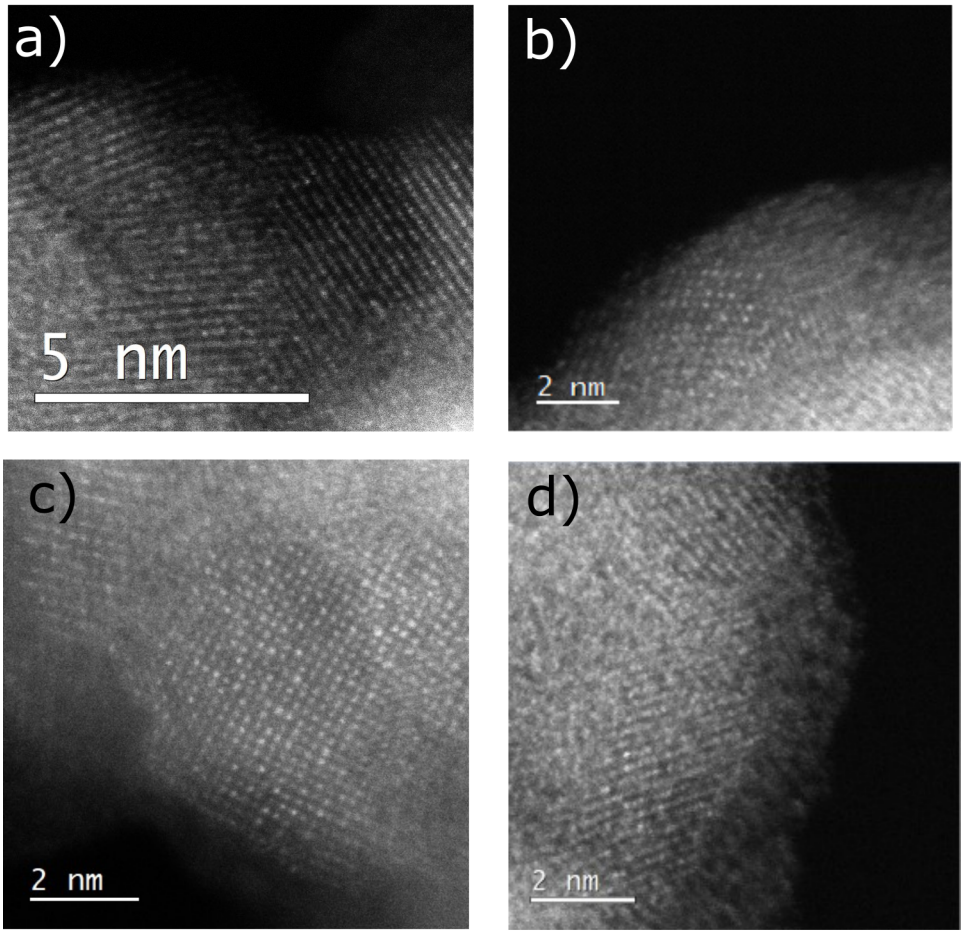


Figure 8.6: ADF images of ball-milled $LiMnO_2$. **a** and **b**) were acquired from a sample ball-milled at $900\,\mathrm{rpm}$. **c** and **d**) were acquired from a sample ball-milled at $500\,\mathrm{rpm}$.

from ADF was too localised and variable; this necessitates that further work is based on an understanding of the structure over a larger field of view. For this reason, NBED was the primary imaging method used to characterise $LiMnO_2$ in its pristine form and following ex-situ cycling of 1 and 8 cycles. NBED can provide diffraction information from local regions, limited by the interaction volume of the probe with the sample; the field of view is also highly tunable by the choice of step size and number of probe positions. A detailed description of the imaging conditions is given in Section 4.4.6, and a description of setting up this configuration in the microscope is provided in Section 5.3.4.

8.4.1 Results

Prior to conducting the study using NBED, samples were images using HRTEM to establish whether there was any change in the general domain structure and particle morphology after cycling. Figure 8.7, shows HRTEM images of pristine, 1-cycle discharge and 8-cycle discharged $LiMnO_2$ with the respective Fourier transforms of the images below. The primary observation from these images is that the general rocksalt structure with crystalline domains in the region of $5 - 15\,\mathrm{nm}$ is retained after cycling. The Fourier transforms of all of the images show ring features at the spacing of the allowed rocksalt reflections of $<111>$, $<200>$ and $<220>$ reflections annotated in Figure 8.7.**d**. In addition, both cycled samples contain a ring corresponding to a lattice spacing around $3.3\,\text{Å}$, in keeping with the interplanar spacing of graphitic carbon [264]. Due to the poor electronic conductivity of DRS cathode, graphitic carbon is always added to the cathode and subsequently exists in the cycled material being imaged as an impurity. Attempts were made to remove the graphitic carbon from the cycled material by dispersing the powder in a solvent, as per typical preparation methods, sonicating to separate agglomerations of particles and then using the centrifuge to separate the particles by mass. However, these attempts were unsuccessful, and some level of graphitic carbon always remained.

A further weak ring can be observed at a spacing corresponding to a lattice spacing of 4.4 Åin the Fourier transform of the 8-cycle sample (Figure 8.7.**f**) indicated by the blue dashed line. This is twice the lattice spacing of the $<111>$ reflection of the rocksalt phase and is thus associated with forming a spinel phase. Due to the very weak nature of this spatial frequency relative to rocksalt reflection compounded with the nanodomain structure, meaning many grains are viewed in projection, identifying regions of the spinel phase in HRTEM images is impossible. To map the spatial distribution of the spinel phase transformation nanobeam electron diffraction was carried out also on pristine, 1-cycle and 8-cycle samples. Figure 8.8 shows how diffraction patterns can be acquired for regions using a scanning probe. Summing these diffraction patterns over many probe positions produces ring diffraction patterns as would be acquired in SAED for a nanodomain structure.

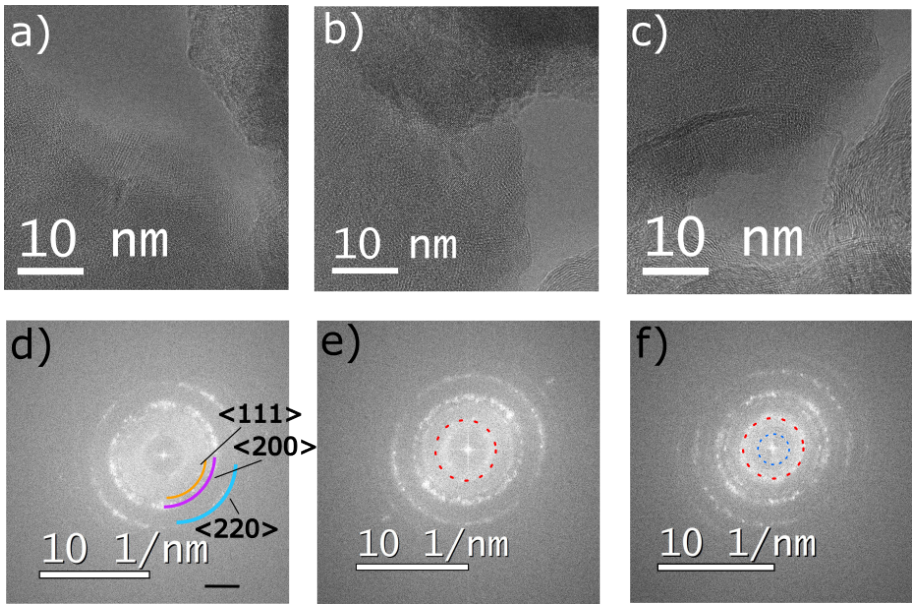


Figure 8.7: HRTEM images of pristine, 1-cycle and 8-cycle $LiMnO_2$. **a**) HRTEM image of pristine $LiMnO_2$ **b**) HRTEM image of discharged $LiMnO_2$ after 1-cycle. **c**) HRTEM image of discharged $LiMnO_2$ after 8-cycles. The Fourier transform of each of the images is given below in **d-f**, respectively. Rocksalt spacings corresponding to the $<111>$ (orange), $<200>$ (pink) and $<220>$ (blue) are annotates in **d**. The Red dashed line indicates the interplanar spacing of graphitic carbon.

Figure 8.9 shows the integrated radial profile of the sum of the diffraction patterns across all probe positions, plotted alongside the maximum diffraction pattern, which takes the maximum signal as each detector pixel across all probe positions. In each radial profile, the direct beam intensity has been blocked, and the rings from the summed diffraction patterns appear as bumps on a gradually decaying background. In Figure 8.9.**a**, the measured peak spacings are slightly higher than the expected peak positions whereas, in 8.9.**b** and 8.9.**c** the peaks appear in the expected locations. It is notable that the dataset in 8.9.**a** was obtained at a different camera length to 8.9.b and 8.9.**c**, and the calibration of the pixel size is reciprocal space is carried out based on a measurement of diffraction patterns from a gold sample with known spacings for a series of different camera lengths. This error is most likely to occur as a result of the method used to calibrate the reciprocal space pixel size, such as a small error in the calibration of the actual camera length of the microscope.

Grey, red, and blue lines indicate the scattering angles of the $<111>$, $<200>$ and $<220>$ respectively. The yellow line indicates the graphitic carbon peak, which is only present in the cycled samples as an impurity. The green line indicates the scattering angle associated with the spinel $<111>$ peak, which is half of the DRS $<111>$ peak since the spinel formation corresponds with a doubling of the lattice parameter. The radial profile of the pristine sample contains a broad bump at just below 0.2 Å, corresponding to ≈ 5 Å, similar to the broad peak in XRD below 25 degrees 2θ Cu Kα which is typically assigned to SRO.

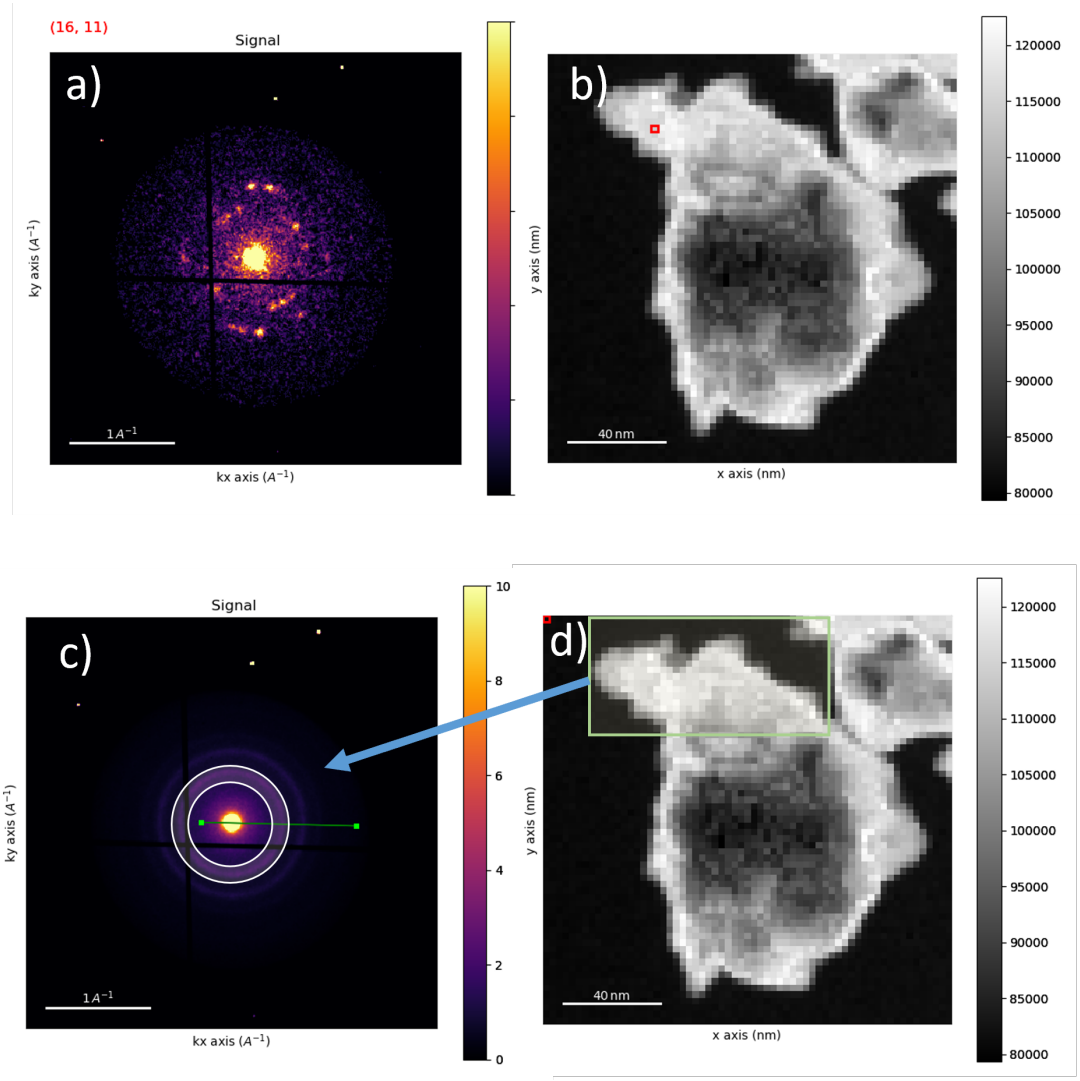


Figure 8.8: **a**) Diffraction pattern from a single probe position acquired in NBED mode. **b**) Virtual-ADF image of the sample, with a red pixel indicating the location of a single diffraction pattern. **c**) The sum of diffraction patterns from all pixels indicated in the green box **d**. Virtual- ADF detector is also shown by a transparent annulus.

This feature is not obvious in the 8-cycle sample; instead, a spinel feature is observed as a plateau of the radial profile intensity decay.

Spatial information can be extracted from NBED data by integrating the intensity at particular spatial frequencies, for each position. Doing so using an annular detector, such as shown in Figure 8.8.**c** produces virtual ADF images. Figure 8.10, shows virtual-ADF images produced by integrating regions as A, B, C, and D corresponding to the broad SRO bump, spinel, graphitic carbon and DRS $<200>$ peak respectively.

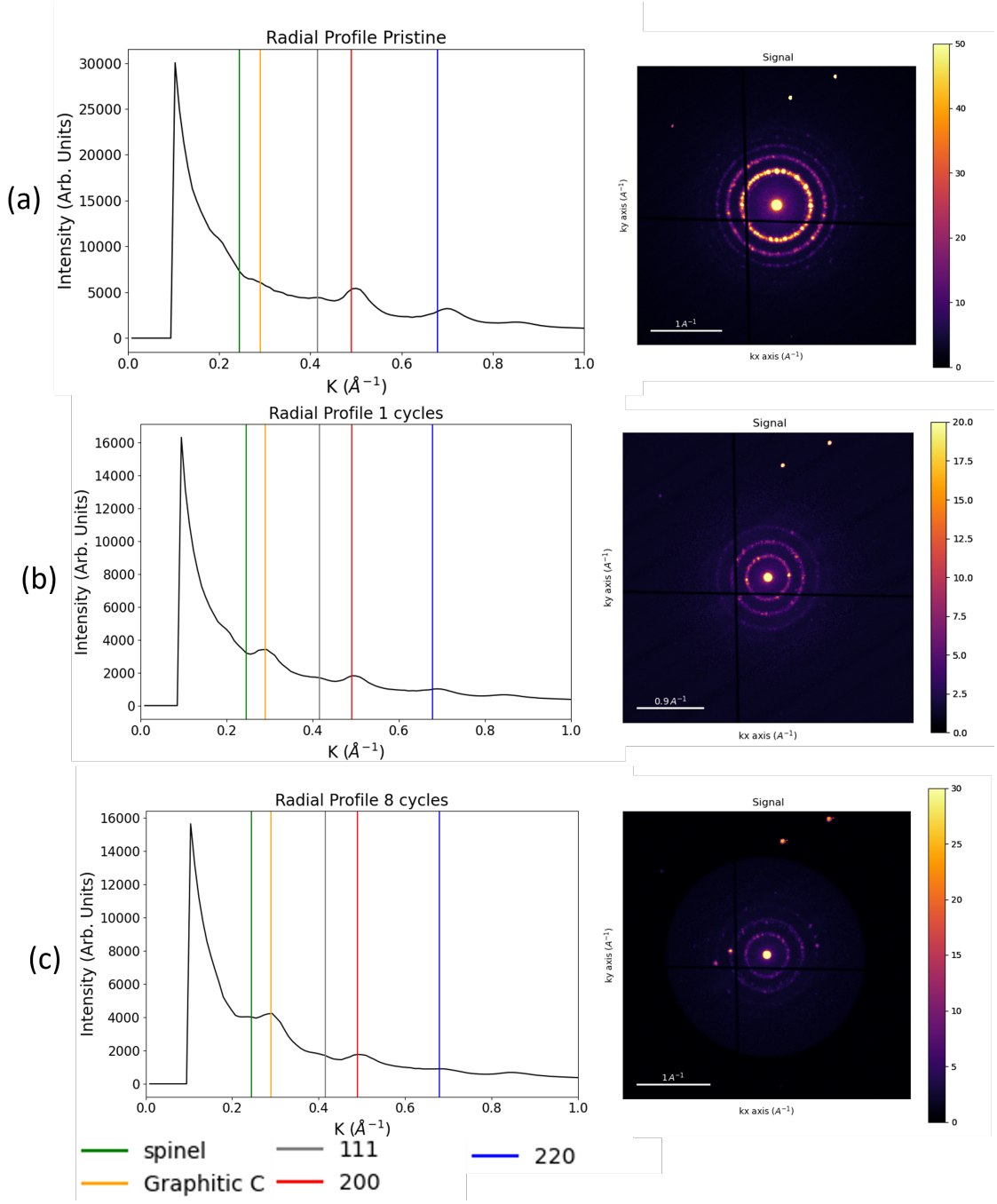


Figure 8.9: Integrated radial profile of summed diffraction patterns from **a**) pristine, **b**) 1 cycle and **c**) 8 cycle datasets. Lines indicate spacing corresponding to spinel <111> peak - green, graphite - yellow, DRS <111> - grey, DRS <200> - red, DRS <220> - blue.

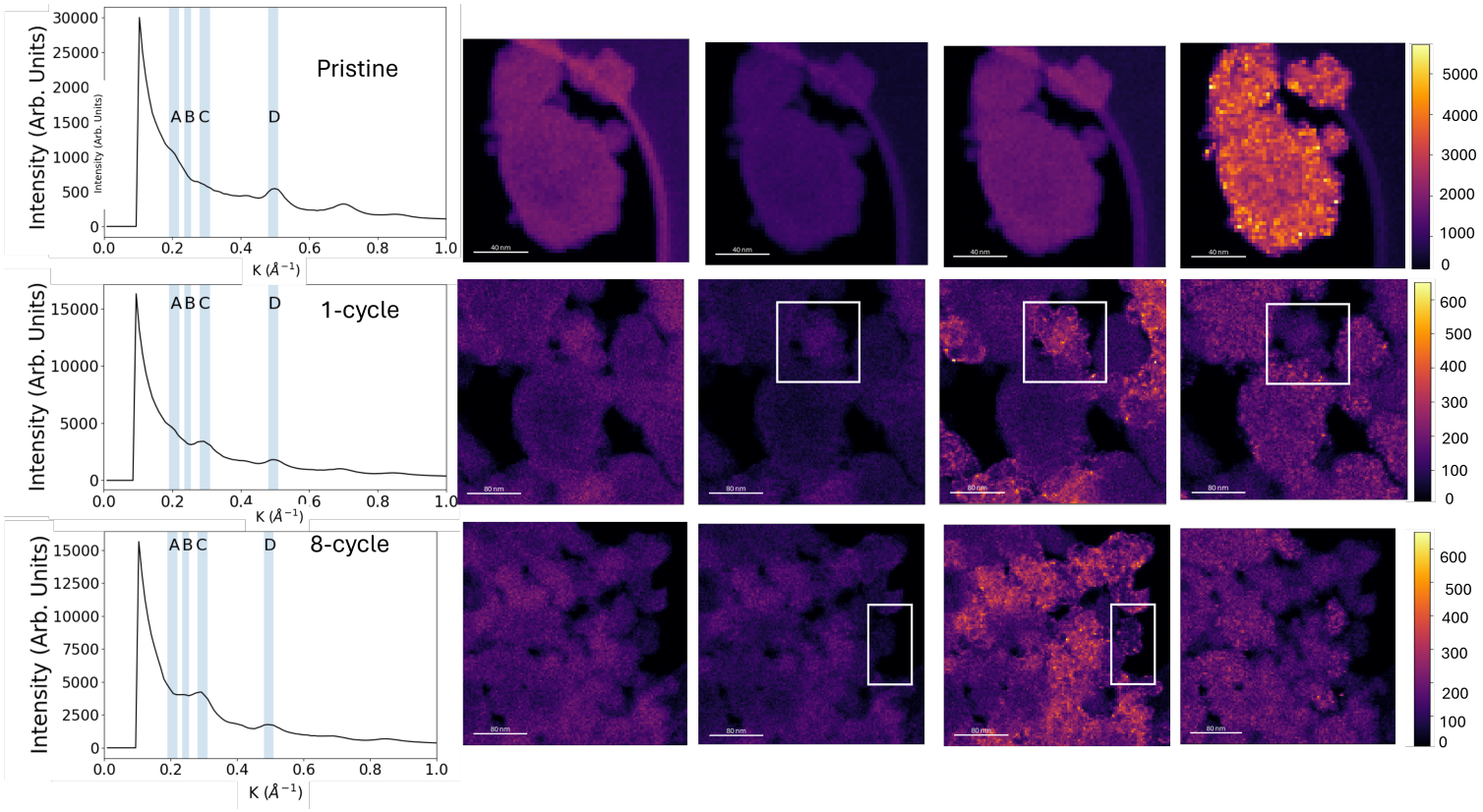


Figure 8.10: Radial profiles for pristine (**top-row**), 1-cycle, (**top-row**) and 8-cycle,(**top-row**) indicating regions A, B, C, and D integrated for virtual-ADF images. The virtual ADF images are shown for the respective regions in adjacent columns to the radial profiles; the real space scale bars are $40\,\mathrm{nm}$ for the pristine dataset and $80\,\mathrm{nm}$. for both the 1-cycle and 8-cycle datasets. The colour scales are self-consistent between the datasets; for each dataset the colour bar is given at the end of each row.

Integrating the signal from the scattering angles associated with SRO, it appears that the SRO is homogeneously distributed in the pristine sample; however, this is not the case in the cycled material in which some particles show brighter than others. As expected, the virtual-ADF images corresponded to the spinel and graphite peaks show weak intensity, attributed to background scattering. In contrast, the virtual-ADF images of the DRS $<200>$ peak has a granular appearance, correlating to the nanodomain structure observed in the HRTEM. Both 1-cycle and 8-cycle samples show small areas of graphitic carbon impurities coating the cathode particles. The presence of carbon in the cycled material is anticipated as the DRS is ball-milled alongside a carbon additive prior to forming the cathode in order to improve the conductivity. Larger particles of graphite were removed by the centrifuge procedure.

Plotting the intensity from the graphitic carbon peak for both samples results in a more granular appearance; however, in most instances, the brightest peaks correspond to regions where the spinel phase is also bright, such as the particle indicated in the 1-cycle data by a white box. However, small regions can also be identified where this is not the case, as in the region identified in the 8-cycle data. Other sources have proposed that the spinel phase, $LiMn_2O_4$, forms during cycling when delithiation causes a reduction in the lithium to manganese ratio closer to the spinel 1:2 ratio, as opposed to the 1:1 ratio in the DRS composition. During cycling, lithium is extracted, and the lithium to manganese ratio is reduced toward that of the spinel, making this phase energetically preferred [62, 253]. Alongside the evidence that the formation of the spinel phase coincides with the presence of the carbon additive, the rationale for the spinel formation indicates preferential delithiation of the particles in regions where the carbon is present due to its role in promoting improved conductivity.

The broad peak attributed to the SRO, region A, diminishes after 1-cycle and is not visible in the 8-cycle radial profile. In the pristine sample, the SRO begins as homogeneous across the particle; from the ADF imaging we also see that regions of SRO occur within regions of 1-2 neighbouring columns, bearing in mind the probe in NBED is in the region of a $1\,\mathrm{nm}$ the homogeneity is unsurprising. In both 1-cycle and 8-cycle data, the intensity from the SRO region and spinel peak are closely correlated [1]. In Section 8.2, the SRO is visualised and identified to be related correlations of octahedral geometry. The cubic spinel-like structure discussed in Chapter 7 (depicted in Figure 7.19.**b**) is associated with a longer range order of octahedral clusters, which would correspond to a sharper peak. However, the stable spinel structure with the composition $LiMn_2O_4$ structure is orthorhombic due

[1] It is also the case that at lower scattering angles, there is more mass-thickness contrast, which may be influencing both images.

to the Jahn-Teller distortion of Mn in its 3+ oxidation state. It is plausible that SRO is a precursor for the formation of the spinel structure, which is formed by its thermodynamic stability when the material is delthiated. In this case, any inhomogeneity in de-lithiation could feasibly be an initiating factor in the formation of the spinel phase in particular regions.

8.5 Conclusions

In this chapter, the first direct visualisation of the SRO in DRS, the SRO is broadly understood to be associated with octahedral clusters. A study of the effect of ball-milling rates in relation to changes in capacity provided inconclusive results on the effect of SRO and particle morphology. However, the inhomogeneity of the particle morphology produced by ball-milling synthesis routes is highlighted. In hindsight, this study would be more appropriately carried out using a technique which affords a wider field of view than HRTEM such as NBED. A study of the cycling changes in $LiMnO_2$ after ex-situ cycling is also carried out, and visualised using NBED methods to map structural changes across entire particles. A correlation is identified between the formation of the spinel phase and the presence of the graphitic carbon, which, based on the change in lithium to manganese ratio, can, in turn, be associated with inhomogeneous delithiation.

Chapter 9

Ptychography Application to Disordered Rocksalt Cathodes

This Chapter details several areas where the application of ptychography can be used to gain insight into some of the outstanding questions in the literature on disordered rocksalt cathodes. Samples were synthesised by Liquan Pi.

9.1 Motivation

Li-rich compositions of DRSs are necessary to allow for effective lithium migration; it also has the effect of enabling anionic redox processes, which are understood to be a major cause of degradation in these materials by inducing structural changes after cycling [9]. A more extensive discussion on reasons that Li-rich compositions are essential and the details of O-redox processes are described in Sections 2.3 and 2.5, respectively.

Ptychography has been widely demonstrated to enable simultaneous imaging of heavy and light atomic species [18, 149]. The majority of the reported work using ptychography on cathode materials has been the analysis of layered cathodes, where ptychography can provide very clear images of the lithium within the channels of the layered structure [18]. Due to the strong atomic number dependence of contrast in ADF images, the anion sublattice of most cathode materials is also not visible in ADF images, and as such, ptychography has become a useful tool for studying the anion lattice [119]. In layered materials, anionic redox processes can initiate the loss of oxygen near the surface and promote under-coordinated transition metals to migrate into alkali metal layers of the structure, thus forming a transition metal dense layer at the surface [13, 17, 172]. Surface reconstruction layers are linked to impeding the reversibility of intercalation and deintercalation of lithium [155]; thus, imaging of the entire structure is vital to providing a full picture of the degradation processes.

The work presented in Chapter 7 focuses on SRO within the cation sublattice. This work was possible because scattering from the light elements, specifically lithium, is overshad-

owed by the contrast from transition metals in these images. However, the contrast from oxygen in the anion sublattice is also very weak. In this chapter, ptychography is used to provide insight into the structural elements of DRS cathodes relating to the light elements in the structure.

9.2 Method

Focused probe ptychography was used to obtain the data presented in this chapter; this allows in-focus ADF and ABF images to be formed by virtual imaging as well as the ptychography reconstruction from a single 4D-dataset. The masks used to specify regions of the detector plane, which are integrated for each probe position to construct the ABF and ADF images, are shown in Figure 9.1. In Figure 9.1.**b**, by masking the intensity of the bright field disk, the intensities of the diffracted beams show some asymmetry, indicating a slight mistilt from the zone axis is present; studies have shown that despite some specimen mistilt, ptychographic reconstruction methods can still result in high-quality reconstructions [265, 266], in comparison, other studies have discussed the highly sensitive nature of ABF imaging to mistilt of the specimen [12]. The robustness of an imaging method to sample mistilt is especially important when imaging beam-sensitive materials, as precise tilting requires additional time when the sample is exposed to the electron beam before obtaining data. The data in this chapter was obtained using the JEM-ARM200CF microscope in the DCCEM, at $200\,\mathrm{kV}$, using a probe semi-convergence angle of $22.5\,\mathrm{mrad}$ with a probe current of $8.93\,\mathrm{pA}$. The only exception to this is the data described in Section 9.4.2 regarding the investigation of $Li_{1.2}Mn_{0.7}Ti_{0.1}O_{1.9}F_{0.1}$, which was obtained at $300\,\mathrm{kV}$ acceleration voltage, using the JEOL JEM-ARM300CF at ePSIC.

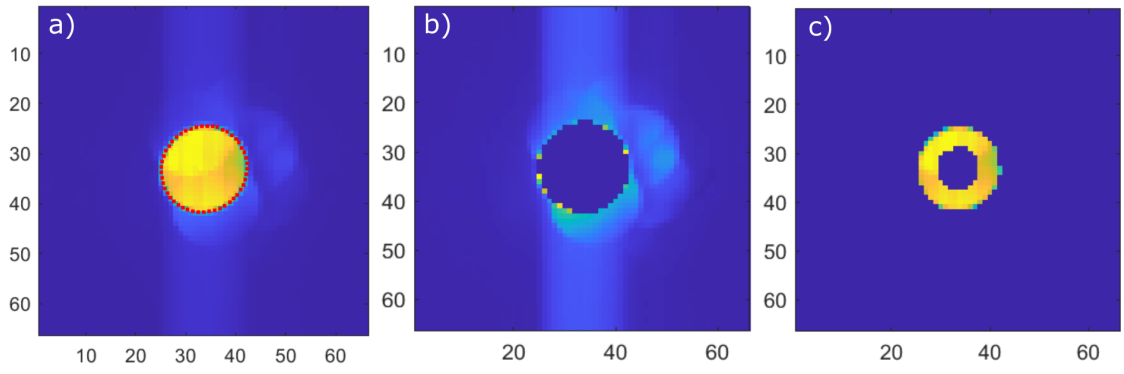


Figure 9.1: Example masks for the formation of virtual images using pixelated detector: **a**) Average CBED across all probe positions, the dashed red line defines the outside of the bright field disk. **b**) The masked region outside the bright field disk, which is used to generate simultaneous ADF image **c**) The masked annulus region within the bright field disk is used to generate ABF images.

9.3 Results and Discussion

In the following sections, three insights are highlighted, each of which can only be achieved by imaging methods that can reveal the light elements' positions (Li and O). These results focus on pristine $Li_{1.2}Mn_{0.4}Ti_{0.4}O_2$; later in the chapter, initial investigations in the fluorinated composition $Li_{1.2}Mn_{0.7}Ti_{0.1}O_{1.9}F_{0.1}$ are also described. The phase reconstructions presented have post-acquisition aberration correction procedures, as described in Section 4.4.5 applied. Examples of the calculated aperture phase surface and probe function applied to SSB and WDD reconstruction methods are given in Appendix E, alongside a comparison of phase reconstruction with and without aberration correction.

9.3.1 Rocksalt Structure

4D-STEM datasets have been used to form the virtual images and reconstruct the phase image for, $Li_{1.2}Mn_{0.4}Ti_{0.4}O_2$, shown in Figure 9.2. The presence of the transition metals means that this sample cannot strictly be considered a weak-phase object, as assumed in the SSB method described in Section 4.4.3. The SSB reconstruction is compared to the WDD reconstruction method, which does not use the WPOA. Both reconstruction methods produce remarkably similar results, showing the anion positions in the expected octahedral sites within the cation FCC lattice. It is notable from the power spectrum image (Figure 9.2.**e**) that the information on the SRO is also present in the phase data in the form of the band of diffuse intensity in the same position as in the ADF and SAED. However, the lack of a simple relationship between atomic number and phase makes it more difficult to interpret this contrast in the image.

It has been proposed that the ordering in DRS materials may lead to the formation of a spinel-like phase on cycling. Several spinel structures involve the presence of lithium in tetrahedral sites within the lattice. Figure 9.3 shows examples of three common spinel-like arrangements of ions in cathode materials; in both the Mn_2O_3 and $LiMn_2O_4$ structures there are occupied tetrahedral sites, whereas in the LT-$LiCoO_2$ structure, all tetrahedral sites are unoccupied. The LT-$LiCoO_2$ structure is often referred to as spinel-like due to the fact that it has a cubic rocksalt-type structure; however, there is cobalt found in what would be the alkali metal layer in layered compounds resulting in a spinel-like symmetry.

The phase reconstructions in Figure 9.2 show that the tetrahedral sites are unoccupied; from this, it is possible to exclude the presence of the spinel structures which have occupied tetrahedral sites in the pristine material. It is impossible to dismiss any local ordering of the LT-$LiCoO_2$ type spinel configuration, which has no occupation of the tetrahedral sites

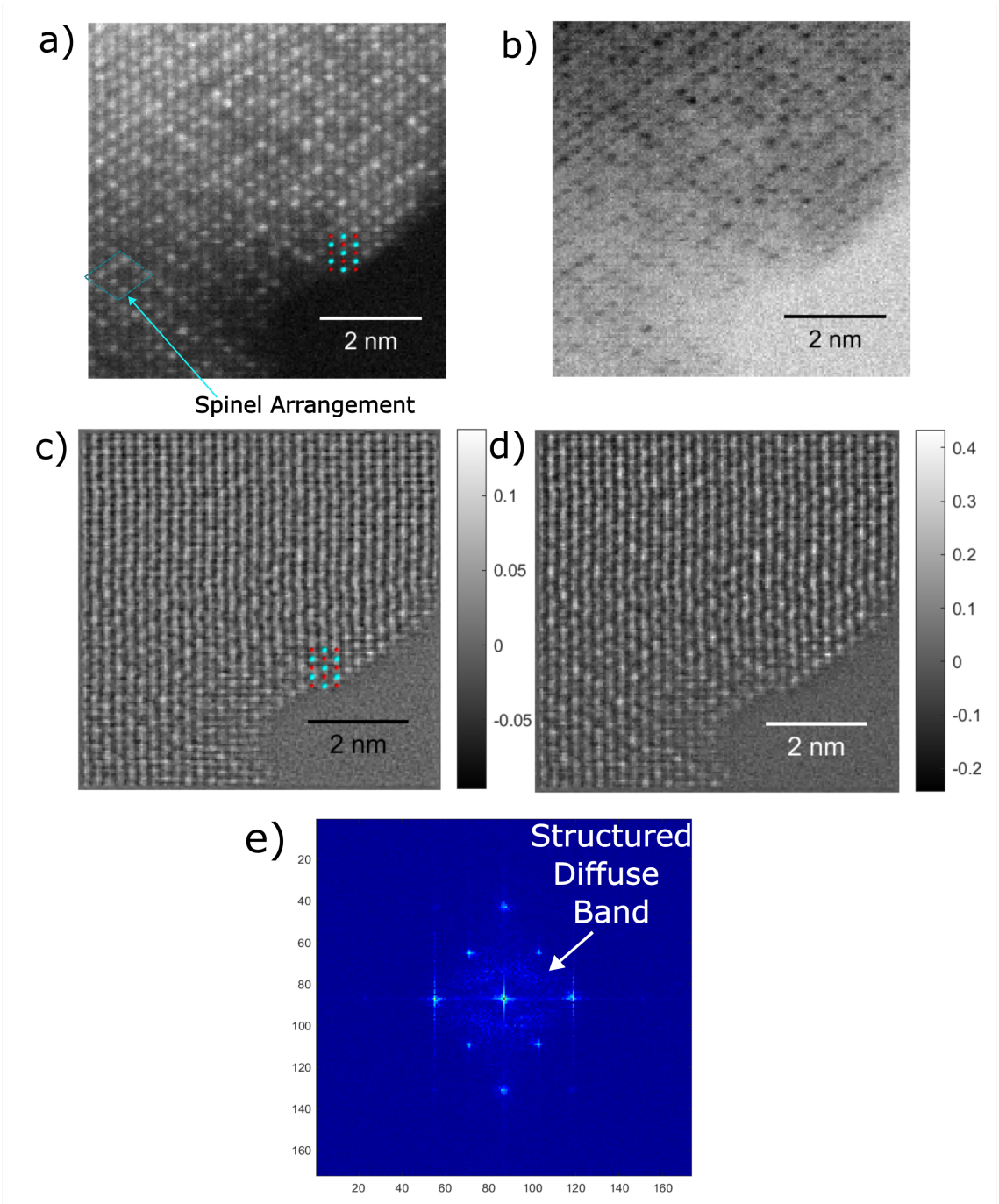


Figure 9.2: Images of $Li_{1.2}Mn_{0.4}Ti_{0.4}O_2$ reconstructed from a single 4D-STEM dataset: **a**) Virtual ADF image. **b**) Virtual ABF image **c**) Aberration-corrected SSB phase reconstruction **d**) Aberration corrected WDD phase reconstruction. **e**) Power spectrum $\sum \mid G(\mathbf{K_f}, \mathbf{Q_p}) \mid^2$, plotted as a function of spatial frequency $\mathbf{Q_p}$. Both **a** and **c** have a rocksalt structure in the <110> projection overlayed with cations indicated by cyan circles and anions by red circles.

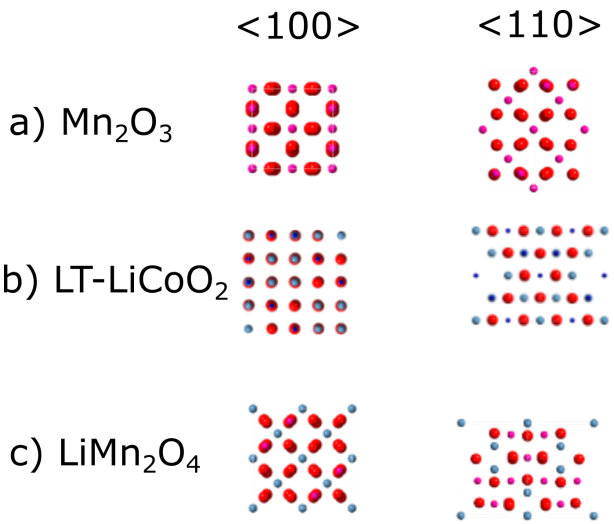


Figure 9.3: Schematics of representative spinel structures of various cathode materials. **a**) Mn_2O_3, manganese - pink and oxygen - red. **b**) Low temperature (LT) $LiCoO_2$, lithium - cyan, cobalt - dark blue, and oxygen - red. **c**) $LiMn_2O_4$, lithium - cyan, manganese- pink and oxygen -red. All structures are shown in both the $<100>$ and $<110>$ projections.

from the phase images alone. Furthermore, the simultaneous ADF image shows evidence of transition metal arrangements which are similar to those in a spinel-like arrangement; one such region is highlighted in Figure 9.2.**a**. However, it should also be considered that polyhedra related to the SRO, particularly octahedral clusters, which are discussed in Section 7.4.2 in terms of their relationship to spinel structures, can result in contrast of this nature but would not necessarily constitute the formation of a true spinel structure.

Although the formation of spinel structures has been widely evidenced after cycling, these cation arrangements are present in the pristine structure for which there is no other evidence of spinel features, such as superlattice peaks in the ED reported in Section 7.2. This suggests that there is no long-range order of the spinel-type structure, and instead, this motif is explained by either local polyhedra correlations related only to the transition metals or highly localised regions of spinel ordering limited to very few unit cells. As this data is based on a projection of mixed atomic columns, three-dimensional information would ultimately be necessary to make this distinction conclusively.

9.3.2 Ptychographic Reconstruction of Surface Facet

Surface stability is a key factor which has been investigated for both layered [21], and DRS cathodes [54] due to the importance of the surface region in allowing lithium percolation. STEM is an ideal technique to enable an atomic-scale insight into the composition of the surface region with a spatial resolution of individual atomic layers. This is demonstrated in Figure 9.4 in which 9.4.**a** shows the ADF image of an edge facet, clearly showing the

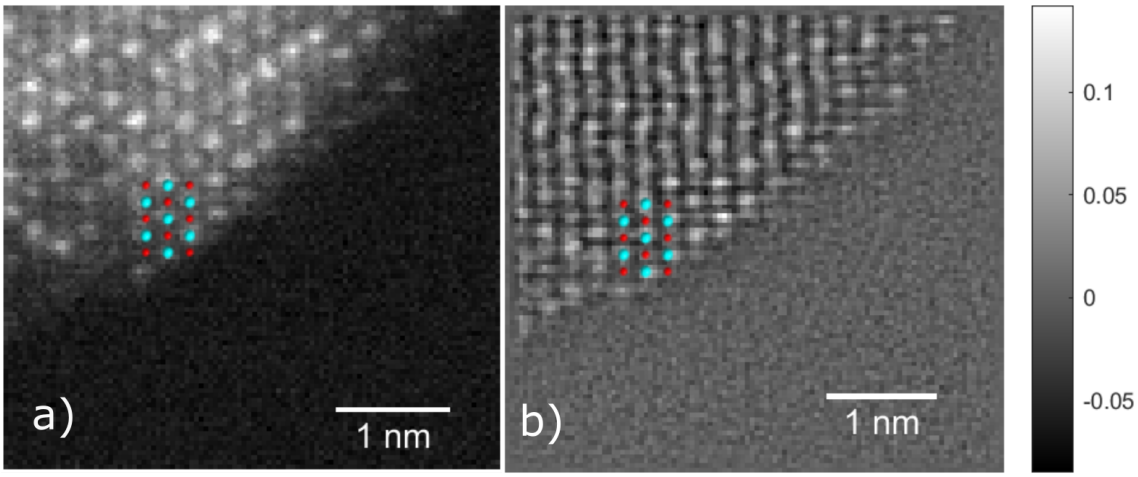


Figure 9.4: Selected region of edge facet from Figure 9.2: **a**) Integrated virtual ADF image **b**) Phase image reconstructed by SSB. In both images a rocksalt structure overlayed with cations displayed in cyan and anions displayed in red.

positions of the cations at the surface edge. However, as has previously been demonstrated, the ADF image is not sensitive to the light elements; analysing the phase image, Figure 9.4.**b** shows a layer of oxygen anions at the termination surface of the facet.

The terminating surface of a crystal can be characterised as polar or non-polar. Assuming equal valence states of the cations and anions, a lattice plane such as the $<100>$ plane, which has an equal number of cations and anions, would have no overall charge and be characterised as non-polar [267]. The surface facet in question is a $<111>$ surface; in a rocksalt lattice, given that the $<111>$ plane consists of either all anions or cations, this is a polar surface. It is generally recognised that non-polar surfaces should have lower surface energy [267]. However, in the case where a $<111>$ plane is present at the surface, it has been noted in studies of other metal oxides that polar surfaces tend to be terminated by a layer of oxygen since it is more readily able to form a strong dipole [268]. It is also possible that any surface terminating in metal cations would readily adsorb any oxygen from the surrounding environment, which goes on to become the terminating surface of the lattice. Since the sample will almost always have been exposed to some level of residual oxygen in the atmosphere, this would be very challenging to rule out [269].

9.3.3 Nanovoids at surface

Ptychographic reconstructions have also revealed that nanovoids, which have previously been reported as a feature of structural changes due to cycling, may also be present in the pristine sample. Referring to ADF images of cycled material, Li et al. have reported that darker regions indicate the presence of nanovoids [54]. Similar features have been observed in the ADF images of pristine materials considered in this study. The imaging of

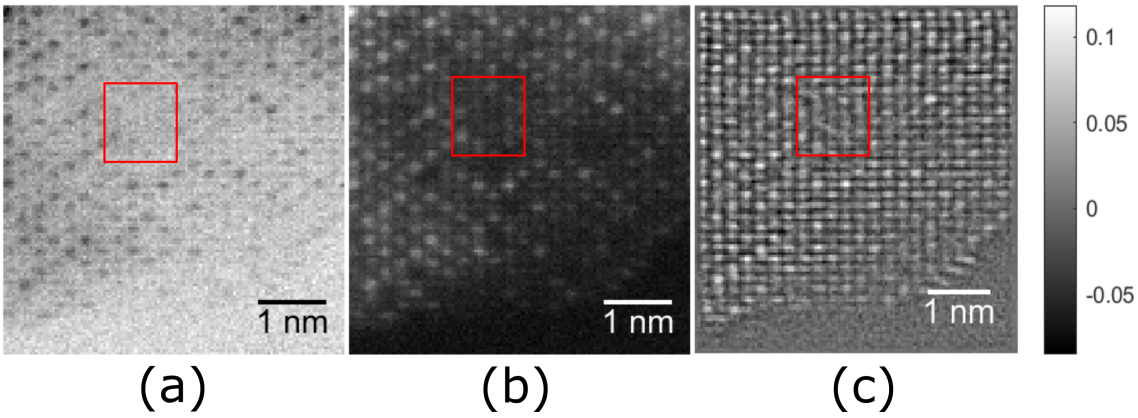


Figure 9.5: Images of defect region, highlighted in red box: **a**) virtual ABF image **b**) virtual ADF images and **c**) SSB phase image.

these samples is carried out across regions which are not homogeneous in sample thickness, meaning that a reduction in intensity could be associated with either fewer heavy elements within a region or a change in particle thickness. Since the contrast in ADF images is sensitive to atomic number and sample thickness, darker regions in ADF images alone are not conclusive evidence of the presence of nanovoids. Since phase images are sensitive to both heavy and light elements, this data can make a much more reliable indication of the presence of nanovoids. Figures 9.5 and 9.6 provide evidence of the nanovoids in two separate regions by simultaneously reconstructing the phase, ABF and ADF images.

Figure 9.5 shows the ADF image of the LMTO sample, where the region of interest is highlighted, the contrast appears to be weaker than in surrounding areas. Reconstructing the phase in this region, a defect in the structure is observed in the highlighted region (indicated by the red box in Figure 9.5) of the phase image not visible in the ADF image. It is proposed that this defect is likely to be related to a nanovoid in the structure; this suggestion is based on the decrease in contrast in this region in the ABF, ADF and phase images. ABF images are sensitive to both heavy and light elements; however, the contrast mechanism of ABF imaging, described in Section 4.3.1, is heavily influenced by channelling effects, which a void in the structure would disrupt.

Figure 9.6 shows a much larger void region which is visible in the ABF, phase, and ADF images. Both the ABF and phase images, which are highly sensitive to thin regions and light, show a vacuum region in the centre, confirming that this void extends through the thickness of the sample. The contrast in the ABF images is dominated by channelling effects in thicker regions [204]; this appears to dominate in the image contrast, making the edge of the void region difficult to resolve. The void appears smaller in the phase reconstruction as this method appears to be more sensitive to thin regions at the edge of the void.

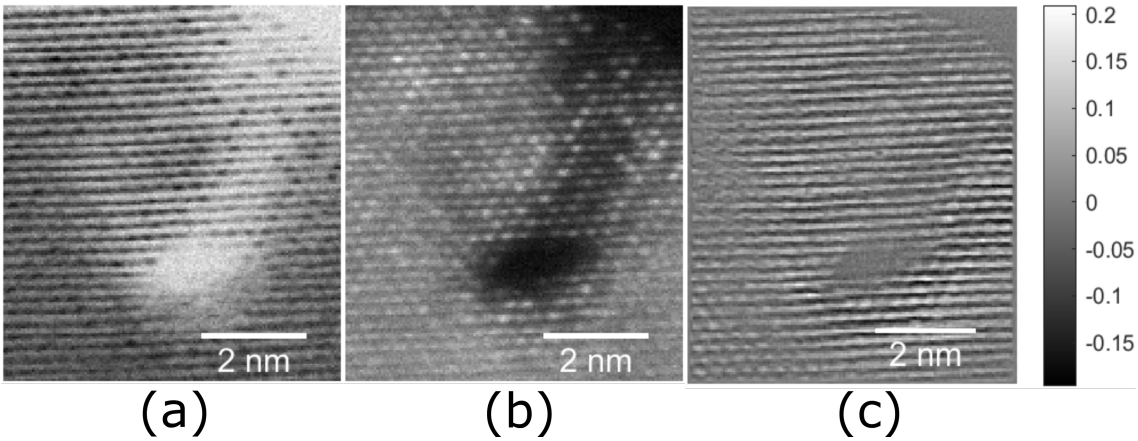


Figure 9.6: Images of nanovoid region: **a**) virtual ABF image **b**) virtual ADF images and **c**) SSB phase image.

Nanovoid structures have been associated with degradation mechanisms associated with irreversible O-redox processes [76]. In layered cathodes, the formation of molecular oxygen (O_2) within the structure has been well documented by spectroscopy techniques [75, 270]. Oxygen molecules, very close to the surface of the material, may be able to escape in the form of O_2 gas; however, beyond the first few atomic layers, oxygen molecules become trapped and unable to diffuse through the structure [77]. Specifically for DRSs, oxygen molecules within the structure have been suggested to be stabilised when O^- holes on the anion sublattice are able to pair up within nanovoid regions to form caged molecular oxygen [76]. The nanovoid structures elucidated here are identified within the pristine structure but can feasibly provide sites where degeneration processes, such as the formation and trapping of O_2 molecules, can occur.

9.4 Additional Investigations - Fluorinated Disordered Rocksalts

9.4.1 Motivation

Adding fluorine to the anion sublattice has been demonstrated to improve cycling stability in several DRS compositions, including;

- $Li_{1.2}Ti_{0.2}Mn_{0.6}O_{1.8}F_{0.2}$ [54],
- $Li_{1.2}Nb_{0.15}Mn_{0.65}O_{1.9}F_{0.1}$ [79],
- $Li_{1.23}Ni_{0.3}Nb_{0.33}Fe_{0.14}O_{1.9}F_{0.1}$ [25],
- Li_2NiO_2F [271].

For example, in $Li_{1.2}Mn_{0.7}Ti_{0.1}O_{1.9}F_{0.1}$ (LMTOF), the addition of fluorine to the anion sublattice is suggested to prevent amorphisation of the DRS structure at the surface after cycling [54]. It is feasible that having a mixed anion lattice can also result in SRO being present in the anion lattice; this would likely have a subsequent influence on the nature of the cation ordering due to the preferential bonding of lithium and fluorine. Ptychography provides an opportunity to distinguish the light elements and make a connection to relate the ordering of fluorine and its influence on the nature of the SRO on the cation lattice. A comprehensive study of these features would require a more in-depth study with a comparison of both oxide and oxy-fluoride compositions for both pristine and cycled samples.

9.4.2 Study of $Li_{1.2}Mn_{0.7}Ti_{0.1}O_{1.9}F_{0.1}$

During an investigation of the fluorinated disordered rocksalt LMTOF, it was found that this material was significantly more beam sensitive than the oxide with a similar cation composition ($Li_{1.2}Mn_{0.4}Ti_{0.4}O_2$). The damage appears as a form of mass loss, alongside the build-up of an amorphous layer on the edge of the particle; this is evident as blurring of the edge of the particle in Figure 9.7.**a** and in Figure 9.7.**b** as a build-up of amorphous material. The amorphous layer on the surface is significantly thicker in data acquired at $300\,\mathrm{kV}$ (Figure 9.7.**b**) than the data acquired at $200\,\mathrm{kV}$ (Figure 9.7.**a**) with a similar electron dose, suggesting the damage was more extensive at higher accelerating voltage. Since knock-on damage is usually worse at higher accelerating voltages [272], this would suggest a form of knock-on damage at the surface of the particles. Additionally, lighter elements tend to be more susceptible to knock-on damage [273]; therefore, a tendency towards knock-on damage could be related to the surface of the material being lithium and fluorine-rich. Some work has also suggested that upon cycling, a layer of LiF forms on the surface of fluorinated-DRS [274]. It is common in other cathode materials that the electron beam damage mechanisms are similar to the structural changes induced on cycling [64], and it is possible that energy from the electron beam could also facilitate the formation of an amorphous surface layer. An attempt to understand the composition of the amorphous layer was made using EELS; however, the layer was not thick enough to achieve sufficient signal-to-noise in the EELS spectra.

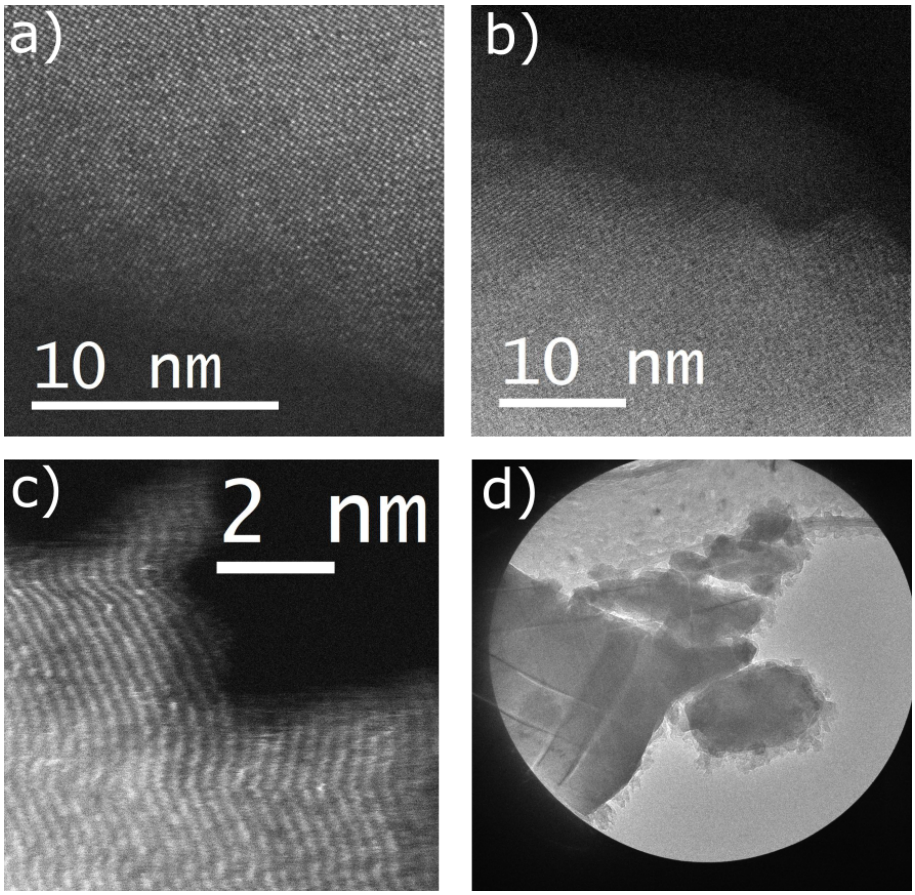


Figure 9.7: Demonstration of beam damage and imaging challenges associated with fluorinated DRS: **a**) ADF image of LMTOF acquired at 200 kV at room temperature **b**) ADF image of LMTOF acquired at 300 kV at room temperature **c**) ADF image of LMTOF acquired at 300 kV using cyro-holder and **d**) ronchigram image of LMTOF after several hours of imaging shows ice build-up on the sample.

This damage mechanism was significantly reduced by cooling the sample to cryogenic temperatures, with Figure 9.7.**c** achieved using an accelerating voltage of 300 kV with the sample cooled in Gatan double tilt, liquid nitrogen cooling holder. However, the vibrations from the liquid nitrogen bubbling in the holder, caused the image distortions, such as in Figure 9.7.**c** when imaging at high magnifications. When sufficient time was allowed for the bubbling to stop, the formation of ice crystals, which also hampered the acquisition of high-resolution data, had started, see Figure 9.7.**d**.

A high resolution ADF image of the fluorinated sample is shown in Figure 9.8, the Fourier transform of this image shows weak diffuse features of a similar nature to the < 100 > orientation diffuse scattering features from the non-fluorinated samples discussed in Chapter 7. However, an analysis of the anion lattice again necessitates using a phase imaging technique sensitive to light elements, such as ptychography. In principle, the phase image should be sensitive to the difference in projected potential between oxygen and fluorine;

however, a very clean sample would be required in practice. Any subtle differences would inevitably be obscured by the formation of the surface layer, which forms part of the damage mechanism. Due to the combination of beam damage effects and vibrations when cooling the sample, ptychographic reconstructions of the LMTOF structure have not been obtained.

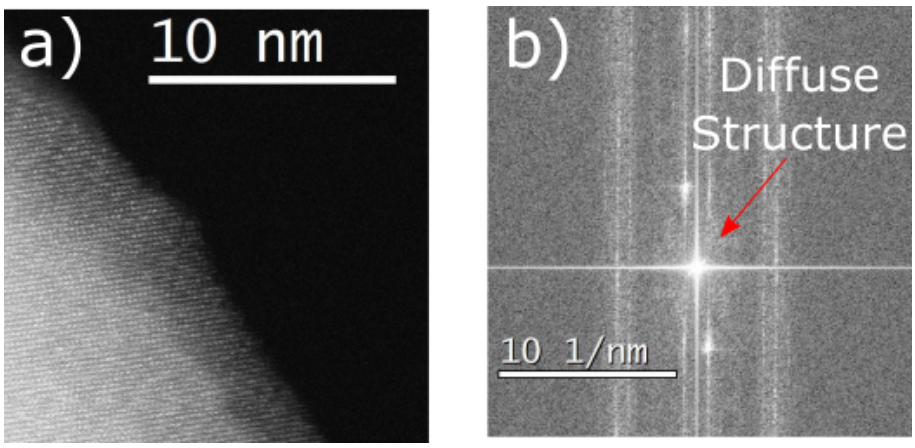


Figure 9.8: Demonstration of cryogenic imaging conditions for LMTOF: **a**) ADF image of LMTOF acquired at 300 kV using cyro-holder **b**) FFT of image **a**, with subtle feature from SRO indicated by arrow.

9.5 Conclusion

In this Chapter, the application of ptychography to understand important structural aspects of DRS cathodes, specifically in relation to the anion lattice, has been demonstrated. Ptychography has been used to provide evidence of a pure rocksalt phase in the pristine structure, including the positions of the light elements, which are typically weakly scattering and do not contribute strongly to other scattering-based structure determination methods.

The specific functionality of ptychography to provide insight into local features of the local structure, such as the observation of the oxygen-terminated surface facet, has been illustrated. The oxygen termination of the surface has potentially important consequences for structural changes, which may occur if oxygen is oxidised and O_2 is released from the surface. The elucidation of nanovoid structures in pristine material highlights the fact that although the density of these defects in the pristine material may be low enough that they are impossible to detect using bulk averaging techniques, they are still present. Although we often consider structural defects such as voids to be present as a consequence of cycling, there may indeed be a link between the defects in the pristine structure and the initiation of a particular degradation mechanism. The direct link between particular defects and specific degradation mechanisms linked with poor cycling stability is impos-

sible to clarify without applying a full suite of characterisation techniques, which is out of the scope of this study.

Some of the challenges and complications of extending the surface feature observations to compare them with the fluorinated compositions are demonstrated alongside initially promising results utilising cryogenic temperature to minimise this. The complicated nature of beam damage is an interesting aspect of this material, and further studies are warranted to establish the underlying cause.

The subsequent and final chapter in this thesis re-iterates the most important conclusions of this thesis as a whole and expands on potential future directions for the research.

Chapter 10

Conclusions and Future Directions

In this chapter, the primary conclusions of the work addressed in this thesis are summarised, and the reader is provided with a concluding overview of the new science that has come to fruition.

The research work in this thesis addresses several questions around the short range order (SRO) in disordered rocksalt (DRS) cathodes, with new insights into the nature of the local arrangements having been discussed. Structural changes due to cycling are observed in a case study on the structure of ball-milled $LiMnO_2$ (LMO). An investigation into enhancing the dose efficiency of ptychography, particularly in its application to beam-sensitive materials, with the aim of improving the dose efficiency is presented. Ptychography is also utilised to investigate specific structural features of DRS cathodes relating to the light elements.

10.1 Influence of transition Metal composition on SRO

A study has investigated the nature of the SRO and its dependence on the combination of transition metals. This investigation highlights the nature of SRO in the Ti, Nb and Ta samples as an octahedral cluster with different distributions of these clusters. This understanding of the SRO in relation to the cluster model is gained by linking the diffuse scattering to intensity variations in the annular dark field (ADF) images and its fundamental link to the composition by the underlying Z contrast of ADF images. A method has also been proposed to link intensity fluctuations to correlations with specific lengths and directions by matching correlations from the correlograph to intensity fluctuations in ADF images. This provides a quantitative method of determining the real-space correlation length of the SRO in each sample. As discussed, it was observed that the correlation length of the SRO is considerably longer in the Zr sample than in the other samples, which corresponds with a lower amount of extractable lithium in this composition.

In this study, the influence on the nature of SRO by the interaction between Li, Mn and the respective d^0 transition metal was probed. This may present as many interactions, including synthesis conditions and post-synthesis annealing, as has been investigated in

other materials [41, 44]. Further work is required to link the understanding of the clusters and their distribution to degradation mechanisms by investigating cycled materials.

In addition to the study of DRS materials, this method has the potential to be applied to any material which exhibits SRO on lattice sites where elements possess a sufficient difference in atomic number. Examples in the literature to which this could be applied include the distribution of vacancies in defective half-Heusler structures and clusters of solute atoms in Magnesium-Zinc-Gadolinium alloys [43, 275].

10.2 Investigation of LMO Structure

The investigation of LMO presents the first direct observations of SRO within the nano-sized domain of LMO synthesised by ball-milling methods. The variability in particle morphology of ball-milled particles is highlighted in ADF images; based on this result, future studies on ball-milled samples should carefully consider the reproducibility of results across many particles. The findings of this study also highlight the broader need to consider the influence of defects such as vacancies and amorphisation of the particles on the lithium transport properties. Finally, results demonstrating the structural change to a spinel-type phase on cycling are presented with NBED. Now that it has been shown that the spinel phase can be formally evidenced and spatially resolved, an outstanding question remains whether the spinel phase continues to develop over many more cycles or whether the amount of the spinel structure plateaus. To test this, the study should be extended to samples that have been cycled upwards of 50-100 times.

10.3 Development of Ptychography for low-dose applications

A method has been proposed to streamline the processing of 4-dimensional scanning transmission electron microscopy (4D-STEM) datasets for low-dose imaging. This includes an alternative Fourier transform method using electron coordinates, which can be applied directly to event-based datasets, using significantly less computer memory in the case of low-dose datasets. In order to further reduce the number of electron counts, a point of entry neural network (POE-NN) is investigated to isolate individual electron hits from a cluster of activated pixels. Significant improvements are demonstrated in the POE-NN's ability to determine electron hits by adapting the training datasets and loss function. Despite the benefits of applying this method to ptychographic datasets were not found to compensate for the time taken to perform the analysis by the POE-NN or to enhance the

resolution of the phase reconstructions markedly. Despite this, the flexibility to tailor the machine learning approach to this problem has been demonstrated in the improvements observed by tuning the training conditions and loss function. Applying the POE-NN to other imaging methods requiring higher detector precision, such as low-dose HRTEM, is worthy of further investigation.

10.4 Applying ptychography to DRS cathodes

In Chapter 9, the applicability of ptychography for understanding local structural features in DRS cathodes has been demonstrated. Evidence has been presented which adds to the wider understanding of the relationship between SRO and the formation of spinels in DRS cathode by confirming that lithium does not occupy the tetrahedral sites. To take this observation beyond its current state and to further investigate the nanovoid structures which have been investigated, the collection of three-dimensional information is required. Recent developments have shown improved depth resolution for ptychography reconstructions using inverse multislice methods [142] and reconstructions over a series of tilt angles [102]. These methods have not widely been applied to cathode materials, and doing so has the potential to reveal new structural insights.

Having observed that the polar $<111>$ surface is terminated by anions, a logical next step in this investigation would be comparing the termination surfaces of fluorinated DRS compositions. To achieve this, further optimisation of the cryogenic sample handling procedure is required to minimise ice formation. If high-resolution images of the termination surface of LMTOF can be achieved, it would be of value to investigate whether the termination surface was predominately oxygen or fluorine. Determination of terminal species could be performed by examining bond lengths or phase quantification.

Appendix A

Binary Fourier Transform Extenstion

A.1 Extention of Binary Fourier Transform Sum in 2D

A 2-dimensional discrete Fourier transform can be calculated using Equation A.1.1. Here, the simplification of the DFT for binary data is outlined for computing the DFT of a 2D array.

$$F[k,l] = \frac{1}{MN} \sum_{m=0}^{M-1} \sum_{n=0}^{N-1} f[m,n] e^{-j2\pi(\frac{k}{M}m + \frac{l}{N}n)} \tag{A.1.1}$$

Taking an example 2D array such as $f(m,n)$, in A.1.2.

$$f[m,n] = \begin{bmatrix} 1 & 0 \\ 0 & 1 \end{bmatrix} \tag{A.1.2}$$

Similarly, for the 1-dimensional discrete dataset in Section 6.2.3, the DFT can be simplified to a sum of exponential components for the non-zero terms. The double sum of the non-zero exponential components ($f[m,n] = 1$, i.e. $f[0,0]$ and $f[1,1]$) gives Equation A.1.3. Again, the multiplication step can be ignored for each component since this analysis is limited to a binary signal.

$$X[k,l] = e^{-i\frac{2\pi}{4}(k(0)+l(0))} + e^{-i\frac{2\pi}{4}(k(0)+l(1))} + e^{-i\frac{2\pi}{4}(k(1)+l(0))} + e^{-i\frac{2\pi}{4}(k(1)+l(1))} \tag{A.1.3}$$

Writing the constants in the exponential terms as c, defined in Equation A.1.4, simplifies A.1.3 to A.1.5.

$$c = -i\frac{2\pi}{4} \tag{A.1.4}$$

$$F[k,l] = e^{0} + e^{c(l)} + e^{c(k)} + e^{c(k+l)} \tag{A.1.5}$$

The matrix elements are then the sum of the terms in $F[K,L]$ () for the respective terms of $F[k,l]$, shown in the array A.1.6 and inserting the terms of the summation gives A.1.7.

$$F[k,l] = \begin{bmatrix} f(0,0) & f(1,0) \\ f(1,0) & f(1,1) \end{bmatrix} \tag{A.1.6}$$

$$F[k,l] = \begin{bmatrix} 1+1+1+1 & 1+1+e^{c}+e^{c} \\ 1+e^{c}+1+e^{c} & 1+e^{c}+e^{c}+e^{2c} \end{bmatrix} \tag{A.1.7}$$

Evaluating each matrix element gives the Fourier transform of $f[m,n]$, denoted by $F[k,l]$ in Equation A.1.8.

$$F[k,l] = \begin{bmatrix} 4 & 0 \\ 0 & 0 \end{bmatrix} \tag{A.1.8}$$

Appendix B

Detector Corrections

B.1 Detector Corrections

B.1.1 Offset/Noise Map

Small differences in gains and leakage currents are accounted for by a combination of noise and offset maps, both calculated from a set of dark frames acquired for each dataset. The offset is the pixel-wise average of the dark frames Equation B.1.1. The noise map is the standard deviation of the dark frames Equation B.1.2. Examples of both offset and noise correction maps are given in Figure B.1.

$$O_{xy} = \bar{D_{ixy}} = \frac{1}{n}\sum^{n} D_{ixy} \tag{B.1.1}$$

$$n_{xy} = \sigma_{D(ixy)} = \sqrt{\frac{1}{n}\sum_{i}^{n}[D_{ixy} - O_{xy}]^2} \tag{B.1.2}$$

Gain Map

Gain correction is required due to the in-homogeneous amplification of pixels in the detector. The gain map is acquired by acquiring a homogeneous illumination of the detector. The gain map is highly sensitive to both electron energy and dose on the detector, accurate correction of the Gain reference required obtaining homogeneous illumination of the detector matching the appropriate beam energy and dose as the experiment. An example gain map for the pnCCD by expanding the bright field disk to obtain homogeneous illumination of the detector is given in Figure B.2.

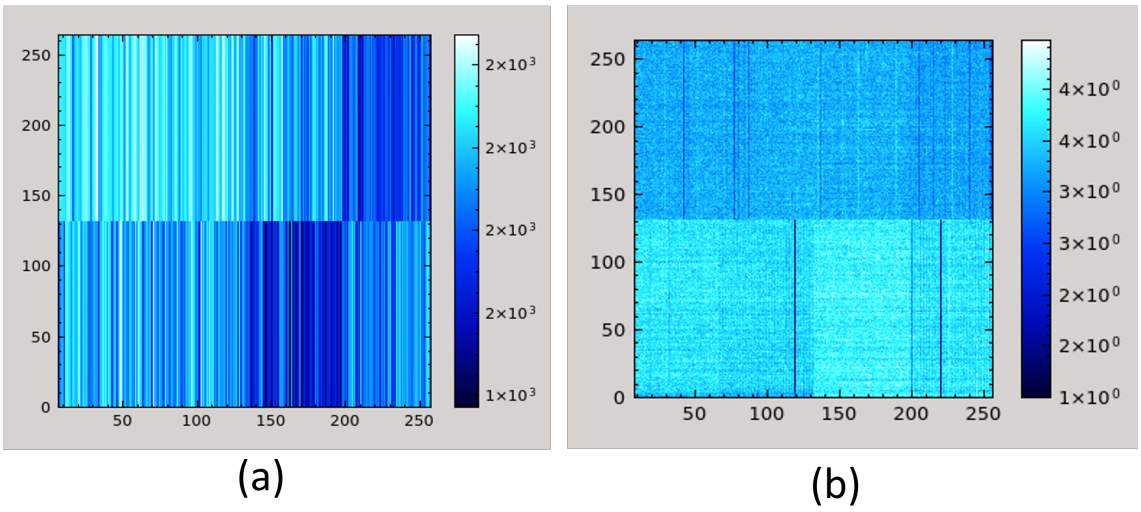


Figure B.1: Example detector corrections for both **a**) Offset and **b**) noise, based on dark frames from the pnCCD.

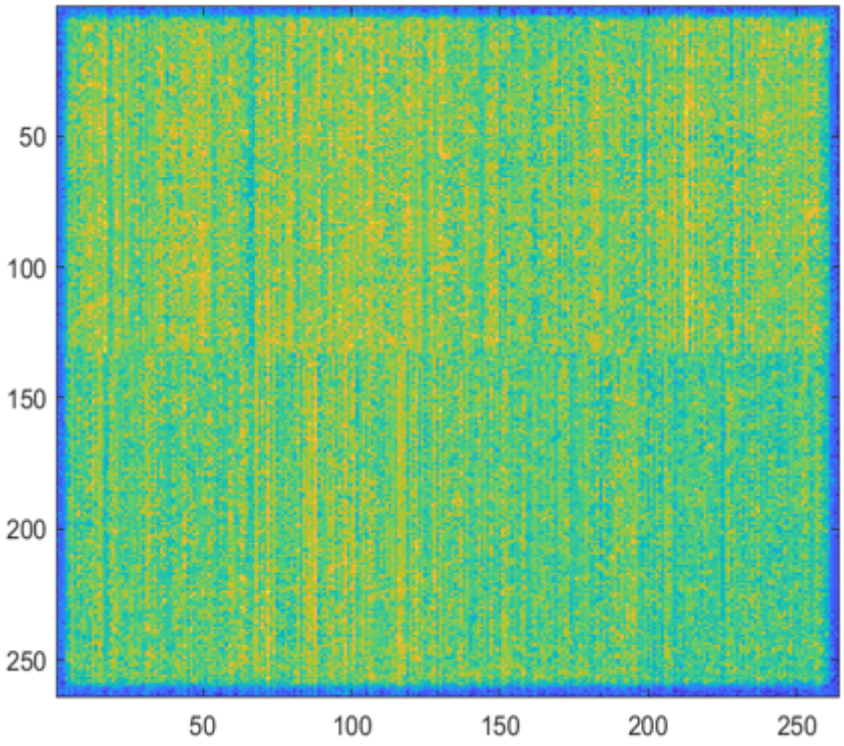


Figure B.2: Gain map acquired by homogeneous illumination of the pnCCD with 200 kV electrons.

Appendix C

Scattering Surface Intersections

C.1 Scattering Surface Intersections

The intersection of the octahedral, cubic and tetrahedral scattering surfaces with the $< 100 >$, $< 110 >$ and $< 111 >$ reciprocal lattice planes are plotted in Figure C.1. The intersection of the irregular tetrahedron, pyramidal and 5-point planar scattering surfaces scattering surfaces with the $< 100 >$, $< 110 >$ and $< 111 >$ reciprocal lattice planes are plotted in Figure C.2.

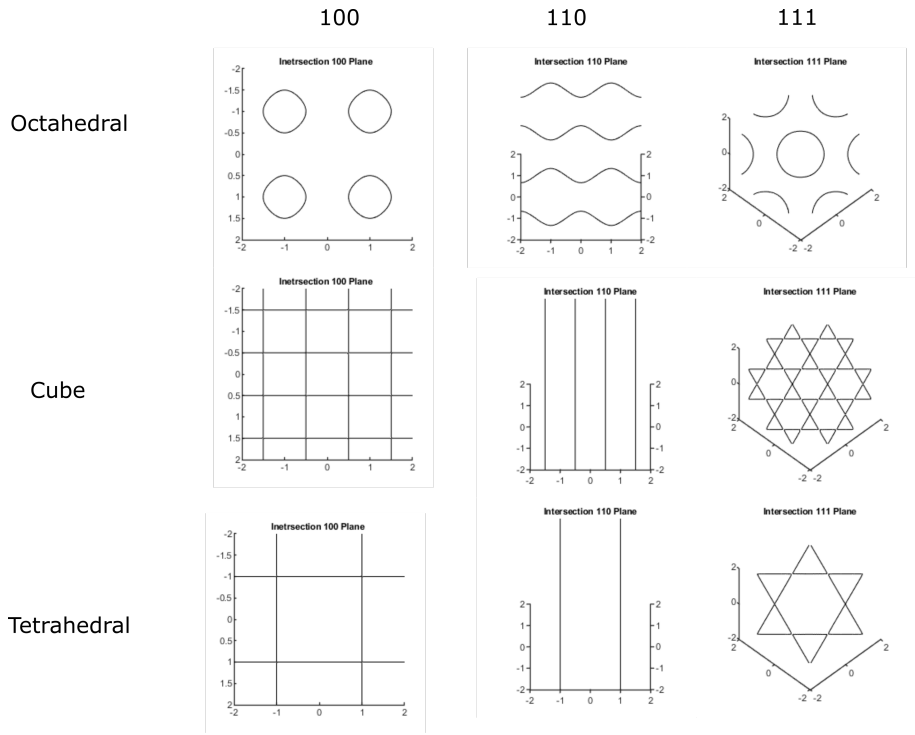


Figure C.1: Plotted intersections of the octahedral, cube and tetrahedral scattering surfaces, with the $<100>$, $<110>$ and $<111>$ reciprocal lattice planes.

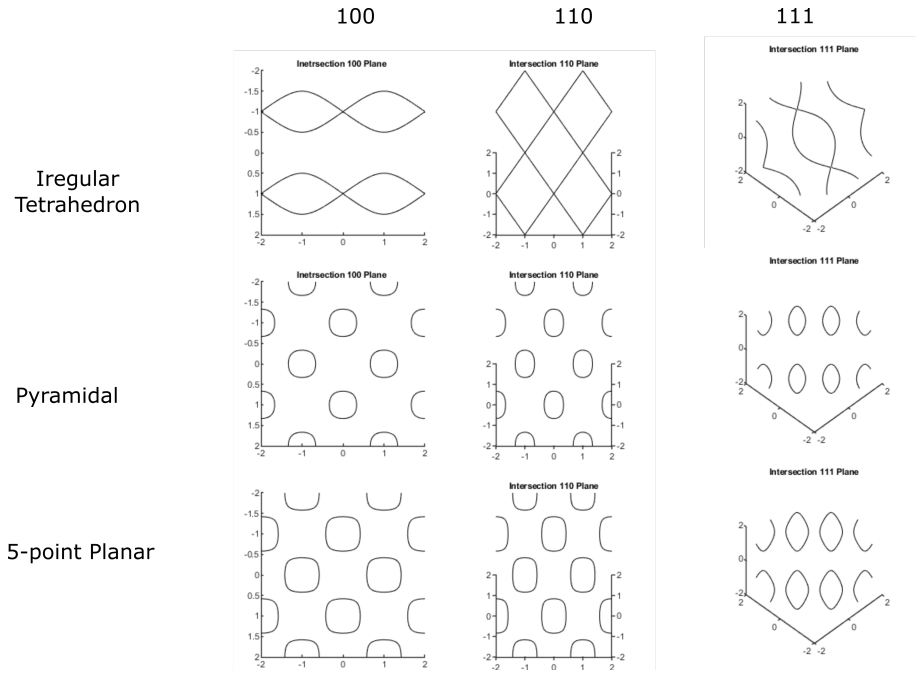


Figure C.2: Plotted intersections of the irregular tetrahedron, pyramidal and 5-point planar scattering surfaces, with the $<100>$, $<110>$ and $<111>$ reciprocal lattice planes.

Appendix D

Scattering Surface Linear Combinations

D.1 Scattering Surface Linear Combinations

Scattering surface equations for octahedral and tetrahedral clusters are combined in Equation D.1.1, scaled by parameters a and b, respectively. Variations of this linear combination corresponding to ratios $[a : b]$ of 2:1, 1:1 and 1:2 are plotted in Figure D.1 with the intersection of the <100>, <110> and <111> plotted below each.

$$a(cos(\pi h) + cos(\pi k) + cos(\pi l)) + b(cos(\frac{\pi h}{2})cos(\frac{\pi k}{2})cos(\frac{\pi l}{2})) = 0 \qquad \text{(D.1.1)}$$

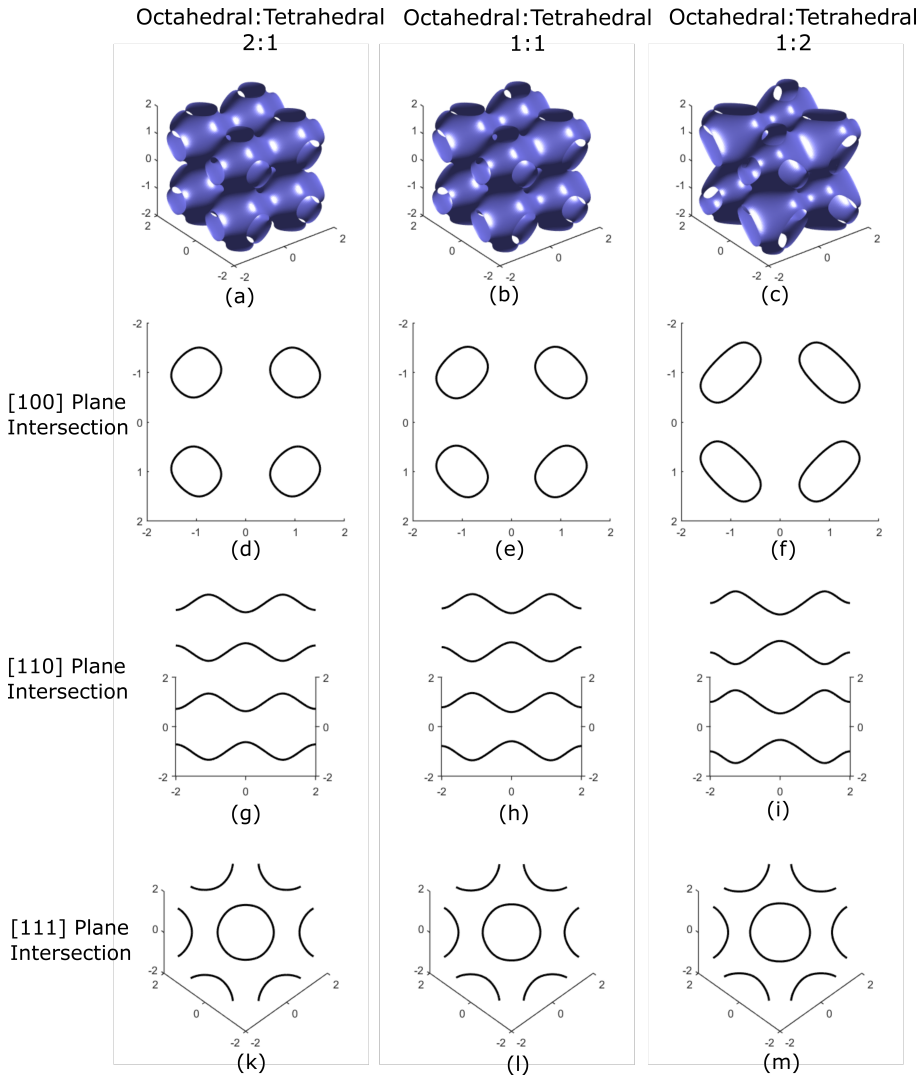


Figure D.1: a-c) Plotted Scattering surface for a linear combination of the octahedral and tetrahedral scattering surface equation in ratios of 2:1, 1:1 and 1:2, respectively, according to Equation D.1.1. In the columns below each, the intersections of the scattering surfaces with the $<100>$ plane (**d-f**), the $<110>$ plane (**g-i**) and the $<110>$ plane (**k-m**).

Appendix E

Post-acquisition Aberration Correction

E.1 Post-acquisition Aberration Correction

The aberration correction of Figure 9.2 is applied using the aperture phase surface presented in Figure E.1.**a** and correction of WDD reconstruction is carried out using the probe function shown in Figure E.1.**b**.

Figure E.2, shows both the real and imaginary SSB and WDD reconstructions corresponding to the modulus and phase images based on the data shown in Figure 9.2 (Section 9.3.1). Comparing Figure E.2.**b** and E.2.**c** shows the effect of performing post-acquisition aberration correction on the SSB phase reconstruction.

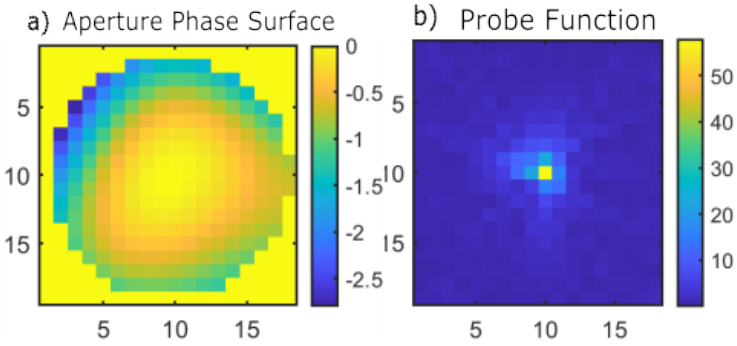


Figure E.1: Calculated aperture phase surface and probe function for data in Figure 9.2 used to apply post-acquisition aberration correction to images.

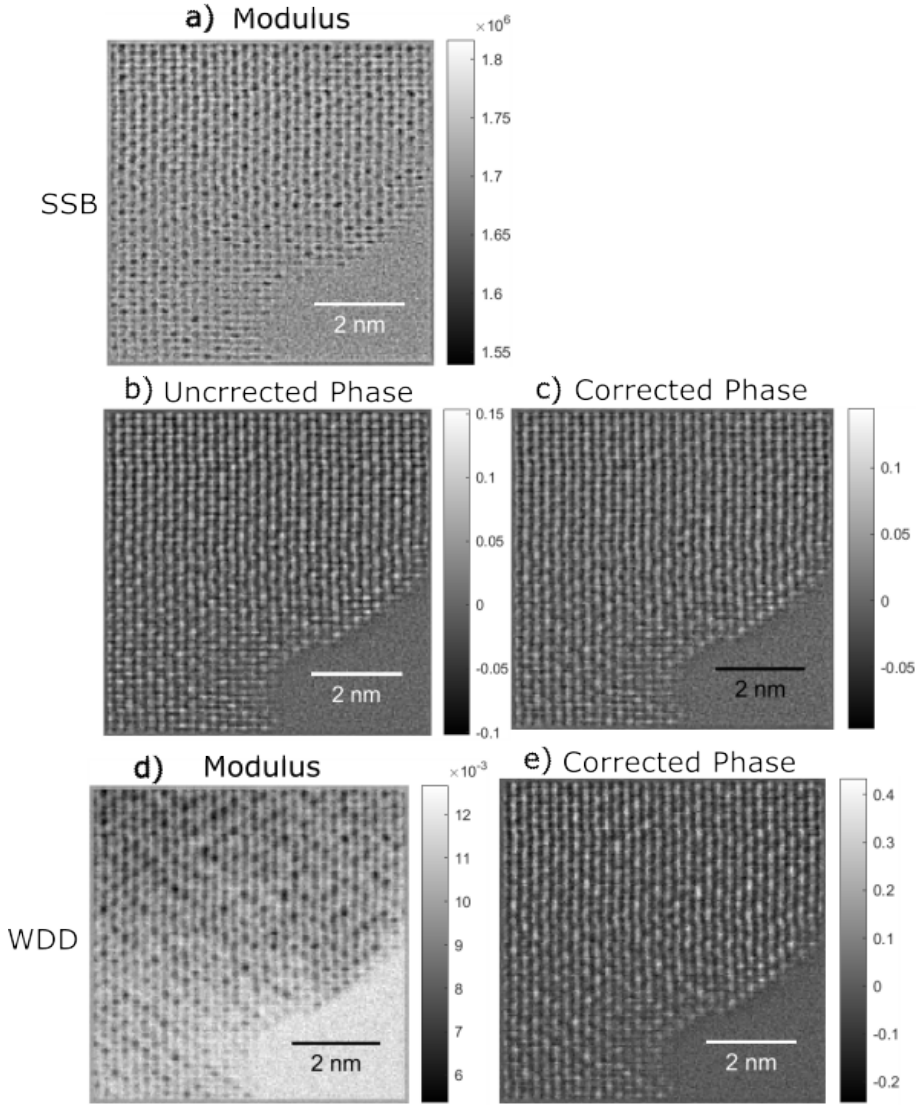


Figure E.2: **a**) Modulus of SSB reconstruction. **b**) Phase reconstruction without post-acquisition aberration correction i.e uncorrected phase. **c**) Aberration corrected SSB phase reconstruction. **d**) Modulus of the WDD phase reconstruction. **e**) Aberration corrected WDD phase reconsrcutions

List of Publications

List of publications contributed to by the author during the completion of their DPhil studies.

1. **E. Hedley**, L. Pi, M. Danie, W. Song, E. Liberti, P. G. Bruce and P. D. Nellist, ”A Quantitative Understanding of the Short Range Order in Disordered Rocksalt Cathode Materials”, *Microscopy and Microanalysis*, Vol.28, Issue S1, 458–460, 2022.

2. **E. Hedley**, B. Eckert, H. Soltau and P. D. Nellist, ”Fast Ptychographic Reconstruction for Sparse Binary Ptychography Data”, *Microscopy and Microanalysis*, Vol. 28, Issue S1, 438–439, 2022.

3. B Eckert, S Aschauer, **E. Hedley**, M Huth, P Majewski and L Strüder, ”Electron Image Reconstruction for Pixelated Semiconductor Tracking Detectors Based on Neural Networks”, *Microscopy and Microanalysis*, Vol. 28, Issue S1, 3040–3042, 2022.

4. J.J.P. Peters, T. Mullarkey, **E. Hedley**. et al. ”Electron counting detectors in scanning transmission electron microscopy via hardware signal processing” *Nat Communications*, 14, 5184, 2023.

5. E. Hedley, L. Pi, W. Song, M. Danie, P. G. Bruce, P. D. Nellist, ”A real space understanding of short range order in disordered rocksalt cathodes.” [Manuscript in preparation] Department of Materials, University of Oxford.

Bibliography

[1] *The Nobel Prize in Chemistry 2019*, en, PRESS RELEASE, Oct. 2019. [Online]. Available: https://www.nobelprize.org/uploads/2019/10/press-chemistry-2019-2.pdf (visited on 06/26/2023).

[2] J. B. Goodenough and K.-S. Park, "The Li-Ion Rechargeable Battery: A Perspective," *Journal of the American Chemical Society*, vol. 135, no. 4, pp. 1167–1176, 2013, ISSN: 0002-7863, 1520-5126. DOI: 10.1021/ja3091438. [Online]. Available: https://pubs.acs.org/doi/10.1021/ja3091438.

[3] K Ozawa, "Lithium-ion rechargeable batteries with LiCoO2 and carbon electrodes: The LiCoO2/C system," *Solid State Ionics*, vol. 69, no. 3-4, pp. 212–221, 1994, ISSN: 01672738. DOI: 10.1016/0167-2738(94)90411-1.

[4] B. L. Ellis, K. T. Lee, and L. F. Nazar, "Positive Electrode Materials for Li-Ion and Li-Batteries," *Chemistry of Materials*, vol. 22, no. 3, pp. 691–714, 2010, ISSN: 0897-4756, 1520-5002. DOI: 10.1021/cm902696j. [Online]. Available: https://pubs.acs.org/doi/10.1021/cm902696j.

[5] M. Azevegdo, N. Campagnol, T. Hagenbruch, K. Hoffman, A. Lala, and O. Ramsbottom, "Lithium and cobalt - a tale of two commodities," English, McKinsey & Company, Metal and Mining, 2018, p. 19. (visited on 11/22/2023).

[6] "The Role of Critical Minerals in Clean Energy Transitions," en, IEA, Tech. Rep., May 2021, p. 283. [Online]. Available: https://www.iea.org/reports/the-role-of-critical-minerals-in-clean-energy-transitions (visited on 07/13/2023).

[7] Y. Sun *et al.*, "Expandable Li Percolation Network: The Effects of Site Distortion in Cation-Disordered Rock-Salt Cathode Material," *Journal of the American Chemical Society*, jacs.3c02041, 2023, ISSN: 0002-7863, 1520-5126. DOI: 10.1021/jacs.3c02041.

[8] Z. Lun *et al.*, "Cation-disordered rocksalt-type high-entropy cathodes for Li-ion batteries," *Nature Materials*, vol. 20, no. 2, pp. 214–221, 2021, ISSN: 1476-1122, 1476-4660. DOI: 10.1038/s41563-020-00816-0.

[9] J. Lee, A. Urban, X. Li, D. Su, G. Hautier, and G. Ceder, "Unlocking the Potential of Cation-Disordered Oxides for Rechargeable Lithium Batteries," en, *Science*, vol. 343, no. 6170, pp. 519–522, Jan. 2014, ISSN: 0036-8075, 1095-9203. DOI: 10.1126/science.1246432.

[10] A. Simonov and A. L. Goodwin, "Designing disorder into crystalline materials," en, *Nature Reviews Chemistry*, vol. 4, no. 12, pp. 657–673, Dec. 2020, ISSN: 2397-3358. DOI: 10.1038/s41570-020-00228-3.

[11] G. Li, H. Zhang, and Y. Han, "4D-STEM Ptychography for Electron-Beam-Sensitive Materials," *ACS Central Science*, vol. 8, no. 12, pp. 1579–1588, 2022, ISSN: 2374-7943, 2374-7951. DOI: 10.1021/acscentsci.2c01137. (visited on 12/19/2023).

[12] E. Liberti, J. Lozano, M. Pérez Osorio, M. Roberts, P. Bruce, and A. Kirkland, "Quantifying oxygen distortions in lithium-rich transition-metal-oxide cathodes using ABF STEM," *Ultramicroscopy*, vol. 210, p. 112 914, 2020, ISSN: 03043991. DOI: 10.1016/j.ultramic.2019.112914.

[13] A. Boulineau, L. Simonin, J.-F. Colin, E. Canevert, L. Daniel, and S. Patroux, "Evolutions of Li1.2Mn0.61Ni0.18Mg0.01O2 during the Initial Charge/ Discharge Cycle Studied by Advanced Electron Microscopy," *Chem. Mater.*, vol. 24, 3558−3566, 2012. DOI: dx.doi.org/10.1021/cm301140g.

[14] E. McCalla *et al.*, "Visualization of O-O peroxo-like dimers in high-capacity layered oxides for Li-ion batteries," *Science*, vol. 350, no. 6267, pp. 1516–1521, 2015, ISSN: 0036-8075, 1095-9203. DOI: 10.1126/science.aac8260.

[15] P. Kurzhals, F. Riewald, M. Bianchini, H. Sommer, H. A. Gasteiger, and J. Janek, "The LiNiO $_2$ Cathode Active Material: A Comprehensive Study of Calcination Conditions and their Correlation with Physicochemical Properties. Part I. Structural Chemistry," en, *Journal of The Electrochemical Society*, vol. 168, no. 11, p. 110 518, Nov. 2021, ISSN: 0013-4651, 1945-7111. DOI: 10.1149/1945-7111/ac33e5.

[16] F. Riewald, P. Kurzhals, M. Bianchini, H. Sommer, J. Janek, and H. A. Gasteiger, "The LiNiO $_2$ Cathode Active Material: A Comprehensive Study of Calcination Conditions and their Correlation with Physicochemical Properties Part II. Morphology," *Journal of The Electrochemical Society*, vol. 169, no. 2, p. 020 529, 2022, ISSN: 0013-4651, 1945-7111. DOI: 10.1149/1945-7111/ac4bf3. (visited on 11/23/2023).

[17] A. Boulineau, L. Simonin, J.-F. Colin, C. Bourbon, and S. Patroux, "First Evidence of Manganese−Nickel Segregation and Densification upon Cycling in Li-Rich Layered Oxides for Lithium Batteries," en, *Nano Lett.*, vol. 13, 3857−3863, 2013. DOI: doi.org/10.1021/nl4019275.

[18] J. G. Lozano, G. T. Martinez, L. Jin, P. D. Nellist, and P. G. Bruce, "Low-Dose Aberration-Free Imaging of Li-Rich Cathode Materials at Various States of Charge Using Electron Ptychography," *Nano Letters*, vol. 18, no. 11, pp. 6850–6855, 2018, ISSN: 1530-6984, 1530-6992. DOI: 10.1021/acs.nanolett.8b02718.

[19] R. Sharpe *et al.*, "Redox Chemistry and the Role of Trapped Molecular O_2 in Li-Rich Disordered Rocksalt Oxyfluoride Cathodes," *Journal of the American Chemical Society*, vol. 142, no. 52, pp. 21 799–21 809, 2020, ISSN: 0002-7863, 1520-5126. DOI: 10.1021/jacs.0c10270.

[20] A. R. Armstrong, N. Dupre, A. J. Paterson, C. P. Grey, and P. G. Bruce, "Combined Neutron Diffraction, NMR, and Electrochemical Investigation of the Layered-to-Spinel Transformation in $LiMnO_2$," *Chemistry of Materials*, vol. 16, no. 16, pp. 3106–3118, 2004, ISSN: 0897-4756, 1520-5002. DOI: 10.1021/cm034964b.

[21] B. Xu, C. R. Fell, M. Chi, and Y. S. Meng, "Identifying surface structural changes in layered Li-excess nickel manganese oxides in high voltage lithium ion batteries: A joint experimental and theoretical study," en, *Energy & Environmental Science*, vol. 4, no. 6, p. 2223, 2011, ISSN: 1754-5692, 1754-5706. DOI: 10.1039/c1ee01131f.

[22] R. C. Longo *et al.*, "Phase stability of Li–Mn–O oxides as cathode materials for Li-ion batteries: Insights from ab initio calculations," *Phys. Chem. Chem. Phys.*, vol. 16, no. 23, pp. 11 233–11 242, 2014, ISSN: 1463-9076, 1463-9084. DOI: 10.1039/C4CP00937A.

[23] M Obrovac, "Structure and electrochemistry of $LiMO_2$ (M=Ti, Mn, Fe, Co, Ni) prepared by mechanochemical synthesis," en, *Solid State Ionics*, vol. 112, no. 1-2, pp. 9–19, Sep. 1998, ISSN: 01672738. DOI: 10.1016/S0167-2738(98)00225-2.

[24] J. Lee *et al.*, "Reversible Mn2+/Mn4+ double redox in lithium-excess cathode materials," *Nature*, vol. 556, no. 7700, pp. 185–190, 2018, ISSN: 0028-0836, 1476-4687. DOI: 10.1038/s41586-018-0015-4.

[25] W. Zhao *et al.*, "Improving the electrochemical properties of Ni-based cation-disordered cathode by Fe and F co-doping," *Journal of Alloys and Compounds*, vol. 935, p. 167 881, 2023, ISSN: 09258388. DOI: 10.1016/j.jallcom.2022.167881.

[26] R. J. Clément, D. Kitchaev, J. Lee, and Gerbrand Ceder, "Short-Range Order and Unusual Modes of Nickel Redox in a Fluorine-Substituted Disordered Rocksalt Oxide Lithium-Ion Cathode," *Chemistry of Materials*, vol. 30, no. 19, pp. 6945–6956, 2018, ISSN: 0897-4756, 1520-5002. DOI: 10.1021/acs.chemmater.8b03794.

[27] A. Urban, A. Abdellahi, S. Dacek, N. Artrith, and G. Ceder, "Electronic-Structure Origin of Cation Disorder in Transition-Metal Oxides," *Physical Review Letters*, vol. 119, no. 17, p. 176 402, 2017, ISSN: 0031-9007, 1079-7114. DOI: 10.1103/PhysRevLett.119.176402.

[28] D. Chen, J. Ahn, and G. Chen, "An Overview of Cation-Disordered Lithium-Excess Rocksalt Cathodes," *ACS Energy Letters*, pp. 1358–1376, 2021, ISSN: 2380-8195, 2380-8195. DOI: 10.1021/acsenergylett.1c00203.

[29] D. O. Semykina *et al.*, "Effect of transition metal cations on the local structure and lithium transport in disordered rock-salt oxides," *Physical Chemistry Chemical Physics*, vol. 24, no. 10, pp. 5823–5832, 2022, ISSN: 1463-9076, 1463-9084. DOI: 10.1039/D1CP04993C.

[30] W. H. Kan *et al.*, "Evolution of Local Structural Ordering and Chemical Distribution upon Delithiation of a Rock Salt–Structured $Li_{1.3}Ta_{0.3}Mn_{0.4}O_2$ Cathode," *Advanced Functional Materials*, vol. 29, no. 17, p. 1 808 294, 2019, ISSN: 1616-301X, 1616-3028. DOI: 10.1002/adfm.201808294.

[31] W. H. Kan *et al.*, "Understanding the Effect of Local Short-Range Ordering on Lithium Diffusion in $Li_{1.3}Nb_{0.3}Mn_{0.4}O_2$ Single-Crystal Cathode," *Chem*, vol. 4, no. 9, pp. 2108–2123, 2018, ISSN: 24519294. DOI: 10.1016/j.chempr.2018.05.008.

[32] D.-H. Seo, J. Lee, A. Urban, R. Malik, S. Kang, and G. Ceder, "The structural and chemical origin of the oxygen redox activity in layered and cation-disordered Li-excess cathode materials," *Nature Chemistry*, vol. 8, no. 7, pp. 692–697, 2016, ISSN: 1755-4330, 1755-4349. DOI: 10.1038/nchem.2524.

[33] M. A. Jones, P. J. Reeves, I. D. Seymour, M. J. Cliffe, S. E. Dutton, and C. P. Grey, "Short-range ordering in a battery electrode, the 'cation-disordered' rocksalt $Li_{1.25}Nb_{0.25}Mn_{0.5}O_2$," *Chemical Communications*, vol. 55, no. 61, pp. 9027–9030, 2019, ISSN: 1359-7345, 1364-548X. DOI: 10.1039/C9CC04250D.

[34] J. M. Cowley, "An Approximate Theory of Order in Alloys," *Physical Review*, vol. 77, no. 5, pp. 669–675, 1950, ISSN: 0031-899X. DOI: 10.1103/PhysRev.77.669.

[35] Iam-Choon Khoo, *Liquid Crystals*, 3rd ed. John Wiley & Sons, 2022, ISBN: 1-119-70579-7 978-1-119-70579-6. (visited on 05/28/2023).

[36] A. Fernández-Caballero, J. S. Wróbel, P. M. Mummery, and D. Nguyen-Manh, "Short-Range Order in High Entropy Alloys: Theoretical Formulation and Application to Mo-Nb-Ta-V-W System," *Journal of Phase Equilibria and Diffusion*, vol. 38, no. 4, pp. 391–403, 2017, ISSN: 1547-7037, 1863-7345. DOI: 10.1007/

s11669-017-0582-3. [Online]. Available: http://link.springer.com/10.1007/s11669-017-0582-3.

[37] E. G. Meekel and A. L. Goodwin, "Correlated disorder in metal–organic frameworks," *CrystEngComm*, vol. 23, no. 16, pp. 2915–2922, 2021, ISSN: 1466-8033. DOI: 10.1039/D1CE00210D.

[38] H. Ji *et al.*, "Hidden structural and chemical order controls lithium transport in cation-disordered oxides for rechargeable batteries," *Nature Communications*, vol. 10, no. 1, p. 592, 2019, ISSN: 2041-1723. DOI: 10.1038/s41467-019-08490-w.

[39] L. Bendersky and F. Gayle, "Electron diffraction using transmission electron microscopy," en, *Journal of Research of the National Institute of Standards and Technology*, vol. 106, no. 6, p. 997, 2001, ISSN: 1044677X. DOI: 10.6028/jres.106.051.

[40] C. F. Holder and R. E. Schaak, "Tutorial on Powder X-ray Diffraction for Characterizing Nanoscale Materials," *ACS Nano*, vol. 13, no. 7, pp. 7359–7365, 2019, ISSN: 1936-0851, 1936-086X. DOI: 10.1021/acsnano.9b05157.

[41] D. Chaney *et al.*, "Tuneable correlated disorder in alloys," *Physical Review Materials*, vol. 5, no. 3, p. 035 004, 2021, ISSN: 2475-9953. DOI: 10.1103/PhysRevMaterials.5.035004.

[42] P. Nan *et al.*, "Direct visualization of spatially correlated displacive short-range ordering in $Nb_{0.8}$ CoSb," *Nanoscale*, vol. 12, no. 42, pp. 21 624–21 628, 2020, ISSN: 2040-3364, 2040-3372. DOI: 10.1039/D0NR04957C.

[43] N. Roth, T. Zhu, and B. B. Iversen, "A simple model for vacancy order and disorder in defective half-Heusler systems," *IUCrJ*, vol. 7, no. 4, pp. 673–680, 2020, ISSN: 2052-2525. DOI: 10.1107/S2052252520005977.

[44] N. Roth, J. Beyer, K. F. F. Fischer, K. Xia, T. Zhu, and B. B. Iversen, "Tuneable local order in thermoelectric crystals," *IUCrJ*, vol. 8, no. 4, pp. 695–702, Jul. 2021, ISSN: 2052-2525. DOI: 10.1107/S2052252521005479.

[45] L. Owen, H. Playford, H. Stone, and M. Tucker, "A new approach to the analysis of short-range order in alloys using total scattering," *Acta Materialia*, vol. 115, pp. 155–166, 2016, ISSN: 13596454. DOI: 10.1016/j.actamat.2016.05.031.

[46] P. C. Clapp, "Atomic Configurations in Binary Alloys," *Physical Review B*, vol. 4, no. 2, pp. 255–270, 1971, ISSN: 0556-2805. DOI: 10.1103/PhysRevB.4.255.

[47] L Trxeb and G Veith, "Kinetic Study of Short Range Order in aplha-CuAl alloys," *Acta. Metallurgica.*, vol. 26, pp. 185–196, 1977.

[48] D. M. Arciniegas Jaimes *et al.*, "Effect of B-Site Order–Disorder in the Structure and Magnetism of the New Perovskite Family $La_2MnB'O_6$ with B′ = Ti, Zr, and Hf," *Inorganic Chemistry*, vol. 60, no. 7, pp. 4935–4944, 2021, ISSN: 0020-1669, 1520-510X. DOI: 10.1021/acs.inorgchem.1c00014.

[49] Ouyang, Bin and A, "Effect of Fluorination on Lithium Transport and Short□Range Order in Disordered-Rocksalt-Type Lithium-Ion Battery Cathodes," *Advanced Energy Materials*, vol. 10, p. 1 903 240, 2020. DOI: 10.1002/aenm.201903240.

[50] O. F. Dippo and K. S. Vecchio, "A universal configurational entropy metric for high-entropy materials," en, *Scripta Materialia*, vol. 201, p. 113 974, 2021, ISSN: 13596462. DOI: 10.1016/j.scriptamat.2021.113974.

[51] T. J. Harrington *et al.*, "Phase stability and mechanical properties of novel high entropy transition metal carbides," en, *Acta Materialia*, vol. 166, pp. 271–280, Mar. 2019, ISSN: 13596454. DOI: 10.1016/j.actamat.2018.12.054. [Online]. Available: https://linkinghub.elsevier.com/retrieve/pii/S135964541831005X (visited on 05/09/2023).

[52] C. M. Rost *et al.*, "Entropy-stabilized oxides," *Nature Communications*, vol. 6, no. 1, p. 8485, 2015, ISSN: 2041-1723. DOI: 10.1038/ncomms9485.

[53] M. Font-Bardia and X. Alcobé, "X-ray single crystal and powder diffraction: Possibilities and applications," in *Handbook of instrumental techniques for materials*, 2012.

[54] L. Li *et al.*, "Fluorination□Enhanced Surface Stability of Cation□Disordered Rocksalt Cathodes for Li□Ion Batteries," *Advanced Functional Materials*, vol. 31, no. 25, p. 2 101 888, 2021, ISSN: 1616-301X, 1616-3028. DOI: 10.1002/adfm.202101888. [Online]. Available: https://onlinelibrary.wiley.com/doi/10.1002/adfm.202101888.

[55] J. Billingham, P. S. Bell, and M. H. Lewis, "Vacancy short-range order in substoichiometric transition metal carbides and nitrides with the NaCl structure. I. Electron diffraction studies of short-range ordered compounds," *Acta Crystallographica Section A*, vol. 28, no. 6, pp. 602–606, 1972, ISSN: 0567-7394. DOI: 10.1107/S0567739472001524.

[56] R. De Ridder, G. Van Tendeloo, and S. Amelinckx, "A cluster model for the transition from the short-range order to the long-range order state in f.c.c. based binary systems and its study by means of electron diffraction," *Acta Crystallographica Section A*, vol. 32, no. 2, pp. 216–224, 1976, ISSN: 0567-7394. DOI: 10.1107/S0567739476000508.

[57] Z. R. Dai, Z. L. Wang, Y. R. Chen, H. Z. Wu, and W. X. Liu, "Local ordering of oxygen vacancies in cubic zirconia (ZrO_2) stabilized with yttria (Y_2O_2) and magnesia (MgO) I. Electron diffuse scattering study," *Philosophical Magazine A*, vol. 73, no. 2, pp. 415–430, 1996, ISSN: 0141-8610, 1460-6992. DOI: 10.1080/01418619608244391. (visited on 07/19/2023).

[58] H. Euchner, J. H. Chang, and A. Groß, "On stability and kinetics of Li-rich transition metal oxides and oxyfluorides," *Journal of Materials Chemistry A*, vol. 8, no. 16, pp. 7956–7967, 2020, ISSN: 2050-7488, 2050-7496. DOI: 10.1039/D0TA01054E.

[59] M. M. Thackeray, P. J. Johnson, and L. A. de Picciotto, "ELECTROCHEMICAL EXTRACTION OF LITHIUM FROMLiMn20W," en, *Mat. Res. Bull.*, vol. 19, no. 2, pp. 179–187, 1984.

[60] A. Urban, J. Lee, and G. Ceder, "The Configurational Space of Rocksalt-Type Oxides for High-Capacity Lithium Battery Electrodes," *Advanced Energy Materials*, vol. 4, no. 13, p. 1 400 478, 2014, ISSN: 16146832. DOI: 10.1002/aenm.201400478.

[61] D. A. Kitchaev *et al.*, "Design principles for high transition metal capacity in disordered rocksalt Li-ion cathodes," *Energy & Environmental Science*, vol. 11, no. 8, pp. 2159–2171, 2018, ISSN: 1754-5692, 1754-5706. DOI: 10.1039/C8EE00816G.

[62] T. Sato, K. Sato, W. Zhao, Y. Kajiya, and N. Yabuuchi, "Metastable and nanosize cation-disordered rocksalt-type oxides: Revisit of stoichiometric $LiMnO_2$ and $NaMnO_2$," *Journal of Materials Chemistry A*, vol. 6, no. 28, pp. 13 943–13 951, 2018, ISSN: 2050-7488, 2050-7496. DOI: 10.1039/C8TA03667E.

[63] J. Ahn *et al.*, "Exceptional Cycling Performance Enabled by Local Structural Rearrangements in Disordered Rocksalt Cathodes," *Advanced Energy Materials*, vol. 12, no. 27, p. 2 200 426, 2022, ISSN: 1614-6832, 1614-6840. DOI: 10.1002/aenm.202200426.

[64] J. Ahn, "A Fluorination Method for Improving Cation□Disordered Rocksalt Cathode Performance," *Advanced Energy Materials*, vol. 10, p. 2 001 671, 2020. DOI: https://doi.org/10.1002/aenm.202001671.

[65] D.-H. Kwon *et al.*, "The Impact of Surface Structure Transformations on the Performance of Li-Excess Cation-Disordered Rocksalt Cathodes," *Cell Reports Physical Science*, vol. 1, no. 9, p. 100 187, 2020, ISSN: 26663864. DOI: 10.1016/j.xcrp.2020.100187.

[66] H. Uematsu *et al.*, "Nanoscale domain imaging of Li-rich disordered rocksalt-type cathode materials with X-ray spectroscopic ptychography," *Physical Chemistry Chemical Physics*, vol. 25, no. 5, pp. 3867–3874, 2023, ISSN: 1463-9076, 1463-9084. DOI: 10.1039/D2CP04087E.

[67] J. Tarascon *et al.*, "In Situ Structural and Electrochemical Study of Ni1−xCoxO2 Metastable Oxides Prepared by Soft Chemistry," *Journal of Solid State Chemistry*, vol. 147, no. 1, pp. 410–420, 1999, ISSN: 00224596. DOI: 10.1006/jssc.1999.8465.

[68] K. Luo *et al.*, "Charge-compensation in 3d-transition-metal-oxide intercalation cathodes through the generation of localized electron holes on oxygen," *Nature Chemistry*, vol. 8, no. 7, pp. 684–691, 2016, ISSN: 1755-4330, 1755-4349. DOI: 10.1038/nchem.2471.

[69] M. Saubanère, E. McCalla, J.-M. Tarascon, and M.-L. Doublet, "The intriguing question of anionic redox in high-energy density cathodes for Li-ion batteries," *Energy & Environmental Science*, vol. 9, no. 3, pp. 984–991, 2016, ISSN: 1754-5692, 1754-5706. DOI: 10.1039/C5EE03048J.

[70] M. Sathiya *et al.*, "Reversible anionic redox chemistry in high-capacity layered-oxide electrodes," en, *Nature Materials*, vol. 12, no. 9, pp. 827–835, 2013, ISSN: 1476-1122, 1476-4660. DOI: 10.1038/nmat3699.

[71] R. A. House *et al.*, "What Triggers Oxygen Loss in Oxygen Redox Cathode Materials?" *Chemistry of Materials*, vol. 31, no. 9, pp. 3293–3300, 2019, ISSN: 0897-4756, 1520-5002. DOI: 10.1021/acs.chemmater.9b00227.

[72] E. Zhao *et al.*, "Stabilizing the Oxygen Lattice and Reversible Oxygen Redox Chemistry through Structural Dimensionality in Lithium□Rich Cathode Oxides," *Angewandte Chemie International Edition*, vol. 58, no. 13, pp. 4323–4327, 2019, ISSN: 1433-7851, 1521-3773. DOI: 10.1002/anie.201900444.

[73] R. A. House *et al.*, "Superstructure control of first-cycle voltage hysteresis in oxygen-redox cathodes," *Nature*, vol. 577, no. 7791, pp. 502–508, 2020, ISSN: 0028-0836, 1476-4687. DOI: 10.1038/s41586-019-1854-3.

[74] R. Wang *et al.*, "A disordered rock-salt Li-excess cathode material with high capacity and substantial oxygen redox activity: Li 1.25 Nb 0.25 Mn 0.5 O 2," en, *Electrochemistry Communications*, vol. 60, pp. 70–73, 2015, ISSN: 13882481. DOI: 10.1016/j.elecom.2015.08.003.

[75] R. A. House *et al.*, "Delocalized electron holes on oxygen in a battery cathode," en, *Nature Energy*, 2023, ISSN: 2058-7546. DOI: 10.1038/s41560-023-01211-0.

[76] K. McColl *et al.*, "Transition metal migration and O2 formation underpin voltage hysteresis in oxygen-redox disordered rocksalt cathodes," en, *Nature Communications volume*, vol. 13, p. 5275, 2022. DOI: https://doi.org/10.1038/s41467-022-32983-w.

[77] R. A. House, J.-J. Marie, M. A. Pérez-Osorio, G. J. Rees, E. Boivin, and P. G. Bruce, "The role of O2 in O-redox cathodes for Li-ion batteries," *Nature Energy*, vol. 6, no. 8, pp. 781–789, 2021, ISSN: 2058-7546. DOI: 10.1038/s41560-021-00780-2.

[78] J. Lee *et al.*, "Mitigating oxygen loss to improve the cycling performance of high capacity cation-disordered cathode materials," en, *Nature Communications*, vol. 8, no. 1, p. 981, 2014, ISSN: 2041-1723. DOI: 10.1038/s41467-017-01115-0. [Online]. Available: https://www.nature.com/articles/s41467-017-01115-0.

[79] Z. Lun *et al.*, "Improved Cycling Performance of Li□Excess Cation□Disordered Cathode Materials upon Fluorine Substitution," *Advanced Energy Materials*, vol. 9, no. 2, p. 1 802 959, 2019, ISSN: 1614-6832, 1614-6840. DOI: 10.1002/aenm.201802959.

[80] RUSKA, ERNST, "ELECTRON MICROSCOPE AND OF ELECTRON MICROSCOPY," *Les Prix Nobel 1986: Nobel prizes, presentations, biographies and lectures*, p. 58, 1987.

[81] M. d. A. Pereira-da Silva and F. A. Ferri, "Scanning Electron Microscopy," en, in *Nanocharacterisation Techniques*, vol. a, William Andrew, 2017, ISBN: 978-0-323-49778-7. (visited on 09/18/2023).

[82] M. Buchely, J. Gutierrez, L. León, and A. Toro, "The effect of microstructure on abrasive wear of hardfacing alloys," *Wear*, vol. 259, no. 1-6, pp. 52–61, 2005, ISSN: 00431648. DOI: 10.1016/j.wear.2005.03.002.

[83] J. J. Liu, "Advances and Applications of Atomic-Resolution Scanning Transmission Electron Microscopy," *Microscopy and Microanalysis*, vol. 27, no. 5, pp. 943–995, 2021, ISSN: 1431-9276, 1435-8115. DOI: 10.1017/S1431927621012125. (visited on 09/15/2022).

[84] A. V. Crewe, J. Wall, and L. M. Welter, "A High Resolution Scanning Transmission Electron Microscope," *Journal of Applied Physics*, vol. 39, no. 13, pp. 5861–5868, 1968. DOI: https://doi.org/10.1063/1.1656079.

[85] A. V. Crewe, J. Wall, and J. Langmore, "Visibility of Single Atoms," *Science*, vol. 168, no. 3937, pp. 1338–1340, 1970, ISSN: 0036-8075, 1095-9203. DOI: 10.1126/science.168.3937.1338.

[86] A. V. Crewe, "Scanning Electron Microscopes: Is High Resolution Possible?: Use of a field-emission electron source may make it possible to overcome existing limitations on resolution.," *Science*, vol. 154, no. 3750, pp. 729–738, 1966, ISSN: 0036-8075, 1095-9203. DOI: 10.1126/science.154.3750.729.

[87] D. B. Williams and C. B. Carter, *Transmission electron microscopy: a textbook for materials science*, en, 2nd ed. New York: Springer, 2008, ISBN: 978-0-387-76500-6.

[88] T. Latychevskaia, "Spatial coherence of electron beams from field emitters and its effect on the resolution of imaged objects," *Ultramicroscopy*, vol. 175, pp. 121–129, 2017, ISSN: 03043991. DOI: 10.1016/j.ultramic.2016.11.008.

[89] X. T. Nguyen and M. S. Altman, "Temporal coherence envelope function of field emission in electron microscopy," *Ultramicroscopy*, vol. 252, p. 113 751, Oct. 2023, ISSN: 03043991. DOI: 10.1016/j.ultramic.2023.113751.

[90] D. Nicholls, J. Lee, H. Amari, A. J. Stevens, B. L. Mehdi, and N. D. Browning, "Minimising damage in high resolution scanning transmission electron microscope images of nanoscale structures and processes," *Nanoscale*, vol. 12, no. 41, pp. 21 248–21 254, 2020, ISSN: 2040-3364, 2040-3372. DOI: 10.1039/D0NR04589F.

[91] O. L. Krivanek, N Dellby, and A. R. Lupini, "Towards sub-As electron beams," en, *Ultramicroscopy*, vol. 78, pp. 1–11, 1999.

[92] O. Krivanek, P. Nellist, N. Dellby, M. Murfitt, and Z. Szilagyi, "Towards sub-0.5Å electron beams," *Ultramicroscopy*, vol. 96, no. 3-4, pp. 229–237, 2003, ISSN: 03043991. DOI: 10.1016/S0304-3991(03)00090-1.

[93] R. Egerton and M. Watanabe, "Spatial resolution in transmission electron microscopy," en, *Micron*, vol. 160, p. 103 304, Sep. 2022, ISSN: 09684328. DOI: 10.1016/j.micron.2022.103304. [Online]. Available: https://linkinghub.elsevier.com/retrieve/pii/S0968432822001007 (visited on 09/07/2023).

[94] G. Noircler, F. Lebreton, E. Drahi, P. De Coux, and B. Warot-Fonrose, "STEM-EELS investigation of c-Si/a-AlO interface for solar cell applications," *Micron*, vol. 145, p. 103 032, 2021, ISSN: 09684328. DOI: 10.1016/j.micron.2021.103032.

[95] K. Kimoto, T. Asaka, T. Nagai, M. Saito, Y. Matsui, and K. Ishizuka, "Element-selective imaging of atomic columns in a crystal using STEM and EELS," *Nature*, vol. 450, no. 7170, pp. 702–704, 2007, ISSN: 0028-0836, 1476-4687. DOI: 10.1038/nature06352.

[96] S. Van Aert, K. J. Batenburg, M. D. Rossell, R. Erni, and G. Van Tendeloo, "Three-dimensional atomic imaging of crystalline nanoparticles," *Nature*, vol. 470, no. 7334, pp. 374–377, 2011, ISSN: 0028-0836, 1476-4687. DOI: 10.1038/nature09741.

[97] O. Dyck, S. Kim, S. V. Kalinin, and S. Jesse, "Placing single atoms in graphene with a scanning transmission electron microscope," *Applied Physics Letters*, vol. 111, no. 11, p. 113 104, 2017, ISSN: 0003-6951, 1077-3118. DOI: 10.1063/1.4998599.

[98] M. Nord *et al.*, "Strain Anisotropy and Magnetic Domains in Embedded Nanomagnets," *Small*, vol. 15, no. 52, p. 1 904 738, 2019, ISSN: 1613-6810, 1613-6829. DOI: 10.1002/smll.201904738.

[99] Y.-Y. Wang, R. Yuan, S. Wang, Z. Wang, and Q. Jin, "Internal Electric Field Profiling of 2D P-N Junctions of Semiconductor Devices by 4D STEM and Dual Lens Electron Holography," en, *Microscopy Today*, vol. 30, no. 1, pp. 24–29, 2022, ISSN: 1551-9295, 2150-3583. DOI: 10.1017/S1551929521001577.

[100] N. Shibata *et al.*, "Imaging of built-in electric field at a p-n junction by scanning transmission electron microscopy," *Scientific Reports*, vol. 5, no. 1, p. 10 040, 2015, ISSN: 2045-2322. DOI: 10.1038/srep10040. [Online]. Available: http://www.nature.com/articles/srep10040.

[101] L. Zhou *et al.*, "Low-dose phase retrieval of biological specimens using cryo-electron ptychography," *Nature Communications*, vol. 11, no. 1, p. 2773, 2020, ISSN: 2041-1723. DOI: 10.1038/s41467-020-16391-6.

[102] Z. Ding *et al.*, "Three-dimensional electron ptychography of organic–inorganic hybrid nanostructures," *Nature Communications*, vol. 13, no. 1, p. 4787, 2022, ISSN: 2041-1723. DOI: 10.1038/s41467-022-32548-x.

[103] W Rarogpilecka, E Miskiewicz, D Szmigiel, and Z Kowalczyk, "Structure sensitivity of ammonia synthesis over promoted ruthenium catalysts supported on graphitised carbon," *Journal of Catalysis*, vol. 231, no. 1, pp. 11–19, 2005, ISSN: 00219517. DOI: 10.1016/j.jcat.2004.12.005. (visited on 09/01/2023).

[104] A. De Backer, S. Bals, and S. Van Aert, "A decade of atom-counting in STEM: From the first results toward reliable 3D atomic models from a single projection," en, *Ultramicroscopy*, vol. 247, p. 113 702, 2023, ISSN: 03043991. DOI: 10.1016/j.ultramic.2023.113702.

[105] C. Dwyer, "Quantitative annular dark-field imaging in the scanning transmission electron microscope—a review," *Journal of Physics: Materials*, vol. 4, no. 4, p. 042 006, 2021, ISSN: 2515-7639. DOI: 10.1088/2515-7639/ac1ab8. [Online]. Available: https://iopscience.iop.org/article/10.1088/2515-7639/ac1ab8.

[106] M. Weyland and P. A. Midgley, "Electron tomography," *Materials Today*, vol. 7, no. 12, pp. 32–40, 2004, ISSN: 13697021. DOI: 10.1016/S1369-7021(04)00569-3.

[107] K. J. Batenburg and J. Sijbers, "DART: A Practical Reconstruction Algorithm for Discrete Tomography," *IEEE Transactions on Image Processing*, vol. 20, no. 9, pp. 2542–2553, 2011, ISSN: 1057-7149, 1941-0042. DOI: 10.1109/TIP.2011.2131661.

[108] R. Yalisove, S. H. Sung, P. Ercius, and R. Hovden, "Limits of Three-Dimensional Resolution and Dose for Aberration-Corrected Electron Tomography," *Physical Review Applied*, vol. 15, no. 1, p. 014 003, 2021, ISSN: 2331-7019. DOI: 10.1103/PhysRevApplied.15.014003.

[109] L. Jones, K. E. MacArthur, V. T. Fauske, A. T. J. Van Helvoort, and P. D. Nellist, "Rapid Estimation of Catalyst Nanoparticle Morphology and Atomic-Coordination by High-Resolution Z-Contrast Electron Microscopy," *Nano Letters*, vol. 14, no. 11, pp. 6336–6341, 2014, ISSN: 1530-6984, 1530-6992. DOI: 10.1021/nl502762m.

[110] J. L. Peters, K. H. W. Van Den Bos, S. Van Aert, B. Goris, S. Bals, and D. Vanmaekelbergh, "Ligand-Induced Shape Transformation of PbSe Nanocrystals," *Chemistry of Materials*, vol. 29, no. 9, pp. 4122–4128, 2017, ISSN: 0897-4756, 1520-5002. DOI: 10.1021/acs.chemmater.7b01103.

[111] E. Arslan Irmak, P. Liu, S. Bals, and S. Van Aert, "3D Atomic Structure of Supported Metallic Nanoparticles Estimated from 2D ADF STEM Images: A Combination of Atom□Counting and a Local Minima Search Algorithm," *Small Methods*, vol. 5, no. 12, p. 2 101 150, 2021, ISSN: 2366-9608, 2366-9608. DOI: 10.1002/smtd.202101150.

[112] H. E *et al.*, "Probe integrated scattering cross sections in the analysis of atomic resolution HAADF STEM images," *Ultramicroscopy*, vol. 133, pp. 109–119, Oct. 2013, ISSN: 03043991. DOI: 10.1016/j.ultramic.2013.07.002.

[113] M. Retsky, "Observed single atom elastic cross sections in a scanning electron microscope," Tech. Rep. COO–1721-81, 4239746, Jan. 1974, COO–1721–81, 4239746. DOI: 10.2172/4239746. (visited on 09/01/2023).

[114] K. E. MacArthur, L. B. Jones, and P. D. Nellist, "How flat is your detector? Non-uniform annular detector sensitivity in STEM quantification," *Journal of Physics: Conference Series*, vol. 522, p. 012 018, 2014, ISSN: 1742-6588, 1742-6596. DOI: 10.1088/1742-6596/522/1/012018.

[115] S. Findlay and J. LeBeau, "Detector non-uniformity in scanning transmission electron microscopy," *Ultramicroscopy*, vol. 124, pp. 52–60, 2013, ISSN: 03043991. DOI: 10.1016/j.ultramic.2012.09.001.

[116] G. Martinez *et al.*, "Quantitative STEM normalisation: The importance of the electron flux," *Ultramicroscopy*, vol. 159, pp. 46–58, 2015, ISSN: 03043991. DOI: 10.1016/j.ultramic.2015.07.010. (visited on 09/01/2023).

[117] A. De Backer, G. Martinez, A. Rosenauer, and S. Van Aert, "Atom counting in HAADF STEM using a statistical model-based approach: Methodology, possibilities, and inherent limitations," *Ultramicroscopy*, vol. 134, pp. 23–33, 2013, ISSN: 03043991. DOI: 10.1016/j.ultramic.2013.05.003.

[118] X. Luo, A. Varambhia, W. Song, D. Ozkaya, S. Lozano-Perez, and P. D. Nellist, "High-precision atomic-scale strain mapping of nanoparticles from STEM images," *Ultramicroscopy*, vol. 239, p. 113 561, 2022, ISSN: 03043991. DOI: 10.1016/j.ultramic.2022.113561. [Online]. Available: https://linkinghub.elsevier.com/retrieve/pii/S0304399122000936.

[119] W. Song *et al.*, "Direct imaging of oxygen shifts associated with the oxygen redox of Li-rich layered oxides," *Joule*, vol. 6, no. 5, pp. 1049–1065, 2022, ISSN: 25424351. DOI: 10.1016/j.joule.2022.04.008.

[120] A. R. Faruqi and S. Subramaniam, "CCD detectors in high-resolution biological electron microscopy," *Quarterly Reviews of Biophysics*, vol. 33, no. 1, pp. 1–27, 2000, ISSN: 0033-5835, 1469-8994. DOI: 10.1017/S0033583500003577.

[121] G. McMullan, A. Faruqi, and R. Henderson, "Direct Electron Detectors," in *Methods in Enzymology*, vol. 579, Elsevier, 2016, pp. 1–17, ISBN: 978-0-12-805382-9. DOI: 10.1016/bs.mie.2016.05.056.

[122] A. Faruqi, R Henderson, and S Subramaniam, "Cooled CCD detector with tapered fibre optics for recording electron diffraction patterns," *Ultramicroscopy*, vol. 75, no. 4, pp. 235–250, Jan. 1999, ISSN: 03043991. DOI: 10.1016/S0304-3991(98)00056-4.

[123] R. R. Meyer and A. I. Kirkland, "Characterisation of the signal and noise transfer of CCD cameras for electron detection," *Microscopy Research and Technique*, vol. 49, no. 3, pp. 269–280, 2000, ISSN: 1059-910X, 1097-0029. DOI: 10.1002/(SICI)1097-0029(20000501)49:3<269::AID-JEMT5>3.0.CO;2-B. [Online]. Available: https://onlinelibrary.wiley.com/doi/10.1002/(SICI)1097-0029(20000501)49:3<269::AID-JEMT5>3.0.CO;2-B.

[124] H. Ryll *et al.*, "A pnCCD-based, fast direct single electron imaging camera for TEM and STEM," en, *Journal of Instrumentation*, vol. 11, no. 04, P04006–P04006, 2016, ISSN: 1748-0221. DOI: 10.1088/1748-0221/11/04/P04006.

[125] M. W. Tate *et al.*, "High Dynamic Range Pixel Array Detector for Scanning Transmission Electron Microscopy," en, *Microscopy and Microanalysis*, vol. 22, no. 1, pp. 237–249, 2016, ISSN: 1431-9276, 1435-8115. DOI: 10.1017/S1431927615015664.

[126] G. McMullan *et al.*, "Electron imaging with Medipix2 hybrid pixel detector," *Ultramicroscopy*, vol. 107, no. 4-5, pp. 401–413, 2007, ISSN: 03043991. DOI: 10.1016/j.ultramic.2006.10.005. (visited on 08/17/2023).

[127] *DE-64-Product-Booklet*. [Online]. Available: https://quantumdetectors.com/wp-content/uploads/2021/12/2885-MerlinEM-Technical-datasheet-3.pdf (visited on 08/17/2023).

[128] A.-C. Milazzo *et al.*, "Active pixel sensor array as a detector for electron microscopy," *Ultramicroscopy*, vol. 104, no. 2, pp. 152–159, 2005, ISSN: 03043991. DOI: 10.1016/j.ultramic.2005.03.006. [Online]. Available: https://linkinghub.elsevier.com/retrieve/pii/S0304399105000513.

[129] X. Li, S. Q. Zheng, K. Egami, D. A. Agard, and Y. Cheng, "Influence of electron dose rate on electron counting images recorded with the K2 camera," *Journal of Structural Biology*, vol. 184, no. 2, pp. 251–260, 2013, ISSN: 10478477. DOI: 10.1016/j.jsb.2013.08.005.

[130] X Llopart and M Campbell, "First test measurements of a 64k pixel readout chip working in single photon counting mode," *Nuclear Instruments and Methods in Physics Research Section A: Accelerators, Spectrometers, Detectors and Associated Equipment*, vol. 509, no. 1-3, pp. 157–163, 2003, ISSN: 01689002. DOI: 10.1016/S0168-9002(03)01565-1.

[131] I. MacLaren, T. A. Macgregor, C. S. Allen, and A. I. Kirkland, "Detectors—The ongoing revolution in scanning transmission electron microscopy and why this important to material characterization," *APL Materials*, vol. 8, no. 11, p. 110 901, 2020, ISSN: 2166-532X. DOI: 10.1063/5.0026992.

[132] G. W. Paterson, R. J. Lamb, R. Ballabriga, D. Maneuski, V. O'Shea, and D. McGrouther, "Sub-100 nanosecond temporally resolved imaging with the Medipix3 direct electron detector," *Ultramicroscopy*, vol. 210, p. 112 917, 2020, arXiv:1905.11884 [cond-mat, physics:physics], ISSN: 03043991. DOI: 10.1016/j.ultramic.2019.112917. (visited on 09/26/2022).

[133] *MerlinEM-Technical-datasheet-3*. [Online]. Available: https://quantumdetectors.com/wp-content/uploads/2021/12/2885-MerlinEM-Technical-datasheet-3.pdf (visited on 08/17/2023).

[134] M. Esposito, J. Jakubek, G. Mettivier, S. Pospisil, P. Russo, and J. Solc, "Energy sensitive Timepix silicon detector for electron imaging," *Nuclear Instruments and Methods in Physics Research Section A: Accelerators, Spectrometers, Detectors and Associated Equipment*, vol. 652, no. 1, pp. 458–461, 2011, ISSN: 01689002. DOI: 10.1016/j.nima.2011.01.148.

[135] D. Jannis *et al.*, "Event driven 4D STEM acquisition with a Timepix3 detector: Microsecond dwell time and faster scans for high precision and low dose applications," *Ultramicroscopy*, vol. 233, p. 113 423, 2022, ISSN: 03043991. DOI: 10.1016/j.ultramic.2021.113423. (visited on 07/18/2023).

[136] C. Ophus, "Four-Dimensional Scanning Transmission Electron Microscopy (4D-STEM): From Scanning Nanodiffraction to Ptychography and Beyond," en, *Microscopy and Microanalysis*, vol. 25, no. 3, pp. 563–582, 2019, ISSN: 1431-9276, 1435-8115. DOI: 10.1017/S1431927619000497.

[137] J. Rodenburg, "The phase problem, microdiffraction and wavelength-limited resolution — a discussion," *Ultramicroscopy*, vol. 27, no. 4, pp. 413–422, 1989, ISSN: 03043991. DOI: 10.1016/0304-3991(89)90009-0.

[138] J. Rodenburg, B. McCallum, and P. Nellist, "Experimental tests on double-resolution coherent imaging via STEM," *Ultramicroscopy*, vol. 48, no. 3, pp. 304–314, 1993, ISSN: 03043991. DOI: 10.1016/0304-3991(93)90105-7.

[139] J. Rodenburg, A. Hurst, and A. Cullis, "Transmission microscopy without lenses for objects of unlimited size," *Ultramicroscopy*, vol. 107, no. 2-3, pp. 227–231, 2007, ISSN: 03043991. DOI: 10.1016/j.ultramic.2006.07.007. (visited on 11/06/2023).

[140] K. A. Nugent, "Coherent methods in the X-ray sciences," en, *Advances in Physics*, vol. 59, no. 1, pp. 1–99, 2010, ISSN: 0001-8732, 1460-6976. DOI: 10.1080/00018730903270926.

[141] P. D. Nellist, B. C. McCallum, and J. M. Rodenburg, "Resolution beyond the 'information limit' in transmission electron microscopy," *Nature*, vol. 374, no. 6523, pp. 630–632, 1995, ISSN: 0028-0836, 1476-4687. DOI: 10.1038/374630a0.

[142] Z. Chen *et al.*, "Electron ptychography achieves atomic-resolution limits set by lattice vibrations," *Science*, vol. 372, no. 6544, pp. 826–831, 2021, ISSN: 0036-8075, 1095-9203. DOI: 10.1126/science.abg2533.

[143] Von Walter Hoppe, "Beugung im Inhomogenen Prim~irstrahlwellenfeld. I. Prinzip einer Phasenmessung von Elektronenbeugungsinterferenzen," *Acta Cryst*, vol. A25, p. 495, 1969.

[144] J. Rodenburg and R. Bates, "The theory of super-resolution electron microscopy via Wigner-distribution deconvolution," en, *Philosophical Transactions of the Royal Society of London. Series A: Physical and Engineering Sciences*, vol. 339, no. 1655, pp. 521–553, 1992, ISSN: 0962-8428, 2054-0299. DOI: 10.1098/rsta.1992.0050.

[145] T. J. Pennycook, A. R. Lupini, H. Yang, M. F. Murfitt, L. Jones, and P. D. Nellist, "Efficient phase contrast imaging in STEM using a pixelated detector. Part 1: Experimental demonstration at atomic resolution," *Ultramicroscopy*, vol. 151, pp. 160–167, 2015, ISSN: 03043991. DOI: 10.1016/j.ultramic.2014.09.013. (visited on 11/06/2023).

[146] J. M. Rodenburg and H. M. L. Faulkner, "A phase retrieval algorithm for shifting illumination," en, *Applied Physics Letters*, vol. 85, no. 20, pp. 4795–4797, 2004, ISSN: 0003-6951, 1077-3118. DOI: 10.1063/1.1823034.

[147] Y. Jiang, "Electron ptychography of 2D materials to deep sub-ångström resolution," en, *Nature*, vol. 559, p. 343, 2018. DOI: https://doi.org/10.1038/s41586-018-0298-5.

[148] J. Song *et al.*, "Atomic Resolution Defocused Electron Ptychography at Low Dose with a Fast, Direct Electron Detector," en, *Scientific Reports*, vol. 9, no. 1, p. 3919, Mar. 2019, ISSN: 2045-2322. DOI: 10.1038/s41598-019-40413-z. [Online]. Available: https://www.nature.com/articles/s41598-019-40413-z (visited on 08/29/2023).

[149] H. Yang *et al.*, "Simultaneous atomic-resolution electron ptychography and Z-contrast imaging of light and heavy elements in complex nanostructures," *Nature Communications*, vol. 7, no. 1, p. 12 532, 2016, ISSN: 2041-1723. DOI: 10.1038/ncomms12532. (visited on 09/26/2022).

[150] A. M. Maiden and J. M. Rodenburg, "An improved ptychographical phase retrieval algorithm for diffractive imaging," *Ultramicroscopy*, vol. 109, no. 10, pp. 1256–1262, 2009, ISSN: 03043991. DOI: 10.1016/j.ultramic.2009.05.012.

[151] W. H. Press, S. A. Teukolsky, W. T. Vetterling, and B. P. Flannery, *Numerical recipes in C: The art of scientific computing,* en, Second Edition. Cambridge University Press, Jan. 1993, vol. 1, ISBN: 0 521 43108 5. (visited on 08/29/2023).

[152] H. Yang, J. G. Lozano, T. J. Pennycook, L. Jones, P. B. Hirsch, and P. D. Nellist, "Imaging screw dislocations at atomic resolution by aberration-corrected electron optical sectioning," *Nature Communications*, vol. 6, no. 1, p. 7266, 2015, ISSN: 2041-1723. DOI: 10.1038/ncomms8266.

[153] P. Favia, M. Bargallo Gonzales, E. Simoen, P. Verheyen, D. Klenov, and H. Bender, "Nanobeam Diffraction: Technique Evaluation and Strain Measurement on Complementary Metal Oxide Semiconductor Devices," *Journal of The Electrochemical Society*, vol. 158, no. 4, H438, 2011, ISSN: 00134651. DOI: 10.1149/1.3546851.

[154] A. Bridger, W. I. F. David, T. J. Wood, M. Danaie, and K. T. Butler, "Versatile domain mapping of scanning electron nanobeam diffraction datasets utilising variational autoencoders," *npj Computational Materials*, vol. 9, no. 1, p. 14, 2023, ISSN: 2057-3960. DOI: 10.1038/s41524-022-00960-y.

[155] H. Liu *et al.*, "Spatially resolved surface valence gradient and structural transformation of lithium transition metal oxides in lithium-ion batteries," *Physical Chemistry Chemical Physics*, vol. 18, no. 42, pp. 29 064–29 075, 2016, ISSN: 1463-9076, 1463-9084. DOI: 10.1039/C6CP05262B.

[156] M. Gallagher-Jones *et al.*, "Nanoscale mosaicity revealed in peptide microcrystals by scanning electron nanodiffraction," *Communications Biology*, vol. 2, no. 1, p. 26, 2019, ISSN: 2399-3642. DOI: 10.1038/s42003-018-0263-8.

[157] D. N. Johnstone, F. C. N. Firth, C. P. Grey, P. A. Midgley, M. J. Cliffe, and S. M. Collins, "Direct Imaging of Correlated Defect Nanodomains in a Metal–Organic Framework," en, *Journal of the American Chemical Society*, vol. 142, no. 30, pp. 13 081–13 089, Jul. 2020, ISSN: 0002-7863, 1520-5126. DOI: 10.1021/jacs.0c04468. [Online]. Available: https://pubs.acs.org/doi/10.1021/jacs.0c04468 (visited on 09/04/2023).

[158] C. Ophus *et al.*, "Automated Crystal Orientation Mapping in py4DSTEM using Sparse Correlation Matching," en, *Microscopy and Microanalysis*, vol. 28, no. 2, pp. 390–403, Apr. 2022, arXiv:2111.00171 [cond-mat], ISSN: 1431-9276, 1435-8115. DOI: 10.1017/S1431927622000101. [Online]. Available: http://arxiv.org/abs/2111.00171 (visited on 03/21/2024).

[159] G. C. Ortiz, M. Zhu, L. Dou, and J. Hwang, "4D-STEM Quantification of Nanoscale Ordered Domains in Organic Semiconducting Polymers," *Microscopy and Microanalysis*, vol. 26, no. S2, pp. 1740–1742, 2020, ISSN: 1431-9276, 1435-8115. DOI: 10.1017/S1431927620019170.

[160] C. Mahr *et al.*, "Theoretical study of precision and accuracy of strain analysis by nano-beam electron diffraction," *Ultramicroscopy*, vol. 158, pp. 38–48, 2015, ISSN: 03043991. DOI: 10.1016/j.ultramic.2015.06.011.

[161] T. Grieb *et al.*, "Optimization of NBED simulations for disc-detection measurements," *Ultramicroscopy*, vol. 181, pp. 50–60, 2017, ISSN: 03043991. DOI: 10.1016/j.ultramic.2017.04.015.

[162] M. E. Holtz, E. Padgett, A. C. Johnston-Peck, I. Levin, D. A. Muller, and A. A. Herzing, "Mapping Polar Distortions using Nanobeam Electron Diffraction and a Cepstral Approach," *Microscopy and Microanalysis*, vol. 29, no. 4, pp. 1422–1435, 2023, ISSN: 1431-9276, 1435-8115. DOI: 10.1093/micmic/ozad070.

[163] M. Wu, C. Harreiß, C. Ophus, M. Johnson, R. H. Fink, and E. Spiecker, "Seeing structural evolution of organic molecular nano-crystallites using 4D scanning confocal electron diffraction (4D-SCED)," *Nature Communications*, vol. 13, no. 1, p. 2911, 2022, ISSN: 2041-1723. DOI: 10.1038/s41467-022-30413-5.

[164] P. Nellist, E. Cosgriff, G. Behan, and A. Kirkland, "Imaging Modes for Scanning Confocal Electron Microscopy in a Double Aberration-Corrected Transmission Electron Microscope," *Microscopy and Microanalysis*, vol. 14, no. 1, pp. 82–88, 2008, ISSN: 1431-9276, 1435-8115. DOI: 10.1017/S1431927608080057.

[165] F. Lin, I. M. Markus, M. M. Doeff, and H. L. Xin, "Chemical and Structural Stability of Lithium-Ion Battery Electrode Materials under Electron Beam," *Scientific Reports*, vol. 4, no. 1, p. 5694, 2014, ISSN: 2045-2322. DOI: 10.1038/srep05694.

[166] R. Egerton, "Mechanisms of radiation damage in beam-sensitive specimens, for TEM accelerating voltages between 10 and 300 kV," *Microscopy Research and Technique*, vol. 75, no. 11, pp. 1550–1556, 2012, ISSN: 1059910X. DOI: 10.1002/jemt.22099.

[167] R. Egerton, "Control of radiation damage in the TEM," *Ultramicroscopy*, vol. 127, pp. 100–108, 2013, ISSN: 03043991. DOI: 10.1016/j.ultramic.2012.07.006.

[168] N. Jiang, "Electron beam damage in oxides: A review," *Reports on Progress in Physics*, vol. 79, no. 1, p. 016 501, 2016, ISSN: 0034-4885, 1361-6633. DOI: 10.1088/0034-4885/79/1/016501.

[169] J.-H. Shim, H. Kang, Y.-M. Kim, and S. Lee, "In Situ Observation of the Effect of Accelerating Voltage on Electron Beam Damage of Layered Cathode Materials for Lithium-Ion Batteries," en, *ACS Appl. Mater. Interfaces*, vol. 11, 44293−44299, 2019. DOI: 10.1021/acsami.9b15608.

[170] P. Lu, P. Yan, E. Romero, E. D. Spoerke, J.-G. Zhang, and C.-M. Wang, "Observation of Electron-Beam-Induced Phase Evolution Mimicking the Effect of the Charge–Discharge Cycle in Li-Rich Layered Cathode Materials Used for Li Ion Batteries," *Chemistry of Materials*, vol. 27, no. 4, pp. 1375–1380, 2015, ISSN: 0897-4756, 1520-5002. DOI: 10.1021/cm5045573.

[171] H. Buschmann *et al.*, "Structure and dynamics of the fast lithium ion conductor "Li7La3Zr2O12"," *Physical Chemistry Chemical Physics*, vol. 13, no. 43, p. 19 378, 2011, ISSN: 1463-9076, 1463-9084. DOI: 10.1039/c1cp22108f.

[172] F. Lin *et al.*, "Surface reconstruction and chemical evolution of stoichiometric layered cathode materials for lithium-ion batteries," en, *Nature Communications*, vol. 5, p. 3529, 2014. DOI: 10.1038/ncomms4529.

[173] L. Bursill and D. J. Smith, "Electron irradiation effects in (Cs,Ba)-hollandites," *Journal of Solid State Chemistry*, vol. 69, no. 2, pp. 343–354, 1987, ISSN: 00224596. DOI: 10.1016/0022-4596(87)90092-2.

[174] X. San, B. Zhang, J. Wang, B. Wu, and X. Ma, "In situ tracking the reversible spinel-rocksalt structural transformation between Mn3O4 and MnO," *Micron*, vol. 92, pp. 13–18, 2017, ISSN: 09684328. DOI: 10.1016/j.micron.2016.09.008.

[175] L. Jones *et al.*, "Optimising multi-frame ADF-STEM for high-precision atomic-resolution strain mapping," *Ultramicroscopy*, vol. 179, pp. 57–62, 2017, ISSN: 03043991. DOI: 10.1016/j.ultramic.2017.04.007.

[176] L. Jones *et al.*, "Managing dose-, damage- and data-rates in multi-frame spectrum-imaging," *Microscopy*, vol. 67, no. suppl_1, pp. i98–i113, 2018, ISSN: 2050-5698, 2050-5701. DOI: 10.1093/jmicro/dfx125.

[177] A. Velazco, A. Béché, D. Jannis, and J. Verbeeck, "Reducing electron beam damage through alternative STEM scanning strategies, Part I: Experimental findings," *Ultramicroscopy*, vol. 232, p. 113 398, 2022, ISSN: 03043991. DOI: 10.1016/j.ultramic.2021.113398.

[178] C. S. Goldsmith and S. E. Miller, "Modern Uses of Electron Microscopy for Detection of Viruses," *Clinical Microbiology Reviews*, vol. 22, no. 4, pp. 552–563, 2009, ISSN: 0893-8512, 1098-6618. DOI: 10.1128/CMR.00027-09.

[179] X. Wang, Y. Li, and Y. S. Meng, "Cryogenic Electron Microscopy for Characterizing and Diagnosing Batteries," en, *Joule*, vol. 2, pp. 2225–2234, DOI: https://doi.org/10.1016/j.joule.2018.10.005.

[180] S. Findlay, N. Lugg, N. Shibata, L. Allen, and Y. Ikuhara, "Prospects for lithium imaging using annular bright field scanning transmission electron microscopy: A theoretical study," *Ultramicroscopy*, vol. 111, no. 8, pp. 1144–1154, 2011, ISSN: 03043991. DOI: 10.1016/j.ultramic.2011.03.005.

[181] H. Zhang and Y. Qi, "Investigating lithium metal anodes with nonaqueous electrolytes for safe and high-performance batteries," *Sustainable Energy & Fuels*, vol. 6, no. 4, pp. 954–970, 2022, ISSN: 2398-4902. DOI: 10.1039/D1SE01739J.

[182] F. Wang *et al.*, "Chemical Distribution and Bonding of Lithium in Intercalated Graphite: Identification with Optimized Electron Energy Loss Spectroscopy," *ACS Nano*, vol. 5, no. 2, pp. 1190–1197, 2011, ISSN: 1936-0851, 1936-086X. DOI: 10.1021/nn1028168.

[183] R. R. Unocic, K. L. Jungjohann, B. L. Mehdi, N. D. Browning, and C. Wang, "*In situ* electrochemical scanning/transmission electron microscopy of electrode–electrolyte interfaces," *MRS Bulletin*, vol. 45, no. 9, pp. 738–745, 2020, ISSN: 0883-7694, 1938-1425. DOI: 10.1557/mrs.2020.226.

[184] C.-M. Wang, "In situ transmission electron microscopy and spectroscopy studies of rechargeable batteries under dynamic operating conditions: A retrospective and perspective view," *Journal of Materials Research*, vol. 30, no. 3, pp. 326–339, 2015, ISSN: 0884-2914, 2044-5326. DOI: 10.1557/jmr.2014.281.

[185] Rayleigh, "XXXI. *Investigations in optics, with special reference to the spectroscope*," en, *The London, Edinburgh, and Dublin Philosophical Magazine and Journal of Science*, vol. 8, no. 49, pp. 261–274, Oct. 1879, ISSN: 1941-5982, 1941-5990. DOI: 10.1080/14786447908639684. [Online]. Available: https://www.tandfonline.com/doi/full/10.1080/14786447908639684 (visited on 03/30/2024).

[186] O. Scherzer, "Uber einige Fehler von Elektronenlinsen.," *Z. Physik 101*, vol. 101, p. 593, 1936.

[187] Z. Shao and A. Crewe, "Ideal lenses and the Scherzer theorem: A supplement," *Ultramicroscopy*, vol. 26, no. 4, pp. 385–388, 1988, ISSN: 03043991. DOI: 10.1016/0304-3991(88)90237-9.

[188] "Aberration-Corrected Analytical Transmission Electron Microscopy," en, in *Aberration□Corrected Analytical Transmission Electron Microscopy*, R. Brydson, Ed., 1st ed., Wiley, Sep. 2011, ISBN: 978-0-470-51851-9 978-1-119-97884-8. DOI: 10.1002/9781119978848.fmatter. [Online]. Available: https://onlinelibrary.wiley.com/doi/10.1002/9781119978848.fmatter (visited on 09/19/2022).

[189] O. Krivanek, N Dellby, A. Spence, R. Camps, and L. Brown, "Aberration correction in the STEM," in *Electron Microscopy and Analysis 1997*, 1st ed., Boca Raton: CRC Press, 1997, pp. 35–40, ISBN: 978-1-00-306305-6. DOI: 10.1201/9781003063056-8.

[190] N. F. Mott and H. S. W. Massey, *The Theory of Atomic Collisions*, en, 2nd Edition. Oxford Univ. Press, 1963. [Online]. Available: https://www.science.org/doi/10.1126/science.112.2900.128.a (visited on 09/13/2023).

[191] C. J. Humphreys, "The scattering of fast electrons by crystals," *Reports on Progress in Physics*, vol. 42, no. 11, pp. 1825–1887, 1979, ISSN: 0034-4885, 1361-6633. DOI: 10.1088/0034-4885/42/11/002.

[192] E. J. Kirkland, *Advanced Computing in Electron Microscopy*, en. Boston, MA: Springer US, 2010, ISBN: 978-1-4419-6532-5 978-1-4419-6533-2. DOI: 10.1007/978-1-4419-6533-2. [Online]. Available: http://link.springer.com/10.1007/978-1-4419-6533-2 (visited on 09/19/2022).

[193] Cowley. J. M., *Diffraction Physics*. Amsterdam: North-Holland, 1981.

[194] C. J. Humphreys, "Theory of Electron Scattering and Electron Diffraction," in *Scattering*, Elsevier, 2002, pp. 1287–1303, ISBN: 978-0-12-613760-6. DOI: 10.1016/B978-012613760-6/50069-3. (visited on 08/07/2023).

[195] J. Yang, "Ultrafast Electron Microscopy with Relativistic Femtosecond Electron Pulses," in *Electron Microscopy - Novel Microscopy Trends*, M. Arita and N. Sakaguchi, Eds., IntechOpen, 2019, ISBN: 978-1-83881-882-1 978-1-83881-883-8. DOI: 10.5772/intechopen.81405.

[196] A. P. Pogany and P. S. Turner, "Reciprocity in electron diffraction and microscopy," *Acta Crystallographica Section A: Crystal Physics, Diffraction, Theoretical and General Crystallography*, vol. 24, no. 1, pp. 103–109, 1968, ISSN: 05677394. DOI: 10.1107/S0567739468000136.

[197] J. M. Cowley, "IMAGE CONTRAST IN A TRANSMISSION SCANNING ELECTRON MICROSCOPE," *Applied Physics Letters*, vol. 15, no. 2, pp. 58–59, 1969, ISSN: 0003-6951, 1077-3118. DOI: 10.1063/1.1652901.

[198] S. Findlay, L. Allen, M. Oxley, and C. Rossouw, "Lattice-resolution contrast from a focused coherent electron probe. Part II," *Ultramicroscopy*, vol. 96, no. 1, pp. 65–81, 2003, ISSN: 03043991. DOI: 10.1016/S0304-3991(02)00381-9.

[199] A.V. Crewe, D. N. Eggenberger, J. Wall, and L. M. Welter, "Electron Gun Using a Field Emission Source," *Rev. Sci. Instrum.*, vol. 39, no. 576-583, 1968. DOI: https://doi.org/10.1063/1.1683435.

[200] P. E. Batson, N. Dellby, and O. L. Krivanek, "Sub-ångstrom resolution using aberration corrected electron optics," *Nature*, vol. 418, no. 6898, pp. 617–620, 2002, ISSN: 0028-0836, 1476-4687. DOI: 10.1038/nature00972.

[201] N. D. Browning, M. F. Chisholm, and S. J. Pennycook, "Atomic-resolution chemical analysis using a scanning transmission electron microscope," *Nature*, vol. 366, no. 6451, pp. 143–146, 1993, ISSN: 0028-0836, 1476-4687. DOI: 10.1038/366143a0.

[202] J. Zuo, M. Gao, J. Tao, B. Li, R. Twesten, and I. Petrov, "Coherent nano-area electron diffraction," *Microscopy Research and Technique*, vol. 64, no. 5-6, pp. 347–355, 2004, ISSN: 1059-910X, 1097-0029. DOI: 10.1002/jemt.20096.

[203] S. Findlay, N. Shibata, H. Sawada, E. Okunishi, Y. Kondo, and Y. Ikuhara, "Dynamics of annular bright field imaging in scanning transmission electron microscopy," *Ultramicroscopy*, vol. 110, no. 7, pp. 903–923, 2010, ISSN: 03043991. DOI: 10.1016/j.ultramic.2010.04.004.

[204] S. D. Findlay, R. Huang, R. Ishikawa, N. Shibata, and Y. Ikuhara, "Direct visualization of lithium via annular bright field scanning transmission electron microscopy: A review," *Microscopy*, jmicro;dfw041v1, 2016, ISSN: 2050-5698, 2050-5701. DOI: 10.1093/jmicro/dfw041.

[205] J. Fatermans, A. den Dekker, K. Müller-Caspary, N. Gauquelin, J. Verbeeck, and S. Van Aert, "Atom column detection from simultaneously acquired ABF and ADF STEM images," en, *Ultramicroscopy*, vol. 219, p. 113 046, 2020, ISSN: 03043991. DOI: 10.1016/j.ultramic.2020.113046.

[206] P. Nellist and S. Pennycook, "Incoherent imaging using dynamically scattered coherent electrons," *Ultramicroscopy*, vol. 78, no. 1-4, pp. 111–124, 1999, ISSN: 03043991. DOI: 10.1016/S0304-3991(99)00017-0.

[207] P. Nellist and S. Pennycook, "The principles and interpretation of annular dark-field Z-contrast imaging," in *Advances in Imaging and Electron Physics*, vol. 113, Elsevier, 2000, pp. 147–203, ISBN: 978-0-12-014755-7. DOI: 10.1016/S1076-5670(00)80013-0.

[208] J. Wall, M. Isacson, and J. P. Langmore, "The collection of scattered electrons in dark field electron microscopy. II Inelastic scattering," vol. 39, no. 4, pp. 359–374, 1979.

[209] L. Reimer, "Electron Diffraction Methods in TEM, STEM and SEM," *Scanning*, vol. 2, no. 1, pp. 3–51, Jan. 1979, ISSN: 0161-0457. DOI: https://doi.org/10.1002/sca.4950020101.

[210] P. D. Nellist, "The Principles of STEM Imaging," en, in *Scanning Transmission Electron Microscopy*, S. J. Pennycook and P. D. Nellist, Eds., New York, NY: Springer New York, 2011, pp. 91–115, ISBN: 978-1-4419-7199-9 978-1-4419-7200-2. DOI: 10.1007/978-1-4419-7200-2_2. (visited on 08/05/2023).

[211] J. A. Hachtel, J. C. Idrobo, and M. Chi, "Sub-ångstrom electric field measurements on a universal detector in a scanning transmission electron microscope," *Advanced Structural and Chemical Imaging*, vol. 4, no. 1, p. 10, 2018, ISSN: 2198-0926. DOI: 10.1186/s40679-018-0059-4.

[212] M. P. Oxley, A. R. Lupini, and S. J. Pennycook, "Ultra-high resolution electron microscopy," en, *Reports on Progress in Physics*, vol. 80, no. 2, p. 026 101, Feb. 2017, ISSN: 0034-4885, 1361-6633. DOI: 10.1088/1361-6633/80/2/026101. [Online]. Available: https://iopscience.iop.org/article/10.1088/1361-6633/80/2/026101 (visited on 03/31/2024).

[213] R Hartmann *et al.*, "pnCCDs as Direct Electron Imaging Detectors for TEMs," *Microscopy and Microanalysis*, vol. 13, no. S02, 2007, ISSN: 1431-9276, 1435-8115. DOI: 10.1017/S143192760707821X.

[214] PNDetector GmbH, *User manual for the pnCCD*, 2018. (visited on 09/11/2023).

[215] R. Zhang, S. Yang, H. Li, T. Zhai, and H. Li, "Air sensitivity of electrode materials in Li/Na ion batteries: Issues and strategies," *InfoMat*, vol. 4, no. 6, e12305, 2022, ISSN: 2567-3165, 2567-3165. DOI: 10.1002/inf2.12305.

[216] M. Haider, S. Uhlemann, E. Schwan, H. Rose, B. Kabius, and K. Urban, "Electron microscopy image enhanced," *Nature*, vol. 392, no. 6678, pp. 768–769, 1998, ISSN: 0028-0836, 1476-4687. DOI: 10.1038/33823.

[217] H. Sawada *et al.*, "Measurement method of aberration from Ronchigram by autocorrelation function," *Ultramicroscopy*, vol. 108, no. 11, pp. 1467–1475, Oct. 2008, ISSN: 03043991. DOI: 10.1016/j.ultramic.2008.04.095.

[218] L. Jones *et al.*, "Smart Align—a new tool for robust non-rigid registration of scanning microscope data," *Advanced Structural and Chemical Imaging*, vol. 1, no. 1, p. 8, 2015, ISSN: 2198-0926. DOI: 10.1186/s40679-015-0008-4.

[219] B. Zitová and J. Flusser, "Image registration methods: A survey," *Image and Vision Computing*, vol. 21, no. 11, pp. 977–1000, 2003, ISSN: 02628856. DOI: 10.1016/S0262-8856(03)00137-9.

[220] H. Landau, "Sampling, data transmission, and the Nyquist rate," *Proceedings of the IEEE*, vol. 55, no. 10, pp. 1701–1706, 1967, ISSN: 0018-9219. DOI: 10.1109/PROC.1967.5962.

[221] H. Yang, T. J. Pennycook, and P. D. Nellist, "Efficient phase contrast imaging in STEM using a pixelated detector. Part II: Optimisation of imaging conditions," *Ultramicroscopy*, vol. 151, pp. 232–239, 2015, ISSN: 03043991. DOI: 10.1016/j.ultramic.2014.10.013.

[222] F. Yi, P. Tiemeijer, and P. M. Voyles, "Flexible formation of coherent probes on an aberration-corrected STEM with three condensers," *Journal of Electron Microscopy*, vol. 59, no. S1, S15–S21, 2010, ISSN: 0022-0744, 1477-9986. DOI: 10.1093/jmicro/dfq052.

[223] B. Eckert, “Image Processing for X-ray and Electron Detection Based on Neural Networks for Pixelated Semiconductor Detectors,” en, PhD Thesis, Universitat Siegen, Siegen, 2022.

[224] A. R. Lupini, M. P. Oxley, and S. V. Kalinin, “Pushing the limits of electron ptychography,” *Science*, vol. 362, no. 6413, pp. 399–400, 2018, ISSN: 0036-8075, 1095-9203. DOI: 10.1126/science.aau7620.

[225] C. M. O’Leary *et al.*, “Phase reconstruction using fast binary 4D STEM data,” *Applied Physics Letters*, vol. 116, no. 12, p. 124 101, 2020, ISSN: 0003-6951, 1077-3118. DOI: 10.1063/1.5143213.

[226] E. Rajaby and S. M. Sayedi, “A structured review of sparse fast Fourier transform algorithms,” *Digital Signal Processing*, vol. 123, p. 103 403, 2022, ISSN: 10512004. DOI: 10.1016/j.dsp.2022.103403.

[227] *Floating-point numeric types (C# reference)*, Sep. 2022. [Online]. Available: https://learn.microsoft.com/en-us/dotnet/csharp/language-reference/builtin-types/floating-point-numeric-types (visited on 10/01/2023).

[228] D. C. Joy, S. Luo, R. Gauvin, P. Hovington, and N. Evans, “Experimental Measurements of Electron Stopping Power at Low Energies,” en, *Scanning Microscopy*, vol. 10, no. 3, pp. 653–666, 1996, ISSN: ISSN 1042-0150;

[229] M. Berger, J. Coursey, and M. Zucker, *ESTAR, PSTAR, and ASTAR: Computer Programs for Calculating Stopping-Power and Range Tables for Electrons, Protons, and Helium Ions (version 1.21)*, en, Jan. 1999.

[230] G. McMullan, A. Faruqi, D. Clare, and R. Henderson, “Comparison of optimal performance at 300keV of three direct electron detectors for use in low dose electron microscopy,” *Ultramicroscopy*, vol. 147, pp. 156–163, 2014, ISSN: 03043991. DOI: 10.1016/j.ultramic.2014.08.002.

[231] S. Ihle *et al.*, “Direct measurement of the position accuracy for low energy X-ray photons with a pnCCD,” *Journal of Instrumentation*, vol. 12, no. 02, P02005–P02005, 2017, ISSN: 1748-0221. DOI: 10.1088/1748-0221/12/02/P02005.

[232] B Eckert, S Aschauer, E Hedley, M Huth, P Majewski, and L Strüder, “Electron Image Reconstruction for Pixelated Semiconductor Tracking Detectors Based on Neural Networks,” *Microscopy and Microanalysis*, vol. 28, no. S1, pp. 3040–3042, 2022, ISSN: 1435-8115, 1431-9276. DOI: 10.1017/S1431927622011357.

[233] C. C. Aggarwal, *Neural Networks and Deep Learning: A Textbook*. Cham: Springer International Publishing, 2018, ISBN: 978-3-319-94462-3 978-3-319-94463-0. DOI: 10.1007/978-3-319-94463-0. [Online]. Available: http://link.springer.com/10.1007/978-3-319-94463-0 (visited on 05/30/2023).

[234] D. Silver *et al.*, "A general reinforcement learning algorithm that masters chess, shogi, and Go through self-play," *Science*, vol. 362, no. 6419, pp. 1140–1144, 2018, ISSN: 0036-8075, 1095-9203. DOI: 10.1126/science.aar6404.

[235] I. G. a. Y. B. a. A. Courville, *Deep Learning*. MIT Press, 2016, ISBN: 0-262-03561-8. [Online]. Available: http://www.deeplearningbook.org.

[236] Y. LeCun *et al.*, "Backpropagation Applied to Handwritten Zip Code Recognition," *Neural Computation*, vol. 1, no. 4, pp. 541–551, 1989, ISSN: 0899-7667, 1530-888X. DOI: 10.1162/neco.1989.1.4.541.

[237] R. Yamashita, M. Nishio, R. K. G. Do, and K. Togashi, "Convolutional neural networks: An overview and application in radiology," en, *Insights into Imaging*, vol. 9, no. 4, pp. 611–629, 2018, ISSN: 1869-4101. DOI: 10.1007/s13244-018-0639-9.

[238] A. D. Rasamoelina, F. Adjailia, and P. Sincak, "A Review of Activation Function for Artificial Neural Network," in *2020 IEEE 18th World Symposium on Applied Machine Intelligence and Informatics (SAMI)*, Herlany, Slovakia: IEEE, 2020, pp. 281–286, ISBN: 978-1-72813-149-8. DOI: 10.1109/SAMI48414.2020.9108717.

[239] Y. LeCun, Y. Bengio, and G. Hinton, "Deep learning," en, *Nature*, vol. 521, no. 7553, pp. 436–444, 2015, ISSN: 0028-0836, 1476-4687. DOI: 10.1038/nature14539.

[240] G. M. Foody, A. Mathur, C. Sanchez-Hernandez, and D. S. Boyd, "Training set size requirements for the classification of a specific class," *Remote Sensing of Environment*, vol. 104, no. 1, pp. 1–14, 2006, ISSN: 00344257. DOI: 10.1016/j.rse.2006.03.004.

[241] C. A. Ramezan, T. A. Warner, A. E. Maxwell, and B. S. Price, "Effects of Training Set Size on Supervised Machine-Learning Land-Cover Classification of Large-Area High-Resolution Remotely Sensed Data," *Remote Sensing*, vol. 13, no. 3, p. 368, 2021, ISSN: 2072-4292. DOI: 10.3390/rs13030368.

[242] S. Kapoor and A. Narayanan, *Leakage and the Reproducibility Crisis in ML-based Science*, en, arXiv:2207.07048 [cs, stat], Jul. 2022. [Online]. Available: http://arxiv.org/abs/2207.07048 (visited on 05/30/2023).

[243] E. Yagis *et al.*, "Effect of data leakage in brain MRI classification using 2D convolutional neural networks," *Scientific Reports*, vol. 11, no. 1, p. 22 544, 2021, ISSN: 2045-2322. DOI: 10.1038/s41598-021-01681-w.

[244] R. D. Shannon, "Revised Effective Ionic Radii and Systematic Studies of Interatomic Distances In Halides and Chalcogenides," *Acta Crystallographica Section A*, vol. 32, pp. 751–767, 1976.

[245] L. Jones, A. Varambhia, H. Sawada, and P. Nellist, "An optical configuration for fastidious STEM detector calibration and the effect of the objective-lens prefield: AN OPTICAL CONFIGURATION FOR FASTIDIOUS STEM DETECTOR CALIBRATION," en, *Journal of Microscopy*, vol. 270, no. 2, pp. 176–187, May 2018, ISSN: 00222720. DOI: 10.1111/jmi.12672. [Online]. Available: https://onlinelibrary.wiley.com/doi/10.1111/jmi.12672 (visited on 08/08/2023).

[246] R. N. Bracewell, *The Fourier transform and its applications* (McGraw-Hill series in electrical and computer engineering Circuits and systems), eng, 3. ed. Boston: McGraw-Hill, 2000, ISBN: 978-0-07-116043-8 978-0-07-303938-1.

[247] "CHAPTER I - Fourier Series and Integrals," in *Partial Differential Equations in Physics*, Elsevier, 1949, ISBN: 978-0-12-654658-3. DOI: 10.1016/B978-0-12-654658-3.50001-X.

[248] R. Hovden, Y. Jiang, H. L. Xin, and L. F. Kourkoutis, "Periodic Artifact Reduction in Fourier Transforms of Full Field Atomic Resolution Images," en, *Microscopy and Microanalysis*, vol. 21, no. 2, pp. 436–441, Apr. 2015, ISSN: 1431-9276, 1435-8115. DOI: 10.1017/S1431927614014639. [Online]. Available: https://academic.oup.com/mam/article/21/2/436/6897007 (visited on 08/07/2023).

[249] A. L. Patterson, "A Fourier Series Method for the Determination of the Components of Interatomic Distances in Crystals," *Physical Review*, vol. 46, no. 5, pp. 372–376, 1934, ISSN: 0031-899X. DOI: 10.1103/PhysRev.46.372.

[250] D. Sherwood and J. Cooper, *Crystals, X-rays and Proteins*. Oxford University Press, Nov. 2010, ISBN: 978-0-19-955904-6. DOI: 10.1093/acprof:oso/9780199559046.001.0001.

[251] M. Barré and M. Catti, "Neutron diffraction study of the β′ and γ phases of LiFeO2," *Journal of Solid State Chemistry*, vol. 182, no. 9, pp. 2549–2554, 2009, ISSN: 00224596. DOI: 10.1016/j.jssc.2009.06.029.

[252] J. N. Reimers, E. W. Fuller, E. Rossen, and J. R. Dahn, "Synthesis and Electrochemical Studies of LiMnO2 Prepared at Low Temperatures," *Journal of The Electrochemical Society*, vol. 140, no. 12, pp. 3396–3401, 1993, ISSN: 0013-4651, 1945-7111. DOI: 10.1149/1.2221101.

[253] G Pistoia, "Synthesis of LiMnO2 and its characterization as a cathode for rechargeable Li cells," *Solid State Ionics*, vol. 78, no. 1-2, pp. 115–122, 1995, ISSN: 01672738. DOI: 10.1016/0167-2738(95)00018-2.

[254] L. Croguennec, P. Deniard, R. Brec, and A. Lecerf, "Preparation, physical and structural characterization of LiMnO2 samples with variable cationic disorder," *Journal of Materials Chemistry*, vol. 5, no. 11, p. 1919, 1995, ISSN: 0959-9428, 1364-5501. DOI: 10.1039/jm9950501919.

[255] G. Vitins and K. West, "Lithium Intercalation into Layered LiMnO2," *Journal of The Electrochemical Society*, vol. 144, no. 8, pp. 2587–2592, 1997, ISSN: 0013-4651, 1945-7111. DOI: 10.1149/1.1837869.

[256] M. Tian, Y. Gao, Z. Wang, and L. Chen, "Understanding structural stability of monoclinic LiMnO $_2$ and NaMnO $_2$ upon de-intercalation," *Physical Chemistry Chemical Physics*, vol. 18, no. 26, pp. 17 345–17 350, 2016, ISSN: 1463-9076, 1463-9084. DOI: 10.1039/C6CP02019D.

[257] T. Uyama, K. Mukai, and I. Yamada, "High-pressure synthesis and electrochemical properties of tetragonal LiMnO $_2$," *RSC Advances*, vol. 8, no. 46, pp. 26 325–26 334, 2018, ISSN: 2046-2069. DOI: 10.1039/C8RA03722A.

[258] Y.-M. Chiang, H. Wang, and Y.-I. Jang, "Electrochemically Induced Cation Disorder and Phase Transformations in Lithium Intercalation Oxides," *Chemistry of Materials*, vol. 13, no. 1, pp. 53–63, 2001, ISSN: 0897-4756, 1520-5002. DOI: 10.1021/cm000569z.

[259] X. Zhu *et al.*, "LiMnO2 cathode stabilized by interfacial orbital ordering for sustainable lithium-ion batteries," *Nature Sustainability*, vol. 4, no. 5, pp. 392–401, 2020, ISSN: 2398-9629. DOI: 10.1038/s41893-020-00660-9.

[260] D. H. Jang, Y. J. Shin, and S. M. Oh, "Dissolution of Spinel Oxides and Capacity Losses in 4 V Li / Li x Mn2 O 4 Cells," *Journal of The Electrochemical Society*, vol. 143, no. 7, pp. 2204–2211, 1996, ISSN: 0013-4651, 1945-7111. DOI: 10.1149/1.1836981.

[261] C. Zhan *et al.*, "Mn(II) deposition on anodes and its effects on capacity fade in spinel lithium manganate–carbon systems," en, *Nature Communications*, vol. 4, no. 1, p. 2437, Sep. 2013, ISSN: 2041-1723. DOI: 10.1038/ncomms3437. [Online]. Available: https://www.nature.com/articles/ncomms3437 (visited on 12/13/2023).

[262] R. A. House *et al.*, "Lithium manganese oxyfluoride as a new cathode material exhibiting oxygen redox," *Energy & Environmental Science*, vol. 11, no. 4, pp. 926–932, 2018, ISSN: 1754-5692, 1754-5706. DOI: 10.1039/C7EE03195E.

[263] Z. Cai *et al.*, "Thermodynamically Driven Synthetic Optimization for Cation□Disordered Rock Salt," *Advanced Energy Materials*, p. 2 103 923, 2022.

[264] D. D. L. Chung, "Graphite Review," *Journal of Materials Science*, vol. 37, pp. 1–15, 2002.

[265] H. Sha, J. Cui, and R. Yu, "Deep sub-angstrom resolution imaging by electron ptychography with misorientation correction," en, *Science Advances*, vol. 8, no. 19, eabn2275, 2022, ISSN: 2375-2548. DOI: 10.1126/sciadv.abn2275.

[266] H. Sha *et al.*, "Sub-nanometer-scale mapping of crystal orientation and depth-dependent structure of dislocation cores in SrTiO3," *Nature Communications*, vol. 14, no. 1, p. 162, 2023, ISSN: 2041-1723. DOI: 10.1038/s41467-023-35877-7.

[267] Henrich, Viktor E., *The Surface Science of Metal Oxides*, illustrated, reprint. Cambridge University Press, 1994, ISBN: 0-521-56687-8 978-0-521-56687-2. (visited on 11/08/2023).

[268] H. A. Al-Abadleh and V. H. Grassian, "Oxide surfaces as environmental interfaces," *Surface Science Reports*, vol. 52, no. 3-4, pp. 63–161, 2003, ISSN: 01675729. DOI: 10.1016/j.surfrep.2003.09.001.

[269] J. F. Banfield and H. Zhang, "Nanoparticles in the Environment," *Reviews in Mineralogy and Geochemistry*, vol. 44, no. 1, pp. 1–58, Jan. 2001, ISSN: 1529-6466. DOI: 10.2138/rmg.2001.44.01.

[270] R. A. House *et al.*, "Detection of trapped molecular O_2 in a charged Li-rich cathode by Neutron PDF," *Energy & Environmental Science*, vol. 15, no. 1, pp. 376–383, 2022, ISSN: 1754-5692, 1754-5706. DOI: 10.1039/D1EE02237G.

[271] X. Xu *et al.*, "Li_2NiO_2F a New Oxyfluoride Disordered Rocksalt Cathode Material.," *Journal of The Electrochemical Society*, vol. 168, no. 8, p. 080 521, 2021, ISSN: 0013-4651, 1945-7111. DOI: 10.1149/1945-7111/ac1be1.

[272] R. Egerton, "Radiation damage to organic and inorganic specimens in the TEM," en, *Micron*, vol. 119, pp. 72–87, 2019, ISSN: 09684328. DOI: 10.1016/j.micron.2019.01.005.

[273] R. Egerton, R. McLeod, F. Wang, and M. Malac, "Basic questions related to electron-induced sputtering in the TEM," *Ultramicroscopy*, vol. 110, no. 8, pp. 991–997, 2010, ISSN: 03043991. DOI: 10.1016/j.ultramic.2009.11.003.

[274] N. Takeda *et al.*, "Reversible Li storage for nanosize cation/anion-disordered rocksalt-type oxyfluorides: LiMoO 2 – x LiF ($0 \leq x \leq 2$) binary system," *Journal of Power Sources*, vol. 367, pp. 122–129, 2017, ISSN: 03787753. DOI: 10.1016/j.jpowsour.2017.09.060.

[275] D. Egusa, K. Kawaguchi, and E. Abe, “Direct Observations of Precursor Short-Range Order Clusters of Solute Atoms in a LPSO-Forming Mg-Zn-Gd Ternary Alloy,” *Frontiers in Materials*, vol. 6, p. 266, 2019, ISSN: 2296-8016. DOI: 10.3389/fmats.2019.00266.